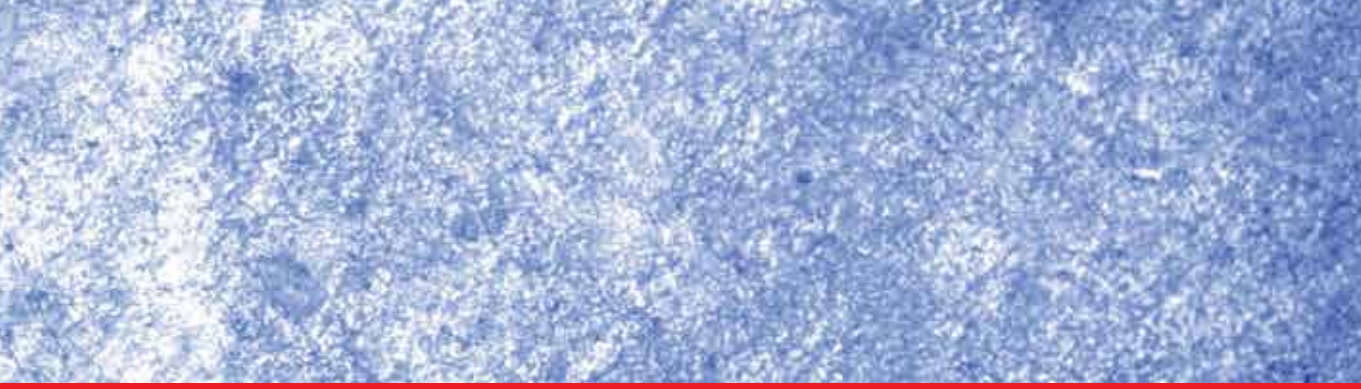

IntechOpen

High Performance Concrete Technology and Applications

Edited by Salih Yilmaz and Hayri Baytan Ozmen

HIGH PERFORMANCE CONCRETE TECHNOLOGY AND APPLICATIONS

Edited by **Salih Yılmaz**
and **Hayri Baytan Özmen**

High Performance Concrete Technology and Applications
http://dx.doi.org/10.5772/61562
Edited by Salih Yilmaz and Hayri Baytan Ozmen

Contributors

Ömürden Genç, Hyoung-Seok So, Qixuan Li, Roszilah Hamid, Haider Mohammed Owaid, Ameer Hilal, Jan Broda, Magdalena Janus, Pavlo Kryvenko, Hai Lin Cao, Lu Qian Weng, Oleg Petropavlovskii, Miguel Vicente, Jesus Minguez, Jose Antonio Martinez, Dorys Gonzalez

Notice

First published in Croatia, 2016 by INTECH d.o.o.
eBook (PDF) Published by IN TECH d.o.o.
Place and year of publication of eBook (PDF): Rijeka, 2019.
IntechOpen is the global imprint of IN TECH d.o.o.
Printed in Croatia

Legal deposit, Croatia: National and University Library in Zagreb

Additional hard and PDF copies can be obtained from orders@intechopen.com

High Performance Concrete Technology and Applications
Edited by Salih Yilmaz and Hayri Baytan Ozmen

p. cm.

Print ISBN 978-953-51-2650-8

Online ISBN 978-953-51-2651-5

eBook (PDF) ISBN 978-953-51-5786-1

Meet the editors

Dr. Salih Yılmaz, graduated from the Department of Civil Engineering of Middle East Technical University, Turkey, in 2001 and received his PhD in Civil Engineering from Pamukkale University in 2007. He is currently an associate professor at the Department of Civil Engineering, İzmir Kâtip Çelebi University, Turkey. Also, Dr. Yılmaz is the founding head of the Department of Civil Engineering and director of Earthquake Engineering Research Center. He was an assistant professor at the Department of Civil Engineering at Pamukkale University, Denizli, Turkey, and research associate at University of Texas at Austin. Dr. Yılmaz provided consultancy for many companies. He has more than 50 research papers published in international journals and has conducted many national-level research projects and was involved in many international projects. His main research areas are seismic performance evaluation and strengthening of structures including material-related problems, urban regeneration, and passive energy design of buildings.

Dr. Hayri Baytan Özmen Dr. Özmen is currently an associate professor at the Department of Civil Engineering, Uşak University, Turkey. He graduated from the Department of Civil Engineering of Middle East Technical University, Turkey, in 2001. He received his PhD in the same field from Pamukkale University in 2011. His research interest includes reinforced concrete structures, earthquake engineering, seismic evaluation, and retrofit. He has more than 50 research papers published in international journals and conferences and has conducted or was involved in more than 10 national and international research projects. He performed seismic evaluation or design of seismic retrofit system of more than 150 RC buildings and provided consultancy for structural engineering studies. He is one of the editors of an international journal on materials and structural engineering.

Contents

Preface

Rapid population growth and/or advancement of the civilization give rise to larger and more sophisticated needs of humanity. These needs and limited resources put high pressure on the construction practice to find better and more efficient ways to respond.

One of the most innovative regions of the construction practice is the materials sector. The developments in this area always have the potential to cause breakthroughs in the construction technology. Therefore, every participant of the field should follow the progress in the materials technology. This book is prepared to contribute to the dissemination of the knowledge in this essential area focusing on the most common material of construction: concrete.

Concrete is one of the oldest construction materials on earth. It is widely used because of its versatility, affordability, and availability of raw materials, strength, and durability. However, its widespread usage goes back to a few centuries only. On the other hand, it is the tremendous urban development that has taken place through the world in the last few decades, which yielded significant developments of concrete properties. The term high-performance concrete (HPC) is relatively new, and it refers to many properties such as strength, durability, sound and heat insulation, waterproofing, and side advantages such as air purification, self-cleaning, etc.

The book *High Performance Concrete Technology and Application*s contains nine chapters written by researchers and experts of the field. This book provides the state of the art on recent progress in the high-performance concrete applications. The book should be useful to graduate students, researchers, and practicing engineers.

The book chapters are organized in two sections. Chapters in the first section mainly focus on microstructure and behavior of HPC, while the second one is mostly on the HPC-related technologies and applications.

Chapter 1 introduces microstructure of concrete and high-performance concrete. Chapter 2 deals with explosive spalling of high-performance concrete under fire effect. Chapter 3 provides insight into fracture properties under freeze-thaw cycles and freeze-thaw resistance of alkali-slag concrete. Chapter 4 describes the fatigue behavior of high-performance concrete and fiber-reinforced high-performance concrete. Chapter 5 deals with mechanical properties of high-performance multiple-blended binders concrete incorporating thermally activated alum sludge ash at high temperature. As for the second part of the book, Chapter 6 introduces energy-efficient technologies in cement grinding. Chapter 7 presents concretes with photocatalytic activity. Marine engineering applications of high-performance concrete are explained in Chapter 8. Finally, Chapter 9 is on the application of fibrillated polypropylene fibers for the reinforcement of cement mortars.

We would like to place on record our immense sense of gratitude to academicians, scientists, concrete technologists, and our colleagues and friends globally who have contributed significantly in the broader area of concrete technology and our sincere appreciation and acknowledgment to the published work of the researchers on the subject, which has been referred in this book. We are also extremely grateful to InTech for publishing the book in an excellent form in the shortest possible time. Finally, the editors wish to acknowledge Ms. Romina Rovan for providing valuable assistance in bringing out this book.

Salih Yılmaz and Hayri Baytan Özmen
İzmir Kâtip Çelebi University and Uşak University
Turkey

Section 1

Microstructure and Behavior

Chapter 1

Microstructure of Concrete

Ameer A. Hilal

Additional information is available at the end of the chapter

http://dx.doi.org/10.5772/64574

Abstract

Concrete is a composite material that consists of a binding medium and aggregate particles and can be formed in several types. It may be considered to consist of three phases: a cement paste, the aggregate, and the interfacial transition zone (ITZ) between them. In addition to ordinary Portland cement, the essential components of the base of concrete are aggregates and water. For practical requirements, additives and admixtures can be added to these raw materials to improve some desirable characteristics. The following requirements should be considered in producing high performance concrete (HPC): (i) low water/cement (w/c) ratio; (ii) fine aggregate; (iii) large quantity of mineral additives, silica fume, and fly ash; (iv) high dosage of superplasticizer; and (v) high-pressure steam curing. The microstructure of high performance concrete (HPC) is more homogenous than that of normal concrete (NC) due to the physical and chemical contribution of the additives (silica fume and fly ash) as well as it is less porous due to reduced w/c ratio with the addition of a superplasticizer. Inclusion of additives (individually or in combination) helped in improving the strength and durability of concrete mixes due to the additional reduction in porosity of cement paste and an improved interface between it and the aggregate.

Keywords: concrete, mineral additives, microstructure, strength, durability

1. Introduction

Concrete is a construction material that is extensively used because of its excellent properties such as durability, workability, satisfactory strength, and the easy availability of raw materials (cement, aggregates, and water), which are used to produce it [1].

By definition, concrete is a composite material that consists of a binding medium and aggregate particles and can be formed in several types [2]. It may be considered to consist of three phases:

a cement paste, the aggregate, and the interfacial transition zone (ITZ) between them [3]. Concrete is a heterogeneous substance. On a macroscopic scale, it is a mixture of cement paste and aggregates, whereas on a microscopic scale, the cement paste itself consists of unreacted cement grains, amorphous hydration products (crystals of calcium hydroxide, needles of ettringite, and fibrous crystals of calcium silicate hydrate), and pores [4] (see **Figure 1**).

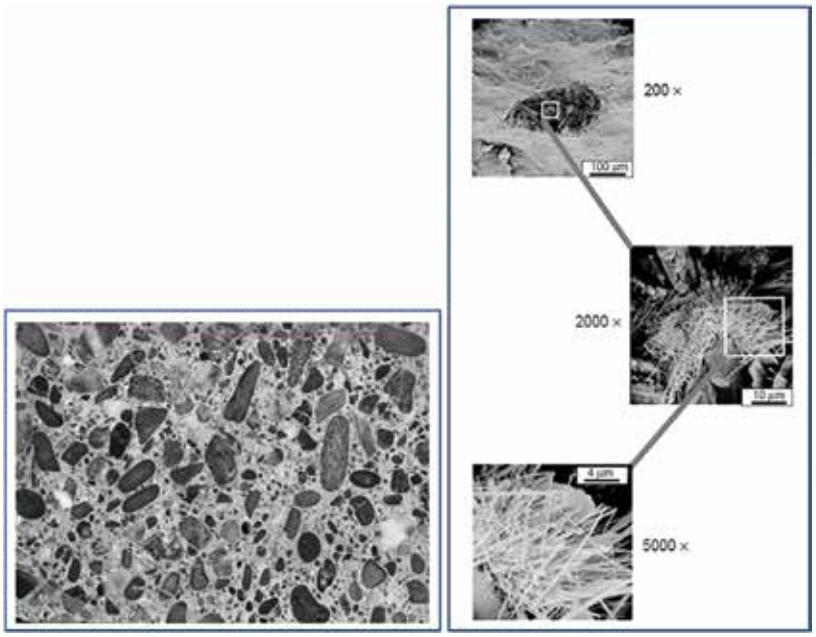

Figure 1. Left: polished section of concrete specimen. Right: microstructure of a hydrated cement paste [1].

Concrete with superior properties such as high compressive strength and excellent durability can be produced by taking into account the following: (i) optimizing particle size distribution to obtain high density; (ii) using water reducer agents to reduce water/cement (w/c) ratio; (iii) adding pozzolanic admixtures to improve rheological properties, fill voids, and form additional calcium silicate hydrate; and (iv) preventing brittle failure to include steel fibers [5].

	Regular (plain)	**High strength**	**Very high strength**
Compressive strength (MPa)	<50	50–100	100–150
Water/cement ratio	>0.45	0.30–0.45	0.25–0.30
Chemical admixtures	Not required	Superplasticizer	Superplasticizer
Mineral admixtures	Not required	Fly ash	Silica fume
Permeability (m/s)	$>10^{-12}$	10^{-13}	$<10^{-14}$

Table 1. Characteristics of concrete mixes in terms of strength and permeability [6].

http://dx.doi.org/10.5772/64574

To produce a concrete with specific requirements such as high performance concrete (HPC), additives and admixtures should be added to raw materials of normal concrete to improve some properties by pozzolanic and physical actions. The pozzolanic reactions resulted in changes in pore structure caused by the reduction in the grain size, while the obstruction of pores and voids by the finer grains is called the physical or filer effect. This means that the enhancement of paste microstructure caused by not only the pozzolanic reactions but also the filler effect of the finer particles. These two effects improve the concrete microstructure by making it denser, more homogeneous, and uniform, leading to enhance its properties such as strength and durability compared to the plain mix (see **Table 1**). Porosity of cement paste has a significant effect on the strength of concrete, while its permeability has affected by the pore structure and pore connectivity. Usually, a high permeability indicates a low durability and vice versa.

To achieve high strength and good durability requirements (prevent a concrete deterioration, see **Figure 2**) [7], reducing the capillary porosity and also a substantial reduction in the total porosity should be achieved by reducing the gel porosity as well. This leads to change the C-S-H structure from porous to more crystalline phase, i.e., change in concrete microstructure. It is well known that the microstructure of concrete (cementitious paste, pore structure, and interfacial transition zone between the cement paste and the aggregate) has a significant role in effecting its properties such as strength and durability due to controlling the porosity, permeability, and pore size distribution. Therefore, understanding how performance of concrete links to its microstructure is important.

Figure 2. Deterioration of normal concrete [7].

2. Microstructure investigation methods

Mercury intrusion porosimetry, light optical microscopy with an associated digital image analysis, scanning electron microscopy, and X-ray computed tomography with image processing were, in addition to others, methods suited to examining concrete samples.

2.1. Mercury intrusion porosimetry (MIP)

Mercury intrusion porosimetry characterizes a material porosity by applying a pressure to a sample immersed in mercury. The size of the accessible pores that will be filled by mercury is inversely proportional to the pressure applied. For each externally applied pressure, the pore diameter (mercury-pore space interface) is determined by the Washburn equation:

$$P_c = \frac{-4\rho \times cos\theta}{d} \tag{1}$$

where P_c is the capillary pressure, ρ is the surface tension, θ is the contact angle, and d is the diameter of the pore space [8]. See **Figure 3** as presented in Ref. [9].

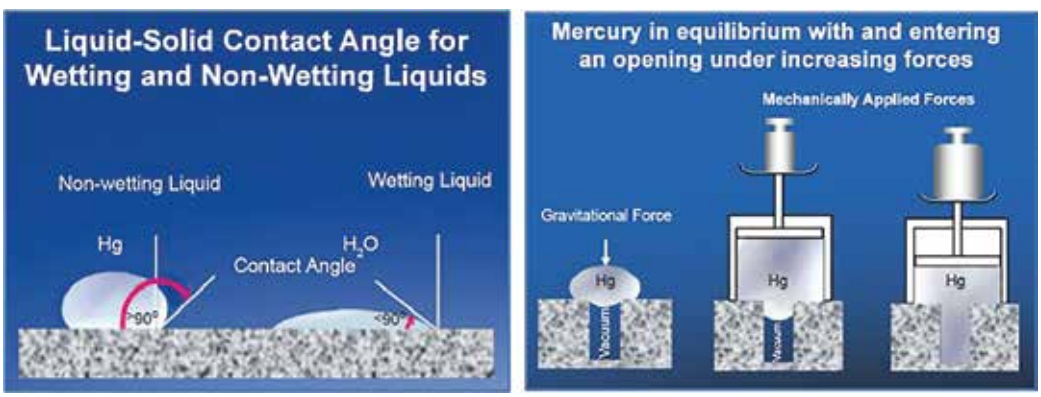

Figure 3. Left: different angles of contact for wetting and non-wetting liquids. Right: mercury (not-wetting liquid) does not penetrate pores by capillary, but it must be forced into them by the application of external pressure [9].

In a review of mercury porosimetry (MIP), Diamond [10] concluded that this technique is an inappropriate method for the measurement of pore size distributions in cement-based materials. However, he added that MIP measurements are useful to provide threshold diameters and intrudable pore volume, which may be helpful as comparative indices of the cement paste or concrete pores. This is because the Washburn equation is applicable to a pore system characterized by percolative chains with ever finer pores at each step from the surface to the middle of sample (**Figure 4a**). From this figure, the larger pore (open to the exterior) fills with mercury at pressure P_1, whereas the smaller pore (open to the large pore) will not fill until a higher pressure P_2, corresponding to its smaller diameter, is reached.

In a hydrated cement system, a pore structure illustrated in **Figure 4b** is likely to occur leading to mistakenly allocating a large pore and the diameter of a small pore at high pressure step P_2. Therefore, the MIP technique was used in this project to determine the total porosity, the

http://dx.doi.org/10.5772/64574

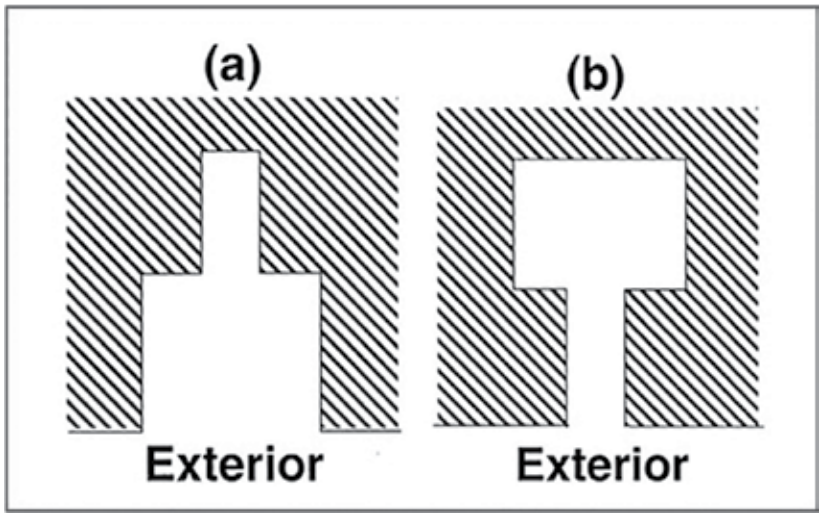

Figure 4. (a) A small cylindrical pore connected to the exterior of a specimen through a large cylindrical pore (MIP model is applicable). **(b)** A large cylindrical pore connected to the exterior of a specimen through a small cylindrical pore (the large diameter pore will not be detected) [10].

characteristic length (l_c), and the conductivity factor of the selected mixes not to investigate the pore size distribution of them.

2.2. Optical microscopy (OM)

Optical and electron microscopies are the two principle microscopy techniques widely used for studying cementitious materials. An optical microscope uses normal (visible) light and a system of lenses to magnify images of small samples. It has been extensively used for studying cementitious materials due to its easy use and rapid operation. However, the main limitation of this technique is the resolution [11].

2.3. Scanning electron microscopy (SEM)

In general, the SEM consists of an electron gun, condenser lenses (to de-magnify the electron beam), objective lenses (to focus the probe onto the specimen surface), a control system for the beam movement, platform for specimen, electron detector, signal amplifier, and display unit [11]. The SEM principle can be described briefly as follows: when the electron beam (primary electrons) hits the specimen surface, it may elastically change its direction with no loss of energy (elastic scattering process), or a detectable amount of the primary electron energy may be absorbed resulting in most of the primary electrons being stopped while a few of them are

backscattered (inelastic scattering process). In general, these processes produce other types of electrons, which are useful for the materials analysis, as shown in **Figure 5** [11].

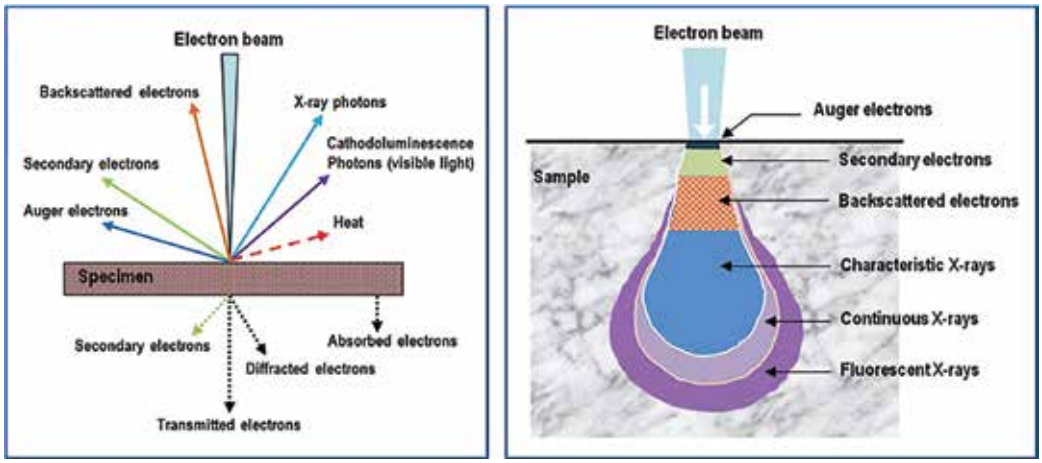

Figure 5. Left: the results of interaction of electron beam with specimen. Right: the interaction volume and the regions of the various signals that may be detected after [11].

In the elastic scattering process, most of the primary electrons will stop in the specimen forming a volume of a tear drop shape below the specimen surface known as the interaction volume, which affects the lateral resolution of the image produced from each signal. The depth and shape of the interaction volume depend on both the average atomic number of the sample and the accelerating voltage. The secondary electrons (SE) are used to describe those having energy less than about 50 eV (electron volts). Being close to the specimen surface, they will be able to leave the specimen giving information about the first very thin layer below the surface. Thus, they are very useful for investigating the topography of the material surface. For this reason, the secondary electron (SE) mode uses to qualify, analyze, and investigate the microstructure of concrete mixes.

Backscattered electrons (BSEs) are primary electrons leaving the specimen surface with energy greater than 50 eV (from 50 eV to that of the primary electrons). Compared to secondary electrons, they have very high energy. The BSE mode, in combination with the ImageJ software, uses to perform quantitative image analysis of the void structure and the ITZ of concrete mixes.

2.4. Micro-computed tomography (μCT)

A μCT scanner consists of a source for the X-ray beam with a collimator. The beam is transmitted through the sample and then detected by a detector, as shown in **Figure 6**. This technique utilizes the ability of X-rays, which are produced by accelerated electrons striking the X-ray tube target (e.g. tungsten), to penetrate objects and measures the intensity before and after passing through the objects. Its principle is as follows: when an X-ray beam passes through a sample, some of the X-ray radiation is absorbed and scattered (with intensity I_o),

http://dx.doi.org/10.5772/64574

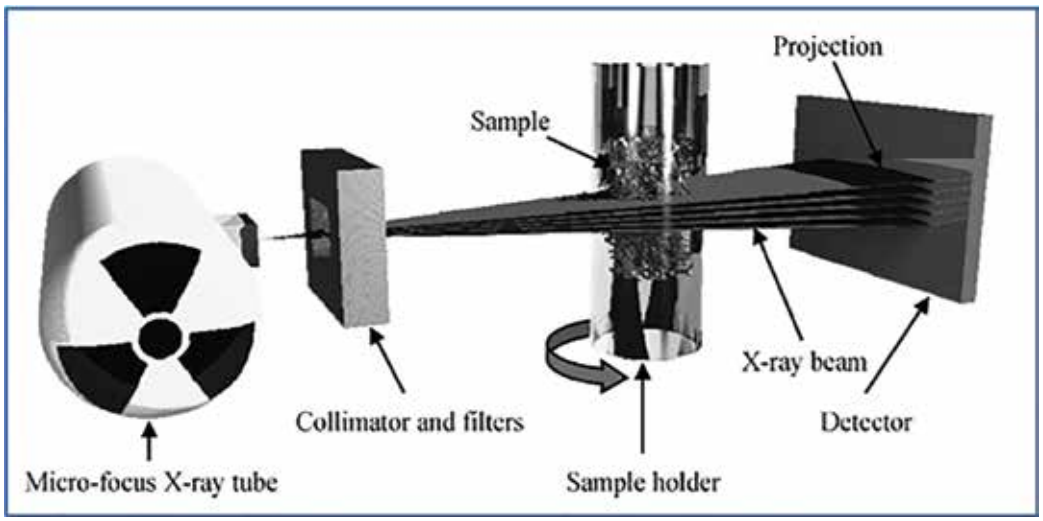

Figure 6. The key components of μCT scanner [13].

while the rest penetrates through the sample (with intensity I) (see **Figure 7**). The amount of penetration depends on the X-rays' energy, molecule atomic number, and the density and thickness of the object. Depending on the material density, the amount of absorption is a function of the linear attenuation coefficient (L_{att}) at each point. The denser the material, the more the absorbed radiation. The L_{att} can be expressed as L_{att} (x, y), where x and y are the Cartesian coordinates of the locations within the scanned section. The raw data of a series of intensity measurements, at different orientations around the sample, are converted to form a 2-D slice image by a mathematical process within the software indicating the different internal features and their distribution within the scanned section. Depending on the differences in density within the scanned object, the image consists of a range in the gray spectrum [0 (black) to 255 (white) for an eight-bit image]. Within the composite material, the higher the difference in component densities, the better the identification and distinguishing between them. Finally, the 2-D images may be converted to a three-dimensional (3-D) image to observe the location of voids, defects, or inclusions without sectioning the sample, i.e., allowing the three-dimensional internal structure of a specimen to be determined non-destructively [12].

2.5. Vacuum saturation method

Total porosity of concrete samples can be determined using a vacuum saturation approach, in which porosity measurements are conducted on dry samples (dried at 100 ± 5°C until a constant weight) that placed in a desiccator under vacuum for at least 3 hours. After that, the desiccator is filled with de-ionized water to 30 mm above the samples and left under a vacuum pump for another 3 hours. Then, the samples are remained under water overnight. Finally, the samples are weighed in air and water to calculate their total (vacuum determined) porosity from Eq. (2), assuming them to now be fully saturated.

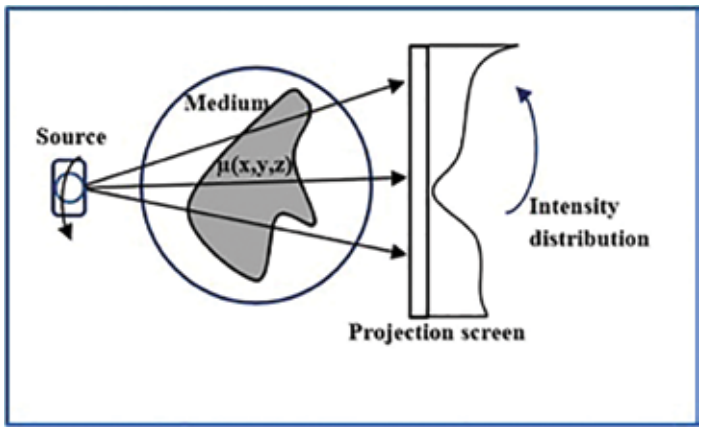

Figure 7. Intensity distribution in X-ray tomography after [14].

$$\emptyset_T = \frac{W_{s,a} - W_{dry}}{W_{s,a} - W_{s,w}} \times 100 \tag{2}$$

where ϕ_T is the total porosity (%), $W_{s,a}$ is the weight of a saturated sample in air, $W_{s,w}$ is the weight of the saturated sample in water, and W_{dry} is the weight of the oven-dried sample.

Table 2 illustrates the limitations of the above methods used in investigating the concrete microstructure in terms of pore size distribution, pore volume (porosity), and pore connectivity.

Method	Pore range	Image processing	2-Dimention	3-Dimention	Gel pores (<10 nm)	Capillary pores (10nm-10μm)	Entrapped pores (>10 μm)	Pore size distribution	Pore volume (porosity)	Pore connectivity
MIP	4nm-400μm			√	√	√		√	√	√
OM	>10 μm	√	√				√	√	√	
SEM	>1 nm	√	√		√	√		√	√	
μCT	>10 μm	√	√	√			√	√	√	√
Vac. Satu.	accessible pores			√	√	√	√		√	

Table 2. The limitations of microstructure investigation methods.

3. Microstructure of concrete

Concrete has a heterogeneous microstructure, which consists of three components, namely, cement paste, pore structure, and interfacial transition zone between the cement paste and aggregates. Improving these three components leads to enhance mechanical strength and durability of concrete.

3.1. Cementitious binder

Cement mainly consists of silica (SiO_2) or (S), alumina (Al_2O_3) or (A), lime (CaO) or (C), and iron oxide (Fe_2O_3) or (F). The main compounds of ordinary Portland cement are tri-calcium silicate (C_3S), di-calcium silicate (C_2S), tri-calcium aluminate (C_3A), and tetra-calcium aluminoferrite (C_4AF).

The main phases present in hydrated cement paste microstructure can be listed as follows: (i) calcium silicate hydrate (C-S-H); (ii) calcium hydroxide (CH); (iii) ettringite; (iv) monosulfate; (v) unhydrated (UH) cement particles; and (vi) air voids [1].

In addition to ordinary Portland cement, the essential components of the base of concrete are aggregate and water. For practical requirements, additives with various particle sizes and specific surface areas can be added to the raw materials to improve some desirable characteristics of the final product. **Figure 8** represents the raw materials of concrete and some supplementary additives in terms of their particle size and specific surface area [15].

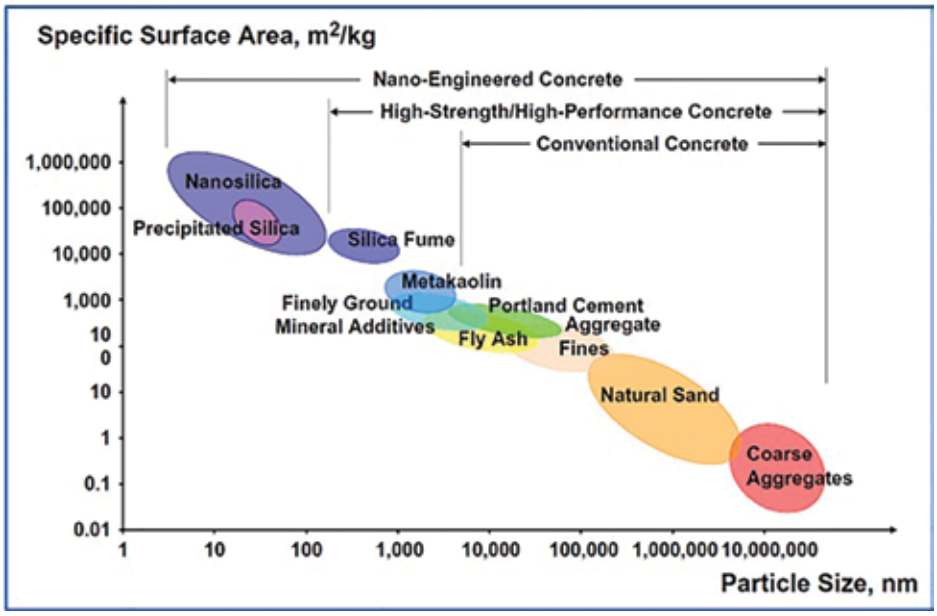

Figure 8. Raw materials of concrete and some supplementary additives [15].

Cement is the most commonly used binder; however, other supplementary materials can also be used. The most available supplementary cementing materials are silica fume, a by-product of the reduction in high-purity quartz with coal in electric furnaces in the production of silicon and ferrosilicon alloys, and fly ash, a by-product of the burning of coal in thermal power stations [16]. **Figure 9** shows that the particles in a typical fly ash vary from <1 μm to about 100 μm in diameter with more than 50% by mass less than 10 μm. In addition, compared to Portland cement and fly ash, silica fume shows finer particle size distribution by two orders of magnitude with a mean particle diameter of about 0.1 μm.

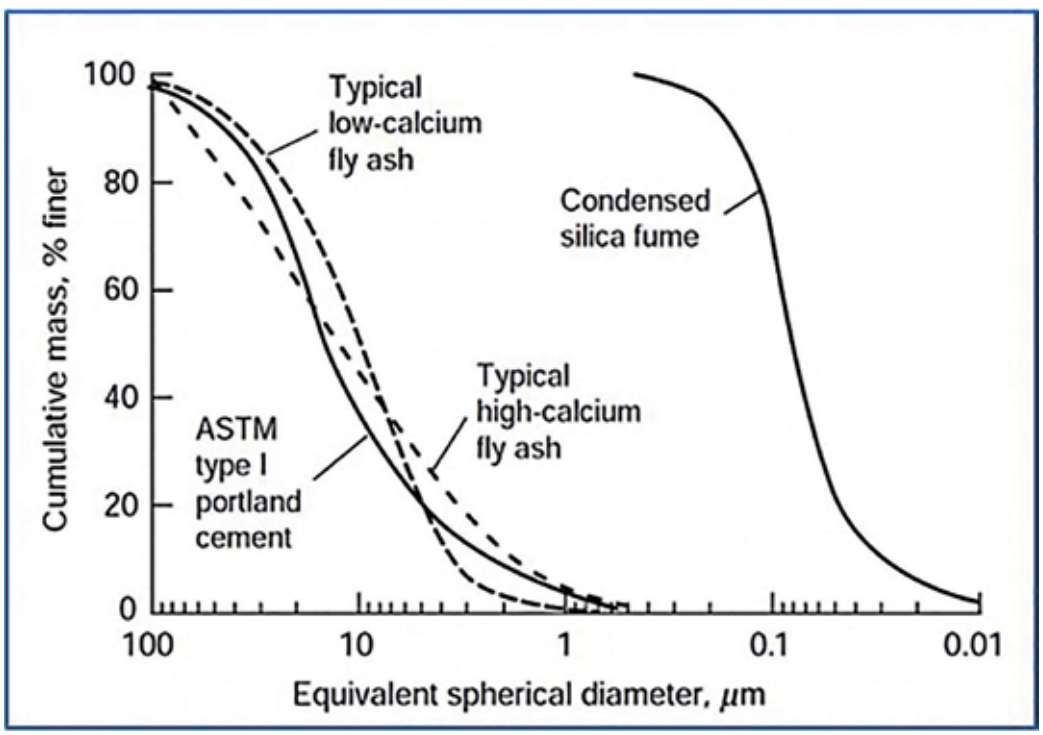

Figure 9. Particle size distribution of cement, fly ash, and silica [1].

Superplasticizers and water-reducing admixtures are important to increase the strength, which were developed in the 1970s and have found wide acceptance in the concrete construction industry. The surfactant imparts a strong negative charge when adsorbed on cement particles, which leads to lower the surface tension of the surrounding water and greatly improves the fluidity of the system [1]. The mechanism of action is shown in **Figure 10** and can be summarized as follows: when the cement particles (which have a mixture of positive and negative charges) are mixed with water, they coalesce into flocks resulting in trapping a considerable amount of mixing water and therefore reducing the fluidity. To solve this, adding the superplasticizer (which constitutes a negative ionic group) will form a negative charge on the cement

http://dx.doi.org/10.5772/64574

particles after adsorbing onto them. Now, the cement particles repel each other and become more dispersed, releasing the trapped water and increasing the fluidity [17].

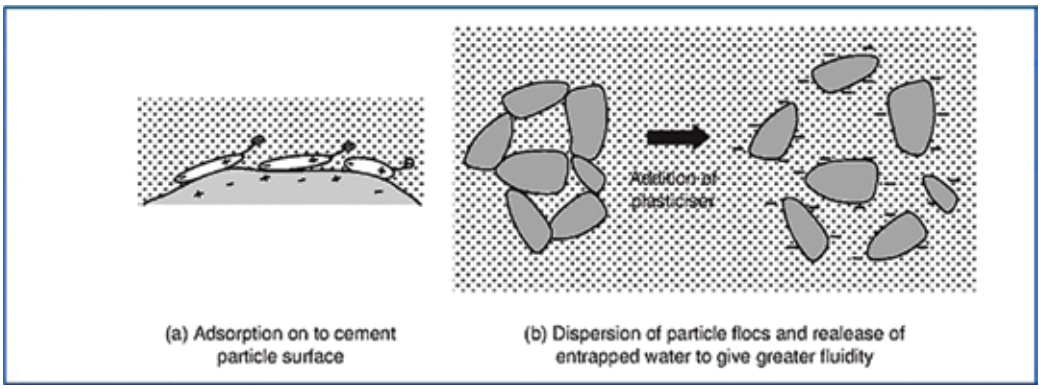

Figure 10. Diagrammatic representation of plasticizers' action [17].

3.2. Pore structure

It is well known that the pore structure of cementitious material is a significant characteristic because it affects properties such as strength and durability due to their dependence on material porosity, permeability, and pore size distribution [18]. The typical sizes of the voids in hydrated cement paste are shown in **Figure 11**.

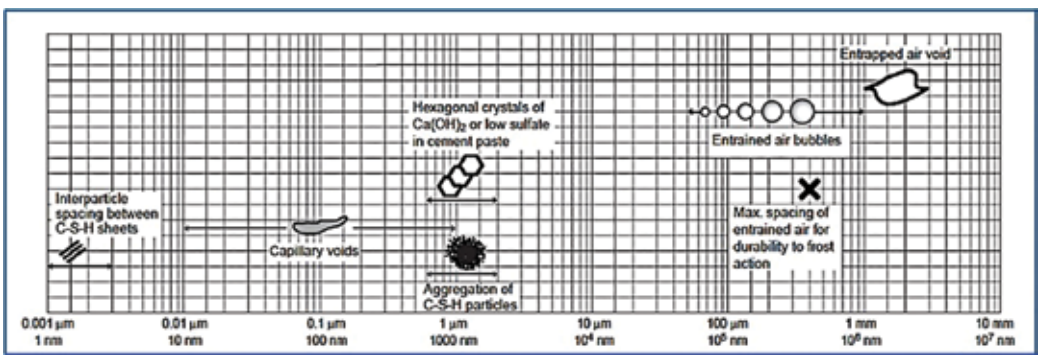

Figure 11. Dimensional range of pores in a hydrated cement paste [1].

Just and Middendorf [19] stated that by using low w/c ratio and adding microsilica, density increases and the average air voids' diameter decreases. Furthermore, decreasing the diameter of the pores may lead to regularly formed air voids, resulting in increasing compressive strength for the same densities. Therefore, understanding the pore parameters is important for producing a product with a high strength to weight ratio and good properties.

3.3. Interfacial transition zone (ITZ)

Concrete may be considered to consist of three phases: a cement paste, the aggregate, and the interfacial transition zone (ITZ) between them. In the ITZ, the structure of the cement paste is different from that of the bulk paste in terms of morphology, composition, and density. Compared to the bulk paste, the ITZ has less unhydrated cement, less C-S-H, large crystals of calcium hydroxide, greater concentration of ettringite, and higher porosity (lower density) [20]. As in the bulk paste, calcium, sulfate, hydroxyl, and aluminate ions are produced by the dissolution of calcium sulfate and calcium aluminate compounds. These ions combine to form ettringite and calcium hydroxide, which, due to the high w/c ratio, become larger in the vicinity of the aggregate resulting in more porous framework than in the bulk cement paste or unfoamed matrix [1]. The microstructure of an interfacial transition zone in concrete is presented schematically in **Figure 12**.

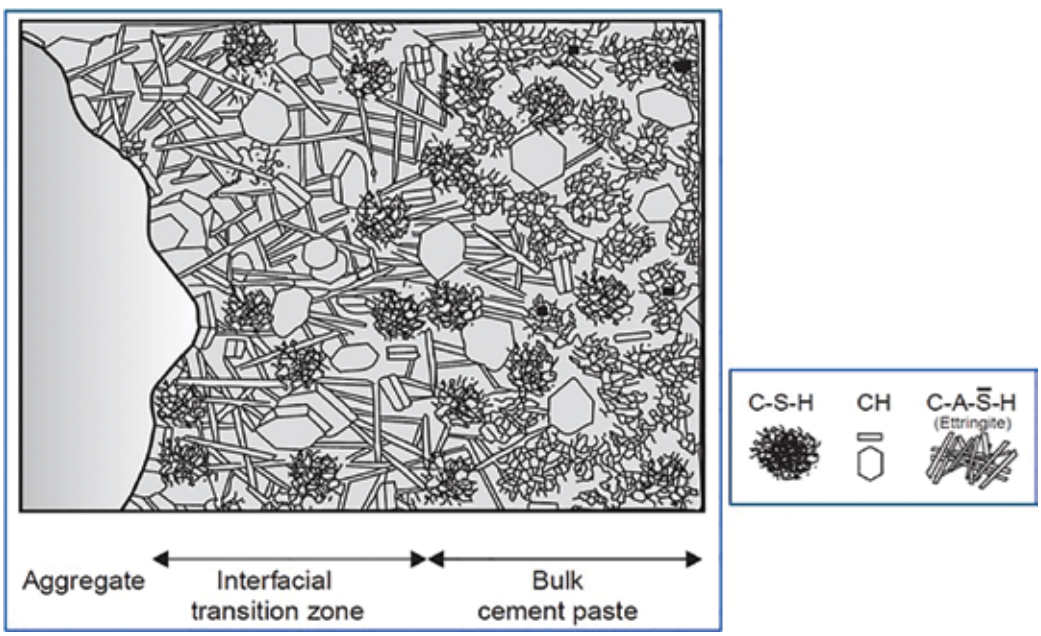

Figure 12. Schematic diagram of ITZ in concrete [1].

Quantitative characterization of the ITZ between the aggregate and the cement paste in concrete confirms that it arises due to the packing of cement grains (1–100 μm) against the larger aggregate particles. In other words, this difference in size means that each aggregate particle is a mini "wall," disrupting the normal packing of the cement grains and leading to accumulation of smaller grains in the zone close to the aggregate while larger grains are found further out (see **Figure 13**). This packing leads to a more porous zone, and the deposition of hydration products, especially calcium hydroxide, tends to fill this zone [21].

http://dx.doi.org/10.5772/64574

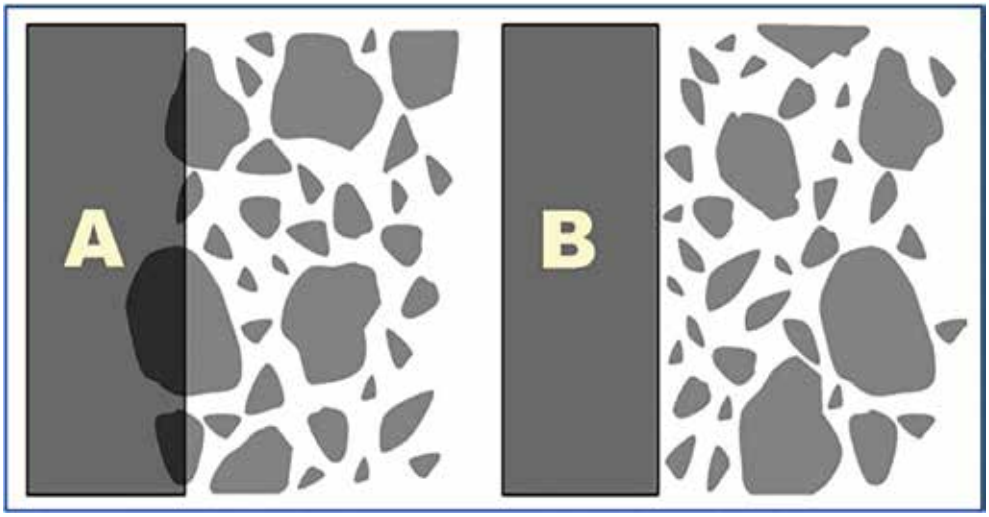

Figure 13. Schematic diagram showing "wall" effect of aggregate: **(A)** imaginary case and **(B)** reliable case [21].

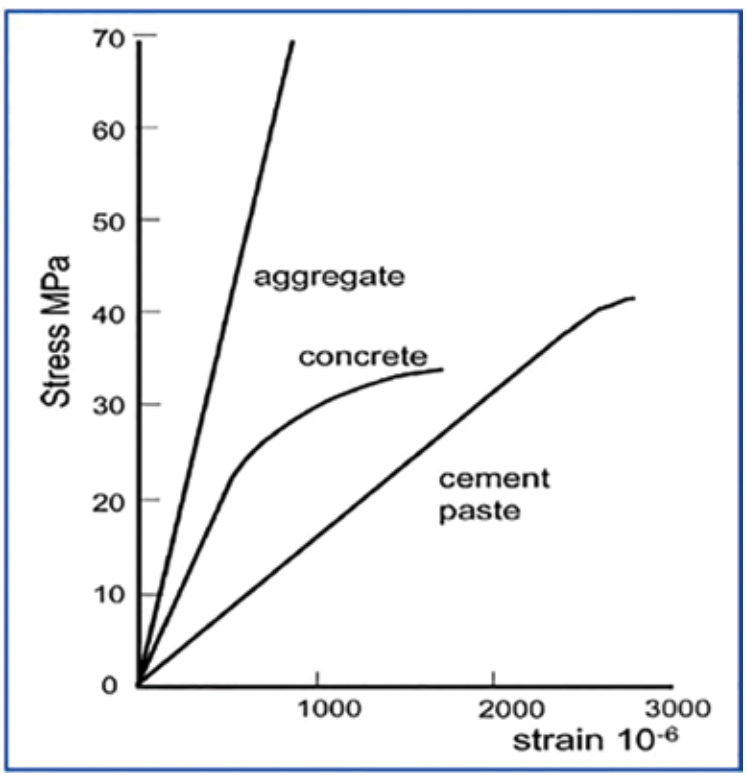

Figure 14. Effects of the ITZ on mechanical properties of concrete [21].

The ITZ, about 50 μm thick, plays a role in the stiffness, strength, and permeability of cementitious materials containing aggregate due to its generally lower density and strength compared to bulk cement paste. When the material is subjected to loads, microcracks may appear within the ITZ due to its weakness leading to the quasi-brittle nature of concrete [22] (see **Figure 14**). This explains the phenomenon that the components of concrete (aggregates and hydrated cement paste) usually remain elastic until failure during a uniaxial compression test, while concrete shows inelastic behavior at levels higher than 70% of ultimate strength [1].

The quality of the bond between the paste matrix and aggregates is influenced by the shape, size, mineral composition, surface roughness, surface moisture content, and porosity of aggregates as well as water/cement ratio [22].

In a study on the effect of water/cement (w/c) ratio, aggregate size, and age on the microstructure of the interfacial transition zone between the normal weight aggregate and the bulk cement paste, it was concluded that the w/c ratio plays an important role in controlling the microstructure of the ITZ and its thickness. In addition, at the same w/c ratio and age, reducing the aggregate size tends to reduce the porosity and increase the content of unhydrated (UH) particles in the region surrounding the aggregate. Moreover, at the same w/c ratio (0.55), they reported that the ITZ is more porous compared to the bulk paste at 180 days than at 7 days due to deficiency of UH content in the ITZ compared to bulk paste at an early age [23].

4. Microstructure of high performance concrete

The following requirements should be considered in producing HPC: (i) low w/c ratio; (ii) fine aggregate; (iii) large quantity of mineral additives, silica fume and fly ash; (iv) high dosage of superplasticizer; and (v) high-pressure steam curing [6].

It should be noted here that before discussing the factors influencing some of the important engineering properties of concrete, strength, and durability, an understanding of the essential features of its microstructure would be helpful.

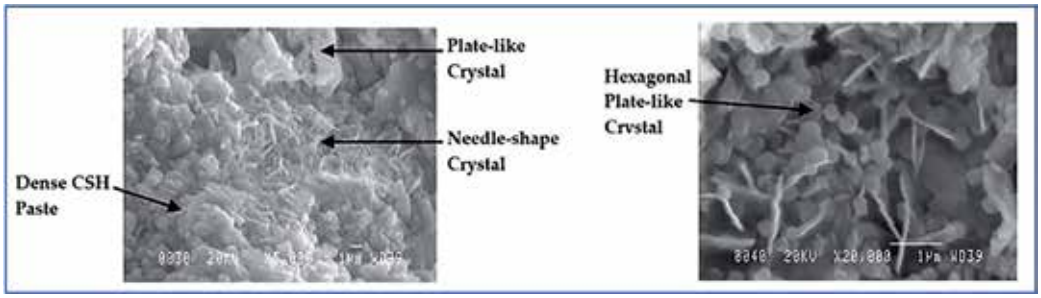

Figure 15. Microstructure of high performance concrete: C-S-H gel becomes denser with dense ettringites in the form of pike and flower [24].

http://dx.doi.org/10.5772/64574

The type, size, amount, shape, and distribution of phases in a solid constitute its microstructure at a microlevel. The microstructure of concrete can be described in the following three aspects: (i) hydrated cement paste, which represents the hydration products of cement and water reaction, and the main product of this reaction is the calcium silicate hydrate (C-S-H) gel; (ii) pore structure, which refers to the gel pores, capillary pores, and voids; and (iii) interfacial transition zone (ITZ), which represents the boundaries between the cement paste and the aggregate particles [6].

It was suggested that C-S-H exhibited from different microscopic shapes: (a) needle shape crystals with a size of 0.5–2 μm long and <0.2 μm wide; (b) plate-like crystals; (c) irregular hexagonal panel crystals; and (d) dense C-S-H paste (see **Figure 15**) [24].

In terms of the volume of capillary voids in the hydrated cement paste, it decreases with deceasing the w/c ratio or with increasing the age of hydration. Moreover, in the presence of aggregate, the microstructure of hydrated cement paste in the vicinity of large aggregate particles (ITZ) is usually very different from that of bulk paste or mortar in the concrete. This ITZ is the weakest region in concrete due to its higher porosity resulting from the poor packing of cement particles [1].

To improve the concrete performance, the following three aspects should be considered [6]:

- Strengthening the hydrated cement paste: this can be achieved by adding the mineral additives, which help in generating a crystalline C-S-H gel with lower gel porosity, compared to a conventional amorphous C-S-H gel, resulting in reducing the gel porosity in addition to the reduction in capillary porosity.
- Lowering the porosity: this can be achieved by filling the empty spaces in cement paste, resulting in lowering the pore connectivity as well and then reducing the total paste porosity.
- Toughening the ITZ: this can be done by using a superplasticizer to reduce the w/c ratio and improving the particle packing in this zone by adding the mineral admixture.

In addition to the microstructure evolution, chemical changes, and attention should be paid to the rheological properties of freshly mixed cement paste. This is due to the flocs phenomena, which causes from entrapping large quantities of mixing water by anhydrous particles of cement. Thus, the resulted microstructure of high performance concrete, the crystalline products of hydration, and the volume, size, and shape of pores would be different compared to the traditional concrete [1].

Compared to a traditional concrete, the addition of silica fume and fly ash leads to reduce the pore proportion in the enlarged ITZ, reduced CH crystals and ettringites, as well as with this addition, a denser C-S-H gel has been noticed [6]. **Figure 16** displays the hydrated cementitious products in cement mortars, impregnated with nano silica, silica fume, and fly ash [25]. From this figure, it was observed that small and large crystals are dispersed in the ordinary Portland mix and sometimes in fly ash and silica fume mixes. While, compared to these three mixes, the texture of the hydration products of nano silica mix is denser and more compact without large crystals of CH.

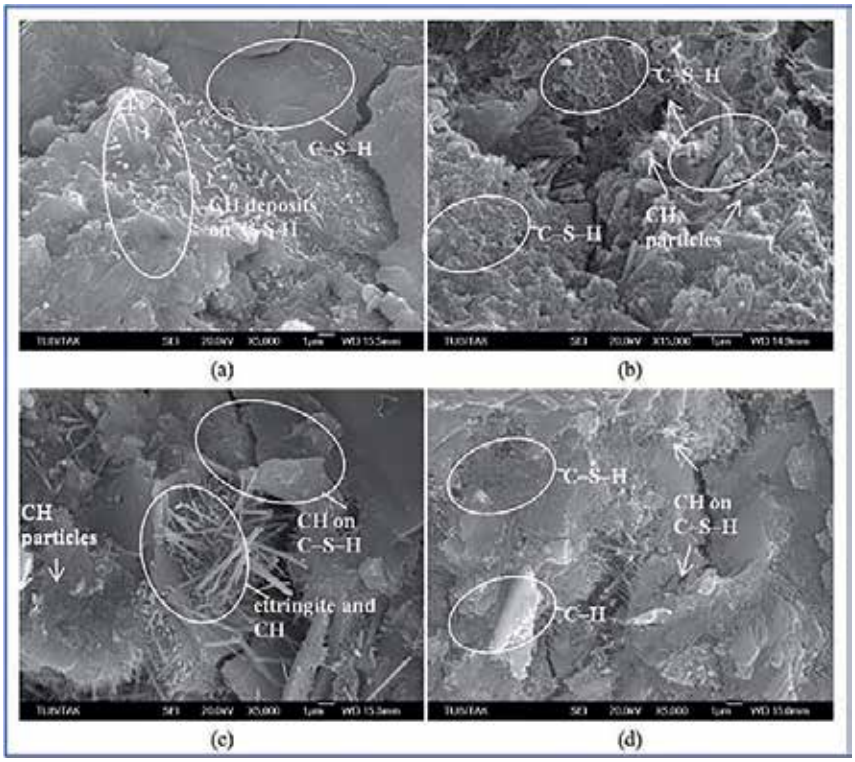

Figure 16. SEM images of the mortar specimens after 28 days of curing: **(a)** ordinary Portland cement (control group), magnification ×5000; **(b)** nano silica, magnification ×15,000; **(c)** silica fume, magnification ×5000; and **(d)** fly ash 10, magnification ×5000 [25].

From the above information, it can be concluded that the microstructure of high performance concrete (HPC) is more homogenous than that of normal concrete (NC) due to the physical and chemical contribution of the additives (SF and FA) as well as being less porous due to reduced w/c ratio with the addition of a superplasticizer. As concrete has a highly heterogeneous and complex microstructure, it is very difficult to reliably predict its behavior from constituting realistic models of its microstructure. However, knowledge of the microstructure of concrete and its relationships to the material properties is useful for enhancing these properties.

5. Effect of microstructure on strength and durability

High performance concrete (HPC) consists of cement, water, fine sand, superplasticizer, fly ash, and silica fume. Additionally, to have ultrastrength and ultraductility, quartz flour and fiber may be added, respectively [6].

It is important to understand how concrete performance is linked to its microstructure.

http://dx.doi.org/10.5772/64574

The main source of strength in concrete is the adhesion between the solid products of hydrated cement paste. This adhesion can be attributed to the van der Waals forces of attraction with a degree of adhesive depends on the extent and the nature of the solid surfaces involved. Some of hydrated products, such as C-S-H crystals, calcium sulfoaluminate hydrates, and hexagonal calcium aluminate hydrates, possess vast surface areas and adhesive capability. Therefore, they tend to adhere strongly to each other and at the same time to solids with low surface areas such as lime, anhydrous cement particles, and aggregate particles (fine and coarse) [1].

When fly ash (amorphous alumina silicate with varying amount of calcium) is added to concrete mixture and in the presence of cement and water, products of pozzolanic reaction, between the silica glass (SiO_2) in the fly ash composition and the calcium hydroxide ($Ca(OH)_2$), which released by the hydration of cement, fill the interstitial pores reducing the pore connectivity and then the microstructure porosity. In addition, in the absence of a source of calcium hydroxide, some fly ash will display cementitious behavior. Thus, more C-S-H will produce by a reaction between this fly ash, with higher amount of calcium, and water (see **Figure 17**) [26].

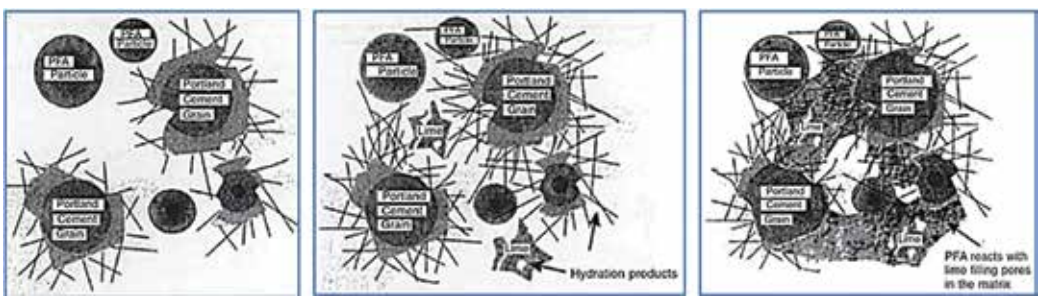

Figure 17. Left: hydration products of Portland cement; middle: lime is formed a by-product of hydration; right: the pozzolanic reaction products fill the interstitial spaces [26].

Depending on the type of mix, cement type, silica fume amount, use of water reducer agents, aggregate type, and curing regimes, the addition of silica fume to a concrete mix will increase its strength by between 30 and 100% of that of the conventional mix [26]. This strength enhancement is due to a reaction of C-S-H gel formed by conventional hydration, with the silica fume at high temperature, which forms a dense phase crystalline hydrate resulting in enhancing the aggregates-cement interfaces and improving the strength. Additionally, it is found that the silica fume, in combination with superplasticizer, improved the bonding between the paste and the aggregate due to the formation of dense microstructure in the ITZ. It was suggested that the addition of water-reducing agent can help increase the density of the microstructure, by reducing its porosity, and thus improve the properties of concrete [6].

As the various phases in the hydrated cement paste are neither uniformly distributed nor uniform in size and morphology (microstructural inhomogeneity), series effects on mechanical properties and durability can be raised.

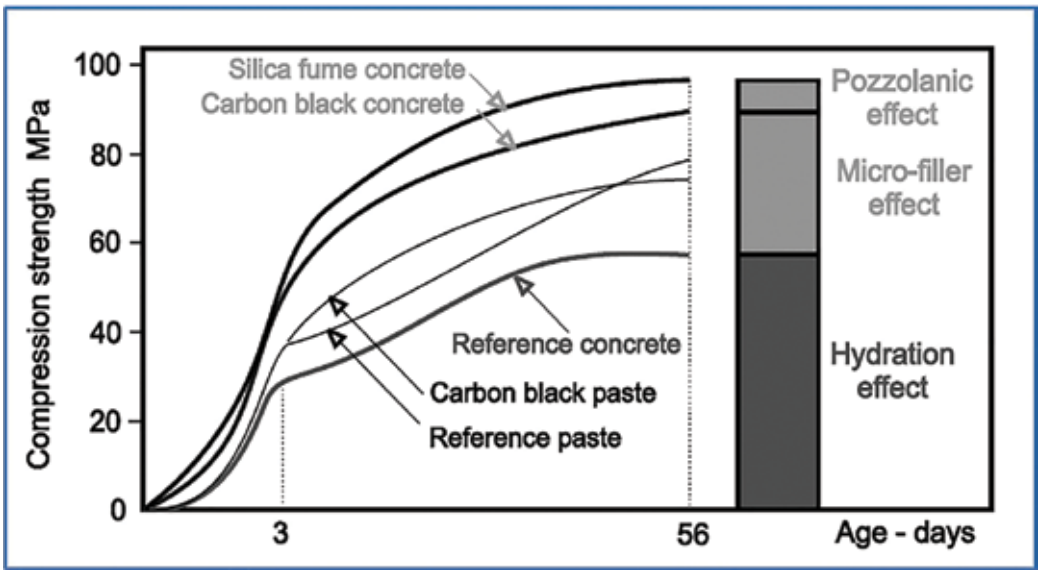

Figure 18. Hydration, pozzolanic, and filler effects of cementitious pastes with silica fume [28].

To achieve the high strength requirements (generally higher than 50 MPa), only reducing the capillary porosity is not enough, but also a substantial reduction in the total porosity should be achieved by reducing the gel porosity. This substantial porosity reduction is required to change the C-S-H structure from porous to more crystalline phase, i.e., change in concrete microstructure [6].

When added to the cement paste, pozzolanic materials play an important role leading to enhance the mechanical and durability properties. The most important effect on microstructure is the change in pore structure by the reduction in the grain size, which resulted, chemically, from the pozzolanic reactions (pozzolanic effect) and, physically, from the obstruction of pores by the action of the finer grains (filler effect) [27]. **Figure 18** shows the pozzolanic, physical, and hydration effects of cement pastes with silica fume [28].

Relative comparisons between the pozzolanic and the filler effects of concrete mixes are shown in **Figure 19**. On average, from this figure, it can be seen that, at higher age (91 days), the pozzolanic effect was more significant in the lower strength (35 MPa), whereas the filler effect was more effective in the higher strength (65 MPa). However, at both 28 and 91 days, the physical effect exceeded that of Pozzolan for mixture containing 50% Pozzolan and with 65 MPa strength. In general, from the findings, it was observed that the pozzolanic and physical effects have increased as the mineral addition increased. Meanwhile, for the same strength value, the filler effect was higher than that of Pozzolan.

http://dx.doi.org/10.5772/64574

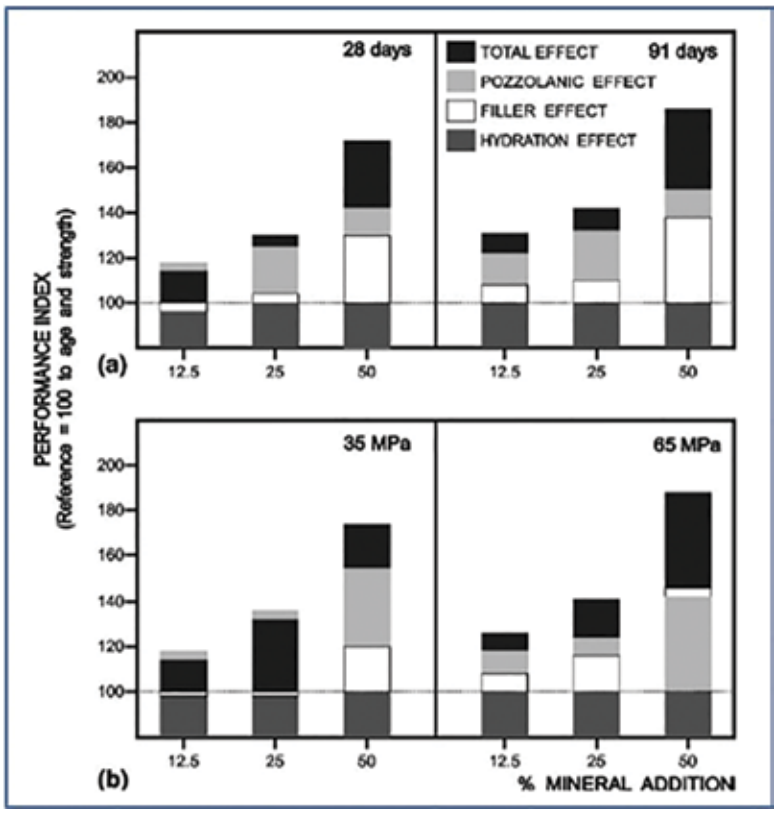

Figure 19. Total, filler, and pozzolanic effect performance indexes related to reference concrete **(a)** at 28 and 91 days and **(b)** 35 and 65 MPa strength levels [27].

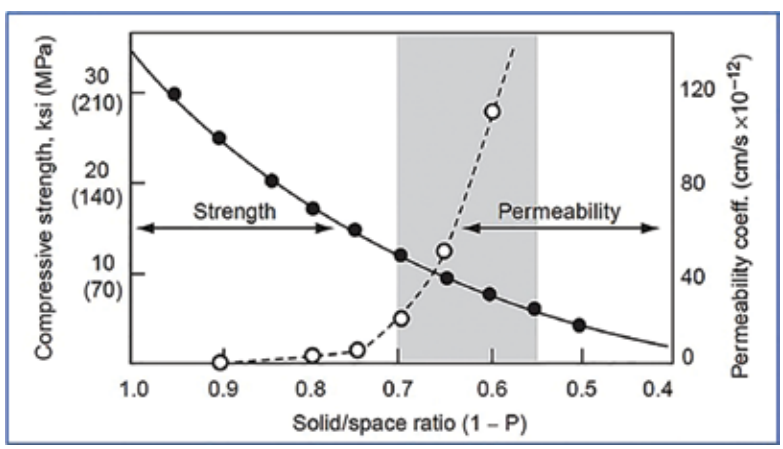

Figure 20. Influence of water/cement ratio and degree of hydration on permeability and strength [1].

In term of durability, it is well known that durability problems of concrete are related to its resistance to water and chemical ion penetration. The liquid penetration may lead to steel reinforcement corrosion, alkaline-silica reaction, and freeze-thaw damage. Therefore, a key factor influencing the durability of concrete is its permeability, which is primarily related to pore structure of cement paste in terms of pore size, volume, and connectivity. Since that the prestructure is a function of the water/cement ratio and the degree of hydration, the permeability is a function of them as well [6] (see **Figure 20**), and it is noted that the shaded area represents the typical capillary porosity range in hydrated cement paste.

It was discussed that the ITZ is a weakest zone, which is strengthened and being less porous with the inclusion of mineral admixtures resulting in improving the concrete microstructure. This improvement, reducing porosity and pore connectivity, leads to reduce the permeability and finally improve the durability.

In summary, it can be seen from the above information that inclusion of additives (individually or in combination) helped in improving the strength and durability concrete. This is due to the additional reduction in porosity of cement paste and an improved interface between it and the aggregate by (i) a substantial reduction in mixing water (using a superplasticizer); (ii) forming calcium silicate hydrate (C-S-H) from a pozzolanic reaction of fly ash with the lime produced from the hydration of cement and water; and (iii) acting as fine filler (silica fume).

Author details

Ameer A. Hilal

Address all correspondence to: ameer_amn@yahoo.com; Ameer.Hilal@outlook.com

Department of Civil Engineering, Faculty of Engineering, University of Anbar, Anbar, Iraq

References

[1] Mehta, P. K. and Monteiro, P. J. Concrete: Microstructure, Properties and Materials. 3rd ed. London: McGraw-Hill; 2006. DOI: 10.1036/0071462899.

[2] Kosmatka, S. H., Panarese, W. C. and Portland Cement Association. Design and Control of Concrete Mixtures. Skokie, IL: Portland Cement Association; 2002.

[3] Akçaoğlu, T., Tokyay, M. and Çelik, T. *Effect of coarse aggregate size and matrix quality on ITZ and failure behavior of concrete under uniaxial compression*. Cement and Concrete Composites. 2004; Vol. 26; pp. 633–638.

[4] Nemati, K. M., Monteiro, P. J. M. and Scrivener, K. L. *Analysis of compressive stress-induced cracks in concrete*. ACI Materials Journal. 1998; Vol. 95: pp. 617–630.

[5] Justs, J., Bajare, D., Korjakins, A., Mezinskis, G., Locs, J. and Bumanis, G. *Microstructural investigations of ultra-high performance concrete obtained by pressure application within the first 24 hours of hardening*. Construction Science. 2013; Vol. 14, pp. 50–57.

[6] Büyüköztürk, O. and Lau, D. *High Performance Concrete: Fundamentals and Application*. Cambridge: Department of Civil and Environmental Engineering, Massachusetts Institute of Technology.

[7] Portland Cement Association. Types and Causes of Concrete Deterioration. Illinois: Portland Cement Association; 2002.

[8] Katz, A. and Thompson, A. *Quantitative prediction of permeability in porous rock*. Physical Review B. 1986; Vol. 34; pp. 8179–8181.

[9] Micromeritics Instrument Corporation. Mercury Intrusion Porosimetry Theory. Available at: www.micromeritics.com [Online] [accessed March 25, 2015].

[10] Diamond, S. *Mercury porosimetry: An inappropriate method for the measurement of pore size distributions in cement-based materials*. Cement and Concrete Research. 2000; Vol. 30: pp. 1517–1525.

[11] Hemavibool, S. The Microstructure of Synthetic Aggregate Produced from Waste Materials and Its Influence on the Properties of Concrete. Leeds/UK: University of Leeds; 2007.

[12] Maire, E., Colombo, P., Adrien, J., Babout, L. and Biasetto, L. *Characterization of the morphology of cellular ceramics by 3D image processing of X-ray tomography*. Journal of the European Ceramic Society. 2007; Vol. 27: pp. 1973–1981.

[13] Bouxsein, M., Boyd, S., Christiansen, B., Guldberg, R., Jepsen, K. and Müller, R. *Guidelines for assessment of bone microstructure in rodents using micro-computed tomography*. Journal of Bone and Mineral Research. 2010; Vol. 25: pp. 1468–1486.

[14] Khan, R. Quantification of Microstructural Damage in Asphalt. Nottingham: University of Nottingham; 2010.

[15] Sanchez, F. and Sobolev, K. *Nanotechnology in concrete – A review*. Construction and Building Materials. 2010; Vol. 24: pp. 2060–2071.

[16] Agarwal, S. K. *Pozzolanic activity of various siliceous materials*. Cement and Concrete Research. 2006; Vol. 36: pp. 1735–1739.

[17] Domone, P. and Illston, J. Construction Materials: Their Nature and Behaviour. 4th Ed. Taylor and Francis; 2010. This edition published 2010 by Spon Press 2 Park Square, Milton Park, Abingdon, Oxon OX14 4RN.

[18] Ramamurthy, K., Kunhanandan Nambiar, E. K. and Indu Siva Ranjani, G. *A classification of studies on properties of foam concrete*. Cement and Concrete Composites. 2009; Vol. 31: pp. 388–396.

[19] Just, A. and Middendorf, B.: *Microstructure of high-strength foam concrete*. Materials Characterization. 2009; Vol. 60. 741–748.

[20] Mindess, S., Young, J. and Darwin, D. Concrete. Pearson Education, Inc.; 2003. Prentice Hall, Pearson Education, Inc. Upper Saddle River, NJ 07458,USA

[21] Scrivener, K., Crumbie, A. and Laugesen, P. *The interfacial transition zone (ITZ) between cement paste and aggregate in concrete*. Interface Science. 2004; Vol. 12: pp. 389–397.

[22] Mondal, P., Shah, S. and Marks, L. *A reliable technique to determine the local mechanical properties at the nanoscale for cementitious materials*. Cement and Concrete Research. 2007; Vol. 37: pp. 1440–1444.

[23] Elsharief, A., Cohen, M. and Olek, J.: *Influence of aggregate size, water cement ratio and age on the microstructure of the interfacial transition zone*. Cement and Concrete Research. 2003; Vol. 33: pp. 1837–1849.

[24] Gao, X. F., Lo, Y. T. and Tam, C. M. *Investigation of micro-cracks and microstructure of high performance lightweight aggregate concrete*. Building and Environment. 2002; Vol. 37: pp. 485–489.

[25] Biricik, H. and Sarier, N. *Comparative study of the characteristics of nano silica-, silica fume- and fly ash-incorporated cement mortars*. Materials Research. 2014; Vol. 17: pp. 570–582.

[26] Lewis, R., Sear, L., Wainwright, P. and Ryle, R.. Cementitious additions. In Newman, J. and Choo, B. S. Advanced Concrete Technology: Constituent Materials. Butterworth-Heinemann; 2003. Linacre House, Jordan Hill, Oxford OX2 8DP 200 Wheeler Road, Burlington MA 01803

[27] Isaia, G., Gastaldini, A. and Moraes, R. *Physical and pozzolanic action of mineral additions on the mechanical strength of high-performance concrete*. Cement and Concrete Composites. 2003; Vol. 25: pp. 69–76.

[28] Goldman, A. and Bentur A. *The influence of microfillers on enhancement of concrete strength*. Cement and Concrete Research. 1993; Vol. 23: pp. 962–972.

Chapter 2

Spalling Prevention of High Performance Concrete at High Temperatures

Hyoung-Seok So

Additional information is available at the end of the chapter

http://dx.doi.org/10.5772/64551

Abstract

In recent year, the use of high performance concrete (HPC) has significantly increased in applications such as prestressed concrete structures, bridges, large-span roof structures, and containers for hazardous fluids or nuclear wastes due to its outstanding structural performance and higher durability. However, its fire resistance performance remains a concern, especially in relation to explosive spalling in a fire. Therefore, it is essential to understand the spalling properties (mechanism, influencing factors, and prevention measures, etc.) of high performance concrete exposed to high temperature, so that the safety of a structural fire design involving HPC can be ensured. This report presents a state-of-the-art review for the prevention measures and explosive spalling of high performance concrete under fire situations.

Keywords: high performance concrete, fire, explosive spalling, mechanism, spalling prevention, PP fiber, thermal barrier

1. Introduction

Recently, high performance concrete (HPC), as it can satisfy the expectations for excellent mechanical properties and a long service life, is increasingly applied in various structures such as bridges, tunnels, high-rise buildings, and large-span infrastructures. HPC is now well established as a very dense homogeneous concrete microstructure, especially in the interface region between hydrated paste and aggregate [1]. This is generally achieved through the use of low w/c ratio (0.2~0.3) with the help of superplasticizers that can produce slumps ranging from 75 to 125 mm [1]. Additional densification and homogeneity of the interfacial region are achieved through the inclusion of mineral admixtures such as fly ash, silica fume,

etc. However, this beneficial microstructure, ironically, causes a critical problem exposure to a fire, especially in relation to explosive spalling, which is defined as the violent breaking off of layers or pieces of concrete from the surface of a structural element when exposed to high and rapidly rising temperature under fire conditions [2]. Some investigations have shown that HPC is more vulnerable to explosive spalling under high temperatures compared to normal strength concrete (NSC), which seriously jeopardizes the safety of HPC applications. The experience of Madrid Windsor Tower fire in Spain (2005), explosive spalling of HPC, has highlighted a serious social problems in the public's mind, as shown in **Figure 1**. Thus, solving of the spalling problem is now a primary requirement in any new structures design. However, there is a lack of data on design and performance of HPC, especially under fire situations.

Figure 1. Damage of concrete and reinforcement after Madrid Windsor Tower fire (Spain, 2005).

This report presents a state-of-the-art review of the phenomenon of the spalling of HPC in general and explosive spalling in particular. The mechanisms and the factors of explosive spalling are discussed.

2. Spalling of high performance concrete

2.1. Definition and types of spalling

As the most typical form, spalling is defined as the violent or nonviolent breaking off of layers or pieces of concrete from the surface of a structural element when exposed to high and rapidly

http://dx.doi.org/10.5772/64551

rising temperature under fire conditions [3]. Gary [4] suggested that spalling could be grouped into four categories: (a) aggregate spalling, (b) corner spalling, (c) surface spalling, and (d) explosive spalling. As shown in **Figure 2**, aggregate spalling, surface spalling, and explosive spalling occur during the first 7–30 minutes in a fire, accompanied by popping sounds (aggregate spalling) or violent explosions (surface and explosive spalling) [5]. Spalling may also occur nonviolently (corner spalling) later in a fire when the concrete has so weakened after a period of heating of 30–90 minutes that cracks develop and pieces fall off its surface [5]. The most important of these is explosive spalling, which occurs violently and results in serious loss of material.

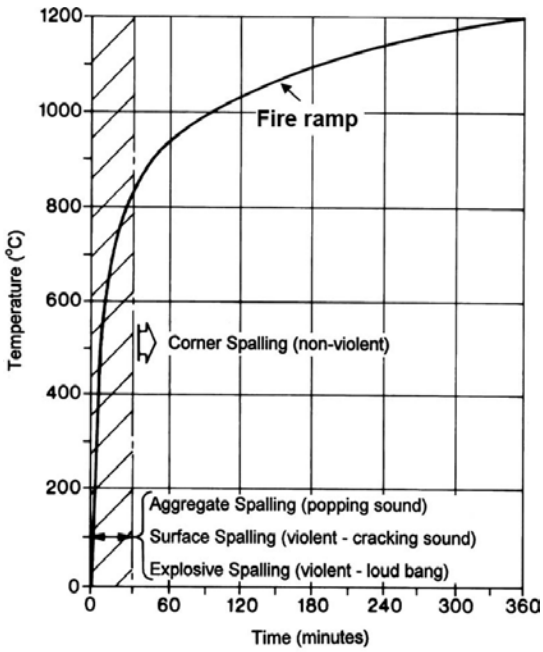

Figure 2. Time of occurrence of different types of spalling in a fire [5].

2.2. Mechanisms of explosive spalling

The most recent theories of the causes of explosive spalling indicate that three factors play a crucial role, i.e., (a) the build-up of pore pressure, (b) thermal stresses, and (c) combined high pore pressure and thermal stress in the concrete when exposed to a rapidly increasing temperature. The first hypothesis supposes that heating produces water vapor in concrete and as the permeability of HPC is low, which limits the ability of vapor to escape, a build-up of vapor pressure results. The second possibility is thermal stresses close to the heated surface due to preload or a high temperature gradient caused by a high heating rate. Third, a combination of both phenomena is also possible. These different mechanisms may act individually or on combination depending upon the moisture content, the section size, and the material.

2.2.1. Pore pressure spalling

This mechanism is proposed by Shorter and Harmathy [6], Meyer-Ottens [7], and Aktarruz-zaman et al. [8]. The hypothesis is that the spalling is due to the build-up of very high pore pressures within the concrete as a result of the liquid-vapor transition of the capillary pore water as well as that bound in the cement paste component of the concrete (so-called moisture clog spalling) [6, 7]. As shown in **Figure 3**, heating on the surface of concrete results in a temperature gradient, which forces moisture into the internal of the concrete as well as out of the surface. Then, three moisture zones develop with depth from heated surface of concrete: a dry zone near the heated surface (a), an evaporation intermediate zone (b), and a moisture saturated zone (c), which could contain more moisture than the initial moisture content. As a result, pore pressures build-up to reach a maximum level at a distance from the surface depending upon the permeability of the concrete and contribute to explosive spalling. The maximum pore pressure is greater in HPC (or HSC: high strength concrete) and develops nearer the surface than in NSC. The pore pressure spalling, therefore, introduces that HPC has dense microstructure and many disconnected pores, which significantly prevents water vapor from free transport and escapes in the matrix when exposed to elevated temperature. The explosive spalling occurs when the pore pressure in the matrix accumulates to a threshold exceeding their tensile strength [9, 10].

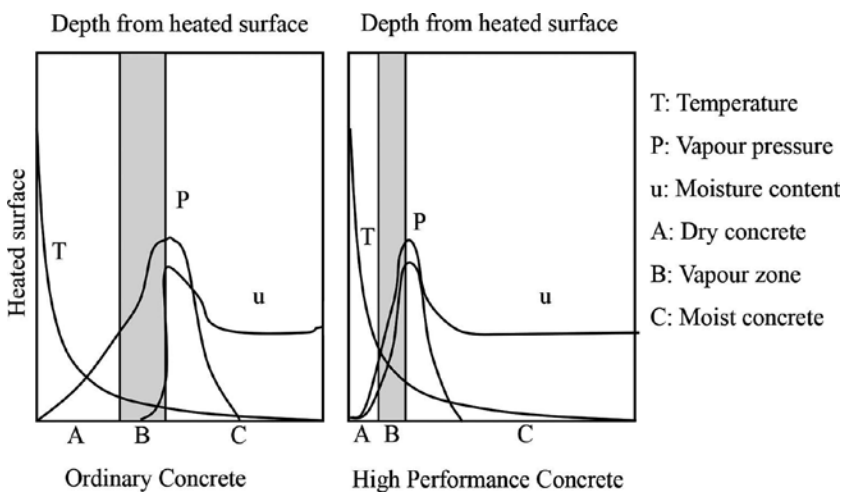

Figure 3. Changes in temperature (*T*), vapor pressure (*P*), and moisture content (*u*) in moist concrete heated from one face [10].

2.2.2. Thermal stress spalling

This mechanism is proposed by Saito [11] and Dougill [12]. Thermal stresses will occur inside the concrete due to temperature gradients from the heated surface toward the inner, cooler sections of the concrete, as shown in **Figures 4** and **5**. These gradients will increase with rapid heating rates. Different strains due to the thermal gradient are deemed to cause tensile and

http://dx.doi.org/10.5772/64551

compressive stresses, depending on the thermal and mechanical properties of the concrete. Hindered expansion, loads, and restraints as well as the heating rate are mentioned as further parameters [13]. Failure due to spalling is considered to exceed the compressive strength of the concrete close to the heated surface. The compressive stresses due to the thermal gradient also lead to tensile stresses in the cooler sections of the concrete. Moisture migration is not considered with spalling due to thermal stresses [14] and spalling of HPC or of NSC with high moisture content cannot be explained by thermal stress spalling. Explosive spalling only due to thermal stresses is relatively a rare occurrence [14].

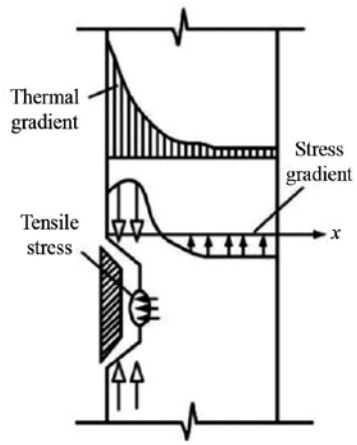

Figure 4. Mechanism of thermal stress spalling [11].

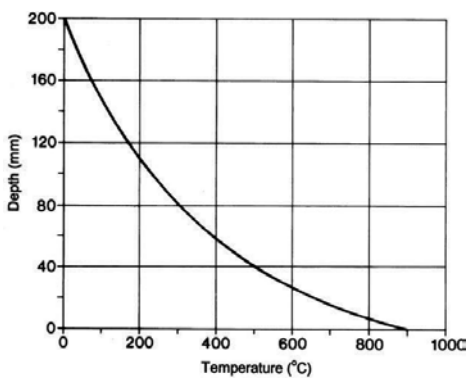

Figure 5. Typical temperature distribution in concrete at 60 minutes of heating in BS476 fire [13].

2.2.3. Combined pore pressure and thermal stress-induced explosive spalling

This mechanism is proposed by Zhukov [15], Sertmehetoglu [16], and Connelly [17]. According to the Zhukov's model, the stresses developed within a heated concrete member may be

superimposed upon each other and their summation compared to the material strength of concrete. He considered that the stresses acting could be categorized as load-induced stresses, thermal stresses, and pore pressures. Based on Zhukov's ideas, Khoury [13] presented a general sketch of combined thermal stress and pore pressure-induced explosive spalling, as shown in **Figure 6**. Generally, high performance concrete tends to undergo the multiple spalling (combined pore pressure and thermal stress spalling) of thinner sections as experienced in the great Belt tunnel fire in Denmark (1994).

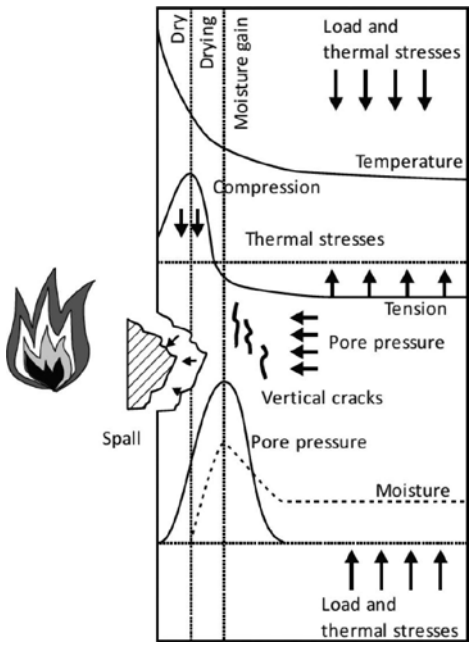

Figure 6. Explosive spalling caused by combined thermal stresses and pore pressure by Khoury based on Zhukov [13].

Although theoretical modeling for the various spalling forms has been attempted in the past, it is recently that significant development has been made in this field. The complex combined nature of the influences of moisture content, pore pressures, and thermal stresses in the heterogeneous concrete material with complex pore structure, which varies markedly with temperature during first heating, does not lend themselves easily to analytical modeling [15].

2.3. Factors influencing spalling

Based on the spalling mechanisms, the main factors leading to the explosive spalling of concrete at high temperatures are heating rate, permeability of concrete, moisture content, presence of reinforcement, and level of external applied load, but more factors have been identified in the literature review as influencing on the risk and extent of spalling [18, 19]. The factors influencing to the explosive spalling of concrete can be classified into three categories as follows:

a. Material-related factors.

b. Structural or mechanical factors.

c. Heating characteristics.

However, some of these factors would fit into more than one category.

2.3.1. Material-related factors

The research on concrete spalling at high temperatures identifies several material-related parameters with a big influence on spalling. **Table 1** shows a brief overview on these governing parameters in relation to the concrete mix design or the selection of materials used for the concrete.

Factors	Risk of spalling	Influences
Moisture content	Very high	Higher moisture content (mainly free water) significantly increases the risk of explosive spalling due to high vapor pressure, but it is depending on the permeability of the concrete.
Silica fume	Very high	Silica fume decrease the permeability and increases the possibility of explosive spalling due to the reduced release of high vapor pressure.
Permeability of concrete	High	Low permeability and insufficient temperature-dependent increase in permeability increases the risk of spalling due to insufficient release of pore pressure.
Cement content	High	High cement content increases the total amount of water added to the concrete, even with low w/c ratios.
Compressive strength	High	Higher strength grade usually increases risk of explosive spalling, mainly due to the lower w/c ratio and permeability
Quartzite aggregates	High	Can increase the risk of spalling due to a change in the quartzite phase at 573°C.
Limestone filler	High	Lowers permeability, similar behavior compared to silica fume.
Aggregate size	Moderate	Larger aggregates increase the risk of explosive spalling due to a poor surface to mass ratio.
Internal cracks	Variable	Two opposite effects. Small cracks might promote the release of high pressure and reduce the risk of spalling. However, parallel cracking close to the heated surface due to loads might increase the risk of spalling.
Concrete age	Variable	Young concrete has a high amount of free water, which increases the risk of spalling. This effect decreases with HPC and UHPC due to the low permeability.
Lightweight aggregates	Variable	Higher porosity and permeability enables the release of high pore pressure and decreases the risk of spalling. The higher moisture content of lightweight aggregates promotes the risk of spalling.

Table 1. Material-related factors with an influence on spalling.

2.3.2. Heating characteristics

Among the factors associated with heating characteristics, the heating rate and temperature gradients have a strong influence on explosive spalling. **Table 2** summarizes the governing factors depending on the heating characteristics that influence spalling in general.

Factors	Risk of spalling	Influences
Heating rate	Very high	Higher heating rates usually lead to explosive spalling with HPC mixes.
Temperature gradient	High	Temperature gradient is closely related to the heating rate. Higher temperature gradients promote the risk of explosive spalling due to thermal stresses.
Exposure on multiple surface	High	Heat exposure on more than one side increases the risk of corner or explosive spalling due to higher temperature gradients and thermal stresses
Absolute temperature	Moderate	Explosive spalling might occur with temperatures of less than 300~350°C. Very high temperatures $T > 1000$°C increase the risk of postcooling spalling.

Table 2. The governing factors depending on the heating characteristics with an influence on spalling.

2.3.3. Structural or mechanical factors

The main structural or mechanical factors with a significant influence on spalling are presented in **Table 3**. It is difficult to distinguish between pure material and pure structural or mechanical factors leading to spalling in some cases, since some factors can be attributed to both categories.

Factors	Risk of spalling	Influences
Applied load (compressive stress and restraint)	High	The risk of spalling increases with applied higher load levels. High compressive stresses caused by restraint to expansion develop when the rate of heating is such that the stresses cannot be relieved by creep quickly enough.
Cross section geometry (section size and shape)	High	Round cross section, rounded corners, sufficient reinforcement cover and spacing and modified tie design lowers the likelihood of spalling or increases the remaining load bearing capacity of concrete members after spalling.
Thermal expansion	High	Fixed ends as boundary conditions, eccentric load or bending increases risk.
Tensile strength	Low	A high tensile strength is considered as lowering the risk of explosive spalling since it offers a higher resistance.

Table 3. Structural or mechanical factors with an influence on spalling.

3. Design against explosive spalling

3.1. Preventive measures

Today, the explosive spalling of concrete is an important requisite to consider in fire safety design of RC structures. Various preventive measures against explosive spalling of concrete

http://dx.doi.org/10.5772/64551

under fire attack have been studied and discussed by many researchers for a long period of time. However, the available standards for the protection of structures against explosive spalling are insufficient. In the BS 8110: Part 2: 1985 [20], the standard adds that "In any method of determining fire resistance where loss of cover can endanger the structural element, measures should be taken to avoid its occurrence." As the fire-proof design recommendations according to the European design standard EN 1992-1-2 [21], the possible use and effectiveness of steel fiber and polypropylene (PP) fiber are discussed in addition to general thoughts on the use of a protective lining and changes to the structural design of concrete members. Several measures based on the factors influencing the spalling of concrete have been suggested to eliminate spalling or to reduce the damage (**Table 4**). These measures can be employed singly or in combinations.

Factors influencing spalling	**Basic measures**	**Specific measures**
Concrete conditions - High performance concrete - Light-weight concrete - Thermal properties - Moisture contents - Materials	- Thermal barrier - Control of temperature rise in concrete surface layer - Reduction of temperature gradient - Relief & reduction of vapor pressure	- Use of fire resistive materials - Coating of fire-proof paints - Plastering of fire-proof mortars - Covering of concrete by steel pipe etc. - Addition of synthetic fiber (Polypropylene fiber, etc.) - Forced-drying of structural members - Installation of moisture eliminatory tubes
Fire behavior & conditions - High heating rate - Fire exposure time	- Prevention of temperature rise	- Elimination of inflammable materials in building - Make noncombustible of Materials - Expansion of fire prevention facilities
Structural member conditions - Section size & shape - Concrete depth	- Fire safety design	

Table 4. Preventive measures response to the factors causing spalling [22].

As the most effective methods to reduce the risk of explosive spalling, the addition of polypropylene fibers and the use of a thermal barrier are recommended. The risk of explosive spalling, which can occur during the first 7–30 minutes of a fire attack, is also weakened by reducing the moisture content of the concrete to less than 5% by volume, by avoiding thin sections and rapid changes in shape, and by limiting the compressive stress.

3.2. Reduction in the high vapor pressure

A major recent development in the prevention of explosive spalling has been in the use of synthetic fibers in the concrete mix, especially polypropylene fibers. Polypropylene fibers melt at about 170°C, thus it could reduce the build-up of high pore pressure within the concrete due to creating channels for vapor to escape easily, as shown in **Figure 7**. This measure was first reported in Japan [23] and subsequently studied by Diederichs [24] and Connelly [17]. Connelly [17] reported that the addition of 0.05% by weight of fibers in concrete (w/c = 0.4, 10 mm aggregate) completely eliminated spalling in fire (heating rate 25°C/min), while 83% of similar specimens without fibers was broken explosively. It is clearly shown that the addition

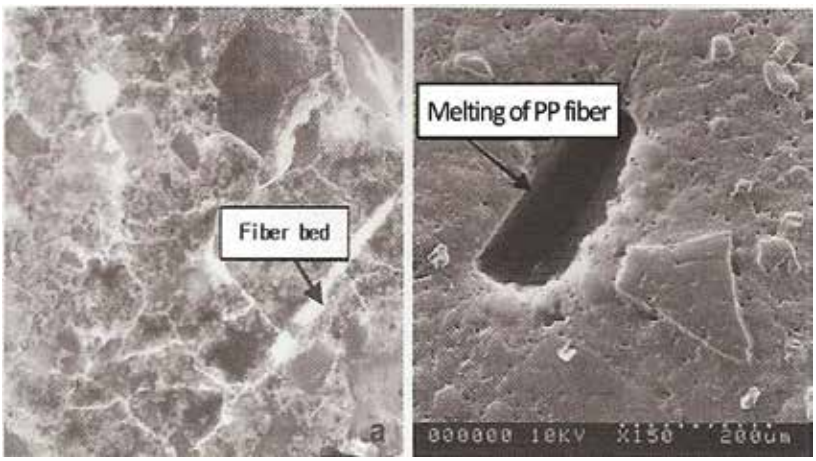

Figure 7. Melting of PP fibers in concrete at about 170°C [22].

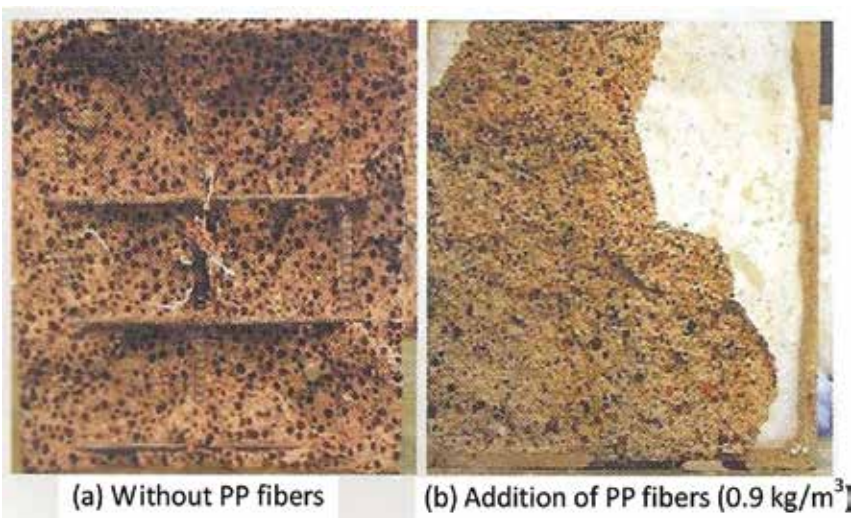

Figure 8. Fire resistance performance of the concrete with PP fibers of 0.9 kg/m^3 [22]. **(a)** Without PP fibers; and **(b)** addition of PP fibers (0.9 kg/m^3).

http://dx.doi.org/10.5772/64551

of polypropylene fibers is an effective means of preventing explosive spalling, as shown in **Figure 8**. The Euro Code 2 (Design of Concrete Structures, Part 1-2: Structural Fire Design, 1993) [25] also suggests PP fiber content of at least 2.0 kg/m^3 for effectively preventing the explosive spalling of HSC. However, more recent studies have reported that this fiber content in ultra-high-strength concrete (UHSC) of more than 150 N/mm^2 such as reactive powder concrete (RPC) was not enough for preventing explosive spalling in a fire, although they were found to be beneficial when used with HSC of 60~110 N/mm^2 [26]. Hence, the use of such fibers is more effective in lower strength concrete.

Meanwhile, in recent decades, different synthetic fibers have been tested in terms of melting characteristics, workability, and overall performance with the aim of reducing the risk of spalling. **Table 5** gives a brief overview of various fibers available to prevent explosive spalling of concrete.

Type of fibers	Effectiveness
Polypropylene fiber	- Melting (170°C) of PP fibers within concrete, increases permeability of concrete and releases high pore pressure. - Fibers might have negative influence on workability, in particular very thin fibers. - Fiber contents of 2~3 kg/m^3 seems to be most effective in spalling protection.
Nylon fiber	- A rather high melting temperature of 200°C, which might be too high for some mixes.
PVC	- Releases hazardous chlorides, should not be used with concrete.
Polyethylene fiber	- Low melting temperature of 90°C, but high viscosity of molten fibers minimizes the increase in permeability (less applicable).
Steel fiber	- Increases ductility of HPC and increases spalling resistance of columns with narrow spacing between the ties. - However, no noticeable increase in resistance with other structures was observed in tests.

Table 5. Use of various fibers to prevent the explosive spalling of concrete.

3.3. Thermal barrier

Thermal barriers usually limit the temperature increase and the maximum temperature at the surface of the concrete and thus reduce the risk of explosive spalling as well as loss of mechanical strength. Their layer thickness has to keep these temperatures below a critical level for spalling of concrete. However, critical temperatures leading to spalling are not generally available because they change with each individual concrete mix. Thermal barrier measures could be classified as two categories: (a) materials methods and (b) construction methods. In materials methods, the protective coating on the surface of the concrete by high fire resistive materials is usually used, as shown in **Figure 9**. In construction methods, the covering methods concrete with a steel pipe, the use of the metal-lath, or confinement steel reinforcement against spalling (**Figure 10**), and the surrounding methods concrete with a fire-proof board are presented as protective measure of spalling.

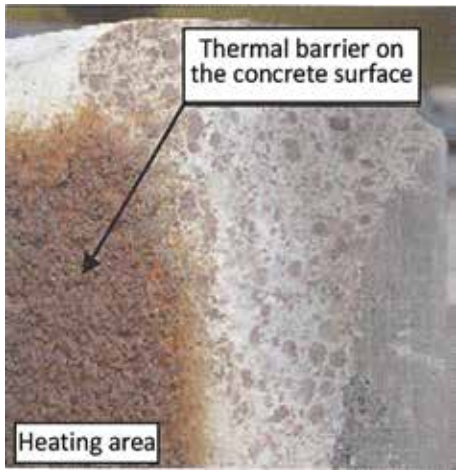

Figure 9. Fire resistance performance of the concrete coated with high fire resistive materials.

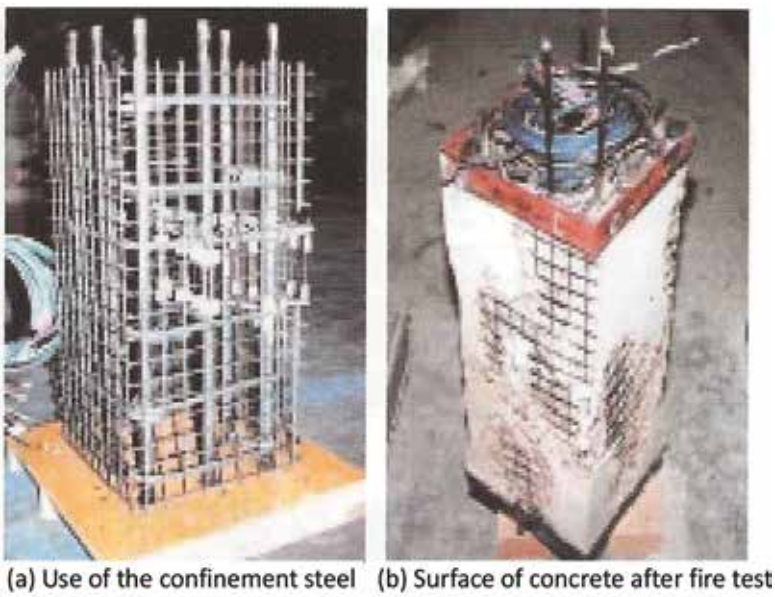

Figure 10. Fire resistance performance of the concrete with the confinement steel reinforcement against spalling. **(a)** Use of the confinement steel and **(b)** surface of the concrete after fire test.

In terms of the reduction of the peak temperatures within the concrete, these measures are the very effective method (PP fibers do not reduce that). However, there are two potential drawbacks: (1) the cost of the insulation is likely to be more than that of the fibers and (2) with some of the manufacturers there has been a problem with delimitation during normal service conditions. In general, the design criteria are to apply a sufficient thickness of coating so as to

http://dx.doi.org/10.5772/64551

reduce the maximum temperature at the surface of the concrete to below about 300°C and the maximum temperature at the steel rebar to about 250°C within 2 hours of the fire [13]. It should be noted that experience indicates that while 25 mm of coating may be adequate for concrete strength up to about f_c = 60 N/mm^2, but a coating thickness of 35 mm may be required for high strength concrete to avoid explosive spalling [13].

3.4. Spalling control techniques in the field

3.4.1. Advanced fire resistance (AFR) concrete

Advanced fire resistance concrete is manufactured with the polypropylene fibers (diameter: 0.012–0.2 mm, length: 5–20 mm) of 0.1–0.35% by volume and practically used in the HSC of 80–120 N/mm^2. In this concrete, the addition of polypropylene fibers is derived to prevent explosive spalling on the surface of concrete by the release of high vapor pressure and thermal expansions due to the melting of the PP fibers at about 160°C, which resulted in channels for water vapor to escape within the concrete. **Figure 11** shows the fire resistance performance of the column specimens applied in the ARF concrete [22].

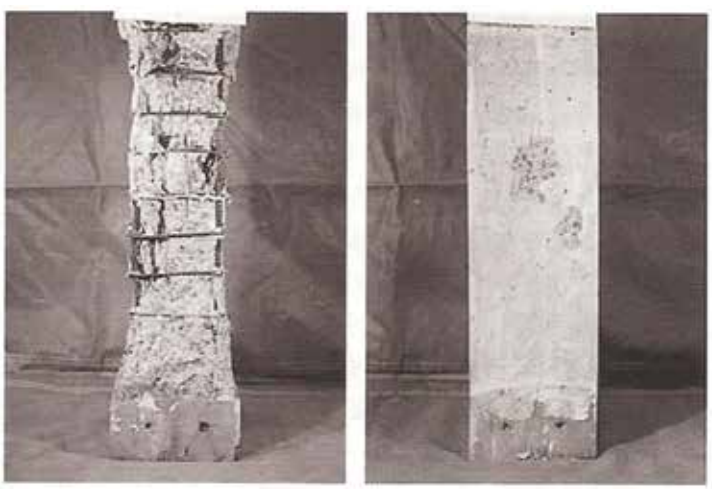

Figure 11. Fire resistance performance of the column specimens applied on the ARF concrete.

3.4.2. Fire performance concrete (FPC) method

Fire performance concrete method is to apply the PP powder instead of PP fibers in high strength concrete. The melting point of the PP powder is 165°C, the density is 0.9 g/cm^3, and it is usually used in the addition contents of 1~3 kg/m^3 by weight. Especially, PP powder has the excellent dispersibility and reduces the difficulty such as fiber ball when mixing it. **Figure 12** shows the fire resistance performance of the column specimen applied in the FPC method [8].

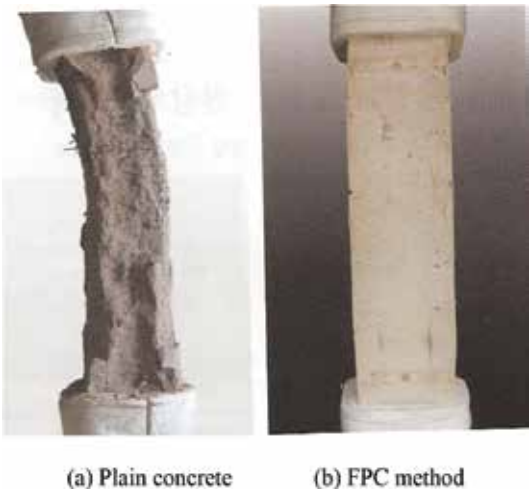

Figure 12. Fire resistance performance of the column specimen applied in the FPC method. **(a)** Plain concrete and **(b)** FPC method.

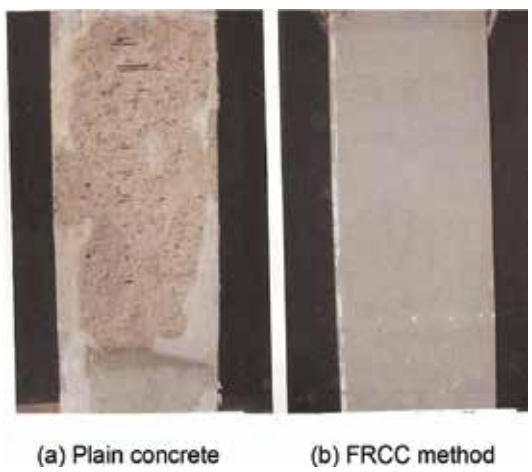

Figure 13. Fire resistance performance of the column specimen applied the FRCC method. **(a)** Plain concrete and **(b)** FRCC method.

3.4.3. Fire reinforced concrete column (FRCC) method

Fire reinforced concrete column method is to apply the protective coating on the surface of concrete by high fire resistive materials. As the high fire resistive materials, the calcium silicate board with fibers, the ceramic fire-proof mortars, the mortars mixed cellulose fibers, etc. are usually used. This is a thermal barrier method to limit the temperature increase and the maximum temperature at the surface of concrete in order to reduce the risk of explosive spalling. Their layer thickness has to keep more than 20 mm for the HSC of 80–120 N/mm^2 to

avoid explosive spalling, in general [22]. **Figure 13** shows the fire resistance performance of the column specimen applied in the FRCC method.

4. Conclusions

Explosive spalling is a very violent form of spalling, which is characterized by the breaking off of layers or pieces of concrete from the surface of a structural element, accompanied a typically loud explosive noise when exposed to high and rapidly rising temperature under fire conditions. It normally occurs within the first 7–30 minutes in a fire. The most recent theories of the causes of explosive spalling indicate that three factors play a crucial role: (a) the build-up of pore pressure, (b) thermal stresses, and (c) combined phenomena in the concrete when exposed to a rapidly increasing temperature. Explosive spalling generally occurs singly or on combination depending upon the moisture content, the section size, and the material. It is noticed that the high performance concrete tends to experience multiple spalling (combined pore pressure and thermal stress spalling) of thinner sections. In fact, a large number factors influence explosive spalling of concrete. Based on the mechanisms, the major factors leading to explosive spalling are heating rate, permeability of concrete, moisture content, presence of reinforcement, and level of external applied load. The factors can be classified into three categories: material-related factors, structural or mechanical factors, and heating characteristics. The majority of these factors can be directly associated with explosive spalling. However, some are also related to other types, and a clear separation between individual parameters is difficult to match. As the most effective methods to reduce the risk of explosive spalling, the addition of polypropylene fibers and the use of a thermal barrier are recommended. The risk of explosive spalling is also weakened by reducing the moisture content of the concrete to less than 5% by volume, by avoiding thin sections and rapid changes in shape, and by limiting the compressive stress.

Author details

Hyoung-Seok So

Address all correspondence to: sohs01@daum.net

Department of Architectural Engineering, Seonam University, Namwon, Republic of Korea

References

[1] Bentz, D.P.: Fibers, percolation, and spalling of high-performance concrete. ACI Materials Journal. 2000;97:351–359.

[2] Kodur, V.K.R.: Fiber reinforcement for minimize spalling in high strength concrete structural members exposed to fire. ACI Special Publication. 2003;216:221–236.

[3] Khoury, G.A., Grainger, B.N., and Sullivan, P.J.E.: Transient thermal strain of concrete: literature review, conditions within specimen and behaviour of individual constituents. Magazine of Concrete Research. 1985; 37(132):131–144.

[4] Gary, M.: Fire Tests on Reinforced Concrete Buildings (in German). Verlag Wilhelm Ernst und Sohn, Germany; 1916.

[5] British Standards Institution, BS 476. Fire Tests on Building Materials and Structures. BSI, London; 1987. Part 20: Method for determination of the fire resistance of elements of construction (general principles), Part 21: Method for determination of the fire resistance of elements of load-bearing, elements of construction, Part 22: Method for determination of the fire resistance of non-loadbearing elements of construction, Part 23: Method for determination of the contribution of components to the fire resistance of a structure, Part 24: Method for determination of the fire resistance of ventilation ducts.

[6] Shorter, G.W. and Harmathy, T.Z.: Moisture clog spalling. Proceedings of lnstitution of Civil Engineers. 1965;20:75–90.

[7] Meyer-Ottens, C.: The Question of Spalling of Concrete Structural Elements of Standard Concrete under Fire Loading (PhD Thesis). Technical University of Braunschweig, Germany; 1972.

[8] Akhtarnrzaman, A.A. and Sullivan, P.J.: Explosive spalling of concrete exposed to high temperature. Concrete Structures and Technology Research Report. Imperial College. London. 1970.

[9] Khoylou, N.: Modelling of moisture migration and spalling behaviour in non-uniformly heated concrete (PhD thesis). Imperial College. UK; 1997: 1147 p.

[10] Zeiml, M., Leithner, D., Lackner, R., and Mang, H.A.: How do polypropylene fibers improve the spalling, behaviour of in-situ concrete?. Cement and Concrete Research. 2006;36:929–942.

[11] Saito, H.: Explosive Spalling of Pre-stressed Concrete in Fire. Occasional Report No. 22. Building Research Institute, Japan; 1965.

[12] Dougill, J.W.: Modes of failure of concrete panels exposed to high temperatures. Magazine of Concrete Research. 1972;24:71–76.

[13] Khoury, G.A. and Anderberg, Y.: Fire Safety Design (FSD): Concrete Spalling Review. Report submitted to the Swedish National Road Administration. Sweden; 2000;37–40.

[14] Fu, Y. and Li, L.: Study on mechanism of thermal spalling in concrete exposed to elevated temperatures. Materials and Structures. 2011;44(1):361–376.

http://dx.doi.org/10.5772/64551

[15] Zhukov, V.V.: Explosive Failure of Concrete during a Fire (in Russian). Translation No. DT 2124. Joint Fire Research Organization, Borehamwood; 1975.

[16] Sertmehmetoglu, Y.: On a Mechanism of Spalling of Concrete under Fire Conditions (PhD Thesis). King's College, London; 1977.

[17] Connolly, R.J.: The Spalling of Concrete in Fires (PhD Thesis). Aston University. Birmingham;1995; 294 p.

[18] Hertz, K.D.: Limits of spalling of fire-exposed concrete. Fire Safety Journal. 2003;38(2): 103–116.

[19] Kodur, V.K.R.: Spalling in High Strength Concrete Exposed to Fire: Concerns, Causes, Critical Parameters and Cures. Advanced Technology in Structural Engineering. American Society of Civil Engineers; 2000;1–9.

[20] British Standards Institution. BS8110. Part 2: 1985; Structural Use of Concrete. Code of Practice for Special Circumstances. Section Four. Fire Resistance. BSI, London; 1985.

[21] EN 1991-1-2. Euro Code 1: Actions on Structures – Part 1–2: General Actions – Actions on Structures Exposed to Fire. DIN German Institute for Standardization. Germany; 2012.

[22] Hun, S., Lee, S.-H., and Sugahara, S.: Spalling prevention measures of high performance concrete. Magazine of the Korea Concrete Institute. 2005;17(3):33–39.

[23] Nishida, A., Yamazaki, N., Inoue, H., Schneider, U., and Diederichs, U.: Study on the Properties of High Strength Concrete with Short Polypropylene Fibre for Spalling Resistance. International Symposium on Concrete under Severe Conditions. Sapporo, Japan; 1995.

[24] Diederichs U, Jumppanen UM, Morita T, Nause P, Schneider U.: Concerning spalling behaviour of high strength concrete columns under ?re exposure, Braunschweig University of Technology. Germany; 1994;12 p.

[25] ENV 1992-1-2: Euro Code 2: Design of concrete structures. Part 1–2: Structural Fire Design. Comite Europeen de Normalisation, available through British Standards Institution, London, 1994;59–62.

[26] Kalifa, P. Chene, G. and Galle, Ch.: High-Temperature Behaviour of HPC with Polypropylene Fibers from Spalling to Microstructure. Cement and Concrete Research. 2001;31;1487–1499.

Chapter 3

Fracture Theory Under Freeze-Thaw Cycles and Freeze-Thaw Resistance of Alkali-Slag Concrete

Qixuan Li

Additional information is available at the end of the chapter

http://dx.doi.org/10.5772/63810

Abstract

Despite the widespread research on alkali-activated concrete, its fracture properties under freeze-thaws are rarely studied; the response surface methodology (RSM) theory has not been put forward; and unstable fracture toughness, K_{IC}^{S}, influenced by freeze-thaws and slag content has not been researched. The purpose of this article is to investigate the calculation method of alkali-slag concrete (ASC) fracture parameters and provide theoretical support for RSM model of ASC prepared with Na_2SiO_3 and NaOH composite activator. The influence law of freeze-thaw and slag content on unstable fracture toughness, K_{IC}^{S}, is put forward. Results show that after crack mouth opening displacement (CMOD) is measured, other fracture parameters including concrete effective fracture length; crack tip opening displacement (CTOD); and stress intensity factors K_{IC}^{C}, K_{IC}^{C}, and K_{IC}^{S} from closure stress $\sigma(w)$ can be obtained according to double-K fracture criterion and DL/T 5332-2005 "Hydraulic concrete fracture test procedures". RSM principles and advantages, its optimization content and procedure, the data processing software Design-Expert and verification analysis procedure of RSM model are put forward. Since the ASC structure is compact, characterized for water and air penetration resistance, its antifreezing characteristic is desirable.

Keywords: alkali-slag concrete, fracture parameter, response surface theory, unstable fracture toughness, composite activator

1. Introduction

It has been nearly 200 years since the advent of Portland cement in 1824. Then there were mortar, concrete and reinforced concrete generated from it. Concrete has become the most widely and

largely used construction material. Construction of highways, bridges, ports, oil platforms, airports, dams, tunnels; underground constructions; and construction above and under sea level are all inseparable from concrete. Today, with the continuous progress of human demand and technology, research on concrete materials and structures is constantly moving toward depth and breadth. High performance and new special concrete is more and more widely used in projects, the construction technology is also maturing day by day.

With social progress and the advent of low-carbon economy, environmental protection and sustainable development attract more and more attention around the world. However, cement production causes serious pollution and consumes a large amount of energy and nonrenewable resources such as coal, using large amount of limestone, iron ore, clay, etc. The traditional production process emits large amount of dust, and also exhausts huge amount of CO_2, SO_2, NO_X and other emissions. It is calculated that 1 t of cement clinker's atmospheric emissions will be 1 t of CO_2, 0.86 kg of SO_2, 1.75 kg of NOx and 130 kg of dust. Cement production will continue to see a significant increase from the existing level, which will cause serious burden on the environment.

Production of new green and high performance concrete should make full use of industrial waste, such as slag, fly ash, limestone, gangue, etc., with no or little use of cement clinker. Minimizing clinker production reduces the environmental impact, and making new "cement" through technical means results in green cementitious materials.

Most of the world is in cold region, where winter temperature is below-5°C and concrete damage in those areas is the most relevant to freezing and thawing. Hypothermia is very unfavorable for concrete; the low temperature and freeze-thaw cycles usually lead to concrete deterioration in airports, highways, bridges, hydraulic structures, etc. Freeze-thaw damage is a persistent historic problem, receiving widespread attention from academia and engineering field. Internationally renowned concrete expert Sun proved in 1999 that the concrete damage process is accelerated and the extent of damage increased under the simultaneous action of load and freeze-thaw cycles [1]. Therefore, freezing is an important factor affecting the durability of concrete structures. Where there are alternating positive and negative temperatures, there exists concrete freeze-thaw damage.

During freeze-thaw process, there are heaving pressure cycles inside the concrete material, producing freeze-thaw internal stress. The structural organization will appear in irreversible microscopic changes such as microcrack formation, expansion, empty initiation and crystal dislocations. Internal concrete defects will gradually expand and accumulate, causing deterioration of material macroscopic mechanical properties, and resulting in damage. Damage caused by freeze-thaw stress gradually accumulates with freeze-thaw cycles, resulting in deterioration and even damage in concrete, which can be explained with percolation theory and damage theory, namely no damage → damage (formation of microcracks) → macrocracks → damage.

Thus, concrete freeze-thaw damage mechanism mainly lies in various microcracks, defects formation and expansion under external freeze-thaw cycles, resulting in damage and failure. Concrete freeze-thaw damage process indicates its complicated constitutive behavior, and it

http://dx.doi.org/10.5772/63810

would be difficult to achieve the desired results if only describing with classical elastic or plastic mechanics. In order to fully reflect mechanical behavior of concrete structures under external factors, concrete body must be treated as deformable solid containing microcracks, other defects and even macroscopic cracks, and studied with fracture mechanics and damage mechanics.

There are many studies about alkali-activated concrete these years including application in railway sleepers [2], characteristics after exposure to high temperature [3], mixed fine aggregates [4], static and dynamic performances [5], mechanical properties [6], durability [7], eco-efficiency [8] and heat resistance characteristics [9]. Ravikumar [10] and Neithalath [11] successively published papers about chloride ion transport and electrical impedance of alkali-activated slag concrete. Qixuan [12] proposed the RSM model for ASC fracture property prediction. However, the RSM theory has not been clarified and systematically studied. Provis [13] summarized the progress in understanding alkali-activated materials since 2011, which is of great value. Kovtun [14] studied the chemical acceleration of blastfurnace slag activated by sodium carbonate. Ma [15] corrected one misunderstanding in the shrinkage of alkali-activated fly ash, and is beneficial for future researchers. Ke [16] implemented calcined layered double hydroxides into the controlling of sodium carbonate-activated slag cements.

As can be seen, fruitful research results have been achieved in concrete deterioration and damage, but most of them focus on properties under load conditions at room temperature, ignoring environmental impact on concrete mechanical properties. There is little research on concrete fracture properties under freeze-thaw cycles, even less analyzing concrete fracture behavior and fracture characteristics after freeze-thaw cycles. Since fracture toughness is an important basis for the analysis of concrete crack propagation stability, it is extremely urgent and necessary studying concrete fracture properties under freeze-thaw cycles.

Through calculating, calculation method of ASC fracture parameters such as critical effective fracture length a_c, stress intensity factor K_{IC}^{C} caused by closure stress, initiation toughness K_{IC}^{Q} and unstable fracture toughness K_{IC}^{S} are investigated. The response surface methodology theory is systematically put forward, including RSM principles and advantages, optimization content and procedure, data processing software Design-Expert and verification of RSM model. Influence law of freeze-thaw on K_{IC}^{S} under different slag content is studied.

2. Test materials and methods

2.1. Raw materials and preparation

ASC material consists of a quaternary system (slag, activator, sand, stone), and the correct choice of raw material is especially important. Through investigation and analysis, this chapter ultimately determines the test raw materials as follows:

(1) Activator

Type and dosage of activator have a great impact on ASC performance. Currently, there are Na_2SiO_3 or K_2SiO_3 water glass solution and NaOH or KOH solution, and alkali metal carbonates and alkaline earth metal chlorides, among which water glass is more widely used and has better properties.

In this study, the activator is composed of Na_2SiO_3 sodium silicate (27.21% SiO_2, 8.14% Na_2O, Ms = 3.1) and NaOH complex solution, which density was 1.43 g/cm^3.

(2) Blast furnace slag powder

Blast furnace slag powder is a pig iron smelting slag discharged from the blast furnace. From the aspect of chemical composition, blast furnace slag belongs to silicate material, whose chemical compositions are mainly CaO, Al_2O_3, SiO_2, and the content is generally above 90%. In addition, there are MgO, MnO, Fe_2O_3, CaS, FeS and TiO_2 chemical compositions.

The metallurgy blast furnace slag powder used in this study has the specific surface area of 410 m^2/kg and density of 2.86 g/cm^3. The main chemical composition of slag powder is shown in **Table 1**.

CaO	SiO_2	Al_2O_3	MgO	MnO	Fe_2O_3	TiO_2	Loss
38.95	33.91	10.71	9.41	0.31	3.28	3.43	1.27

Table 1. Chemical compositions of slag/w%.

According to GB/T 18046-2000 "Ground granulated blast furnace slag used for cement and concrete" [17], GB/T 18736-2002 "Mineral admixtures for high strength and high performance concrete" [18] and GB/T 12957/2005 "Test method for activity of industrial waste slag used as addition to cement" [19], 7 and 28 days activity indexes of the slag are 96.2% and 105.7%, which are high.

(3) Fine aggregate

Fine aggregate should be hard, durable, clean, with smooth grain shape, good gradation and suitable fineness modulus, and the impurity should be less than a predetermined value. Besides, the natural river sand should be preferred, because it is generally hard, with good grain shape and low clay content, which is beneficial to the fresh concrete workability and hardened concrete performance. When using artificial sand, it should paid attention that the content of coarse particles and small particles are not too high. Zone II river sand should be preferred in concrete preparation.

The role of fine aggregate in the ASC is similar to forkability and strengt with filling effect on the one hand, while being the bond between coarse aggregate and cementitious materials on the other hand. This chapter uses natural river sand with fineness modulus of 2.86, densi-

http://dx.doi.org/10.5772/63810

ty of 2.63 g/cm^3, bulk density of 1.50 g/cm^3 and 0.5% clay content. Gradation screening testing results are shown in **Table 2**.

Particle size/mm		Accumulated sieve (by mass)/%				
		Mesh size (square hole sieve)/mm				
		2.36	**4.75**	**9.50**	**19.0**	**37.5**
Screening results	5–10	100	68	1	–	–
	10–20	100	97.2	81.5	18	–
	20–40	–	–	–	100	0
After screening	5–40	–	95.86	84.6	65.4	0

Table 2. Fine aggregates screening test results.

(4) Coarse aggregate

Coarse aggregates commonly used in concrete are gravel and pebbles. The coarse aggregate should be hard, durable, clean and has a certain gradation. The main technical requirements are as follows:

1. Varieties: coarse aggregate should be hard texture unweathered rock, such as basalt, limestone, granite and diabase. The more dense is the rock, the lower is the water absorption, the smaller is the crushing index and the better are the mechanical properties.
2. Grain shape: rough gravel with angular is generally used; gravel grain shape produced by hammer crusher is good, which has good mechanical properties, and can bond relatively more firm with cement. Flakiness particle content should not be over 5%, and the clay content should not exceed 1.0%.
3. Grading: to obtain dense concrete, coarse aggregate should have a good grading. With good grading, the porosity will be small, less cement will be needed to achieve the same mobility and concrete shrinkage deformation will be small, forming good volume stability to enhance strength and durability.

This chapter uses limestone gravel (45% 5–20 mm, 55% 20–40 mm) with density of 2.76 g/cm^3 and bulk density 1.69 g/cm^3.

2.2. Workability and strength test

Test workability according to GB/T 50080-2002 "Standard for test method of performance on ordinary fresh concrete" [20]. The measuring method is as follows: Add the concrete mix according to the provided method into the standard tapered slump cone (bottomless). After the cone is filled elaborately, lift the cartridge straight up. The mixture will appear slump

because of its own weight. Measure the size of the downward slump (mm), which is slump as liquidity indicator, as shown in **Figure 1**.

Figure 1. Determination of concrete mixture slump.

When measuring the fresh concrete slump, visually evaluate the following properties at the same time:

1. Cohesiveness: observe the mutual cohesion situation of the components. Use a tamper to tap on the concrete cone side already slumped, if the cone gradually sinks after tapping, the mixture cohesiveness is favorable; on the other hand, if the cone suddenly collapses, partially crack or the stones segregate, it means that its cohesiveness is bad.
2. Water retention: According to the condition of water saturating out of the mixture, there are three degrees as "a lot", "small" and "no".

"A lot" means that there is much water separating out of the bottom after pulling up the slump cone; "small" indicates that a small amount of water comes from the cone after it is pulled up; and "no" means that no water penetrates from the cone even it is pulled up.

Figure 2. Wt60 t Universal Bending Test Machine and 200 t Compression Testing Machine.

http://dx.doi.org/10.5772/63810

According to GB/T 50081-2002 "Standard for test method of mechanical properties on ordinary concrete" [21], strength tests are carried out using wt60 and 200 t Universal Testing Machine (as shown in **Figure 2**). Test the specimen flexural and compressive strength after 7 and 28 days of curing.

3. ASC fracture properties under freeze-thaw cycles

3.1. Fracture toughness parameter calculation method

Crack mouth opening displacement (CMOD) was measured directly using clip-on extensometer. The extensometer was connected to computer automatic acquisition system, through which loads could be obtained [22]—crack mouth opening displacement curve under loads, which is P-CMOD curve to get $CMOD_C$. At the same time, the test can also directly measure ASC load-displacement curve that is P-V curve, and take the load when the specimen fractures at ultimate load P_{max}. After P_{max} and $CMOD_C$ are set, concrete effective fracture length; crack tip opening displacement CTOD; and stress intensity factors K_{IC}^{C}, K_{IC}^{Q} and K_{IC}^{S} from closure stress $\sigma_{(w)}$ can be calculated according to double-*K* fracture criterion and concrete fracture toughness calculation equations formulated by DL/T 5332-2005 "Norm for fracture test of hydraulic concrete" [23].

3.1.1. Calculation of critical effective fracture length a_C

Due to stable crack extension phase of concrete specimens before unstable fracture, the actual crack length is greater than the initial crack length before unstable fracture. It is difficult to accurately measure critical crack subcritical extension length Δa_C and load when the crack starts to expand (crack initiation load, corresponding to K_{IC}^{Q}). They are usually obtained with advanced testing technologies such as photoelastic patch. Therefore, they are more frequently got through calculation.

For the standard three-point bending beam (span-height ratio $S/h = 3$, hereinafter the same), the load *P* and CMOD has following relationship [24]:

$$\begin{cases} CMOD=\dfrac{6PSa}{thE}F_1(\alpha) \\ F_1(\alpha)=0.76-2.28\alpha+3.87\alpha^2-2.04\alpha^3\dfrac{0.66}{(1-\alpha)^2} \end{cases} \quad (1)$$

where *P* is load, *N*; *S* is the test piece beam span, m; *t* and *h* are the specimen width and height, m; *a* is the effective fracture length, m; CMOD is the crack mouth opening displacement corresponding to *P*, m; α is the effective fracture length and specimen height ratio, *a*/*h* and *E* is the concrete calculation elastic modulus, MPa.

Wherein the elastic modulus *E* is calculated according to formula (2):

$$E = \frac{1}{tC_i}\left[3.70 + 32.6\tan^2\left(\frac{\pi}{2}\frac{a_0 + h_0}{h + h_0}\right)\right] \tag{2}$$

Where a_0 is the initial crack degree, m; h_0 is the steel sheet thickness equipped on the clip-on extensometer, m; $C_i = V_i/F_i$ is an initial value of the specimen, $\mu m/kN$, which is calculated with V, P values of any point of straight line segments on curve rise.

Substitute P_{max} and $CMOD_C$ into formula (1) and get the nonlinear equation of a_C. Through iteration, a_C can be calculated, but the procedure is cumbersome. Literature [24] provides a simplified formula as follows:

$$CMOD = \frac{P}{Et}\left[3.70 + 32.60tg^2\left(\frac{\pi}{2}\alpha\right)\right] \tag{3}$$

Where the symbols have the same meaning as in Eqs. (1) and (2).

Calculations show that when $0.2 \le \alpha \le 0.75$, the maximum relative error between formula (3) and formula (1) is 2%. Therefore, a_C can be calculated according to formula (3):

$$a_C = \frac{\pi}{2} harctg\sqrt{\frac{Et}{32.6P}CMOD_C - 0.1135} - h_0 \tag{4}$$

3.1.2. Calculation of stress intensity factor K_{IC}^C caused by closure stress

Because of the cracks stable expansion phase before concrete unstable fracture, according to the fictitious crack model, when the crack opening displacement w is smaller than w_0 (w_0 is the opening displacement when cracks cannot transfer stress), it can still pass the stress $\sigma(w)$, which is called closure stress. Therefore, in addition to external loads, there also exists the closure stress preventing crack propagation in three-point bending beam. Stress intensity factor caused by closure stress $\sigma_{(w)}$ at the crack tip is denoted as K_{IC}^C. Shilang X et al. derived standard three-point bending beam specimen K_{IC}^C calculation formula based on fictitious crack model [25]:

$$K_{IC}^C = \int_{a_0}^{a} \frac{2}{\sqrt{\pi a}}\sigma(u)F(u,v)dx \ (a \le a_c) \tag{5}$$

$$F(u,v) = \frac{3.52(1-u)}{(1-u)^{3/2}} - \frac{4.35 - 5.28u}{(1-v)^{3/2}} + \left[\frac{1.30 - 0.30u^{3/2}}{(1-u^2)^{1/2}} + 0.83 - 1.76u\right][1-(1-u)v]$$

http://dx.doi.org/10.5772/63810

$$\frac{\sigma(u)}{f_t} = \beta + (1-\beta)\frac{u - \frac{v_0}{v}}{1 - \frac{v_0}{v}}$$

$$\beta = \frac{\sigma_s(CTOD_C)}{f_t} CTOD_C = CMOD_C\{(1-\beta)^2 + (1.081 - 1.149\alpha)(\beta - \beta^2)\}^{1/2}$$

$$\sigma_S(CTOD_C) = f_t\left[1 + \left(C_1\frac{CTOD_C}{w_0}\right)^3\right]\exp\left(-C_2\frac{CTOD_C}{w_0}\right) - \frac{CTOD_C}{w_0}\left(1 + C_1^3\right)\exp\left(-C_2\right)$$

In the formula, $u = x/a$; $v = a/h$; a is the effective fracture length, m; x is the distance from integral point to initial crack tip, m; f_t is concrete tensile strength, MPa, generally take $f_t = 0.95\, f_{SP}$ [26]; $\beta = a_0/a_c$; $CTOD_C$ is the crack tip critical level opening displacement, m; $C1$ and $C2$ are concrete material constant; and w_0 is the crack opening displacement when transfer stress is zero, mm, and is relevant with concrete characteristics such as strength.

Since the integral nonlinearity and integral singularity when $u = 1$, the above K_{IC}^C calculation process becomes very complicated. Literature [27] simplified it as follows: make $F(u, v) = A \cdot u + B + 1/\sqrt{1-u^2}$, then the simplified K_{IC}^C calculation method is given as follows:

$$K_{IC}^C = 2\sqrt{\frac{a}{\pi}} \times \left[\frac{A \cdot D}{3}u^3 + \frac{A \cdot F + C \cdot D}{2}u^2 + C \cdot F \cdot u - D\sqrt{1-u^2} + F \cdot \arcsin(u)\right]_{\frac{v_0}{v}}^{1} \tag{6}$$

Where $v_0 = a_0/h$; $A = \frac{2.23v^2 + 1.16v + 0.17}{(1-v)^{1.5}}$; $C = \frac{1.65v^2 + 1.67v + 0.24}{(1-v)^{1.5}}$; $D = \frac{f_t - \sigma_s}{v - v_0}v$; $F = \frac{v\sigma_s - v_0 f_t}{v - v_0}$ and the other symbols are the same as defined above.

Paper [28] points out that when CTOD = $CTOD_C$, C_1, C_2 and w_0 values have little effect on K_{IC}^C, and $C_1 = 3$, $C_2 = 7$ and $w_0 = 0.16$ mm are generally preferable for concrete. Qijin Zhang also calculated $C_1 = 3$, $C_2 = 7$ and $w_0 = 0.16$ mm; $C_1 = 2$, $C_2 = 6$ and $w_0 = 0.14$ mm; and $C_1 = 4$, $C_2 = 8$ and $w_0 = 0.18$ mm through experiments, to verify the impact degree of changing these three parameters on K_{IC}^C. Results show that, using different C_1, C_2 and w_0, the calculated K_{IC}^C was close to each other [29]. Therefore, this paper directly takes $C_1 = 3$, $C_2 = 7$ and $w_0 = 0.16$ mm.

3.1.3. Calculation of initiation toughness K_{IC}^Q and unstable fracture toughness K_{IC}^S

The formula in [25] derived computational formula of K_{IC}^S with the boundary collocation method: for the standard three-point bending beam specimen, K_{IC}^S can be calculated as follows:

$$K_{IC}^{S} = \frac{1.5P_{\max}S}{th^2}\sqrt{a_c}F_1(\alpha) \tag{7}$$

$$F_1(\alpha) = \frac{1.99 - \alpha(1-\alpha)(2.15 - 3.93\alpha + 2.7\alpha^2)}{(1+2\alpha)(1-\alpha)^{3/2}}$$

$$P_{max} = F_{\max} + \frac{mg}{2} \times 10^{-2}$$

Where $P_{\max}$ is the ultimate load, kN; $F_{\max}$ is the maximum load, KN; m is the mass between specimen seats, kg; g is the acceleration of gravity, 9.81 m/s^2; S is the beam span, m; and α is the critical effective fracture length and specimen height ratio, a_c/h.

Thus, the following is obtained:

$$K_{IC}^{Q} = K_{IC}^{S} - K_{IC}^{C} \tag{8}$$

Thus, according to Eq. (7), concrete K_{IC}^{S} can be calculated; K_{IC}^{C} is calculated according to formula (6); and then K_{IC}^{Q} is obtained according to Eq. (8).

In addition, DL/T 5332-2005 "Norm for fracture test of hydraulic concrete" also gives K_{IC}^{Q} calculation formula similar to formula (7). Only when calculating K_{IC}^{Q}, a is taken as a_0, F is for the crack initiation load F_Q, α is the initial crack length and specimen height ratio a_0/h, namely

$$K_{IC}^{Q} = \frac{1.5\left(F_Q + \frac{mg}{2} \times 10^{-2}\right)S}{th^2}\sqrt{a_0}F_1(\alpha) \tag{9}$$

$$F_1(\alpha) = \frac{1.99 - \alpha(1-\alpha)(2.15 - 3.93\alpha + 2.7\alpha^2)}{(1+2\alpha)(1-\alpha)^{3/2}}$$

In the formula, initiation load F_Q transforms into corresponding load of elected segment turning point. A large number of experiments show that most of the turning point is in the range of (0.6~0.9)$F_{\max}$.

3.2. RSM model analysis

Most structures in cold regions of northern China are under the impact of low temperature and freeze-thaw action, resulting in freeze-thaw damage. Freezing and thawing have a

http://dx.doi.org/10.5772/63810

significant impact on the safety and durability of concrete structures in cold regions. There are lots of researches about effect of freeze-thaw cycles on Portland cement, but study on ASC performance degradation under freezing and thawing is still insufficient. In this study, the development law of ASC fracture properties under freezing and thawing is studied. According to ASC fracture parameters before and after freeze-thaw cycles: double-*K* fracture toughness K_{IC}^{Q} and K_{IC}^{S}, CMOD and effective fracture length test, sol ratio, slag content and age are selected as parameters, and K_{IC}^{Q}, K_{IC}^{S}, $CMOD_C$ and a_c are response values. Using RSM and BBD methods, influence law and degree of parameters and their interaction on ASC fracture parameters before and after freeze-thaw cycles are investigated. With Design-Expert 7.0 statistical analysis software, the regression equation prediction model is obtained, and response surface is analyzed, whose effects on ASC fracture properties are obtained.

With many specimens, the test duration time is long. In order to ensure the relationship between material strength and fracture toughness, concrete strength measurement is carried out with fracture tests.

3.2.1. RSM principles and advantages

In examining the impact of multivariate on concrete performance, other factors are usually fixed, while changing a single factor. Although certain effect could be received, the test amount is large and it is unable to investigate the interaction among various factors. RSM was proposed by Box and Wilson [30] in 1951, which is a combination of mathematical and statistical methods, which obtains certain data with reasonable experimental design and tests. The functional relationship between factor and response value is fitted using multiple quadratic regression equation, and the optimal process parameters are found through regression analysis, so RSM is a statistical method for solving multivariate problems.

This method is mainly used to analyze the response of interest affected by a number of variables through modeling and analysis, which can combine random and deterministic simulation problems together more easily. In this way, influence of each variable on indicators (response) in the experiment will be reflected, and the impact of interactions between variables can also be reflected, whose inner relationship is revealed with a perspective view. The ultimate aim is to optimize the response, becoming suitable for solving issues related to nonlinear data processing.

As a new experimental optimization and data processing method, RSM includes experimental design, modeling, model suitability testing, finding the best combination of conditions, and many other testing and statistical techniques that can be very suitable for experimental design and response surface analysis on experimental results.

Through process regression and response surface, contour line drawing, the response corresponding to each factor level can be easily obtained. Based on the response value of each factor level, the predicted optimal response value and corresponding experimental condition can be found, thus obtaining experimental optimal conditions ultimately.

Compared with traditional mathematical statistical methods (linear regression analysis and orthogonal design), RSM has a clear advantage in comparison. Although regression equation between the factors and response value can be obtained with experimental data through linear regression analysis, a large amount of data is required, costing much time and effort. It discusses the impact of only one factor and cannot consider the combined effect of several factors; orthogonal design focuses on scientific and reasonable arrangement for the test; and several factors may be considered at the same time and the best combination of factor levels can be found. But only isolated experimental points can be analyzed for orthogonal design, then preferred combination can only be selected from preset several experimental levels. As a result, a clear function expression, namely the regression equation between the factor and response value, cannot be given on the entire region.

The optimal condition obtained is not in the true sense, which can only be the ideal condition, so the optimal factor combination and response value cannot be given on the entire region. The RSM can consider a number of factors that affect the product at different levels; using experimental data, optimal combination problem affected by many factors can be solved through mathematical model, which is more effective than single factor analysis. Since rational experimental design is adopted, taking into account test random error, a comprehensive study on experiments with little time and small number of experiments can be conducted.

During optimization of experimental conditions, each level of experiment can be analyzed continuously. If processing response surface analysis on the experimental data is obtained, the forecasting model will generally be a curved surface, that the forecasting model is obtained continuously and then the best combination of each factor and optimal response on the entire area can be obtained.

Meanwhile, RSM fits unknown complex function on a small area with a linear or quadratic polynomial model, which has relatively simple calculation, and the obtained regression equation has higher precision.

3.2.2. Optimization content and procedure

RSM optimization is usually divided into three parts:

1. Experimental design: there are many experimental design methods for response surface analysis, the most commonly used are Central Composite Design (CCD), Box-Behnken Design (BBD) and Plackett-Burman Design (PBD); experimental design factors may be encoded or not coded.

2. Analysis: complete corresponding statistical analysis such as nonlinear data fitting variance analysis, to obtain the corresponding surface equation, and evaluate the fitting result and effectiveness.

3. Optimization: in this module, optimization requirements can be set up, such as the highest value, lowest value or others; the software automatically calculates the optimal experiment value, and provides one or more experimental conditions under optimal results.

http://dx.doi.org/10.5772/63810

Specific steps of RSM optimization are as follows:

1. Determine the factors: determine the key factors to examine the process, namely important factors affecting the results within the research scope.

2. Determine the factor level: through single factor tests or determining factor level range by single factor tests or sample characteristics and process. If the scope of these levels is too wide to give precise optimum conditions, RSM with smaller factor level range can be done for more precise optimal conditions and regression equation.

3. Determine the experimental point: using appropriate experimental design to determine the experiment points. Experimental design emphasizes that test point should minimize the total experiment times. After test points are determined, experiments are carried out on the points according to the random principle. Certain data are obtained to do statistical analysis.

4. Data analysis: using appropriate statistical methods and computer program, experimental data are analyzed. Nonlinear fitting method is mainly used in response surface analysis to obtain a regression equation. The most common fitting method is the polynomial method; linear polynomial can be used in a simple relationship; quadratic polynomial can be used in a relationship containing interaction; and cubic or higher-degree polynomial can be used in more complicated interaction. A quadratic polynomial is used in general.

According to the fitting equation obtained, a response surface plot can be used to obtain the optimum value; equation solving method can also be used to obtain the optimum value. In addition, using some of the data processing software, the optimal results can be easily obtained. Statistical analysis softwares often used are SAS, SPSS and Design-Expert.

The optimization result obtained from response surface analysis is a prediction, which needs to be verified through experiments. If the corresponding prediction and experimental results are consistent according to predicted experimental conditions, then the response surface optimization analysis is successful; otherwise, it is needed to change the response surface equation, or reselect reasonable experimental factors and levels.

3.2.3. Data processing software Design-Expert

As the world's top-level experimental design software, Design-Expert is the easiest to use and most complete with best affinity. In RSM optimization test papers already published, Design-Expert is the most widely used software. Design-Expert software is a handy business software for response surface optimization, and it is very convenient to use in experimental design and data processing. Although not as powerful as SAS, Design-Expert can be easily used in CCD or BBD response surface analysis, the quadratic polynomial surface analysis can be accessed very well and the data processing requirements can be satisfied. Some of the operations are more convenient than SAS, and the three-dimensional effect is more intuitive. The optimization results analyzed with RSM can be automatically obtained by the software, without solving surface equation with mathematical tools like MATLAB.

During process of using the software, in order to access the experimental condition predictive value with relative accurate optimal results, the decimal digits of factor level can be set as two or more. Of course, the number of effective digits under actual experimental conditions should also be taken into account in setting the effective number of bits.

With the improvement of computer performance, RSM has become an optimization technique with high-precision, wide application and practical value. It is mainly used in three aspects [31, 32]: (1) describing the impact of a single test variable on response values; (2) determining the relationship between variables; and (3) describing the combined effects of all variables on response value.

Thus, RSM can be used in agriculture, biotechnology, food, chemistry, manufacturing and other fields, which has already been widely used in the optimization design, reliability analysis and calculation, kinetics, engineering process control and other aspects. RSM has become an effective way to reduce development costs, optimize processing conditions, improve product quality and solve practical problems in production process. But it has been rarely applied in civil engineering, even less in concrete. Therefore, this section briefly describes the RSM application principles, advantages and steps, hoping to help more researchers use RSM technology, for convenient and effective solution in the design and data processing problems, especially hoping to make RSM more widely used in concrete engineering.

Factor	**Code**	**Levels of code**		
		−1	**0**	**1**
A/S	A	0.54	0.56	0.58
Slag content/(g/cm^3)	B	0.40	0.42	0.44
Age/days	C	28	60	92

Table 3. Levels of factors of RSM.

Test number	**Design of tests**			**Test results**			
	A	***B*/(g/cm^3)**	***C*/*d***	K_{IC}^{Q}**/MPa·m$^{1/2}$**	K_{IC}^{S}**/MPa·m$^{1/2}$**	***CMOD*$_C$/mm**	***a*C/mm**
1	−1	−1	0	7.723353	11.93899	0.1257	68.3752
2	1	−1	0	4.322432	7.597456	0.1213	65.7866
3	1	0	−1	4.288812	7.586042	0.1212	65.7278
4	0	0	0	4.235751	7.546166	0.1207	65.4336
5	1	0	1	4.253227	8.028535	0.1152	62.1978
6	0	0	0	4.431611	8.196176	0.1162	62.7861
7	0	0	0	8.249791	12.45929	0.1293	69.9074
8	0	1	−1	4.199010	7.977579	0.1149	62.0213
9	−1	0	1	8.224674	12.43252	0.1291	69.8436

http://dx.doi.org/10.5772/63810

Test number	Design of tests			Test results			
	A	*B*/(g/cm³)	*C*/*d*	K_{IC}^{Q}/MPa·m$^{1/2}$	K_{IC}^{S}/MPa·m$^{1/2}$	$CMOD_C$/mm	*a*C/mm
10	0	−1	1	4.183162	7.963782	0.1148	61.9624
11	1	1	0	4.026418	7.890307	0.1132	61.0211
12	−1	0	−1	4.322866	8.093164	0.1156	62.4331
13	0	−1	−1	4.117233	7.934421	0.1141	61.5506
14	−1	1	0	4.055794	7.406423	0.1191	64.4922
15	0	0	0	7.824996	12.02145	0.1286	69.0125
16	0	1	1	4.237481	8.011488	0.1149	62.1389
17	0	0	0	4.628621	8.382064	0.1173	63.4332

Table 4. BBD test design and the results.

3.2.4. Verification of RSM model

Setting K_{IC}^{S} as response, using Design-Expert software, BBD test data are used for quadratic regression according to **Tables 3** and **4**. Based on initial fitting equation, insignificant items are manually removed for optimization. Lack of fit of the model is ultimately determined as 0.84, the SNR value Adeq Precision is also high (142.350), showing that this model can be used to predict; PredR^2 (0.9983) and AdjR^2 value (0.9993) difference is very small, indicating a high degree of the response surface equation optimization, which fits well. The regression model is as shown in Eq. (10):

$$K_{IC}^{S} = 8.02 + 0.18A + 0.085B + 2.34C + 0.035AB \\ +0.082AC + 0.093BC + 0.067B^2 + 1.82C^2 \tag{10}$$

Variance analysis is done to the model and significance test is done to the regression coefficients, as shown in **Tables 5** and **6**.

	Quadratic sum	Freedom	Mean square	*F* value	*P* value
Model	58.24	8	7.28	3067.88	<0.0001
Residual error	0.019	8	2.373E–003		
Lack of fit	8.653E–003	4	2.163E–003	0.84	0.5669
Pure error	0.010	4	2.582E–003		
Sum	58.25	16			

Table 5. Variance analysis of the model.

	Regression coefficient	Standard deviation	Lower confidence limit of 95%	Upper confidence limit of 95%	*P* value
A	0.18	0.017	0.14	0.22	<0.0001
B	0.085	0.017	0.045	0.12	0.0011
C	2.34	0.017	2.30	2.38	<0.0001
AB	0.035	0.024	−0.021	0.092	0.1837
AC	0.082	0.024	0.026	0.14	0.0096
BC	0.093	0.024	0.037	0.15	0.0052
B^2	0.067	0.024	0.012	0.12	0.0223
C^2	1.82	0.024	1.76	1.87	<0.0001

Table 6. Significance test of the regression coefficients.

4. Influences of freeze-thaw on K_{IC}^{S} under different slag content

Influence of freeze-thaw on K_{IC}^{S} under different slag content is shown in **Figure 3**.

Various factors may result in the material deterioration and failure of concrete as described above, and the seriousness caused depends to a great extent on the porosity and permeability of internal texture of concrete itself [33, 34]. Generally, if the compactness of a concrete structure is poor or its internal porosity is considerable, more possibly various liquids and gases penetrate into its interior with more quantity and larger depth, than the carbonation layer, and chemical corrosion of concrete and the rust of reinforcement is accelerated, even the liquid can pass easily through the structure.

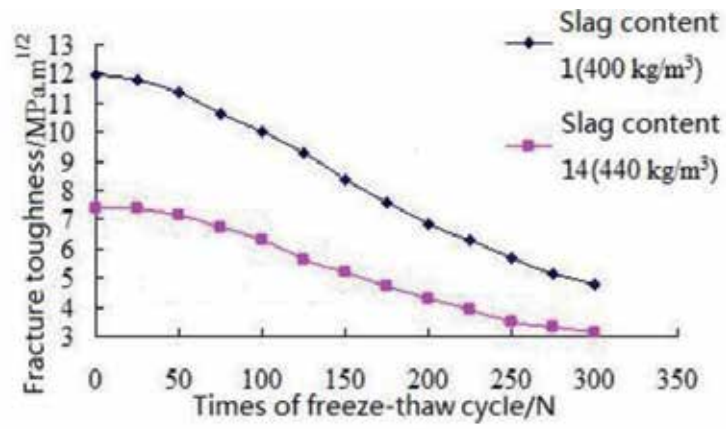

Figure 3. Influence of freeze-thaw on K_{IC}^{S} under different slag content.

http://dx.doi.org/10.5772/63810

The main factors having influence on texture and porosity of concrete are water-cement ratio (or water-binder ratio); kind and fineness of cement; kind of aggregate; producing quality and curing condition. Producing quality and curing condition can be paid attention during construction, but the first three factors are mainly influenced by material characteristic itself.

ASC has a compact structure, which is able to well resist penetration of water and air. Since the strength enhancement of ASC tends to grow at a relatively slow speed, when it is exposed to freeze-thaw cycles, ASC could continue to form hardened structure, which is beyond the destroying speed. Therefore, ASC could be a desirable material to resist carbonation as well as freeze-thaw attack in concrete structures.

5. Conclusions

1. The calculation procedure of ASC fracture parameters is studied. With the CMOD, other indexes including concrete effective fracture length; CTOD; and stress intensity factors K_{IC}^{C}, K_{IC}^{Q} and K_{IC}^{S} from closure stress $\sigma(w)$ can be calculated. And critical effective fracture length a_C, stress intensity factor K_{IC}^{C} caused by closure stress, initiation toughness K_{IC}^{Q} and unstable fracture toughness K_{IC}^{S} are analyzed specifically.

2. The RSM theory is systematically investigated. RSM principles and advantages, optimization content and procedure, data processing software Design-Expert and verification of RSM model are provided. Results show that RSM is suitable for ASC fracture property analysis.

3. Influences of freeze-thaw on K_{IC}^{S} under different slag content are put forward. The main reason for good freezingresistance is that ASC has a dense structure, which is beneficial for preventing water and air penetration. Such property indicates that ASC could have good performance in carbonation environment.

4. In this study, through calculation and analysis, the calculation approach of fracture parameters is researched; theoretical study of RSM is summarized; and the reason why ASC performs well under freeze-thaw cycles is studied. However, since ASC fracture properties are influenced by various factors, more research should be carried out. What is more, the RSM theory is seldom used in ASC analysis, it is worth more deeper and systematical investigation. The ASC performances also require more focus from the angle of cross-disciplinary methods including materials science, mechanics and structural analysis.

Acknowledgements

The author wishes to express his gratitude and sincere appreciation to the National Natural Science Fund [Grant Number: 51578540] for financing this research work and several ongoing research projects related to the properties of ASC.

Author details

Qixuan Li

Address all correspondence to: liqixuan19921210@163.com

Air Force Engineering University, Xi'an, China

References

[1] Sun W, Zhang YM, Yan HD, Mu R. Damage and damage resistance of high strength concrete under the action of load and freeze-thaw cycles. Cem Concr Res 1999; 29(9): 1519–1523. doi:10.1016/S0008-8846(99)00097-6.

[2] Shojaei M, Behfarnia K, Mohebi R. Application of alkali-activated slag concrete in railway sleepers. Mater Des 2015; 69: 89–95. doi:10.1016/j.matdes.2014.12.051.

[3] Ren WB, Xu JY, Bai EL. Strength and ultrasonic characteristics of alkali-activated fly ash-slag geopolymer concrete after exposure to elevated temperatures. J Mater Civ Eng 2016; 28(2). doi:10.1061/(ASCE)MT.1943-5533.0001406.

[4] Mithun BM, Narasimhan MC. Performance of alkali activated slag concrete mixes incorporating copper slag as fine aggregate. J Clean Prod 2016; 112: 837–844. doi: 10.1016/j.jclepro.2015.06.026.

[5] Gao Y, Xu JY, Bai EL, Luo X, Zhu JS, Nie LX. Static and dynamic mechanical properties of high early strength alkali activated slag concrete. Ceram Int 2015; 41(10): 12901–12909. doi:10.1016/j.ceramint.2015.06.131.

[6] Okoye FN, Durgaprasad J, Singh NB. Mechanical properties of alkali activated flyash/ Kaolin based geopolymer concrete. Constr Build Mater 2015; 98: 685–691. doi:10.1016/ j.conbuildmat.2015.08.009.

[7] Torres-Carrasco M, Tognonvi MT, Tagnit-Hamou A, Puertas F. Durability of alkali-activated slag concretes prepared using waste glass as alternative activator. ACI Mater J 2015; 112(6): 791–800.

[8] Kim SW, Jang SJ, Kang DH, Ahn KL, Yun HD. Mechanical properties and eco-efficiency of steel fiber reinforced alkali-activated slag concrete. Mater 2015; 8(11): 7309–7321. doi: 10.3390/ma8115383.

[9] Krivenko P, Kovalchuk G. Achieving a heat resistance of cellular concrete based on alkali activated fly ash cements. Mater Struct 2015; 48(3): 599–606. doi:10.1617/s11527-014-0479-0.

[10] Ravikumar D, Neithalath N. Electrically induced chloride ion transport in alkali activated slag concretes and the influence of microstructure. Cem Concr Res 2013; 47: 31–42. doi:10.1016/j.cemconres.2013.01.007.

[11] Ravikumar D, Neithalath N. An electrical impedance investigation into the chloride ion transport resistance of alkali silicate powder activated slag concretes. Cem Concr Compos 2013; 44: 58–68. doi:10.1016/j.cemconcomp.2013.06.002.

[12] Qixuan Li, LiangcaiCai, Yawei Fu, Haifu Wang, Yong Zou. Fracture properties and response surface methodology model of alkali-slag concrete under freeze-thaw cycles. Constr Build Mater 2015; 93: 620–626. doi:10.1016/j.conbuildmat.2015.06.037.

[13] Provis JL, Palomo A, Shi CJ. Advances in understanding alkali-activated materials. Cem Concr Res 2015; 78: 110–125. doi:10.1016/j.cemconres.2015.04.013.

[14] Kovtun M, Kearsley EP, Shekhovtsova J. Chemical acceleration of a neutral granulated blast-furnace slag activated by sodium carbonate. Cem Concr Res 2015; 72: 1–9. doi: 10.1016/j.cemconres.2015.02.014.

[15] Ma Y, Ye G. The shrinkage of alkali activated fly ash. Cem Concr Res 2015; 68: 75–82. doi:10.1016/j.cemconres.2014.10.024.

[16] Ke XY, Bernal SA, Provis JL. Controlling the reaction kinetics of sodium carbonate-activated slag cements using calcined layered double hydroxides. Cem Concr Res 2016; 81: 24–37. doi:10.1016/j.cemconres.2015.11.012.

[17] GB/T 18046-2000. Ground granulated blast furnace slag used for cement and concrete. Beijing: The state bureau of quality and technical; 2000.

[18] GB/T 18736-2002. Mineral admixtures for high strength and high performance concrete. Beijing: General Administration of Quality Supervision, Inspection and Quarantine of the People's Republic of China; 2002.

[19] GB/T 12957/2005. Test method for activity of industrial waste slag used as addition to cement. Beijing: General Administration of Quality Supervision, Inspection and Quarantine of the People's Republic of China; 2005.

[20] GB/T 50080-2002. Standard for test method of performance on ordinary fresh concrete. Beijing: Ministry of Construction of the People's Republic of China; 2003.

[21] GB/T 50081-2002. Standard for test method of mechanical properties on ordinary concrete. Beijing: Ministry of Construction of the People's Republic of China; 2003.

[22] Thomas RJ, Peethamparan S. Alkali-activated concrete: engineering properties and stress-strain behavior. Constr Build Mater 2015; 93: 49–56. doi:10.1016/j.conbuildmat.2015.04.039.

[23] DL/T 5332-2005. Norm for fracture test of hydraulic concrete. Beijing: National Development and Reform Commission; 2005.

[24] Tada H, Paris PC, Irwin GR. The stress analysis of cracks handbook. St. Louis: Parris Produetions Incorporated; 1985.

[25] Shilang X, Reinhardt HW. A simplified method for determining double-K fracture parameters for three-point tests. Int J Fract 2000; 10(4): 181–209. doi:10.1023/A:1007676716549.

[26] Swaddiwudhi Pong S, Lu HR, Wee TH. Direct tension test and tensile strain capacity of concrete at early age. Cem Concr Res 2003; 33: 2077–2084. doi:10.1016/S0008-8846(03)00231-X.

[27] Shilang X, Zhimin W, Ding S. A practical analytical approach to the determination of double-K fracture parameters of concrete. Eng Mech 2003; 20(3): 54–62. doi:10.3969/j.issn.1000-4750.2003.03.010.

[28] Reinhardt HW, Comelissen HAW, Hordijk DA. Tensile tests and failure analysis of concrete. J Struct Eng 1986; 112(11): 2462–2477.

[29] Zhang Q. Experimental research on high strength wear-resistant concrete cracking and fracture properties [thesis]. Hangzhou: Zhejiang University; 2008.

[30] Box GEP, Wilson KB. On the experimental attainment of optimum conditions. J R Stat Soc Ser B-Stat Methodol 1951; 13(1): 1–45.

[31] Ambati P, Ayyanna C. Optimizing medium constituents and fermentation conditions for citric acid production from palmyrajaggery using response surface method. World J Microbiol Biotechnol 2001; 17(4): 331–335. doi:10.1023/A:1016613322396.

[32] Ahuja SK, Ferreira GM, Moreira AR. Application of plackett-burman design and response surface methodology to achieve exponential growth for aggregated ship-worm bacterium. Biotechnol Bioeng 2004; 85(6): 666–675. doi:10.1002/bit.10880.

[33] Jo BW, Park SK, Park JB. Properties of concrete made with alkali-activated fly ash lightweight aggregate (AFLA). Cem Concr Compos 2007; 29(2): 128–135. doi:10.1016/j.cemconcomp.2006.09.004.

[34] Krivenko P, Drochytka R, Gelevera A, Kavalerova E. Mechanism of preventing the alkali-aggregate reaction in alkali activated cement concretes. Cem Concr Compos 2014; 45: 157–165. doi:10.1016/j.cemconcomp.2013.10.003.

Chapter 4

High-Performance Concrete and Fiber-Reinforced High-Performance Concrete under Fatigue Efforts

Miguel A. Vicente, Jesús Mínguez,
José A. Martínez and Dorys C. González

Additional information is available at the end of the chapter

http://dx.doi.org/10.5772/64387

Abstract

Fatigue is the process of mechanical degradation of a material, which leads to its collapse. Repeated load applications with a maximum value lower than the one that provokes the static failure of the material, causes internal damage in the material that, progressively, reduces its mechanical capacity until it finally collapses. The increasingly widespread use of high-strength concretes permits the construction of more lightweight structures. This implies that the variable loads (which are the causes of fatigue) represent an ever larger percentage of the total load. In consequence, fatigue is an increasingly important factor in concrete structures. In some cases, it even begins to be the dimensioning load of the structure. In addition, the presence of fibers within the concrete modifies the fatigue response of the concrete. In this chapter, the classic theory of fatigue is presented in detail and the most recent developments in the study of concrete fatigue are discussed.

Keywords: fatigue, high-performance concrete, fiber-reinforced high-performance concrete, degenerative process, modulus of elasticity, S-N curves

1. Introduction

1.1. Definition of fatigue. Interest in fatigue

Fatigue is a process of mechanical deterioration of a material leading to its collapse, caused by the repeated action of cyclic loading, in such a way that its maximum applied load is always below the maximum loading that a "healthy" specimen of the material could resist under static loading until failure.

The first research works on material fatigue were completed in the mid-nineteenth century during the industrial revolution. Wöhler was the first to conduct systematic fatigue studies. The first works on concrete date back to the end of the nineteenth century [1, 2].

It was at the beginning of the twentieth century when real concerns over structural fatigue began to appear in civil engineering, applied above all to metallic structures. This concern was prompted by the appearance of catastrophic failure in some structures, the explanations for which could not be solved with classic mechanics.

Fatigue is of growing interest in civil engineering, especially in concrete structures. The development of concretes with stronger mechanical properties (better resistance) means that structures may be built with less specific weight. This aspect means that variable loads of a cyclical nature (live loads, wind, etc.) are of increasing relevance (**Table 1**) [3].

Low-cycle fatigue			**High-cycle fatigue**				**Super-high-cycle fatigue**		
1	**10^1**	**10^2**	**10^3**	**10^4**	**10^5**	**10^6**	**10^7**	**10^8**	**10^9**
Structures subjected to earthquakes			Airport pavements and bridges		Highway and railway bridges, and highway pavements		Mass rapid transit structures		Sea structures

Table 1. Classes of fatigue loads [3].

There has been a surge in the construction of new transport infrastructure in recent years, for the main part involving new high-speed railway lines. These new railways imply a very competitive alternative for intercity transport over medium distances.

These significant engineering works means that one of the most important structural aspects specifically associated with the design of railway bridges and structures is a topical question: the effects of fatigue due to the live loads of trains.

Standards establish a fatigue limit state, because of failure of a structural element when a crack or fissure opens as a consequence of repeated and variable stress loads, produced by the action of traffic, which is expected to continue throughout the useful life of the structure (100 years).

1.2. The fatigue process in concrete

Concrete fatigue is a progressive process of birth and growth of microcracks, which provokes a change in the mechanical properties of the matrix, a reduction in stiffness, and an increase in total deformation. And it leads to the failure of the concrete.

Unlike steel, concrete is a heterogeneous material in which nonlinear fatigue can occur which depend on its stress levels. Concrete fatigue fundamentally depends on the stress level (σ_{max}/f_c) and not only on the stress range ($\Delta\sigma$) as happens with metals.

Research on cumulative damage due to microcracking in concrete began in 1929, when Richardet al. [4] observed that the apparent volume of concrete started to increase under compressive axial loading when it reached a value of 75–85% of the ultimate failure load. This

http://dx.doi.org/10.5772/64387

level of loading is referred to as critical load. The increase of the apparent volume of concrete is due to the internal microcracking.

Many authors have also analyzed fatigue behavior, observing important changes within the concrete as from 75% of the failure load. These changes are due to microcracking in the concrete, which increase its volume and its Poisson's ratio [3].

The later use of ultrasonic techniques has allowed to determine the initial moment when microcracking starts [5]. These microcracks were first recorded at values of around 25–30% of the ultimate failure load and the ultrasonic signal rapidly increased from 75%.

The failure of concrete may be defined at three levels:

(1) At a microscopic level, the bonds between the crystals of calcium silicate hydrate are taken into account. This level is less interesting from the point of view of fracture mechanics. Its behavior is regulated by physical and chemical processes that are activated under certain circumstances.

(2) At an intermediate level, the cement paste, the aggregate, and their interrelations are taken into account. The standard failure process, regardless of the type of load applied, occurs when one or more of the following are surpassed: the friction strength of the aggregate, the shear strength of the aggregate, the friction and the tangential strength of the cementitious matrix, and the friction strength of the aggregate.

Figure 1 describes the stress conditions within the aggregate:

(3) From the macroscopic point of view, concrete can be modeled as a homogenous isotropic material that contains defects in its interior. The properties that are analyzed at this level are the stress levels and the average deformation that is generated, and also the nonlinearity of the mechanical properties.

The macroscopic response (stress-strain diagram) of a concrete specimen subjected to increasing monotonous shortening is a consequence of the evolution of the material at a microscopic level. Microcracks occur because of friction stress due to the specific heterogeneity of the material. The appearance of microcracks in an orthogonal direction to the principal compressive stress direction can be due to:

(1) Existence of pores or microcracks prior to loading.

(2) Difference in stiffness between the aggregate particles and the cement paste.

(3) Loss of adhesion in the aggregate-paste interface.

(4) Sliding zones in the cement paste.

There are mainly two hypotheses that seek to clarify the onset of cracks in concrete under cyclic loads:

The first hypothesis assumes that the cyclic loading provokes cracks that subsequently progresses up until the collapse of the element.

The second hypothesis considers that microcracks has already occurred in the concrete setting and hardening process. Cyclic loads simply propagate these fissures.

In any case, microcracks have macroscopic consequences: the growth of irreversible deformation and a reduction in stiffness take place [7].

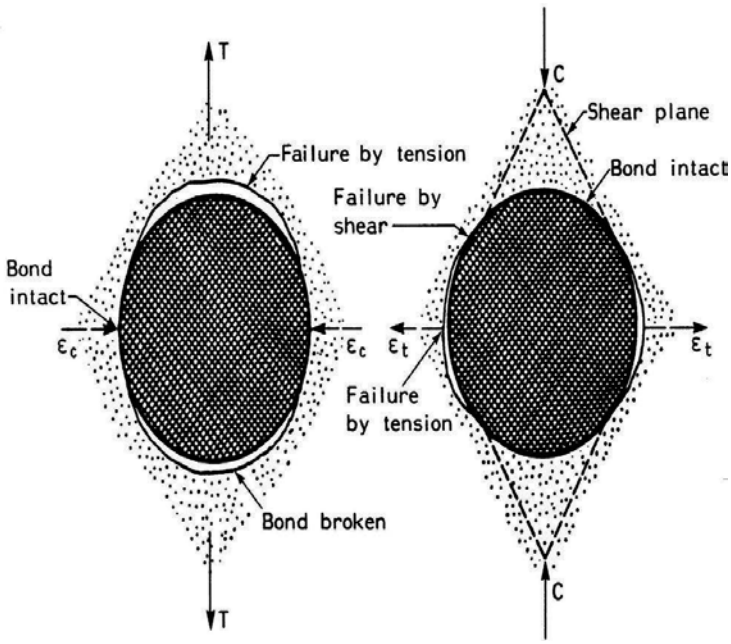

Figure 1. Local stress within the aggregate under compressive and friction stress [6].

Irreversible deformations are the sum of two effects:

1. On the one hand, part of the deformation as viscoelastic properties. Short-term viscoelastic deformation may be because of capillary flows due to thermodynamic imbalance. Long-term viscoelastic deformations are associated with the repositioning of calcium silicate hydrate within the nanopores. If these viscoelastic deformations are locally larger than the deformation capacity of the concrete, fissuring of the concrete will occur.

2. Moreover, cyclic loads cause some of the aggregates or parts of the cement paste to harden when the fissure has opened, producing localized frictional forces.

The fracture mechanics of concrete, like all petrous materials, differ from those of metals. The fracture mechanics of both concrete and steel structures is considered nonlinear due to the development of an area of significant size in which the fracture lines appear. While in metals with a fragile or ductile behavior, the hardening process in most of that area is nonlinear and presents a small fracture generation zone. In contrast, concrete presents a large fracture generation zone that is surrounded by a small nonlinear hardened zone. The concrete may therefore be considered a quasi-fragile material [8].

http://dx.doi.org/10.5772/64387

The cyclic loads and, therefore, the fatigue behavior of concrete may be established for compression, tension, and bending efforts. In case of plain concrete, only fatigue under compression efforts is of interest. In case of fiber-reinforced concrete elements, fatigue under tension and/or bending is of interest too.

1.2.1. Fatigue of high-strength concrete

The fatigue behavior of high-strength concrete differs from that of ordinary concrete due to the differences in its internal structure. The cracks in ordinary concrete are propagated in the cement paste through the aggregate-paste interface. However, cracks in high-strength concrete are propagated in the cement paste and in addition through the aggregates, due to the relatively higher strength of the cementitious matrix. The fatigue life of the aggregates in high-strength concrete should therefore be taken into account where its strength is important [8]. However, the tests undertaken show that the fatigue life is relatively similar for various types of concrete. The studies on fatigue show that higher concrete strength leads to greater fragility, as also happens in the behavior of concrete under monotonous loading.

2. Concept of fatigue life "N" and fatigue strength "S." S-N curves

The conventional approach to the problem of concrete fatigue consists in determining the number of cycles N that a concrete specimen can withstand when subjected to a cyclic load, in such a way that the maximum stress that is applied is lower than the compressive strength of the material.

Concrete strength is empirically assessed through a series of tests. The basic premise, observed in all the materials, is that the lower the maximum tensile stress that is applied, the higher the number of cycles N that the material can withstand.

The value of N depends on the maximum and the minimum stress levels that are applied. The standard way of representing these extremes is relative maximum stress ($S_{c,max} = \sigma_{c,max}/f_c$) in relation to the number of cycles (N), drawing different graphs for different values of minimum relative stress ($S_{c,min} = \sigma_{c,min}/f_c$). These are referred to as the S-N curves (**Figure 2**).

Fatigue strength S is defined as the fraction of static strength that can be withstood in a repeated manner over a certain number of cycles.

The definition of an S-N curve requires many tests. A set of specimens is used to characterize a material and they are subjected to variable forces at different stress levels, measuring the number of cycles that it withstands until failure. In general, there is enormous dispersion in the results of apparently similar specimens. These differences are due to the dispersion of concrete strength [10]. In general, it is necessary to test a large number of specimens for each stress level, before reliable results may be obtained [11].

Many of the S-N fatigue curves shown in the literature were obtained by using different test setups, specimen types and shapes, etc. At present, there is no standard procedure to conduct concrete fatigue tests. Data on fatigue from two different test setups cannot be directly

compared. The use of normalized fatigue strength with static strength partially eliminates the influence of geometric variables, such as the geometry of the specimen, the composition of the material, curing conditions, and age of test specimen.

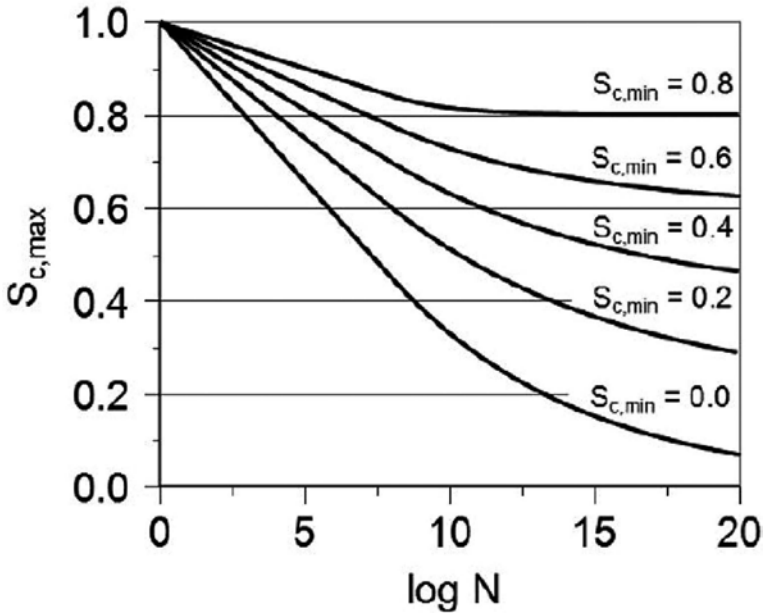

Figure 2. S-N for concrete [9].

3. Variable load cycles. Concept of damage

Structural concrete components are usually subjected to variable loads of random nature. To date, very few works have conducted in-depth examinations of the effect of random loading on the fatigue behavior of concrete. Most of the tests have been performed under low cyclic loads with average stress values and amplitude that are constant.

Traditionally, the Palgrem-Miner rule or hypothesis of the accumulation of linear damage is applied, in order to estimate the number of cycles that provokes the failure of the concrete specimen subjected to different series of cyclic loads, each one of them with different maximum and minimum stress levels.

This rule defines the damage provoked by cyclic loads, with constant values of both average stress and amplitude, as the quotient between the number of cycles that are applied and the number of cycles that it withstands. In addition, the principle of superimposition of damage is assumed, which implies that the damage provoked by one cyclic load is unrelated to the damage provoked by another. Therefore, the global damage applied to an element subjected to cyclic loading may be obtained from the following expression (1):

http://dx.doi.org/10.5772/64387

$$D = \sum_{i=1}^{n} D_i \sum_{i=1}^{n} \frac{n_i}{N_i} \quad (1)$$

where "*D*" is the global damage or accumulated damage. *A* value of 1 is taken as the design value, to determine a situation of maximum damage; n_i is the number of cycles at a certain level of loading; and N_i is the fatigue strength for a certain level of loading.

The theory of linear damage proposed by Miner is not directly applicable to concrete specimens subjected to variable loads of random nature. Numerous investigations call this assumption into question [12–18].

The effects of alternating periods of rest and loading on fatigue behavior are not sufficiently well studied. Laboratory tests have shown that rest periods and/or maintained loads between two periods of cyclic loading tend to increase the fatigue strength of the concrete [19]. However, if the maintained loads are over 75% of static compressive strength, they can provoke negative effects on fatigue life [20]. This contradictory effect of creep stress may be explained if we consider that low levels of continuous loading improve the compressive strength of the concrete, while high values of continuous loading provoke an increase in internal microcracking and can facilitate collapse.

4. Main parameters affecting fatigue strength

Fatigue life and its variation during the fatigue process are conditioned by various factors. The most important ones are shown below.

4.1. Type of load and its variation

The way in which the load is progressively applied to the structural element influences concrete fatigue. It means that the stress range, the eccentricity of the load, and its frequency influences concrete fatigue.

Each one of these variables is analyzed as follows.

4.1.1. Stress range

As explained before, fatigue life depends on maximum stress and minimum stress levels, as can be seen in **Figure 2**.

Maximum stress values imply a shorter fatigue life of the material.

In addition, an increase in the stress range *R*, defined as $\sigma_{min}/\sigma_{max}$, leads to a reduction in fatigue life.

4.1.2. Load eccentricity

Load eccentricity is a very important factor, because when a stress gradient is applied, collapse occurs when the most solicited fiber reaches, approximately, its fatigue life without a significant stress redistribution. There are only very few works in this field. The load is usually applied centered, without any eccentricity, during the fatigue tests under compression. The study carried out by Ople and Hulsbos [21] is worth mentioning.

4.1.3. Load frequency

The frequency of the load has an influence on fatigue life. At present, it is accepted that frequency values between 1 and 15 Hz hardly have any influence on fatigue life, provided that the maximum stress level is not over 75% of the compressive strength [22–26]. Noteworthy is the research developed by Zhang and Wu [27], which proposed, for the first time, an S-N curve as a function of the frequency of the cyclic load.

It is worth highlighting the studies conducted over recent years by Saucedo et al. [28] and Medeiros et al. [29]. Their works offer an in-depth analysis of the response of the concrete to low-frequency cyclic loads. Their results show that the fatigue life N in very low test frequencies (1/16 Hz) is, at least, of a lower order of magnitude than the fatigue life obtained under higher test frequencies (4 Hz).

4.2. Moisture content

It is well known that concrete is a hygroscopic material and its mechanical parameters are conditioned by the moisture content. The fatigue response is also influenced by the concrete moisture content.

The works developed by Waagaard and others [30] are worth mentioning. These researchers investigated the effect of dry and humid mixtures on the fatigue behavior of high-performance concretes with normal and lightweight aggregates. Some of the specimens were tested dry and others saturated moisture. Their principal result was that the fatigue life of the dry specimens was longer than the humid specimens under the same stress levels. This effect was more evident in concretes of normal density.

It is a very interesting conclusion, especially in case of fatigue characterization tests, given that, on some occasions, the differences in behavior between the different specimens may be due to differences in their humidity content.

4.3. Effect of fibers on the fatigue behavior of concrete

Fibers improve the fatigue life of the concrete, especially under tension and bending efforts, and, to a lesser extent, under compression efforts. Their use is very common in concrete pavements. Their use in structural concrete elements (beams and slabs among others) is still very limited.

The most commonly used are metallic and polypropylene fibers. They show good behavior under static loads and they are inexpensive. There are other types of fibers, although they are

http://dx.doi.org/10.5772/64387

far less widely used. Among these, carbon and glass fibers may be mentioned. Both fiber types show a good structural behavior, but their price is still very high. They are more commonly used as external reinforcements, within a polymeric matrix, instead of as an additive placed inside the concrete mix.

The following sections present an analysis of the effect of different fiber types on the fatigue response of the concrete.

4.3.1. Steel fibers

Steel fibers are the most widely used in concrete. They are usually used in reinforced and/or prestressed concrete elements, together with passive and/or active reinforcements, with the purpose of improving their behavior under certain conditions. Over recent years, a significant advance on the use of fibers as a substitute for passive reinforcement is occurring.

In the case of steel fibers, experimental studies [31, 32] show that the metallic fibers improve fatigue bending strength. Depending on the type of fiber employed and its percentage addition, a concrete with steel fibers with an acceptable design can maintain a residual fatigue strength of between 65% and 90% of its static strength after 2,000,000 cycles. The addition of fibers in appropriately reinforced concrete beams increases their fatigue life, and a reduction in fatigue-related cracks. In addition, fiber additions also reduce deformation in beams during the fatigue process.

Benefits of fibers in case of specimens subjected to compression efforts are less significant. As Lee and Barr [33] indicated, it cannot be said, in general terms, that the presence of fibers improves the fatigue life of the concretes. This seems to be due the effect of two opposite phenomena. On the one hand, fibers bind the microcracks that appear within the material due to fatigue loads. On the other hand, fibers produce an increase in the density of the initial microcracking, causing a decrease in the initial strength. The combination of these opposing factors may be the cause of the increased or the decreased fatigue life of the concrete.

As mentioned in this document, there are many variables that influence the fatigue life of a concrete and the presence of fibers will not always improve their behavior.

It is worth highlighting the works of Saucedo et al. [28], which demonstrate that, under low frequencies (of around 0.1 Hz), the fatigue life of fiber-reinforced concrete is as much as 10 times greater than then fatigue life of concrete that contains no fibers.

It is worth noting that fatigue-related deformation is greater in fiber-reinforced concrete. This is because fibers provide ductility to concrete specimen.

4.3.2. Polypropylene fibers

Polypropylene fibers are also widely employed in concrete, because they present good mechanical behavior and they are inexpensive. They moreover manage to improve the fire-resistant behavior of structural concrete components.

The influence of the content of polypropylene fibers on the fatigue life of concrete specimens under bending efforts has been studied [32]. Almost all the research conducted on fiber-reinforced concrete have studied fatigue under bending efforts.

It is worth mentioning the studies carried out by Ramakrishna and Lokvik [34]. They show how the incorporation of polypropylene fibers, even in small quantities, increase fatigue-related bending strength. Fatigue strength increased between 15% and 38% at 2,000,000 cycles at different percentage additions of fibers (between 0.1% and 1% by volume).

In the same way as steel fiber-reinforced concrete, polypropylene-reinforced concrete showed an increase in residual static bending strength, after having been subjected to fatigue loads. It may therefore be said that an increase in bending strength exists in polypropylene fiber-reinforced concrete, when subjected to fatigue cycles below the stress limit for fatigue-related failure.

There is a very limited amount of research focused on the influence of polypropylene fiber on the fatigue response of concrete specimens under compression efforts. The works carried out by Minguez [35] may be highlighted, among others.

4.3.3. Fiber quantity and orientation

According to fluid dynamics, the fibers are oriented along the concrete flow during concreting. In addition, fiber orientation is conditioned by the shape and the effect of the concrete formwork as well as the presence of internal obstacles such as passive and/or active reinforcements. These fibers tend to assume positions in parallel to the walls of the formwork when in their proximity. Moreover, the vibrating process also modifies the fiber orientation.

Fiber orientation influences fatigue insofar as the energy-related processes of damage are delayed or reduced by a binding effect of the fibers in the internal matrix of the concrete mix. It may therefore be expected that orientations in the direction parallel to the direction of cracking will generate disadvantageous effects on fatigue life as opposed to those orientations that bind the cracks provoked during the deterioration process of the material.

There are different methods to measure fiber orientation within the concrete matrix. In the case of metallic fibers, indirect methods permit the determination of fiber orientation by means of electromagnetic capabilities that detect the presence of metallic fibers through the use of magnetic fields or by using impedance-based techniques.

Direct methods permit the definition of fiber position, density, and orientation with greater precision. These methods include the use of computerized tomography technology that provides information on the fibers taken from scanned images [36].

5. Fatigue as a degenerative process

One of the differentiating characteristics of fatigue in concrete as opposed to fatigue in other (especially metallic) materials is that the energy transmitted by the cyclic load to the concrete

http://dx.doi.org/10.5772/64387

elements provokes internal structural damage that manifests itself in the birth and growth of internal microcracks, causing "diffuse damage" (**Figure 3**).

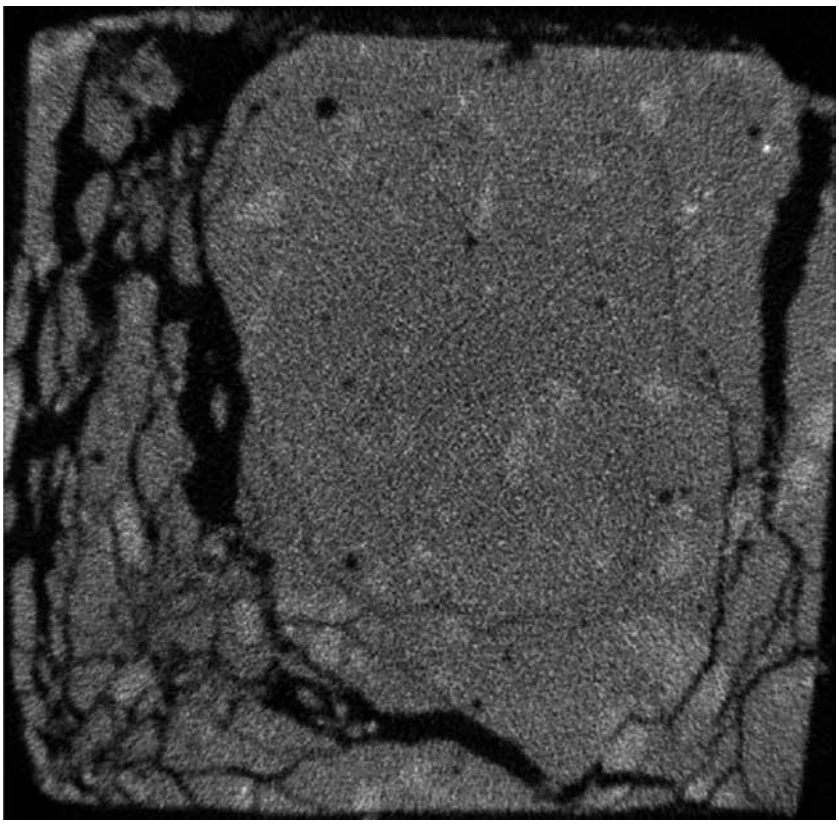

Figure 3. CT scan image of a concrete specimen with internal cracking. Courtesy of Research Group AUSINCO—University of Burgos (Spain).

The macroscopic result is a progressive variation of the mechanical parameters of the concrete, compression strength and Young's modulus, as well as an appearance of residual strain of increasing value.

It is worth noting that the energy transmitted by cyclic loads, in metallic materials, is concentrated at the edge of the crack, causing it to expand. The material that is not close to the crack undergoes no modification whatsoever in its mechanical parameters.

5.1. Variation of deformation with the number of cycles

Concrete specimens subjected to fatigue testing show a progressive modification in the stress-strain diagram with the number of cycles, characterized by the birth and growth of residual deformation, and by a progressive reduction in the modulus of elasticity of the material (**Figure 4**).

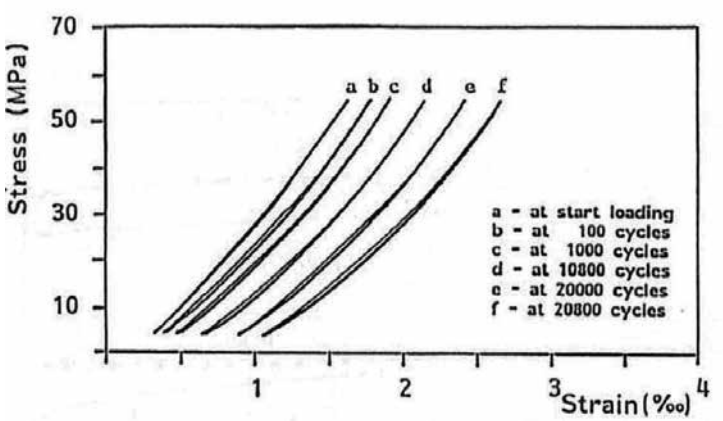

Figure 4. Variation of the stress-strain diagram with the number of cycles [6].

In a continuous fatigue-related degradation process, three phases of increasing damage were noted:

(1) A first phase with an increasing speed of damage. This phase corresponded to the formation of microcracks along the aggregate-paste interface and was characterized by a significant deterioration in the properties of the concrete. It lasts for approximately 10–15% of the fatigue life.

(2) A second phase with a speed of damage that was basically constant. This phase describes the stable propagation of the microcracks and was characterized by a constant speed of deformation and also a constant reduction of the modulus of elasticity. The second phase lasted for 80–90% of the fatigue life.

(3) A third phase with an increased speed of damage. The interconnections between the microcracks take place and finally the specimen collapse. In the third phase, the deterioration of the material is also very important.

This behavior is shown in the deformation-load cycle curves shown below (**Figure 5**).

These three phases were noted in all of the concrete specimens that were tested. However, the second phase is longer for higher strength concretes. The greater the strength of a concrete, the lower the ultimate fatigue-related deformation up until failure, for the same range of stress levels. This indicates that the internal damage is much greater for a high-strength concrete when fatigue-related failure occurs.

The slope of the straight line in the second phase is known as the secondary creep rate. This is a very interesting parameter that may be used as an estimator of fatigue life without any need to conduct failure tests. Numerous investigative works have demonstrated that there is a direct relation between the secondary creep rate and the fatigue life. The secondary creep rate depends on the loading frequency and the maximum strain level [23, 28, 29, 37].

http://dx.doi.org/10.5772/64387

It is worth highlighting the works of Zanuy et al. [38], which propose a theoretical model for the evolution of maximum deformation as a function of damage.

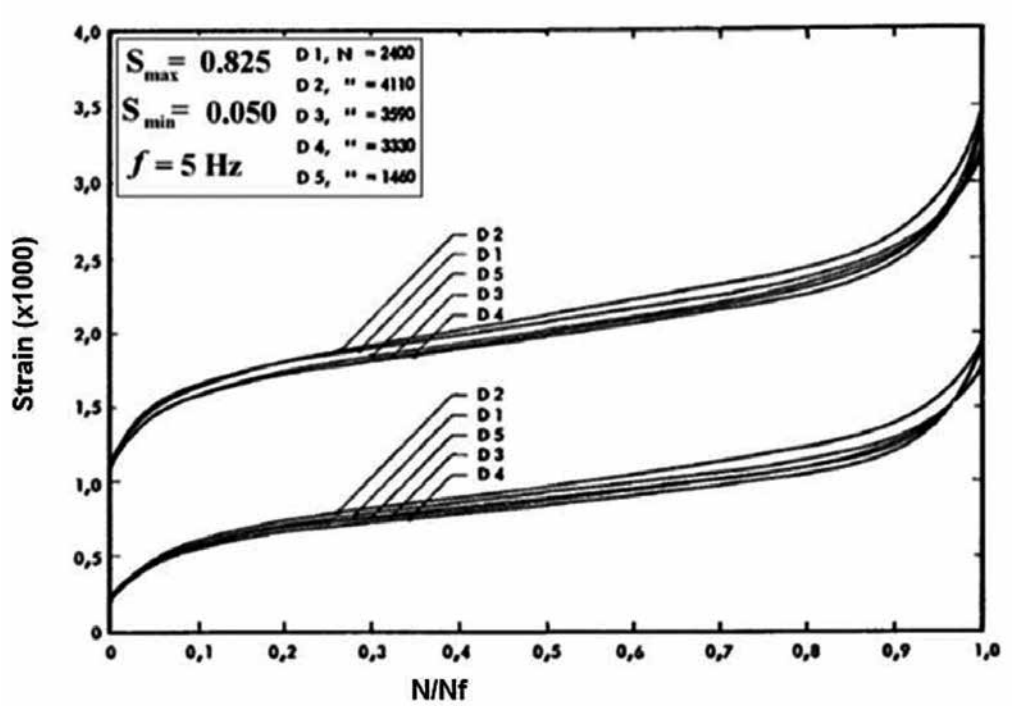

Figure 5. Variation of the maximum and minimum strains with the number of cycles [15].

5.2. Variation of the modulus of elasticity with the number of cycles

As has been described in earlier sections, fatigue provokes changes in the internal structure of the concrete that modifies its mechanical properties. The modulus of elasticity is among the affected properties.

The work developed by Holmer [15] is the most exhaustive for the analysis of the behavior of the modulus of elasticity and deformation with regard to its experimental results. Some of the results are shown in the following figure.

The shape of the curve resembled the shape of the deformation curve observing three different phases. As in the case of deformation, this curve presents three phases. In the first phase, a significant decrease occurs in stiffness, provoked by the birth of cracks. In the second phase, a linear reduction in the modulus of elasticity occurs, corresponding to a stage of progressive increase in cracks. In the third phase, an accelerated decrease in the modulus of elasticity takes place, corresponding to the phase in which the microcracks reach the critical lengths and the concrete specimen become unstable (**Figure 6**).

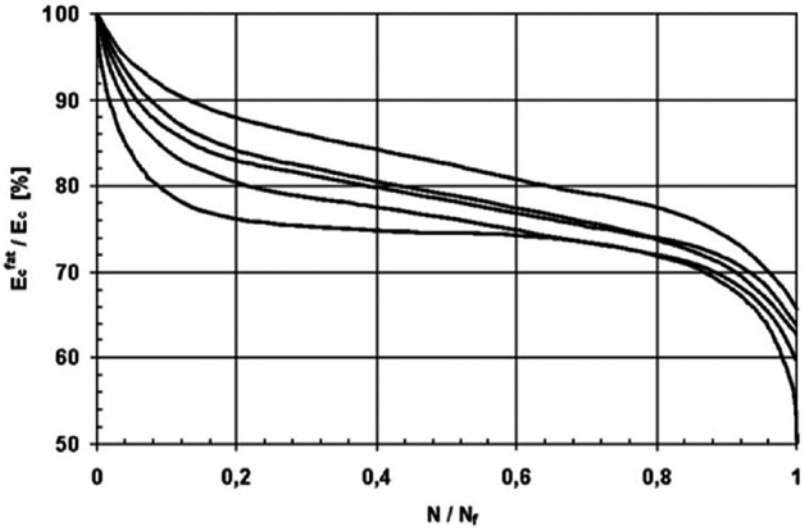

Figure 6. Variation of the modulus of elasticity with the number of cycles [15].

The following conclusions may be drawn from the above figure:

1. During the first phase, the reduction in the modulus of elasticity is greater at lower stress levels.

2. In contrast, in the second phase the contrary occurs, producing a curve close to the horizontal at low-stress levels.

In the same way as for the variation of fatigue-related deformation, Zanuy [38, 39] proposed some adjustment equations that attempted to model the behavior of the variation in the modulus of elasticity with fatigue damage.

It was observed that under the circumstance of stress ranges below 0.40, the maximum stress value had no influence on the model proposed by Zanuy [38, 39]. In contrast, for values over the stress range, the different maximum and minimum stress ranges yielded differentiated curves.

A reduction in the Young's modulus with cyclic loading is of great importance, given its implications for structural elements under cyclic loading, which produces a progressive loss of stiffness, bringing with it many structural consequences [38–41]:

(1) Progressive increase in vertical deflection in bridges and viaducts. Not only under live loads, but also under dead loads.

(2) Progressive reduction in the natural frequency.

(3) Increased losses of prestressing/posttensioning.

(4) Increased anchorage length in reinforcement bars.

(5) Increased transference length in prestressed wires.

http://dx.doi.org/10.5772/64387

It is important to point out that the modulus of elasticity that is obtained corresponds to the dynamic modulus of elasticity measured during the cyclic loading of the specimen (usually named as dynamic modulus of elasticity). This information is slightly different from the static modulus of elasticity, given by the specific test in ASTM C469. Some interesting research has been conducted on the measurement of the variation in the static modulus of elasticity with the number of cycles [42].

5.3. Variation of the compression strength with the number of cycles

Residual fatigue strength may be defined as the static strength, after having subjected the specimen to different fatigue cycles. It is a very important parameter for the analysis of damage that existing structures may present, in order to plan maintenance and repair works.

There are very few works in relation to how compression strength varies with the number of cycles [35, 42]. It is a parameter that cannot be measured during cyclic loading (unlike the deformation and the modulus of elasticity). However, it appears logical to think that residual compressive strength might be reduced with the birth and growth of microcracks under cyclic loading.

Minguez [35] conducted studies to verify postfatigue parameters at low-stress ranges in concretes without fibers and in concretes reinforced with polypropylene fibers. The results of their works showed an increase of the residual compressive strength at the first levels of fatigue. They proposed that, during this early damage stage, a recompacting process of concrete occurs. On the other hand, microcracking leads to a progressive reduction of the compressive strength, but this effect has structural consequences later than the recompacting process. The structural consequence of both phenomena is an initial maturation of concrete, with a progressive increase of the residual compressive strength, and later a progressive reduction of it.

The process of concrete maturing due to fatigue has the following effects in the concrete microstructure:

(1) Consolidation of the concrete at a microscopic level.

(2) Greater stability due to reorientation of the atomic structure.

(3) Reduction of localized stress in the paste-aggregate interface.

(4) Uniform redistribution of localized shrinkage stresses in the concrete.

6. Bi- and tridirectional fatigues

The presence of cyclic stress in two and/or three directions substantially modifies the fatigue response. However, there is, in general, a scarcity of works that have been developed to date.

Relevant works on biaxial compression are scarce [43–48]. The study conducted by Nelson et al. [46] is noteworthy. It describes tests performed on cubic specimens under biaxial compres-

sion, with two different transverse compression values: 10 and 25% of the vertical compression. The levels of maximum load fluctuated between 0.50 and 0.90, and the minimum load level was, in all cases, 10% of the maximum load.

It was observed that, in all cases, the number of cycles that provoked collapse was greater in the case of greater transversal confinement. As a result of their work, they presented a diagram that correlated the number of cycles that provoked failure with the maximum stress in both directions (**Figure 7**):

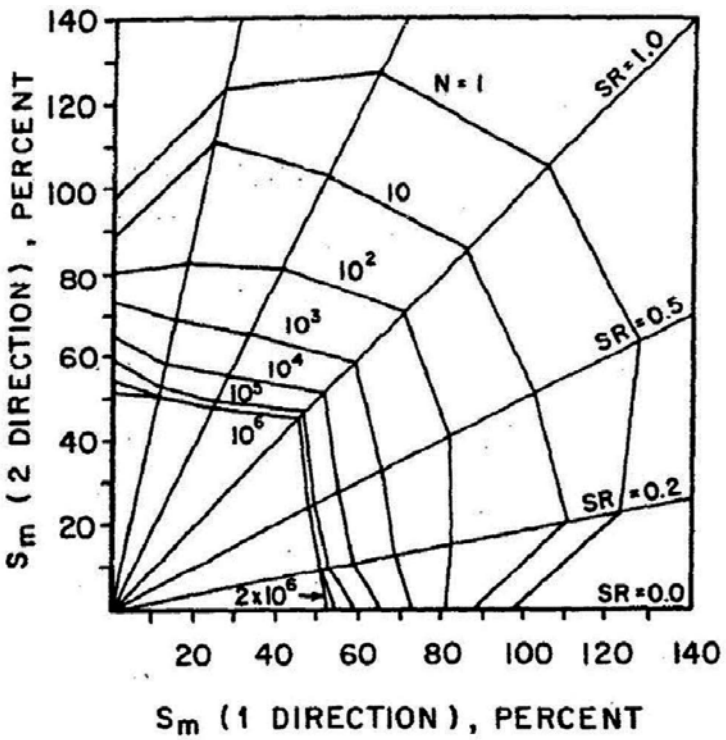

Figure 7. Fatigue envelope diagram [46].

In all cases, the results were not completely conclusive, because they were limited by their test campaign. It was also observed that the confinement improved material ductility that favors the reduction of the modulus of elasticity and the stress redistribution of forces, among other phenomena.

The work conducted by Su and Hsu [47] was also of great interest. In this case, stress with number of cycles of up to 10^7 cycles are performed for different biaxial ratios (**Figure 8**).

Finally, there are very few works related to biaxial friction fatigue [49–52]. It is a topic of much less interest in the case of concrete mixtures, holding greater interest in the case of fiber-reinforced concretes. Moreover, no conclusive results have been obtained to date.

http://dx.doi.org/10.5772/64387

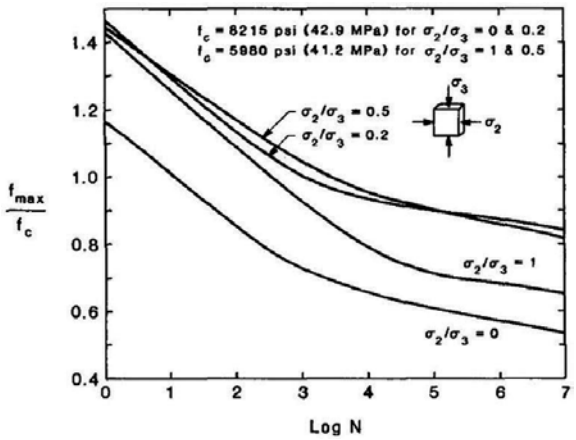

Figure 8. S-N curves for different biaxial compression ratios [47].

7. Deterministic and probabilistic models for the determination of fatigue-related failure

One of the characteristics of concrete, in relation to the number of cycles that it can withstand up until fatigue-related collapse, is its high variability.

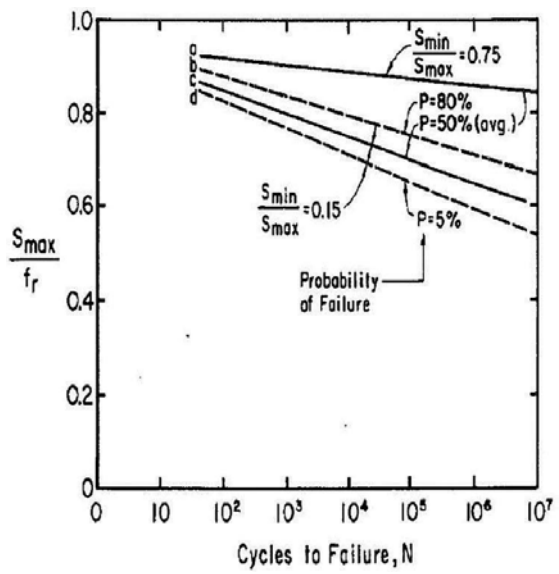

Figure 9. S-N-P curves [53].

Many research works have been developed in this field and they all conclude that the difference in the number of cycles that two "identical" specimens can withstand can be of two orders of magnitude. This observation greatly complicates the analysis of the results.

The analysis of the results in terms of probability is essential. So, it makes greater sense to develop S-N-P curves; it means, to develop S-N curves for different failure probabilities (P) (**Figure 9**).

On this point, two approaches may be found to present S-N curves: through the development of deterministic models and through the development of probabilistic models. The following describes each of the approach.

7.1. Deterministic models

Deterministic models, in essence, consist of showing explicit S-N curves for different failure probability values. In all cases, concrete compression strength is a deterministic value, characterized either by the average strength or by the characteristic strength of the concrete sample.

It is the traditional form of showing S-N curves and many researchers have developed expressions in this way [3, 6, 12, 15, 22, 25, 31, 33, 54–58].

The expressions specified in international standards fit this approach [9, 59].

7.2. Probabilistic models

The main problem of the deterministic models is that they consider the compression strength of concrete as a deterministic value, without taking into account the specific scatter of the concrete compression strength.

Over recent years, probabilistic failure models have been developed that take into account the statistical scatter of concrete strength in the estimation of the number of fatigue cycles [28, 60–63].

8. Conclusions

Fatigue is a degenerative process of concrete leading to collapse. The presence of cyclic loads provokes a progressive degradation that conducts the collapse of the structure. Cyclic loads provoke the birth and growth of microcracks inside the concrete and, finally, the structure fails.

The classic way of approaching fatigue in concrete corresponds, in essence, to an adaptation of metal fatigue. The basic parameter is the fatigue life "N", defined as the number of cycles that provokes the collapse of the element. Unlike metals, the fatigue life of concrete elements depends on its maximum and the minimum stress levels. Alternatively, fatigue strength is defined as the maximum tensile stress that has to be applied to cause the failure of the material, following a certain number of cycles.

http://dx.doi.org/10.5772/64387

Many parameters have relevant influence on the response of concrete under cyclic loads. The most important are: stress range, load eccentricity, load frequency, moisture content, etc. Also the presence of fibers within the concrete improves its behavior under cyclic loads. Related to fibers, the most important parameters are quantity and orientation.

Unlike with metals, the energy of the cyclic loads applied to the material is converted into "diffuse damage." This type of damage has macroscopic consequences, among which a progressive variation of the basic mechanical parameters of the material may be highlighted (compressive strength and elasticity modulus, among others). Its consequences are important and to date are not well studied.

Author details

Miguel A. Vicente*, Jesús Mínguez, José A. Martínez and Dorys C. González

*Address all correspondence to: mvicente@ubu.es

Department of Civil Engineering, University of Burgos, Burgos, Spain

References

[1] De Joly. Strength and elasticity of Portland Cement (La resístanse et l'étasticité des ciments Portland) (in French). Annales dês Ponts et Chaussee, Memoires. 1898;16(7): 216–226.

[2] Considere, M. Influence of rebar on the properties of mortars and concretes (Influence dês armatures métalliques sur lés propriétés dês mortiers et bétons) (in French). Compte Redu de L'Academic des Sciences. 1899;127:992–995.

[3] Hsu, T.C.C. Fatigue of plain concrete. ACI Journal. 1981;78:292–305.

[4] Richard, F.E., Brandzaeg, A., Brown, R.L. The failure of plain and spirally reinforced concrete in compression. Bulletin No 190. University of Illinois. Engineering Experimental Station. Urbana. III. 1929.

[5] Jones, R. A method of studying the formation of cracks in material subjected to stress. British Journal of Applied Physics. 1952;3(7):229–232.

[6] Petkovic, G., Lenschow, R., Stemland, H., Rosseland, S. Fatigue of high-strength concrete. ACI Special Publication. 1990;121:505–526.

[7] Zanuy, C., Albajar, L., De la Fuente, P. Concrete fatigue process and its structural influence (El proceso de fatiga del hormigón y su influencia estructural) (in Spanish). Materiales de Construcción. 2011;61(303):385–399.

[8] Bazant, Z.P. Concrete fracture models: testing and practice. Engineering Fracture Mechanics. 2002;69:165–205.

[9] International Federación for Structural Concrete. FIB Bulletin, 65, editors. MODEL CODE 2010. Lausanne, Switzerland: Ernst & Sohn; 2010.

[10] Cornelissen, H.A.W. Fatigue failure of concrete in tension. HERON. 1984;29(4):68.

[11] Paskova, T., Meyer, C. Optimum number of specimens for low-cycle fatigue test of concrete. Journal of Structural Engineering. 1994;120:2242–2247.

[12] Oh, B.H. Fatigue-life distributions of concrete for various stress levels. ACI Materials Journal. 1991;88(2):122–128.

[13] Cornelissen, H.A.W., Reinhardt, H.W. Uniaxial tensile fatigue failure of concrete under constant amplitude and programme loading. Magazine of Concrete Research. 1984;136(129):216–226.

[14] Shah, S.P. Predictions of cumulative damage for concrete and reinforced concrete. Materiaux et Constructions. 1984;17(47):65–68.

[15] Holmer, J.O. Fatigue of concrete by constant and variable amplitude loading. ACI Special Publication. Fatigue of Concrete Structures. 1982;75:71–110.

[16] Siemes, A.J.M. Miner's rule with respect to plain concrete. ACI Special Publication. Fatigue of Concrete Structures. 1982;75:343–372.

[17] Leeuwen, J.V., Siemes, A.J.M. Miner's rule with respect to plain concrete. HERON. 1979;24(1):1–34.

[18] Tepfers, R., Friden, C., Georgsson, L. A study of the applicability to the fatigue of concrete of Palgrem-Miner partial damage hypothesis. Magazine of Concrete Research. 1977;29(100):123–130.

[19] Hilsdorf, H.K., Kesler, C.E. Fatigue strength of concrete under varying flexural stresses. ACI Journal Proceedings. 1966;63(10):1059–1076.

[20] Shah, S.P., Chandra, S. Fracture of concrete subjected to cyclic loading. ACI Journal Proceedings. 1970;67(10):816–824.

[21] Ople, F.S., Hulsbos, C.L. Probable fatigue life of plain concrete with stress gradient. ACI Proceedings. 1966;63(1):59-82.

[22] Zhang, B., Philips, D.V., Wu, K. Effect of loading frequency and stress reversal of fatigue life of plain concrete. Magazine of Concrete Research. 1996;48(117):361–375.

[23] Sparks, P.R., Menzies, J.B. Effect of rate of loading upon the static and fatigue strengths of plain concrete in compression. Magazine of Concrete Research. 1973;25:73–80.

[24] Awad, M.E., Hilsdorf, H.K. Strength and deformation characteristics of plain concrete subjected to high repeated and sustained loads. Civil Engineering Studies, Structural Research Series. No 372. 1971; pp.266.

[25] Aas-Jakobsen, K. Fatigue of concrete beams and columns. University of Trondheim. Norwegian Institute of Technology. Division of Concrete Structures. 1970;70(1):pp.148.

[26] Murdock, J.W. A critical review of research on fatigue of plain concrete. Engineering Experiment Station. University of Illinois Urbana. Bulletin N0 475. 1965.

[27] Zhang, B., Wu, K. Residual fatigue strength and stiffness of ordinary concrete under bending. Cement and Concrete Research. 1997;27(1):115–126.

[28] Saucedo, L., Yu, R.C., Medeiros, A., Zhang, X.X., Ruiz, G. A probabilistic fatigue model based on the initial distribution to consider frequency effect in plain and reinforced concrete. International Journal of Fatigue. 2013;48:308–318.

[29] Medeiros, A., Zhang, X.X., Ruiz, G., Yu, R.C., Velasco, M. Effect of the loading frequency on the compressive fatigue behavior of plain and fiber reinforced concrete. International Journal of Fatigue. 2015;70:342–350.

[30] Waagaard, K., Keep, B., Stemland, H. Fatigue of high strength lightweight aggregate concrete. Proceedings of the Utilization of high strength concrete, Stavanger (Norway). 1987:291–306.

[31] Cachim, P.B., Figueiras, J.A., Pereira, P.A.A. Fatigue behavior of fiber-reinforced concrete in compression. Cement and Concrete Composites. 2002;24(2):211–217.

[32] ACI Committee 544, editor. State-of-the-art report on fiber reinforced concrete. American Concrete Institute; 2002.

[33] Lee, M.K., Barr, B.I.G. An overview of the fatigue behavior of plain and fibre reinforced concrete. Cement and Concrete Composites. 2004;26:299–305.

[34] Ramakrishnan, V., Lokvik, B.J. Fatigue strength and endurance limit of plain and fibre reinforced concretes. A critical review. Proceedings of the International Symposium on Fatigue and Fracture in Steel and Concrete Structures, Madras (India). 1991:381–407.

[35] Minguez, J. Analysis of the post-cracking mechanical capacity of high performance concrete subjected to axial cyclic loads (Análisis de la capacidad mecánica postfatiga en hormigones de altas prestaciones sometidos a cargas cíclicas axiales) (in Spanish) [thesis]. Burgos (Spain): University of Burgos; 2012. 302 p.

[36] Vicente, M.A., González, D.C., Mínguez, J. Determination of dominant fibre orientations in fibre-reinforced high-strength concrete elements based on computed tomography scans. Nondestructive Testing and Evaluation. 2014;29(2):164–182.

[37] Oneschkow, N. Influence of loading frequency on the fatigue behaviour of high-strength concrete. In: FIB, editor. Proceedings of the 9th FIB International PhD Sym-

posium in Civil Engineering. July 22nd to 25th; Karlsruhe (Germany). 2012. pp. 235–240.

[38] Zanuy, C., Albajar, L., De la Fuente, P. Sectional analysis of concrete structures under fatigue loading. ACI Structural Journal. 2009;106(5):667–677.

[39] Zanuy, C. Sectional analysis of reinforced concrete elements subjected to fatigue loads, including sections between cracks (Análisis seccional de elementos de hormigón armado sometidos a fatiga incluyendo secciones entre fisuras) (in Spanish) [thesis]. Madrid (Spain): Polytechnic University of Madrid. 2008. 275 p.

[40] Vicente, M.A., González, D.C., Martínez, J.A. Mechanical response of partially prestressed precast concrete I-beams after high-range cyclic loading. ASCE Practice Periodical on Structural Design and Construction. 2014;20(1):1-8. DOI: 10.1061/(ASCE)SC.1943-5576.0000225

[41] Bernardo, H., Vicente, M.A., González, D.C., Martínez, J.F. Cyclic bond testing of steel bars in high-performance underwater concrete. Structural Engineering International. 2014;24(1):37–44.

[42] Vicente, M.A., González, D.C., Mínguez, J., Martínez, J.A. Residual modulus of elasticity and maximum compressive strain in HSC and FRHSC after high-stress-level cyclic loading. Structural Concrete. 2014b;15(2):210–218.

[43] Meng, X.H., Wang, W.W., Zhou, J.J., Song, Y.P. Experimental investigation on residual strength of plain concrete under fatigue biaxial compression with constant confined stress. Advances Materials Research. 2011;261–263:581–585.

[44] Wang, H.L., Song, Y.P. Fatigue capacity of plain concrete under fatigue loading with constant confined stress. Materials and Structures. 2011;44(1):253–262.

[45] Zhu, J.S., Song, Y.P., Cao, W. Fatigue behaviour of plain concrete under biaxial compression: Experiments and theoretical model. China Ocean Engineering. 2003;17(4):617–630.

[46] Nelson, E.L., Carrasquillo, R.L., Fowler, D.W. Behaviour and failure of high strength concrete subjected to biaxial-cyclic compression loading. ACI Materials Journal. 1988;85(30):248–253.

[47] Su, E.C.M., Hsu, T.T.C. Biaxial compression fatigue and discontinuity of concrete. ACI Materials Journal. 1988;3:178–188.

[48] Buyukozturk, O., Tseng, T.M. Concrete in biaxial cyclic compression. Journal of Structural Engineering. 1984;110(3):461–476.

[49] Kim, J., Yi, C., Lee, S.J., Zi, G. Flexural fatigue behaviour of concrete under unaxial and biaxial stress. Magazine of Concrete Research. 2013;65(12):757–764.

[50] Subramaniam, K.V., Shah, S.P. Biaxial tension fatigue response of concrete. Cement and Concrete Composites. 2003;25(6):617–623.

[51] Subramaniam, K.V., Popovics, J.S., Shah, S.P. Fatigue fractures of concrete subjected to biaxial stresses in the tensile C-T region. Journal of Engineering Mechanics-ASCE. 2002;128(6):668–676.

[52] Subramaniam, K.V., Popovics, J.S., Shah, S.P. Fatigue response of concrete subjected to biaxial stresses in the compression-tension region. ACI Materials Journal. 1999;96(6): 663–669.

[53] ACI 215R-74, editor. Considerations for design of concrete structures subjected to fatigue loading. American Concrete Institute. 1974. 24 p.

[54] Paskova, T., Meyer, C. Low-cycle fatigue of plain and fiber-reinforced concrete. ACI Materials Journal. 1997;94:273–285.

[55] Kim, J.K., Kim, Y.Y. Experimental study of the fatigue behaviour of high strength concrete. Cement and Concrete Research. 1996;26(10):1513–1523.

[56] Grzybowski, M., Meyer, C. Damage accumulation in concrete with and without fiber reinforcement. ACI Materials Journal. 1993;90:594–604.

[57] Furtak, K. A method for calculating the concrete strength under cyclic loads (Ein Verfahren zur Berchnung der Betonfestigkeit unter schwellender Belastungen (in German). Cement and Concrete Research. 1984;14:855–865.

[58] Tepfers, R., Kutti, T. Fatigue strength of plain, ordinary and lightweight concrete. ACI Journal. 1979;76(5):635–652.

[59] FIB-Fédération International du Béton. Model Code 2010. Final Draft. Volume 1. International Federation for Structural Concrete (fib) Bulletin 65; 2012.

[60] Przybilla, C., Fernández-Cantelli, A., Castillo, E. Deriving the primary cumulative distributive function of fracture stress for brittle materials from 3- and 4-point bending test. Journal of the European Ceramic Society. 2011;31(4):451–460.

[61] Castillo, E., Fernández-Cantelli, A., Koller, R., Ruiz-Ripoll, M.L., García, A. A statistical fatigue model covering the tension and compression Wöhler fields. Probabilistic Engineering Mechanics. 2009;24(2):199–209.

[62] Castillo, E., Fernández-Cantelli, A., Ruiz-Ripoll, M.L. A general model for fatigue damage due to any stress history. International Journal of Fatigue. 2008;30:150–164.

[63] Zhao, D.F., Chang, Q.Y., Yang, J.H., Song, Y.P. A new model for fatigue life distribution of concrete. Key Engineering Materials. 2007;348–349:201–204.

Chapter 5

Elevated Temperature Performance of Multiple-Blended Binder Concretes

Haider M. Owaid, Roszilah Hamid and
Mohd Raihan Taha

Additional information is available at the end of the chapter

http://dx.doi.org/10.5772/64415

Abstract

Concretes that contain binary-blended binders (BBB) and ternary-blended binders (TBB) incorporating thermally activated alum sludge ash (AASA), silica fume (SF), ground-granulated blast-furnace slag (GGBS) and palm oil fuel ash (POFA) are exposed to temperatures as high as 800 °C. The water-binder ratio of the multiple-blended binder (MBB) concretes was 0.30, and the total binder and polypropylene (PP) fibre contents were 493 and 1.8 kg/m^3, respectively. The elevated temperature performance of the MBB concretes is evaluated in terms of the mass loss, compressive strength, ultrasonic pulse velocity (UPV) and surface cracks. The concrete strength deteriorated significantly due to elevated temperature up to 800 °C, but the residual strength of the BBB containing 15 % AASA was higher than that of the control and 20 % AASA concretes. High-temperature exposure decreased measured UPV values. The concrete weight loss was more pronounced for TBB concretes. The elevated temperature performance of all of the TBB concretes was better than that of the BBB concretes with the same AASA replacement levels. It was observed that PP fibres help reduce spalling. BBB concrete containing 15 % AASA combined with either SF or GGBS or POFA exhibits superior performance at elevated temperature than Portland cement concrete at the same mix design proportion.

Keywords: elevated temperature, alum sludge, thermal activation, pozzolanic materials, multiple-blended binders

1. Introduction

Concrete may be exposed to elevated temperatures upon the outbreak of fire or when they are located near furnaces or reactors. The exposure of concrete to high temperatures (above 200 °C) from accidental fire or elevated temperatures in industrial plants leads to high internal tensile stresses that can cause cracks and damage to concrete structures. The compressive strength of concrete also decreases significantly when subjected to elevated temperatures. Therefore, the residual compressive strength (RCS) is an appropriate factor to consider when assessing the strength of concrete after accidental fire exposure. It is vital for concrete that has been exposed to fire to maintain a high RCS to preserve the safety of the whole structure. The mix proportion, curing period, aggregate type and presence of pozzolanic materials are all features that affect the performance of concrete at elevated temperatures. The use of pozzolanic materials such as metakaolin (MK), silica fume (SF), fly ash (FA), ground-granulated blast-furnace slag (GGBS) and palm oil fuel ash (POFA) in concrete mixtures has been described as an efficient technique for improving the strength and other material properties of concrete. However, the temperature resistance of concrete incorporated with pozzolanic materials such as SF and MK was found to be lower than the resistance of control concrete [1, 2]. Over the last decade, therefore, there has been extensive research into the performance of high-strength concrete (HSC) that incorporate FA, GGBS and SF at elevated temperatures, such as those produced by fire. Phan and Carino [3] compiled experimental reports of the mechanical properties of concrete when exposed to rapid heating, as occurs in a fire. They found that the material properties of HSC vary with temperature differently than do those of normal-strength concrete (NSC) in the range between room temperature and approximately 450 °C and noted that the differences narrow at temperatures above 450 °C. Morsy and Shebl [4] found that a composition including 15 % MK and 5 % SF demonstrated improved fire resistance. It appeared that the MK had a more pronounced effect on the residual compressive strength of the concrete. Behnood and Ziari [5] showed that the addition of SF had no significant effect on the relative residual compressive strength when the concrete was subjected to temperatures of 100 and 200 °C, but that the amount of SF had considerable influence on the residual compressive strength when the concrete was subjected to temperatures of 300 and 600 °C.

Phan et al. [6] reported that high-performance concrete (HPC) with higher original strength (lower w/c) and with SF retained more residual strength after exposure to elevated temperature than did those HPC with lower original strength (higher w/c) and without SF. There was a significant reduction in the weight of the specimen and the relative strength of the concrete at elevated temperatures (200–1200 °C) [7]. Ghandehari et al. [8] evaluated the residual mechanical properties of HPC after exposure to elevated temperatures by using SF. They found that after heating the concrete to 200 °C, the strength of all of the concrete samples showed a slight improvement compared with the strength of concrete at 100 °C. Mohammad et al. [9] reported the residual compressive strength of concrete containing 20 % POFA after exposure to elevated temperatures and subsequent cooling. They found that there was a continuous decrease in the residual compressive strength with increasing temperature. The highest reductions were observed in ordinary Portland cement (OPC) concrete: 22.5, 33 and 78 % at 300, 500 and 800 °C,

http://dx.doi.org/10.5772/64415

respectively. They also found that residual performance was higher in POFA concrete than in the OPC concrete.

Demirel and Keleştemur [10] demonstrated that adding pozzolanic materials (finely ground pumice (FGP) and SF) to concrete decreased both unit weight and compressive strength. Morsy et al. [11] evaluated the effects of high temperature on cement paste mixes containing 15–30 % MK and 5–15 % SF OPC replacement. They concluded that the best performance was achieved with cement paste containing 10 and 15 % SF, which increased in strength at 400 °C by 39 and 48 % but decreased in strength at 600 °C by 33 and 43 %, respectively. Rahel et al. [12] studied the replacement of cement by high-volume fly ash combined with colloidal nanosilica to produce high-strength mortars after exposure to temperatures of 400 and 700 °C. They found that high-strength mortars that have equivalent residual strength after exposure to 700 °C to that of control (unheated) cement mortar specimens can be produced by replacing cement with high-volume fly ash and by using colloidal nanosilica. Because of the increasing use of HSC in columns, resistance to spalling has become one of the crucial components of effective fire resistance [13]. Surface spalling occurs when a low-permeability paste is subjected to a high rate of heating and the vapour pressure in the pores consequently develops stresses greater than the material's tensile strength [14].

The internal stresses in compression members make them more vulnerable to spalling. In particular, there is a greater risk that HPC, with its lower permeability, will spall at high temperature compared with conventional concrete. To combat the spalling effect in HSC, it is necessary to add polypropylene (PP) fibres to the concrete mixes. Polypropylene fibres melt at approximately 160–170 °C and become capable of producing moisture escape channels to release the vapour pressure. One major consideration in the design of buildings is the safety of the occupants in case of an outbreak of fire. As such, thorough knowledge of the behaviour of all construction materials is required before incorporating them into structural elements. Additionally, the growing prevalence of engineering structures characterized as large span, high rise and ultra-high rise has necessitated a continual increase in performance requirements.

Water treatment plants (WTPs) produce waste residual sludge, alum sludge (AS), when aluminium sulphate is used as a coagulant in the process of making drinking water for human consumption. Thermally activated alum sludge ash (AASA) is a new pozzolanic material that is acquired from the calcination of AS at 800 °C. Owaid et al. [15] studied the feasibility of using AASA as a pozzolanic material for replacing cement in binary-blended binder (BBB) and ternary-blended binder (TBB) concretes that incorporate SF, GGBS and POFA. According to their results, AASA exhibits pozzolanic behaviour and can be classified as a Class natural (N) pozzolan [15]. The BBB containing 15 % AASA increased the compressive and tensile strength of concrete up to 85.3 and 5.38 MPa at 28 days, respectively, but further increases in AASA content gradually reduced these strengths [15]. The mechanical properties of the ternary combinations are better than those of the binary mixes at the same AASA replacement levels [15].

The performance of multiple-blended binder (MBB) concretes incorporating AASA, SF, GGBS and POFA at elevated temperature is presented in this chapter. The fire resistance of MBB concretes with thermally activated alum sludge ash (AASA) and pozzolanic materials as

replacements for cement in both binary and ternary blends can be used to determine the suitable application of the concrete.

2. Experimental programme

2.1. Materials

The cement used in the concrete mixtures was ordinary Portland cement (OPC) type I from Orang Kuat Berhad, which conforms to ASTM C150-1992 [16].The chemical composition and physical properties of OPC are as reported previously [15]. Alum sludge (AS) is the raw material used in the present research that was obtained from the drinking water purification process. The AS was collected at the ABASS Consortium water treatment plant and then oven dried at 105 °C for 24 h. The dried sludge was crushed and sieved through a 10 mm sieve to remove coarse and foreign particles.

In a previous study by Owaid et al. [15], an effective way of preparing thermally activated alum sludge ash (AASA) by thermal activation of AS was to incinerate dry alum sludge in a laboratory electric furnace at 800 °C for a period of 2 h with the heating rate of 5 °C/min. The chemical composition and physical properties of the AS and AASA are as given in Ref. [15]. Three types of pozzolanic materials, namely, SF, GGBS and POFA, were employed as a partial replacement of OPC by weight in different combinations of binary and ternary cementitious blends. The type of condensed silica fume (SF) was Force 10,000 D microsilica. The chemical and physical properties of these materials have previously been reported [15].

Fine and coarse aggregates obtained from local sources were in accordance with the ASTM standard. The local natural sand used as a fine aggregate had a maximum aggregate size of 4.75 mm and a fineness modulus of 2.89. The maximum size of the local coarse aggregate (crushed granite) was 10 mm; its specific gravity was 2.64, and its water absorption value was 0.48 %. The fine aggregate had a specific gravity of 2.61 and a water absorption value of 0.72 %. The superplasticizer (SP) used in this study was an aqueous solution of modified polycarboxylate-based superplasticizer (ViscoCrete-2044). The specific gravity of 1.08 was utilized to achieve the desired workability in all HPC mixtures. The polypropylene (PP) fibres used in this study were obtained from Timuran Engineering and bore the brand name of fibrillated polypropylene fibre. They were white and 12.19 mm long, and they had a specific gravity of 0.9. The PP fibres were used to eliminate the spall effect for all specimens that were subjected to high temperatures and were added at an amount of 1.8 kg/m^3 for concrete mixes.

2.2. Mix proportions and preparation of specimens

The mix proportions were based on recommendations by Owaid et al. [15]. **Table 1** shows the mix proportions for both categories of concrete. Nine types of concrete mixtures were prepared to explore the effects of elevated temperatures on the properties of MBBC specimens containing AASA in both binary- and ternary-blended cement with the same binder content of 493 kg/m^3, and the ratio of water-binder (w/b) was kept at 0.30. The aggregates used were

http://dx.doi.org/10.5772/64415

in accordance with ASTM standards and comprised crushed granite gravel with a nominal maximum size of 10 mm and local natural sand with a maximum size of 4.75 mm. The superplasticizer used was an aqueous solution of modified polycarboxylates with two OPC mass fractions, 1.5 and 1.8 %.

Mix description (%)	w/b	Water (kg)	Cement (kg)	AASA (kg)	SF (kg)	GGBS (kg/m^3)	POFA (kg)	FA* (kg)	CA** (kg)	SP*** dosage (%)	PP**** (kg)
Control-OPC	0.30	147.9	493	0	0	0	0	684	1027	1.5	1.8
AASA15	0.30	147.9	419.0	74.0	0	0	0	684	1027	1.5	1.8
AASA20	0.30	147.9	394.4	98.6	0	0	0	684	1027	1.5	1.8
SF6	0.30	147.9	463.4	0	29.6	0	0	684	1027	1.5	1.8
GGBS20	0.30	147.9	394.4	0	0	98.6	0	684	1027	1.5	1.8
POFA15	0.30	147.9	419.0	0	0	0	74.0	684	1027	1.5	1.8
AASA20 SF6	0.30	147.9	364.8	98.6	29.6	0	0	684	1027	1.8	1.8
AASA20GGBS20	0.30	147.9	295.8	98.6	0	98.6	0	684	1027	1.8	1.8
AASA20POFA15	0.30	147.9	320.4	98.6	0	0	74.0	684	1027	1.8	1.8

FA* stands for fine aggregates; CA* for coarse aggregates; SP*** for superplasticizer; PP**** for polypropylene fibres.

Table 1. Concrete mix proportions [15].

The content of polypropylene fibres was 1.8 kg/m^3 for all of the concrete mixtures that contained AASA to eliminate the spall effect. All concrete materials were mixed in a rotating pan mixer for approximately 5 min to conform with the mixing process described in ASTM C192-2002 [17]. The mixtures were cast into specimens by using 100 mm standard cube moulds and were compacted with a vibrating table to reduce the air voids content in mixes. The specimens were subsequently covered to prevent evaporative water loss. After casting, the moulded specimens were left in the casting room at a temperature of 26 °C for 24 h. After demoulding, the specimens were cured in a water tank for 28 days. Later, they were removed from the tank and left in the laboratory to air and cure naturally for up to 56 days, under similar conditions of temperature and relative humidity.

2.3. Heating and cooling regimens

After a curing period of 56 days, the concrete specimens were conveyed to an electrical furnace. The specimens were kept in the furnace for 3 h at maximum temperature; the rate of temperature increase in the automatic electric furnace was 5 °C/min [18], as observed in **Figure 1**. Subsequently, the power was shut off, and the specimens remained in the furnace until the temperature dropped to room temperature to prevent the specimens from experiencing thermal shock. For this research study, the concrete specimens were heated in an electric furnace to 400, 600 and 800 °C.

Figure 1. Automatic electric furnace used to heat concrete specimens.

2.4. Testing procedures

The residual properties of the unheated control mix were compared with the properties of the specimens for multiple-blended binder (MBB) concretes containing OPC, AASA and pozzolanic materials. Also, the crack patterns on the surface of the multiple-blended binder concretes were inspected after the heated specimens had cooled down. An electronic digital balance with an accuracy of ±0.1 g was used to determine the concrete mass loss ($M_{\mathbf{loss}}$) before and after each heating temperature. The calculation of the concrete mass loss of specimens was based on Eq. (1); subsequently, specimens were taken out from furnace and weighed (W_d). After the concrete specimens had cooled to room temperature, they were removed from the furnace to determine their mass loss, residual compressive strength and ultrasonic pulse velocity of MBB concrete specimens. For each type of concrete, the residual properties were subsequently compared with the properties of the unheated control specimens. Additionally, crack patterns on the surface of the MBB concrete specimens were inspected after the heated specimens had cooled down. An electronic digital balance with an accuracy of ±0.1 g was used to determine the concrete mass loss ($M_{\mathbf{loss}}$) before and after each heating step and the final weight (W_d). Calculation of the concrete mass loss of specimens was based on Eq. (1):

$$M_{loss} = \frac{M_{initial} - M_{heated}}{M_{initial}} \tag{1}$$

where $M_{\mathbf{initial}}$ and $M_{\mathbf{heated}}$ are the initial mass (before heating) and heated mass (after heating) weighed in air, respectively. The compressive strength of the concrete was determined by crushing three 100 mm^3 cubes for each mix. The test was carried out according to BS EN 12390-3 [19]. The compression load was applied at a rate of 3 kN/s using a compression machine with

http://dx.doi.org/10.5772/64415

a capacity of 5,000 kN. The residual compressive strength (RCS) was calculated using the following Eq. (2):

$$RCS = \frac{\sigma_{elev}}{\sigma_{26}} \times 100 \tag{2}$$

where σ_{elev} is the compressive strength (MPa) of the cubes subjected to elevated temperature and σ_{26} is the compressive strength (MPa) of the cubes kept at room temperature (26 °C).

The portable equipment for ultrasonic non-destructive indicating test (known as PUNDIT) was used to measure ultrasonic velocity (V), in accordance with BS 1881: Part 203 (1986) [20]. Ultrasonic velocity (V) was determined by measuring the ultrasonic pulse transmission time by means of the direct transmission method. The ultrasonic pulse transmission time is the time required for longitudinal vibrations of ultrasonic frequency to travel a known distance through the material. Wave speed was calculated as:

$$V = \frac{L}{T} \tag{3}$$

where L is the transmission distance (m), T is the transmission time in the concrete (s), and V is the velocity of pulse transmission in the concrete (m/s) [20].

3. Results and discussion

The saturated surface-dry specimens were heated to 400, 600 and 800 °C for 3 h and subsequently cooled to room temperature (26 °C). **Figures 2–11** show the results obtained from the tests (losses in weight, compressive strength and ultrasonic pulse velocity) of MBB concrete specimens subjected to elevated temperatures. The finding is analyzed and discussed below.

3.1. Concrete mass loss for different elevated temperatures

Figure 2 and **Table 2** present the percentage of the mass loss relative to the original weight (weight before heating) of the mixtures of OPC, AASA, SF, GGBS and POFA in the binary- and ternary-blended concrete with increasing temperature. It can be observed that the mass loss in all specimens showed a gradual increase from 3.72 to 7.41 % with the increase in temperature from 400 to 800 °C. The results also show that the mass loss increased with increasing amounts of AASA and pozzolanic materials. It is observed that the mass loss was less than 7.5 % for the specimens that did not exceed 800 °C. After being subjected to temperatures of 400, 600 and 800 °C, the mass losses of OPC concrete were 3.78, 5.24 and 6.46 %, respectively. Additionally, the mass losses of AASA 15 % and AASA 20 % concrete were measured to be 3.98, 5.41 and 6.84 % and 4.1, 5.82 and 7.06 %, respectively. This small difference

in the mass loss has not caused significant effects when the AASA replacement ratios are at 15 and 20 %.

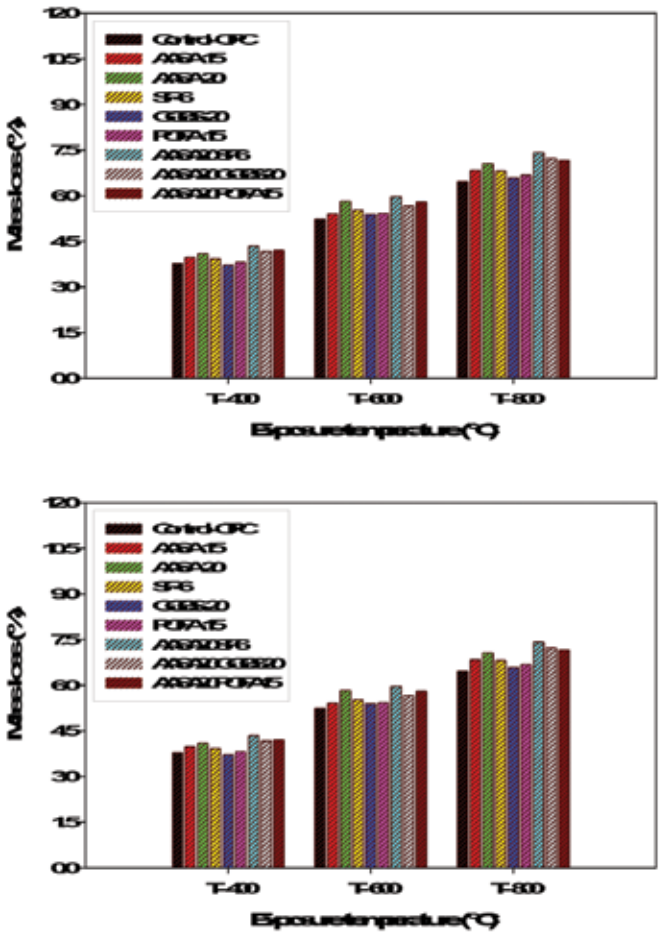

Figure 2. Mass loss of BBB and TBB concrete mixtures subjected to different elevated temperatures.

Mass loss occurs in the specimens due to the loss of water. Because of the loss of bound water from the cement paste, air voids are formed in the concrete. The structural integrity of the specimens deteriorates corresponding to the increase in mass loss with increasing temperature. Similar observations were reported by Janotka and Nurnbergerova [21]. The rate of concrete mass loss was slower when the heating temperature increased from 400 to 800 °C. These findings of the current study agree with observations by Hanaa et al. [22], who reported that approximately 70 % of the water contained in the concrete had evaporated at 300 °C. **Figure 2** shows that the incorporation of SF, GGBS and POFA at 6, 20 and 15 % by total binder

http://dx.doi.org/10.5772/64415

weight, respectively, resulted in a decrease in mass loss of the pozzolanic material concrete with increasing temperature. The observations show that there were higher mass losses in SF concrete compared with GGBS and POFA concretes. The mass loss associated with the SF, GGBS and POFA concretes was 3.93, 3.72 and 3.81 % at 400 °C; 5.53, 5.39 and 5.42 % at 600 °C; and 6.82, 6.59 and 6.68 % at 800 °C, respectively. Similar observations were reported in various studies [9, 10, 23].As observed, all of the ternary binder mixtures shown in **Figure 2** lost more mass compared with the OPC concrete. In this study, the weight losses in the concrete containing both AASA and SF were higher than the losses in AASA + GGBS and AASA + POFA concrete with an increasing temperature from 400 to 800 °C. This result can be attributed to the specific gravity of the selected pozzolanic materials, with the specific gravity of SF being the lower than that of GGBS and POFA. The average mass loss of the ternary-blend binder concrete was 4.2 % at 400 °C, 5.8 % at 600 °C and 7.3 % at 800 °C.

Mix description (%)	**Percentage of the mass loss relative to the original weight at different heating regimens (°C) (%)**		
	26–400	**400–600**	**600–800**
Control-OPC	3.78	5.24	6.46
AASA15	3.98	5.41	6.84
AASA20	4.10	5.82	7.06
SF6	3.93	5.53	6.82
GGBS20	3.72	5.39	6.59
POFA15	3.81	5.42	6.68
AASA20 SF6	4.35	5.97	7.41
AASA20 GGBS20	4.17	5.66	7.23
AASA20 POFA15	4.20	5.80	7.16

Table 2. Percentage of the mass loss relative to the original weight of the BBB and TBB mixtures.

3.2. Residual compressive strength of concrete subjected to elevated temperatures

Figures 3–5 show the results of residual compressive strength (RCS) measurements of the specimens for multiple-blended binder concretes containing OPC, AASA and pozzolanic materials that were subjected to elevated temperatures followed by cooling in ambient air until the 56th day after the heating process. **Figures 6–8** indicate the relative residual compressive strength (ratio of residual compressive strength after elevated temperature to initial compressive strength at room temperature) of the concrete specimens. The residual strength of the MBB concrete specimens decreased as the temperature was increased. **Figure 3** shows that regardless of the presence of PP fibres, the strength of AASA concrete deceased when the temperature was increased from 400 to 800 °C. Hence, there was a significant increase in the compressive strength of the binary concrete blends with 15 % AASA at room temperature (26 °C) compared with the compressive strength of the control mix and concrete mixture with 20 % AASA. The

increase in compressive strength of the concrete mixture with 15 % AASA was approximately 12.4 % compared with the compressive strength of the control mix. However, the concrete with 20 % AASA cement exhibited reduced compressive strength.

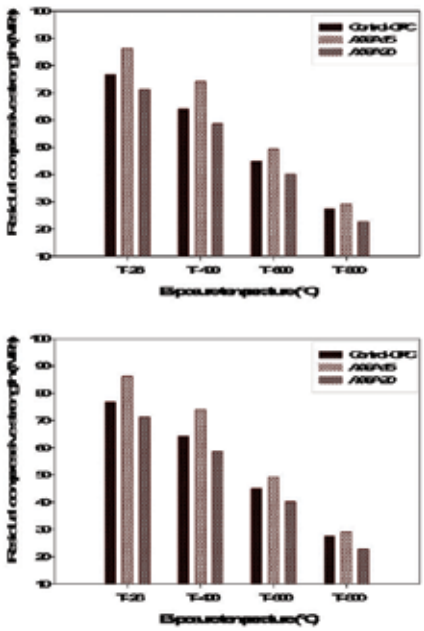

Figure 3. Influence of AASA on the compressive strength of concrete subjected to different elevated temperatures.

The change in the strength of concrete specimens appeared to follow a common trend. Initially, as the temperature was increased to 400 °C, the strength decreased relative to that at room temperature; the relative decrease was approximately 14.2–17.7 %, as shown in **Table 3**. This effect could be due to variations in pore structure, including porosity and pore size distribution, or to an increase in pore diameter [24]. According to several researchers [25–27], this reduction is primarily due to the release of free and physically bound water from the pores of the hydrates and to the first stage of dehydration in the hydrated products (calcium hydroxide, calcium silicate hydrates and calcium aluminosilicate hydrates) and the breakdown of tobermorite gel. The concrete containing 15 % AASA performed better and showed higher residual strength compared with the control-OPC and 20 % AASA concretes. A severe loss in strength was observed in the concrete as the temperature increased from 400 to 600 °C. The average strength loss was of 42.6 % (**Table 3**). The quick loss in compressive strength for concrete mixtures has been attributed to the dense microstructure of this type of concrete, which is the direct cause of the excessive build-up of vapour pressure. This pressure produces large cracks in the specimens during heating. The decomposition of calcium hydroxide and calcium carbonate in cement paste, which occurs from 430 to 600 °C, is an additional reason for the loss of strength [26, 28].

http://dx.doi.org/10.5772/64415

Mix description (%)	Percentage of the strength loss relative to the original weight at different heating regimens (°C) (%)		
	26–400	**400–600**	**600–800**
Control-OPC	12.3	41.3	64.1
AASA15	14.2	42.9	66.2
AASA20	17.7	43.6	68.1
Average	**14.7**	**42.6**	**66.1**
SF6	15.7	43.3	65.2
GGBS20	14.8	42.1	63.4
POFA15	16.1	42.6	64.7
Average	**15.5**	**42.7**	**64.1**
AASA20 SF6	17.6	45.8	69.7
AASA20 GGBS20	16.2	44.2	66.1
AASA20 POFA15	17.7	45.3	67.3
Average	**17.2**	**45.1**	**67.7**

Table 3. Percentage of the strength loss relative to the original weight of the BBB and TBB mixtures.

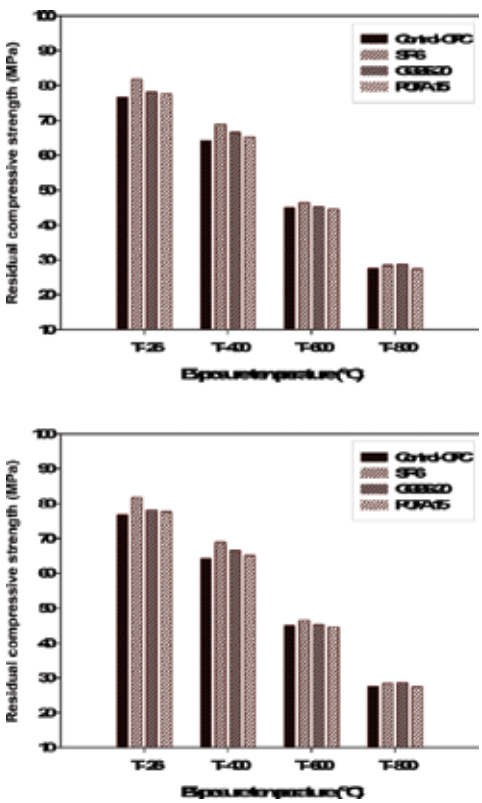

Figure 4. Influence of pozzolanic materials on the compressive strength of concrete subjected to different elevated temperatures.

All types of the MBB concretes showed severe deterioration at high temperatures between 600 and 800 °C temperature ranges, with further reduction in the strength. This reveals that the decomposition of C—S—H greatly affects the loss in the strength of concrete with severe deterioration for all mixtures of concrete [1]. The average loss of strength for the heated specimens was 66.1 %, compared with the strength of the unheated specimens. Thus, the sharp reduction in strength may be due to the formation of microcracks in the specimen, which weakens the interfacial transition zone and bonding between the aggregate and the cement paste. Therefore, the contractions of the paste lead to appear the cracks following the loss of water and expansion of the aggregate [29, 30].

Concrete mixtures that contained AASA exhibited extensive cracking and spalling, and their residual compressive strength was less than that of the control mixture. These effects are attributed to the presence and amount of filler additives in concrete mixtures that produce very dense transition zones between aggregates and paste due to their ultra-fine particles as filler materials and their pozzolanic reactions. During the expansion of the aggregates and contraction of the paste, higher stress concentrations are produced in the transition zone. These stresses worsen the bonding between aggregate and paste that contains filler additives compared with that of the control mixture [27]. The residual strength at 800 °C ranges from 23 to 29 % relative to unheated controls, as shown in **Figure 3**.

Figure 4 presents the changes in the compressive strength of concrete that contained 6, 20 and 15 % of SF, GGBS and POFA, respectively, with increasing temperature from 400 to 800 °C. The observations show a decrease in the strength of the pozzolanic concretes at temperatures from 26 to 400 °C. This drop in strength is quantified as a 14.8–16.1 % reduction of the original strength, as given in **Table 3**. Once again, the concrete containing pozzolanic materials performed better and exhibited higher residual strength [1, 27].

Generally, it can be concluded that the loss in strength of pozzolanic concrete is caused by the dense microstructure in this type of concrete, which causes the build-up of high internal pressures due to the water-vapour transition in the water interlayer. The observations also reveal a severe loss in strength for all four types of concrete at temperatures ranging from 400 to 600 °C. This loss recorded is 41.3, 43.3, 42.1 and 42.6 % of the initial values for OPC, SF6, GGBS and POFA concretes, respectively (see **Table 3**). When the concrete specimens are subjected to high temperatures, the cement paste contracts and the aggregates expand. This response causes the transition zone to weaken and results in bonding between aggregates and cement paste. As a result, this process as well as the chemical decomposition of hydrated products causes severe deterioration and loss of strength in concrete after exposure to high temperatures. All the concrete containing pozzolanic materials exhibited severe deterioration up to 800 °C, and the average loss in strength was 64.1 % because of the decomposition of C—S—H gel. A similar observation has been reported by Demirel and Kelestemur [10]. From their results, it is shown that the pozzolanic material exerts a considerable influence on the residual strength. The concrete mixture containing SF performed poorly compared with the concrete mixtures containing GGBS and POFA. Although the addition of SF increased the initial strength of the concrete, there was a considerable compressive strength loss when the concrete was subjected to high temperatures. This decrease in strength likely arose from the

http://dx.doi.org/10.5772/64415

very dense structure of SF concrete, which resulted in a build-up of vapour pressure due to the evaporation of physically and chemically bound water.

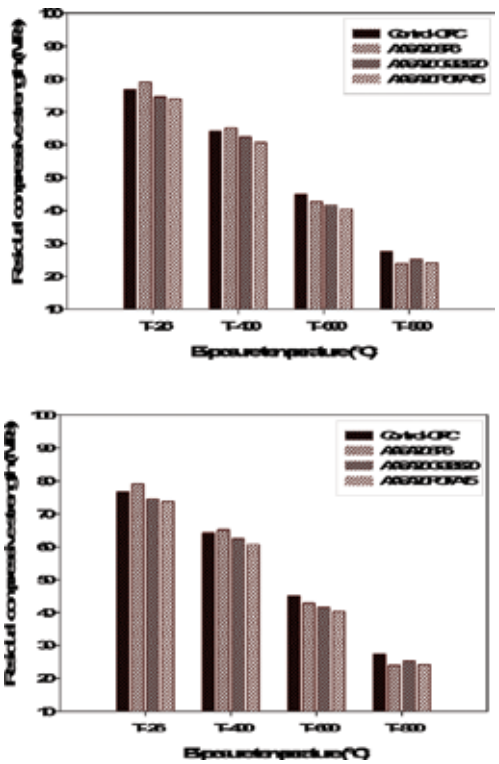

Figure 5. Influence of ternary-blended binders on the compressive strength of concrete subjected to different elevated temperatures.

Figure 5 illustrates the comparison of the residual compressive strengths of ternary-blend binder concrete specimens and the control specimens that were subjected to elevated temperature. It is clear that the residual compressive strength decreased as the treatment temperature increased to 800 °C. The observations show that the performance of the ternary blends with AASA and pozzolanic materials in terms of compressive strength is better than the performance of binary blends with AASA for the same replacement levels of the unheated specimen (26 °C). **Figure 5** shows that the OPC + AASA + SF mix exhibited the highest strength, followed by OPC + AASA + POFA and OPC + AASA + GGBS. This result is due to the transformation of calcium hydroxide, which leads to the formation of calcium silicate hydrate on the surface of the aggregate particles. This transformation occurs because the average particle size of SF is very small compared with the particle sizes of other pozzolanic materials. This has led to the refinement of grains in ternary mixtures that contain AASA. From 26 to 400 °C, a decrease was observed in the performance of ternary blends in terms of the loss of compressive strength in mixtures containing AASA and pozzolanic materials. The loss in strength is from 16.2 to 17.7 % of the original strength, as shown in **Table 3**.

The OPC + AASA + SF mix exhibited the highest loss in strength, followed by OPC + AASA + POFA and OPC + AASA + GGBS. This loss is due to the ultra-fine particles of SF that are used as fillers, along with the pozzolanic reactions of the particles. All concretes that contain ternary blends of AASA and pozzolanic materials lose their strength at a faster rate when they are subjected to temperatures ranging from 400 to 600 °C. The loss is from 44.2 to 45.8 % of the original strength. At these temperatures, the dehydration of the cement paste results in its gradual disintegration. Because the paste tends to shrink and aggregates tend to expand at high temperatures, the bond between the aggregate and the paste is weakened, thereby reducing the strength of the concrete. At 800 °C, the average strength loss is 67.7 % for the ternary-blend binder concrete (see **Table 3**). The test results revealed that all of the tested concretes deteriorated at a temperature over 600 °C, as indicated in previous studies [10, 31].

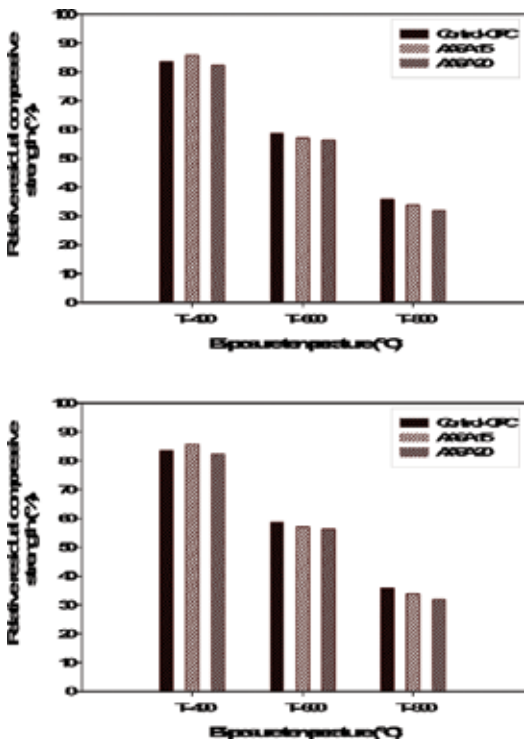

Figure 6. Relative compressive strength of control and AASA specimens subjected to different elevated temperatures.

Figures 6–8 show the values of the relative compressive strengths of the concrete mixtures containing OPC, AASA and pozzolanic materials in the form of binary and ternary blends after being subjected to high temperatures of 400, 600 and 800 °C. The relative strength was calculated as the percentage of strength retained by the concrete relative to the strength of the unheated specimen (26 °C). **Figure 6** shows that the relative compressive strength of the AASA concrete increases slightly when it is heated to 400 °C and then decreases slightly at 600 and 800 °C compared with the control concrete. At 400 °C, the relative compressive strength of

http://dx.doi.org/10.5772/64415

concrete that contains 15 % AASA drops by 85.8 %, whereas that of the control-OPC and 20 % AASA concretes drop by 83.7 and 82.3 %, respectively. Finally, it is observed that a sharp reduction in relative strength occurs when the temperature increases beyond 600 and 800 °C due to the loss of crystal water, which leads to the reduction of the $Ca(OH)_2$ content, morphological changes and the formation of microcracks. The average relative compressive strengths of concrete mixtures are approximately 57.3 and 33.8 % when the concrete is subjected to temperatures of 600 and 800 °C, respectively. Thus, the compressive strength of concrete decreases significantly when the temperature rises beyond 400 °C. Similar results were obtained by Arioz [7].

Figure 7 shows that the average relative compressive strengths of concrete specimens subjected to temperatures at 400, 600 and 800 °C with 6, 20 and 15 % of SF, GGBS and POFA were 84.2, 57.3 and 35.5 % of the strengths at room temperature, respectively. From the results, it can be concluded that below 400 °C, the relative residual compressive strength does not change significantly but that it does drop significantly at temperatures above 400 °C [24].

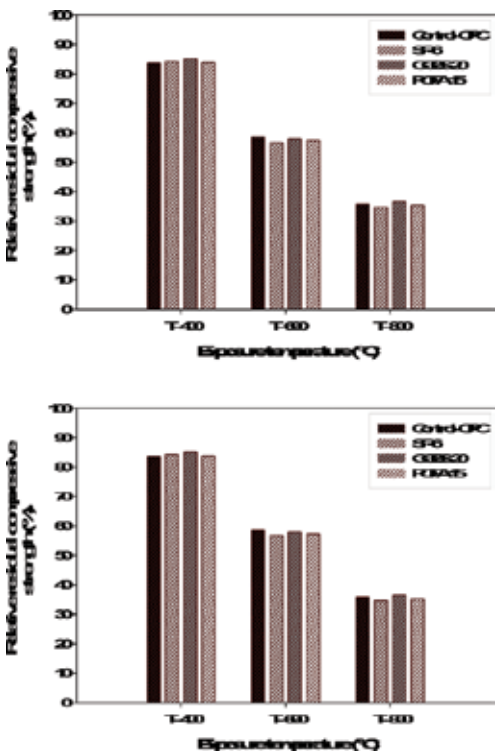

Figure 7. Relative compressive strength of control and pozzolanic material specimens subjected to different elevated temperatures.

Figure 8 shows that the relative compressive strength of TBB concrete exhibits a significant decrease after being subjected to elevated temperatures. The relative compressive strength of

mixtures OPC + AASA + SF, OPC + AASA + GGBS and OPC + AASA + POFA is approximately 82.3, 83.8 and 82.2 %, respectively, at 400 °C compared with 26 °C. A significant reduction of the relative compressive strength for mixtures OPC + AASA + SF, OPC + AASA + GGBS and OPC + AASA + POFA occurred at 600 °C. The loss recorded for each of the mixtures was 54.1, 55.7 and 54.7 %, respectively. The reduction of compressive strength of concrete is primarily attributed to the evaporative loss of free and physically bound water [11, 28]. After the temperature was increased up to 800 °C, the relative compressive strengths of OPC + AASA + SF, OPC + AASA + GGBS and OPC + AASA + POFA concretes were approximately 30.2, 33.8 and 32.7 % of the control concrete. It is clear that the compressive strength of concrete decreased significantly when the temperature was raised above 400 °C, as reported in several studies [32, 33]. The loss in strength was due to the excessive build-up of vapour pressure, which produced large cracks in the specimens [12]. Moreover, the binder products in cement paste dehydrate at this temperature, which causes a reduction in strength. However, specimens that contained AASA and SF had lower relative compressive strength compared with those of the ternary-blend binder specimens that contained GGBS and POFA materials.

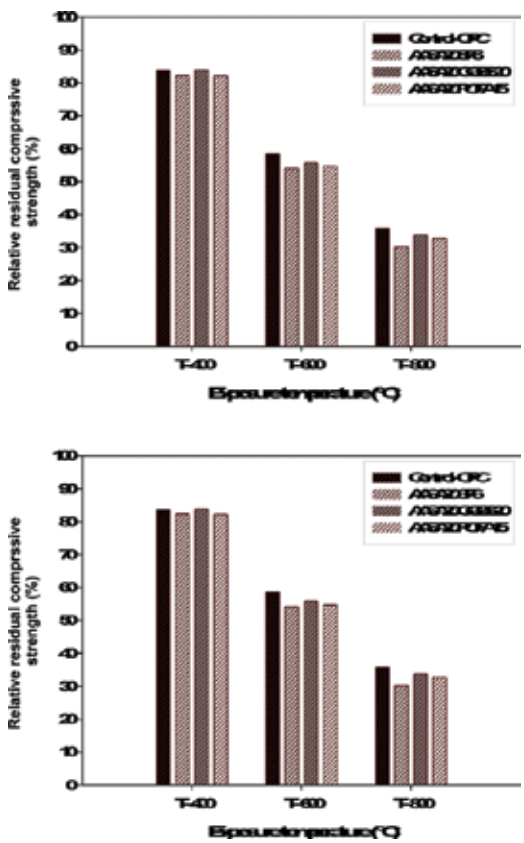

Figure 8. Relative compressive strength of control and ternary-blended binder specimens subjected to different elevated temperatures.

http://dx.doi.org/10.5772/64415

3.3. Ultrasonic pulse velocity of concrete subjected to elevated temperatures

The ultrasonic pulse velocities (UPVs) of the specimens of binary and ternary AASA and pozzolanic material MBB concretes that were subjected to different elevated temperatures are given in **Figures 9–11**. Each data point represents the average of three measurements. With regard to strength, the UPV values of both the binary and ternary AASA and the pozzolanic material MBB concrete specimens decreased with increasing temperatures. However, the rate of reduction in UPV was slightly different from that of strength. **Figure 9** reveals that the UPV values of the binary concrete blend with 15 % AASA were greater than those of the specimens with 20 % AASA and the control concrete at room temperature (26 °C). However, the values of the ultrasonic pulse velocities for AASA concrete were lower than those for the control concrete with increasing temperature, and there was a notable reduction in UPV after the specimens were subjected to elevated temperatures (i.e. higher than 400 °C).

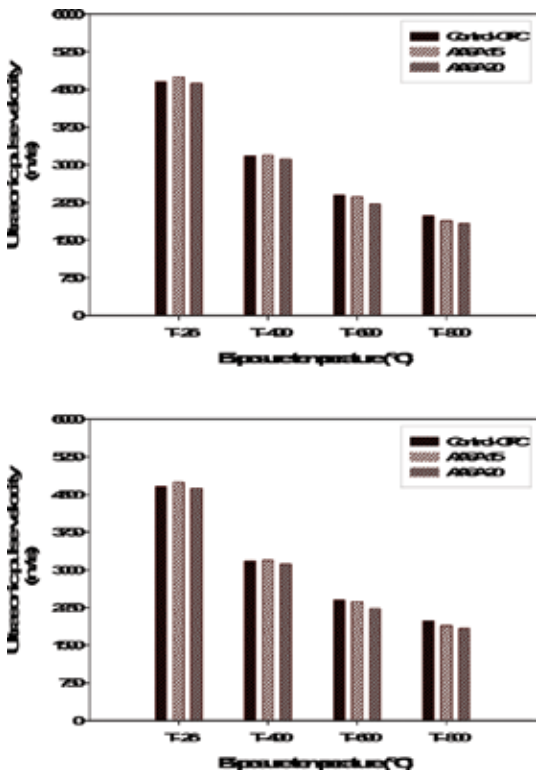

Figure 9. UPV of control and AASA specimens subjected to different elevated temperatures.

Clearly, the transmission of pulse waves through a concrete mass is greatly influenced by the microcracking of the concrete. Thus, the decrease in pulse velocity with increasing temperature is a sensitive measure of the progress of cracking in the material [23, 27, 34]. **Figure 9** also shows that the UPV displayed a continuous drop when the temperature was raised. It was noted that the reduction of pulse velocity for all concrete mixtures was due to the content of PP fibres in

the concrete mixtures. When the temperature was above 162 °C, the melting point of the PP fibres, these fibres created more randomly distributed pathways or voids in the concrete specimens. Moreover, thermal expansion and dehydration of the concrete due to high temperatures tend to cause the formation of fissures in the concrete. With more fissures, the cracks or micro-pathways delayed the pulse velocity in the concrete [35]. Therefore, micro-cracks reduce the UPV, resulting in low UPV values. The UPV values of OPC, AASA15 and AASA20 concrete mixtures were approximately 3173, 3189 and 3113 m/s at 400 °C; 2397, 2364 and 2224 m/s at 600 °C; and 1986, 1886 and 1832 m/s at 800 °C, respectively.

As illustrated in **Figure 10**, replacing part of the OPC with pozzolanic materials with 6, 20 and 15 % of SF, GGBS and POFA at 400, 600 and 800 °C caused a reduction in the UPV values. The specimens deteriorated due to increasing temperature, particularly at 800 °C, as reported by 23, 27, and the UPV values decreased substantially with increasing temperature. The measured UPVs of SF6, GGBS20 and POFA15 concretes after exposure to 400, 600 and 800 °C were approximately 3092, 3188 and 3151 m/s at 400 °C; 2287, 2332 and 2352 m/s at 600 °C; and 1829, 1963 and 1942 m/s at 800 °C, respectively.

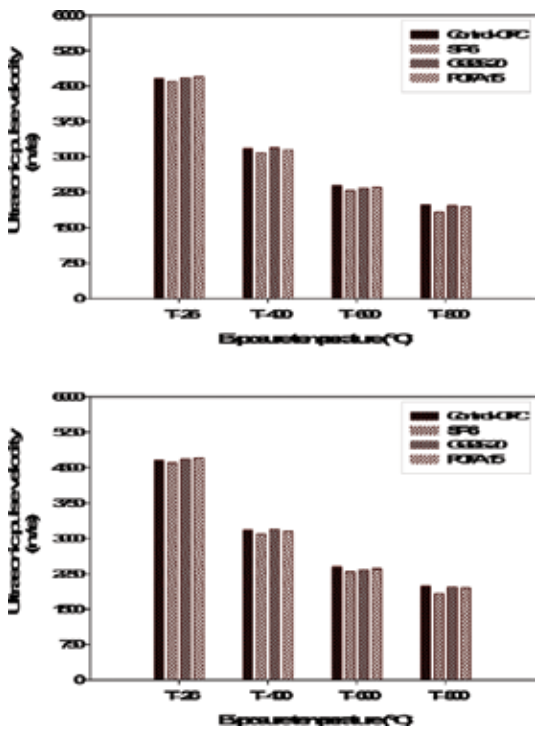

Figure 10. UPV of control and pozzolanic material specimens subjected to different elevated temperatures.

Figure 11 presents the measured UPV of TBB concretes in comparison to control concrete. **Figure 11** shows that there was a noticeable decrease in the UPV of the ternary blends of concrete with AASA and pozzolanic material after being subjected to temperatures higher than

http://dx.doi.org/10.5772/64415

400 °C. This decrease in the UPV values of the concrete specimens that have been subjected to high temperatures is due to the degeneration of the C—S—H gel at temperatures above 600 °C, which increases the amount of air voids and decreases the transmission speed of sound waves through the specimens. The decrease in UPV values was observed to be higher for SF-entrained concrete specimens, especially at 600 and 800 °C. A similar conclusion was reported by Demirel and Kelestemur [10]. This decrease results from the formation of a more porous structure due to the decomposition of the C—S—H gel, which is more abundant in samples containing SF.

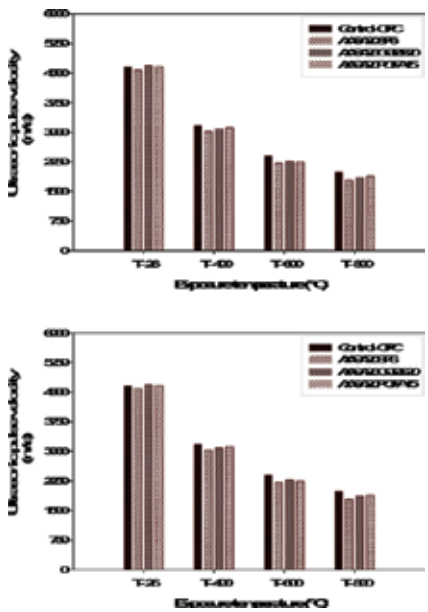

Figure 11. UPV of control and ternary-blended binder specimens subjected to different elevated temperatures.

3.4. Effect of elevated temperatures in multiple-blended-binder concretes on UPV and quality of concrete

The heating regimens of UPV measured after exposure to elevated temperatures could be divided into three stages, ranging from 26 to 400 °C, 400 to 600 °C and 600 to 800 °C. The effects of elevated temperatures on the quality of MBB concretes containing AASA, SF, GGBS and POFA are illustrated in **Table 4**. Whitehurst [36] provided varying ranges of UPV ratings to describe the quality of concrete. For concrete of excellent quality, the UPV must be greater than 4500 m/s; for good-quality concrete, the UPV must be in the range of 3500–4500 m/s; for medium-quality concrete, the UPV should be in the range of 3000–3500 m/s, while for poor-quality concrete, the UPV is in the range of 2000–3000 m/s; and finally, for very poor-quality concrete, the UPV is less than 2000 m/s.

Table 4 illustrates the effects of elevated temperatures in MBB concretes that contain AASA, SF, GGBS and POFA on the quality of concrete within different heating regimens (°C). This

table evaluates the quality of concrete processed at different temperatures for all of the types of mixtures that were subjected to the heating regimens of 26–400, 400–600 and 600–800 °C. The findings indicate that the specimens of the multiple-blended binder concretes degraded from excellent- to good- or medium-quality concrete, from medium- to poor-quality concrete and from poor- to almost very poor-quality concrete, respectively (see **Table 4**). The reason for this degradation is that the quality of concrete depends on the compressive strength. It is observed that the UPV values show a falling trend. The UPV values decrease with decreasing compressive strength for all of the mixtures after being subjected to temperatures of 400, 600 and 800 °C. **Table 5** tabulates the reduction of the UPV values for all concrete types. The UPV values for all mixtures at room temperature (26 °C) range from 4582 to 4743 m/s. Thus, all types of concrete produced at this temperature are classified as excellent-quality concrete, as shown in **Figures 9–11**.

Mix description (%)	**Concrete quality at different heating regimens (°C)**		
Concrete quality	**26–400**	**400–600**	**600–800**
Control-OPC	Medium	Poor	Very poor
AASA15	Medium	Poor	Very poor
AASA20	Medium	Poor	Very poor
SF6	Medium	Poor	Very poor
GGBS20	Medium	Poor	Very poor
POFA15	Medium	Poor	Very poor
AASA20 SF6	Medium	Poor	Very poor
AASA20 GGBS20	Medium	Poor	Very poor
AASA20 POFA15	Medium	Poor	Very poor

Table 4. The effect of elevated temperatures on types of MBB concrete specimens.

Mix description (%)	**Reduction of the UPV values at different heating regimens (°C)**		
	26–400	**400–600**	**600–800**
Control-OPC	3173	2397	1986
AASA15	3189	2364	1886
AASA20	3113	2224	1832
SF6	3092	2287	1829
GGBS20	3188	2332	1963
POFA15	3151	2352	1942
AASA20 SF6	3024	2218	1783
AASA20 GGBS20	3082	2270	1854
AASA20 POFA15	3119	2243	1887

Table 5. Reduction of the UPV relative to the original weight of the BBB and TBB mixtures.

http://dx.doi.org/10.5772/64415

3.5. Surface observations of concrete specimens

A thorough visual inspection was performed to evaluate the visible signs of cracking and spalling on the surface of the specimens after being subjected to elevated temperatures. The surface cracks began to appear after the specimens were subjected to elevated temperatures higher than 400 °C and continued to grow until the final rise in temperature up to 800 °C. There was no visible cracking or spalling for concrete specimens in the 26–400 °C temperature range, as shown in **Figure 12** (**a** and **b**). When the temperature was increased to approximately 600 °C, **Figure 12 (c)**, a network of visible fine surface cracks began to appear extensively and become even more pronounced at 800 °C (see **Figure 12 (d)**). In addition, the presence of PP fibres, which were used in all of the concrete mixtures, reduced or eliminated the risk of explosive spalling in all of the MBB concrete that contained AASA, SF, GGBS and POFA. During the process of rapid temperature increase at approximately 162 °C, polypropylene fibres melt and produce escape channels for vapour. The vapour produced in the specimens due to high temperature can be released without any build-up pressure. Hence, this might be the reason for the absence of explosive spalling in the multiple-blended binder concretes with PP fibres [37]. Generally, crack formations, propagations and pattern were similar in all of the multiple-blended binder concrete control-OPC specimens and specimens containing AASA, SF, GGBS and POFA. However, there were noticeable differences in terms of sizes of cracks, including in the length, width and depth of the specimens.

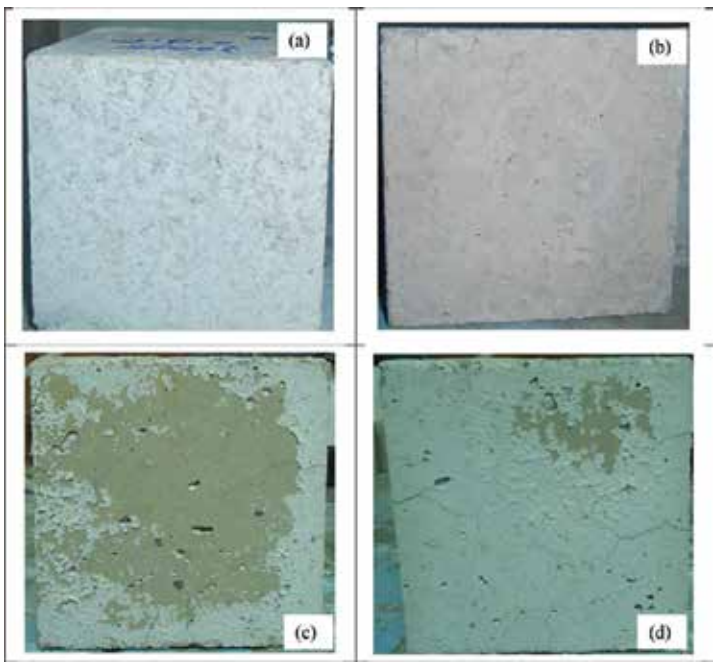

Figure 12. Typical crack patterns observed in multiple-blended binder concretes at different temperatures: (a) 26 °C, (b) 400 °C, (c) 600 °C and (d) 800 °C.

4. Conclusion

This study examines the behaviour of multiple-blended-binder concretes containing AASA and pozzolanic materials to form binary and ternary blends of cement at high temperatures, including the loss in weight, compressive strength and the reduction in ultrasonic pulse velocity as well as observations of surface characteristics of samples. The following conclusions can be drawn from the experimental results presented in this paper.

1. The mass loss decreases when the concrete is subjected to elevated temperature. That is, the mass losses of OPC concrete were recorded at 3.78, 5.24 and 6.46 %, and the mass losses of concrete mixtures of AASA 15 % and AASA 20 % were recorded at 3.98, 5.41 and 6.84 % and 4.1, 5.82 and 7.06% at 400, 600 and 800 °C, respectively. The mass loss of OPC concrete was slightly less than that of the concrete mixtures of AASA 15 % and AASA 20 % replacement levels.

2. As for the replacement levels of SF, GGBS and POFA concrete, the observations revealed a decrease in mass loss with increasing temperature. The loss in mass for the mixtures was in the range of 3.72–6.82 %. All of the ternary binder mixtures tended to show more mass loss compared with OPC concrete. The average mass loss of the concrete of ternary binder mixtures was 4.2 % at 400 °C, 5.8 % at 600 °C and 7.3 % at 800 °C.

3. The residual compressive strengths of specimens were lower than those of the control concrete for all mixtures. The performance of the residual compressive strength of binary-blended concrete mixture with 15 % AASA was observed to be better compared with the performance of the residual compressive strength of control concrete and the binary-blended concrete mixture with 20 % AASA.

4. The pozzolanic concretes containing SF6, GGBS20 and POFA15 exhibited better performance at elevated temperatures than did the control-OPC concrete. The concrete mixture containing SF performed poorly compared with the concrete mixtures containing GGBS and POFA.

5. Based on the experimental results obtained from the ternary mixtures with AASA and pozzolanic materials, the relative compressive strength of concrete exhibited a significant decrease after the specimens were subjected to elevated temperature between 400 and 800 °C.

6. The heated binary and ternary-blended-binder concrete specimens showed decreased UPV values with increasing temperature. UPV values were reduced considerably for concrete specimens that were subjected to temperatures between 400 and 800 °C, which indicates that the physical state of the concrete specimens deteriorated rapidly when the temperature was raised above 400 °C.

7. At high temperatures, the quality of the MBB concretes that contained AASA, SF, GGBS and POFA degraded from excellent to good or medium quality, from medium- to poor-quality concrete and from poor quality to inferior (very poor) quality, respectively, because the quality of concrete depends on the compressive strength.

http://dx.doi.org/10.5772/64415

8. A visual inspection of the surface of the specimens that were subjected to high temperatures in the range of 26–400 °C revealed no visible cracking or spalling on these specimens. However, at 600 °C, visible networks of fine surface cracks were observed on some of the specimens. When the temperature was raised to 800 °C, all of the specimens showed visible spalling and cracking. However, the use of PP fibres reduced or eliminated the risk of explosive spalling and cracking for all specimens of multiple-blended-binder concrete.

Acknowledgements

The authors would like to acknowledge the financial support from Universiti Kebangsaan Malaysia through grants AP-2015-011 and DIP-2014-019.

Author details

Haider M. Owaid[1,2], Roszilah Hamid[2*] and Mohd Raihan Taha[2]

*Address all correspondence to: roszilah@ukm.edu.my

1 Department of Civil Engineering, Faculty of Engineering, University of Babylon, Babil, Iraq

2 Department of Civil and Structural Engineering, Faculty of Engineering and Built Environment, Universiti Kebangsaan Malaysia, Bangi, Selangor Darul Ehsan, Malaysia

References

[1] Poon CS, Azhar S, Anson M, Wong YU. Comparison of the strength and durability performance of normal-and high-strength pozzolanic concretes at elevated temperatures. Cement and Concrete Research. 2001;31(9):1291–1300.

[2] Poon CS, Azhar S, Anson M, Wong YU. Performance of metakaolin concrete at elevated temperatures. Cement and Concrete Composites. 2003;25:83–89.

[3] Phan LT, Carino NJ. Review of mechanical properties of HSC at elevated temperatures. Journal of Materials in Civil Engineering. 1998;10(1):58–64.

[4] Morsy MS, Shebl SS. Effect of silica fume and metakaolin pozzolana on the performance of blended cement pastes against fire. Ceramics Silikáty. 2007;51(1):40–44.

[5] Behnood A, Ziari H. Effects of silica fume addition and water to cement ratio on the properties of high-strength concrete after exposure to high temperatures.Cement and Concrete Composites. 2008;30:106–112.

[6] Phan LT, Lawson JR, Davis FL. Effects of elevated temperature exposure on heating characteristics, spalling and residual properties of high performance concrete. Materials and Structural. 2001;34(236):83–91

[7] Arioz O. Effects of elevated temperatures on properties of concrete. Fire Safety Journal. 2007;42(8):516–522.

[8] Ghandehari M, Ali B, Mostafa K. Residual mechanical properties of high strength concretes after exposure to elevated temperatures. Journal of Materials in Civil Engineering. 2010;20:59–64.

[9] Mohammad I, Mohamed IE, Muhammad B. Influence of elevated temperatures on physical and compressive strength properties of concrete containing palm oil fuel ash. Construction and Building Materials. 2011;25:2358–2364.

[10] Demirel B, Kelestemur O. Effect of elevated temperature on the mechanical properties of concrete produced with finely ground pumice and silica fume. Fire Safety Journal. 2010;45:385–391.

[11] Morsy MM, Shebl SS, Rashad AM. Effect of fire on microstructure and mechanical properties of blended cement pastes containing metakaolin and silica fume. Asian Journal of Civil Engineering (Building and Housing). 2008;9(2):93–105.

[12] Rahel KI, Hamid R, Taha MR. Fire resistance of high-volume fly ash mortars with nanosilica addition. Construction and Building Materials. 2012;36:779–786.

[13] Buchanan A. Structural Design for Fire Safety. UK: Wiley Chichester; 2002.

[14] Caldarone M. High-Strength Concrete: A Practical Guide. London: Taylor & Francis Group; 2008.

[15] Owaid HM, Hamid R, Taha MR. Influence of thermally activated alum sludge ash on the engineering properties of multiple-blended binders concretes. Construction and Building Materials. 2014;61(30):216–229.

[16] ASTM C150. Standard Specification for Portland Cement. Annual Book of ASTM Standard. Vol. 04.02. Philadelphia: America Society for Testing and Materials; 1992.

[17] ASTM C192/C 192M. Standard Practice for Making and Curing Concrete Test Specimens in the Laboratory. West Conshohocken, PA: ASTM International; 2002.

[18] Culfik MS, Ozturan T. Mechanical properties of normal and high strength concretes subjected to high temperatures and using image analysis to detect bond deteriorations. Construction and Building Materials. 2010;24:1486–1493.

[19] British Standard Institution European Standard. BS EN 12390-3. Testing Hardened Concrete. Compressive Strength of Test Specimens. London: BSI; 2002.

[20] British Standard Institution. BS 1881–203. Testing Hardened Concrete. Recommendations for Measurement of Velocity of Ultrasonic Pulses in Concrete. London: British Standards Institution (BSI); 1986.

[21] Janotka I, Nurnbergerova T. Effect of temperature on structural quality of the cement paste and high-strength concrete with silica fume. Nuclear Engineering and Design. 2005;235:2019–2032.

[22] Hanaa F, Albert N, Sébastien R. Self-consolidating concrete subjected to high temperature: Mechanical and physicochemical properties. Cement and Concrete Research. 2009;39(12):1230–1238.

[23] Uysal M, Yilmaz K, Ipek M.Properties and behavior of self-compacting concrete produced with GBFS and FA additives subjected to high temperatures. Construction and Building Materials. 2012;28:321–326.

[24] Chan SYN, Peng GF, Anson M. Residual strength and pore structure of high-strength concrete and normal-strength concrete after exposure to high temperatures.Cement and Concrete Composites. 1999;21(1):23–27.

[25] Ye G, Liu X, De Schutter G, Taerwe L, Vandevelde P. Phase distribution and microstructural changes of SCC at elevated temperatures. Cement and Concrete Research. 2007;37:978–987.

[26] Peng G, Huang Z. Change in microstructure of hardened cement paste subjected to elevated temperatures. Construction and Building Materials. 2008;22:593–599.

[27] Mucteba U. Self-compacting concrete incorporating filler additives: Performance at high temperatures. Construction and Building Materials. 2012;26:701–706.

[28] Zhang B, Bicanic N. Residual fracture toughness of normal-and high-strength gravel concrete after heating to 600°C. Materials Journal. 2002;99(3):217–226.

[29] Tung CL, Chi SP, Shi CK. Influence of recycled glass content and curing conditions on the properties of self-compacting concrete after exposure to elevated temperatures. Cement and Concrete Composites. 2012;34:265–272.

[30] Hanaa F, Remond S,Noumowe A, Cousture A. High temperature behaviour of self-consolidating concrete: Microstructure and physicochemical properties. Cement and Concrete Research. 2010;40(3):488–496.

[31] Morsy MM. Shebl SS, Rashad AM. Effect of elevated temperature on compressive strength of blended cement mortar. Building Research Journal. 2008;56(2–3):173–185.

[32] Xiao J, König G. Study on concrete at high temperature in China – an overview. Fire Safety Journal. 2004;39:89–103.

[33] Qingtao Li, Zhuguo Li, Guanglin Y. Effects of elevated temperatures on properties of concrete containing ground granulated blast furnace slag as cementitious material. Construction and Building Materials. 2012;35:687–692.

[34] Yang H, Lin Y, Hsiao C, Liu JY. Evaluating residual compressive strength of concrete at elevated temperatures using ultrasonic pulse velocity. Fire Safety Journal. 2009;44:121–130.

[35] Yuksel I, Siddique R, Ozkan O. Influence of high temperature on the properties of concretes made with industrial by-products as fine aggregate replacement. Construction and Building Materials. 2011;25:967–972.

[36] Whitehurst EA. Soniscope tests concrete structures. Journal of the American Concrete Institute. 1951;47:443–440.

[37] Chen B, Liu J. Residual strength of hybrid-fiber reinforced high strength concrete after exposure to high temperature. Cement and Concrete Research. 2004;34:1065–1069.

Section 2

High Performance Concrete Technology and Applications

Chapter 6

Energy-Efficient Technologies in Cement Grinding

Ömürden Genç

Additional information is available at the end of the chapter

http://dx.doi.org/10.5772/64427

Abstract

In this chapter an introduction of widely applied energy-efficient grinding technologies in cement grinding and description of the operating principles of the related equipments and comparisons over each other in terms of grinding efficiency, specific energy consumption, production capacity and cement quality are given. A case study performed on a typical energy-efficient Horomill® grinding technology, is explained. In this context, grinding circuit is introduced and explanations related to grinding and classification performance evaluation methodology are given. Finally, performance data related to Horomill® and high-efficiency TSV™ air classifier are presented.

Keywords: Barmac Vertical Shaft Impact Crusher (VSI), High-pressure grinding rolls, Vertical roller mills, CKP pre-grinder, Cemex® mill, Horomill®, TSV™ separator, Grinding, Classification, Energy, Cement

1. Introduction

Cement is an energy-intensive industry in which the grinding circuits use more than 60 % of the total electrical energy consumed and account for most of the manufacturing cost [1]. The requirements for the cement industry in the future are to reduce the use of energy in grinding and the emission of CO_2 from the kilns. In recent years, the production of composite cements has been increasing for reasons concerned with process economics, energy reduction, ecology (mostly reduction of CO_2 emission), conservation of resources and product quality/diversity. The most important properties of cement, such as strength and workability, are affected by its specific surface and by the fineness and width of the particle-size distribution. These can be modified to some extent by the equipment used in the grinding circuit, including its configuration and control.

Performance of grinding circuits has been improved in recent years by the development of machinery such as high-pressure grinding rolls (HPGR) (roller presses), Horomills, high-efficiency classifiers and vertical roller mills (VRM) for clinker grinding which are more energy efficient than machinery which has been in common use for many years such as tube mills. Energy-efficient equipments such as high-pressure grinding rolls, vertical roller mills, CKP pre-grinders, Cemex® mills and Horomills® are used at both finish grinding of cement and raw material-grinding stages due to higher energy consumption of conventional multi-compartment ball milling circuits. Multi-compartment ball mills can be classified as:

- Single-compartment ball mills
- Two- or three-compartment ball mills

Multi-compartment ball mills and air separators have been the main process equipments in clinker grinding circuits in the last 100 years. They are used in grinding of cement raw materials (raw meal) (i.e. limestone, clay, iron ore), cement clinker and cement additive materials (i.e. limestone, slag, pozzolan) and coal. Multi-compartment ball mills are relatively inefficient at size reduction and have high specific energy consumption (kWh/t). Typical specific energy consumption is 30 kWh/t in grinding of cement. Barmac-type crushers found application as a pre-grinder in cement grinding circuits operating with ball mills to reduce the specific energy consumption of ball mill-grinding stage [2]. An overview of technical innovations to reduce the power consumption in cement plants was given by Fujimoto [1].

In this chapter, operating principles of high-pressure grinding rolls, Horomill®, vertical roller mills, CKP pre-grinders and Cemex® mills which are widely applied in finish grinding of cement are briefly explained in addition to the advantages and disadvantages over each other.

2. Energy-efficient grinding systems

2.1. Barmac VSI crusher

The Barmac rock-on-rock crusher has a rotor that acts as a high-velocity, dry stone pump, hurling a continuous rock stream into a stone-lined crushing chamber. Broken rock about 30–50 mm in diameter enters the top of the machine from a feeder set and is accelerated in the rotor to be discharged into the crushing chamber at velocities of up to 85 m/s. Collision of high-speed rocks, with rocks falling in a separate stream or with a rock-lined wall, causes shattering. The product is typically gravel and sand-sized particles. Barmac crushers are available from 75 to 600 kW. The product-size distribution can be controlled by the rotor speed [3]. A schematic of a Barmac-type VSI crusher is given in **Figure 1** [4].

2.2. High-pressure grinding rolls (HPGR)

High-pressure grinding rolls (roller presses) are used in both raw material and cement grinding. The principle of the HPGR is shown in **Figure 2**.

http://dx.doi.org/10.5772/64427

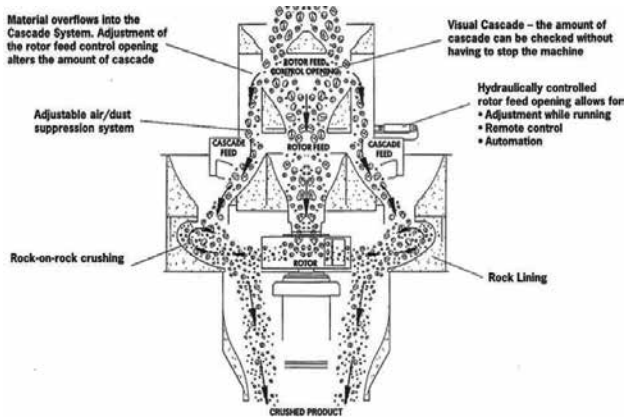

Figure 1. Barmac VSI crusher.

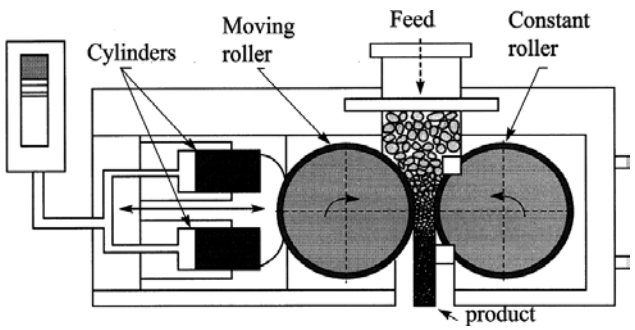

Figure 2. Principle of compressive size reduction.

The material between the rolls is submitted to a very high pressure ranging from 100 to 200 MPa. Special hard materials are used as protection against wear, for example, Ni-hard linings to protect the rollers. During the process, cracks are formed in the particle, and fine particles are generated. Material is fed into the gap between the rolls, and the crushed material leaves as a compacted cake. The energy consumption is 2.5–3.5 kWh/t and about 10 kWh/t when recycling of the material is used. The comminution efficiency of a HPGR is better than ball mills such that it consumes 30–50 % of the specific energy as compared to a ball mill. Four circuit configurations of HPGR can be used in grinding of raw materials, clinker and slag such as [5]:

1. Pre-grinding unit upstream of a ball mill
2. Hybrid grinding
3. Semifinish grinding
4. Finish grinding in closed-circuit operation

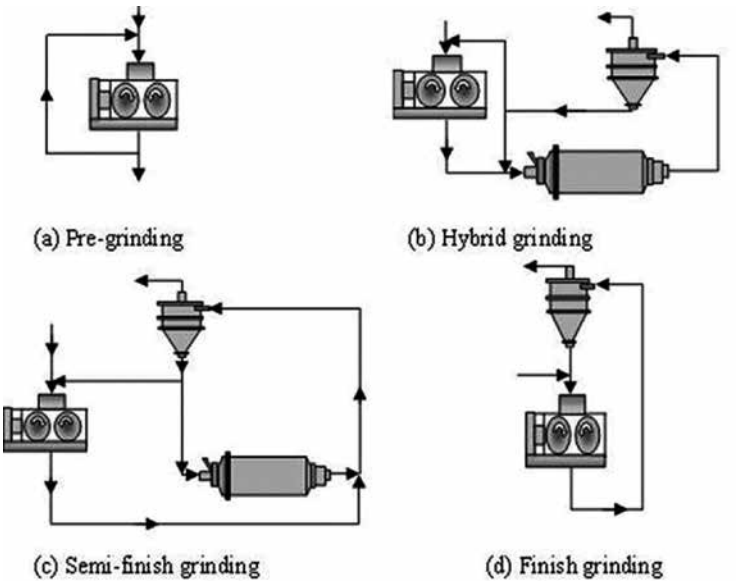

Figure 3. HPGR arrangements.

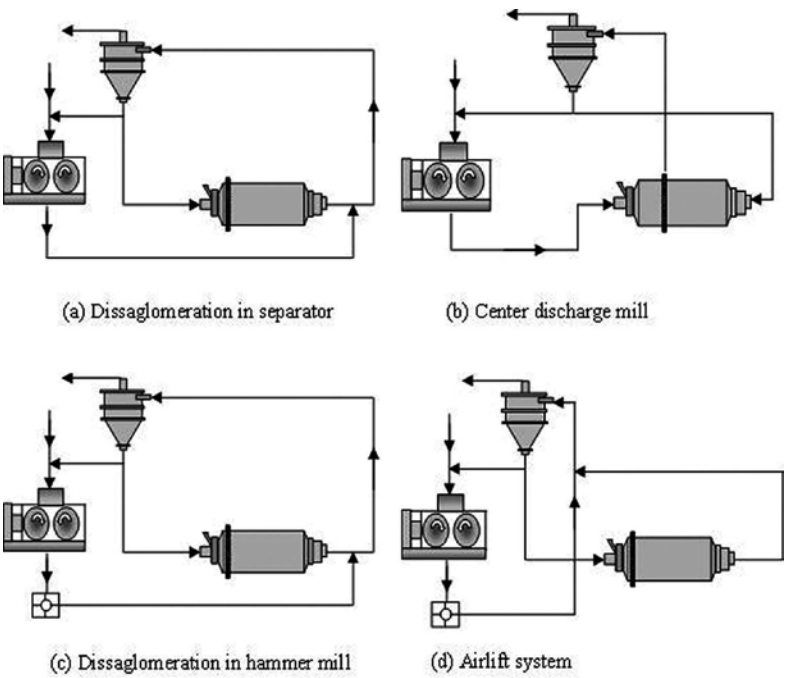

Figure 4. Semifinish-grinding options.

http://dx.doi.org/10.5772/64427

Application of HPGR in cement grinding circuits and the effects of operational and design characteristics of HPGR on grinding performance were discussed by Aydoğan [6]. HPGR arrangements and semifinish-grinding options are given in **Figures 3** and **4**.

2.3. Vertical roller mills (VRM)

Vertical roller mills have a lower specific energy consumption than tumbling mills and require less space per unit and capacity at lower investment costs. Vertical roller mills are developed to work as air-swept grinding mills. Roller mills are operated with throughput capacities of more than 300 t/h of cement raw mix (Loesche mill, Polysius® double roller mill, Pfeiffer® MPS mill). Loesche roller mill and Polysius® roller mills are widely applied in cement raw material grinding. Schematical view of a Pfeiffer MPS mill is given in **Figure 5** [7], and a view from inside of a vertical roller mill is given in **Figure 6**.

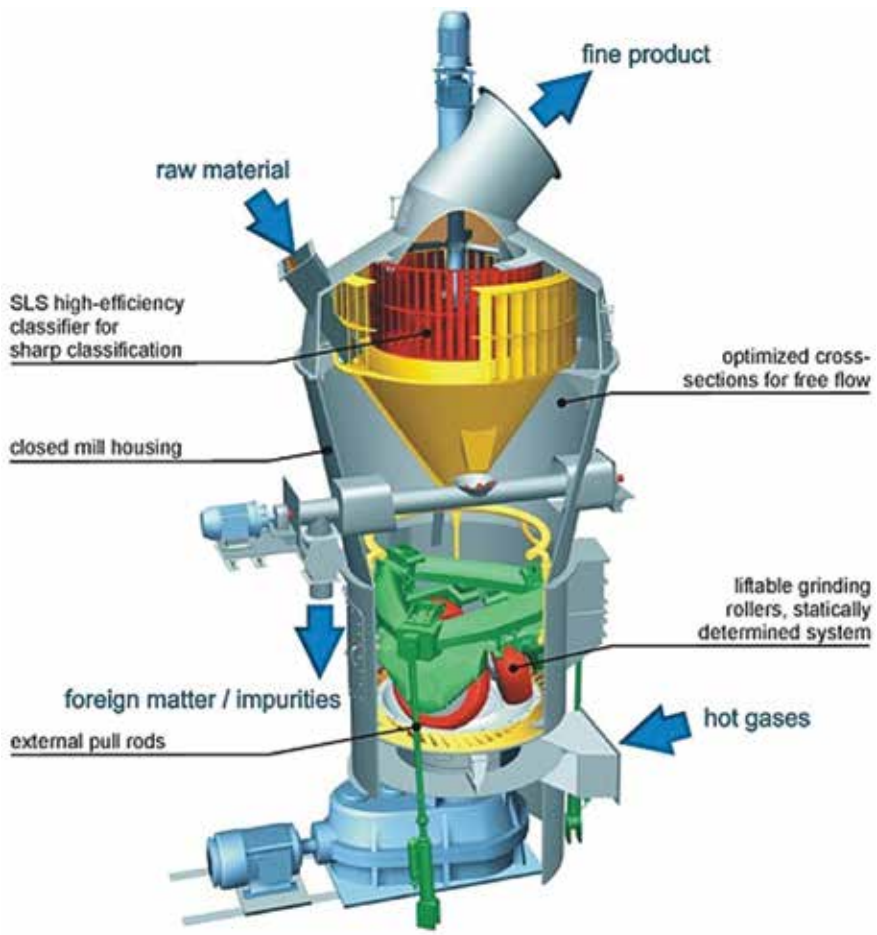

Figure 5. Schematical view of a Pfeiffer MPS mill [7].

Figure 6. A view from the interior of a vertical roller mill.

2.3.1. Loesche vertical roller mill

A cross section of a Loesche mill with a conical rotor-type classifier is shown in **Figure 7**. The pressure arrangement of the grinding rolls is hydraulic. The mill feed is introduced into the mill from above, falling centrally upon the grinding plate; then it is thrown by centrifugal force underneath the grinding rollers. A retention ring on the periphery of the grinding table forms the mill feed into a layer called the grinding bed. The ground material spills over the rim of the retention ring. Here an uprising airstream lifts the material to the rotor-type classifier located at the top of the mill casing where the coarse particles are separated from the fines. The coarse particles drop back into the centre of the grinding compartment for further size reduction, whereas the fines together with the mill air leave the mill and the separator. The separator controls the product sizes from 400 to 40 μm. The moisture of the mill feed (cement raw material) can amount to 15–18 %. The fineness of the mill product can be adjusted in the range between 94 and 70 % passing 170 mesh. Capacities up to 400 t/h of cement raw mix are recorded [8].

2.3.1.1. Cement quality

Better product quality can be achieved as compared to the ball mill product due to the better options for separate grinding. For example, in additive cement production, the blast furnace slag has to be ground to Blaine values of 5,000 cm^2/g. Water demand and setting times are similar to that of a ball mill cement under comparable conditions [9].

http://dx.doi.org/10.5772/64427

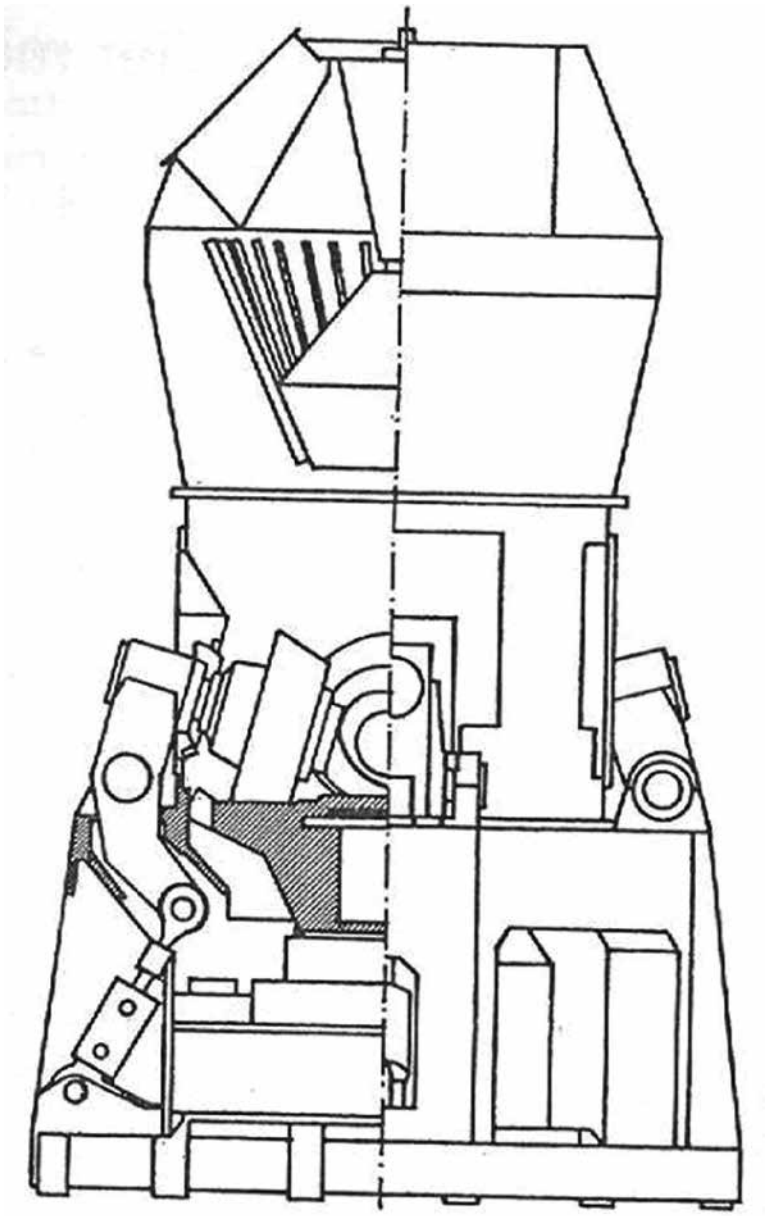

Figure 7. Loesche vertical roller mill [8].

2.3.2. Polysius® vertical roller mill (drying grinding roller mill)

A mill feed arrangement conveys the raw material to the grinding bowl. Two double rollers (representing four grinding rollers) are put in motion by the revolving grinding bowl. The double rollers are independently mounted on a common shaft; they move and adjust them-

selves to the velocity of the grinding bowl as well as to the thickness of the grinding bed. Thus, rollers are in permanent contact with the grinding bed. A hydropneumatic arrangement transfers the grinding pressure to the rollers. The disintegrated mill feed is shifted to the grinding bowl rim from where a gas stream emerging from the nozzle ring surrounding the grinding bowl carries the material upwards to the separator. The coarses precipitated in the separator gravitate centrally back to the grinding bowl, whereas the fines are collected in the electric precipitator. A raw material moisture of up to 8 % can be dried when utilizing the preheater exit gases only. If hot air from an air heater is also supplied, then a raw material moisture of up to 18 % can be handled [8]. The power requirement is 10–20 % lower than a ball mill, depending upon the grindability and moisture content of the raw material [10]. Other types of roller mills such as ball race mill (Fuller-Peters mill) and Raymond bowl-type ring mill are used in coal grinding.

2.4. CKP vertical pre-grinder

The CKP pre-grinder has been under development by Chichibu Cement and Kawasaki Heavy Industries since 1987. It has been commissioned by Technip under licence since 1993. The system is applied widely for clinker grinding and has also been used on raw material grinding. In operation, material is fed through the inlet chute onto the grinding table centre, spread out to the grinding path by the centrifugal force arising from the table rotation, before being compressed and ground by the rollers. The preground material drops down out of the periphery of the table to the bottom of the casing and is discharged by the scrapers through the discharge chute. Grinding principle of the CKP system is shown in **Figure 8**. Typical CKP application is given in **Figure 9** [11].

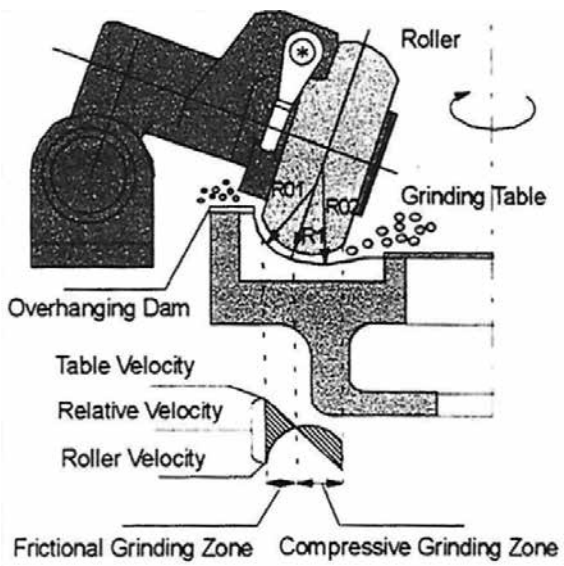

Figure 8. The grinding principle of the CKP [11].

http://dx.doi.org/10.5772/64427

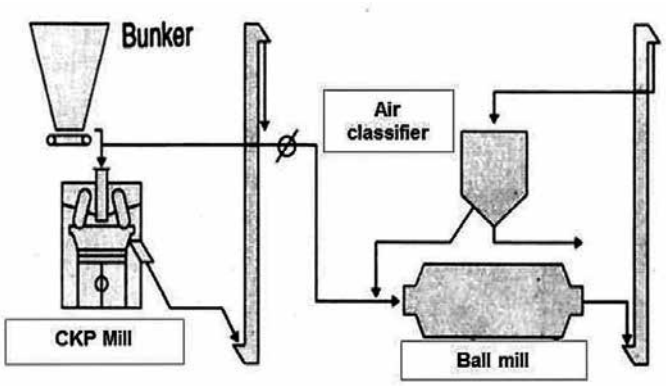

Figure 9. Typical CKP pre-grinding circuit.

Main advantages of the CKP pre-grinders are stated by Dupuis and Rhin [11] as follows:

- The grinding capacity can be increased up to 120 % for some raw materials.
- Installation is very easy due to the compact design as well as the possibility of installing the CKP outdoors.
- The energy consumption of the total grinding plant can be reduced by 20–30 % for cement clinker and 30–40 % for other raw materials.
- The overall grinding circuit efficiency and stability are improved.
- The maintenance cost of the ball mill is reduced as the lifetime of grinding media and partition grates is extended.

2.5. Cemex® ring roller mill

F.L.Smidth has developed this cement grinding system which is a fully air-swept ring roller mill with internal conveying and grit separation. This mill is a major improvement of the cement grinding systems known today which are ball mill, roller press (HPGR)/ball mill, vertical roller mill and closed-circuit roller press for finish grinding. Views of mill interior are given in **Figures 10** and **11**. Cemex® grinds the material by compressing it between a ring and a roller. The roller rotates between dam rings fitted on the sides of the grinding ring, ensuring uniform compaction and grinding. The mill rotates at a subcritical speed, and scooping devices at both ends of the ring ensure effective internal conveying of the material being ground. The material leaves the scooping devices at various points, which ensures good distribution of the material in the airstream between the air inlets and outlets. The process air enters through two inlets at either end of the mill and leaves through an outlet at either end of the mill. The air passes the falling material and carries the finer particles to Sepax® separator, in which the final classification of the product takes place. The oversize particles are returned from Sepax® to Cemex® for further grinding. Due to this unique combination of internal grit separation and air-swept material conveying to Sepax®, no external mechanical conveyor is needed, which

makes the installation very compact and simple. The airflow rate through the mill is relatively low, the only lower limitation being the need for sufficient internal grit separation and conveying of the preseparated material to the final classification in Sepax® separator [12].

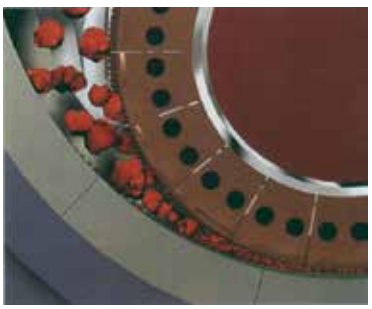

Figure 10. F.L.Smidth Cemex® mill grinding [12].

Figure 11. F.L.Smidth Cemex® mill [12].

Main purposes in designing of the ring roller mill (Cemex®) can be summarized as follows:

- To reduce the specific energy consumption of grinding
- To reduce the wear on the mill elements by applying pressures on the grinding bed
- To reduce the energy consumption of the mill fan by reducing the air consumption in the grinding process
- Simple mechanical design
- Simple and compact design to reduce the external mill load recirculation
- Simple and easy control of product quality and mill operation
- Simple and easy change of product type

Grinding tests by the F.L.Smidth company have shown that Cemex® produces cement which meets the requirements of the standard specifications while enabling substantial savings in

grinding energy consumption compared to the traditional ball mill systems. Due to the more energy-efficient grinding process, Cemex® ground cement will usually have a steeper particle-size distribution curve than corresponding ball mill cements. Consequently, when ground to the same specific surface (Blaine), Cemex® cement will have lower residues on a 32 or 45 μm sieve and tend to have a faster strength development. Grinding of cement to a lower Blaine value will reduce the specific power consumption [12]. A comparison of typical specific energy consumption of Cemex® mill with conventional multi-compartment ball mill grinding and HPGR pre-grinding closed-circuit operations is given in **Table 1**.

Operating equipments	Specific energy consumption (kWh/t)		
	Ball mill closed circuit	Ball mill + HPGR pre-grinding closed circuit	Cemex®
Ball mill	30	20.9	–
HPGR	–	4.5	–
Cemex®	–	–	18
Air classifier	0.40	0.40	0.60
Air classifier fan	2.10	2.10	3.90
Ball mill fan	0.70	0.50	0.20
Auxiliary equipment	1.00	1.30	2.00
Total (kWh/t)	34.20	29.70	24.70
Energy savings %	–	13	28.00

Table 1. Comparison of typical specific energy consumption of Cemex® mill with conventional multi-compartment ball mill grinding and HPGR pre-grinding closed-circuit operations.

Some of the advantages of Cemex® mill can be summarized as follows:

- Up to 40 % lower energy costs compared with conventional grinding installations.
- Low-maintenance cost.
- Fully air-swept mill installation.
- Internal conveying and grit separation.
- No external mechanical conveyor.
- Low noise level.
- Well-proven mill components.
- A third of the grinding pressure of the roller press and moderate grinding pressures.
- Long life of wear segments.
- Drying and cooling ability.
- Compact and simple design.

- High grinding capacity.
- Cement quality meets prevailing standards.
- Same or better strengths than cement from ball mill.

2.5.1. Cement quality

As it was stated in the literature, grinding tests have shown that Cemex® produces cement which meets the requirements of standard specifications while enabling substantial savings in grinding energy consumption compared to the traditional ball mill systems. Due to the more energy-efficient grinding process, Cemex® ground cement will usually have a steeper particle-size distribution curve than corresponding ball mill cements. Consequently, when ground to the same specific surface (Blaine), Cemex® cement will have lower residues on a 32 or 45 μm sieve and tend to have a faster strength development. When grinding to a 28-day-strength target, Cemex® cement can be ground to a lower Blaine value, which further reduces specific power consumption [12].

2.6. Horomill®

Horomill® is a ring roller mill which is a joint development by the French plant manufacturer FCB Ciment and the Italian cement producer Buzzi Unicem Group [13]. Horomill® can be used in grinding of:

- Cement raw materials (i.e. limestone, clay, iron ore, etc.)
- Cement clinker and cement additive materials (i.e. limestone, slag, pozzolan, etc.)
- Minerals and coal

2.6.1. Horomill® design and operational principle

The Horomill® (horizontal roller mill) consists of a horizontal shell equipped with a grinding track in which a roller exerts grinding force. The shell rotates faster than the critical speed which leads to centrifuging of the material. The main feature is the roller inside the shell which is rotated by the material freely on its shaft without a drive. Operating principle is schematically shown in **Figure 12**. Material is fed to the mill by gravity. There are scrapers located in the upper part of the shell. Scrapers cover the entire length of the mill and scrape off the material which falls onto the adjustable panel of the material advance system. Position of the material advance system which is sloping towards the discharge end could be changed in such a way that material could advance slower or faster, and thus it determines the number of passage of material under the roller which means the adjustment of circulating load. Grinding pressures change within a range of 500–800 bars. Concave and convex geometries of the grinding surfaces lead to angles of nip two or three times higher than in roller presses resulted in a thicker layer of ground material [14].

http://dx.doi.org/10.5772/64427

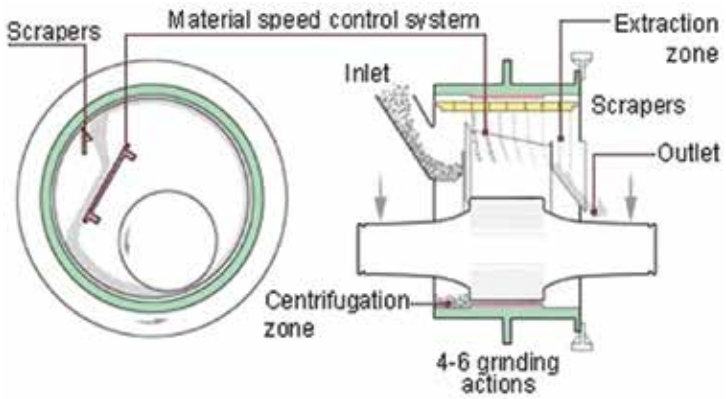

Figure 12. Operating principle of FCB Horomill®.

Horomill® mainly consists of three zones:

- Feeding
- Grinding
- Discharging

In the grinding zone, the cylindrical roller transfers the grinding power onto the material. Material bed in the mill is generated by the centrifugal effect.

As compared to hybrid systems, Horomilling resulted in lower energy consumptions with energy savings of 30–50 % for the same product quality. Noise generated is lower than conventional ball mill. They are smaller and compact units. Frictional forces in the Horomill grinding are kept at its minimum, and hence wear is due to the lack of differential speed between the material and the grinding ring. Horomill® is designed for closed-circuit finish grinding when compared with an HPGR. Bed thickness is two or three times the roll press (HPGR) [15].

It also has the flexibility of a vertical roller mill in grinding of different materials. A larger angle of nip draws the material bed into the grinding gap and reduces wear as compared to vertical roller mills. The recirculation of material within a vertical roller mill is very high. The recycle ratios are 15 or more, but it is practically impossible to measure the recycle ratios in a mill operating on the airflow principle. Material bed passes many times through the stressing gap, and it is possible to adjust the number of stressing during operation in a Horomill®. Also an internal bypass can be implemented if some of the ground material is returned from the mill outlet to the inlet. The external recycle ratio of a Horomill® connected in a closed circuit lies between four and eight and is therefore lower than with a roller press (HPGR) and vertical roller mill [14]. A comparison of the angles of nip of material is given in **Figure 13** [15]. A photograph of an industrial scale Horomill® [13] is shown in **Figure 14**.

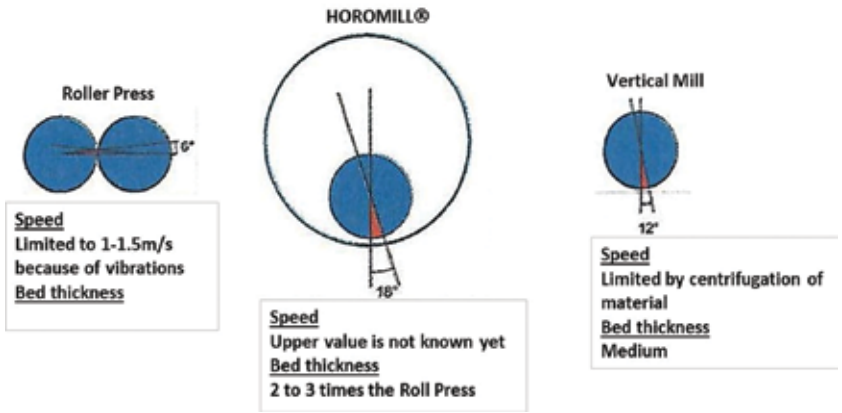

Figure 13. Comparison of the angles of nip [15].

Figure 14. An industrial scale Horomill® [13].

2.6.2. Typical Horomill® grinding application

Typical industrial scale Horomill® grinding and classification closed circuit are given in **Figure 15**. The circuit includes an elevator, a conveyor to the TSV™ classifier, a finished-product recovery filter at the TSV™ outlet and an exhauster. The rejects from the TSV™ classifier are returned by gravity to the mill inlet. The main features of the plant are as follows [15]:

- Horomill®-installed power: 600 kW at variable speed
- Horomill® diameter: 2,200 mm
- Circuit nominal rate in CP42.5R cement production: 25 t/h at 3,200 Blaine
- Nominal-circulating load: 140 t/h
- TSV™ classifier for classification

http://dx.doi.org/10.5772/64427

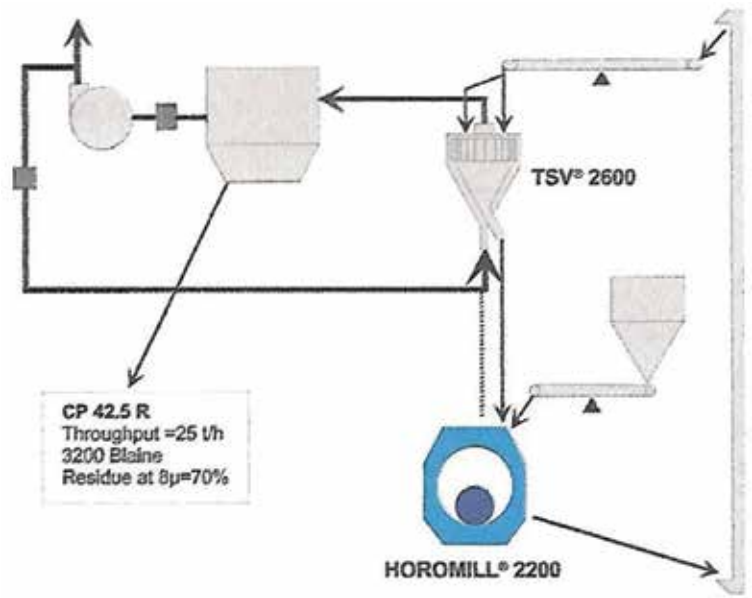

Figure 15. Flowsheet of Trino's Horomill® plant [15].

2.6.3. Typical Horomill® grinding and classification circuit (case study)

An industrial sampling survey was carried out during CPP-30R (pozzolanic portland cement) production around the Horomill® grinding and classification circuit given in **Figure 16**. Sampling points of the circuit are shown in a simplified flowsheet (**Figure 16**). Horomill® was closed circuited with a TSV™-type dynamic separator in the circuit.

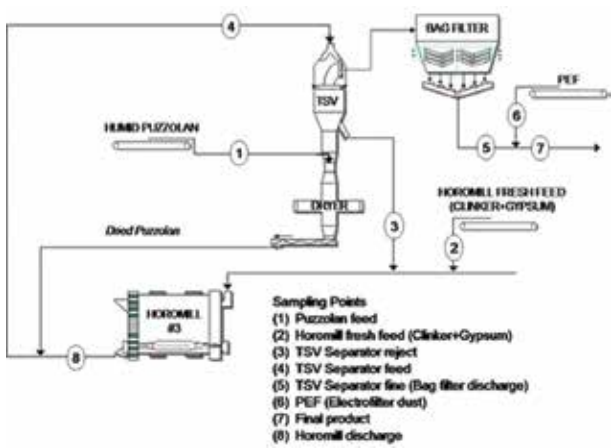

Figure 16. Simplified flowsheet of a Horomill® grinding and classification circuit.

2.6.4. Performance evaluation methodology

Prior to sampling surveys, steady-state conditions were verified by examining the variations in the values of variables in the control room. When steady-state condition was achieved in the circuit, sampling was started, and sufficient amount of samples were collected from each point as shown in **Figure 16**. Due to the physical limitations, dried pozzolan stream was not sampled. Samples collected after stopping the belt conveyors by stripping the material from a length between 3 and 5 m is shown in **Table 2**. The operation during sampling was closed to steady-state conditions. Important variables of the operation were recorded in every 5 min in the control room. Average values of the control room data were used in the mass balance calculations. Mass balance calculations were carried out using JKSimMet computer program. Design parameters of the Horomill are presented in **Table 3**.

2.6.4.1. Laboratory studies

A combination of sieving and laser-sizing techniques was used for the determination of the whole particle-size distributions for each sample. SYMPATEC® dry laser sizer was used to determine the particle-size distribution of subsieve sample of 149 μm for each sample. Size distribution of +149 μm material was determined by dry sieving using a Ro-Tap. The entire size distribution for each sample was calculated using the sieving results obtained from the top size (50.8 mm) down to 149 μm and laser results obtained for the subsieve sample of −149 μm.

Sampling points	Swept length (m)
Pozzolan feed	5.0 m
Clinker + gypsum feed	3.0 m

Table 2. Typical sample amounts taken after stopping the belt conveyors during survey.

Horomill#3®	Value
Inside diameter (m)	3.64
Roller diameter (m)	1.82
Roller/track width (m)	1.365
Nominal pressure (at cylinder) (bar)	220
Type of motor	Slip ring
Installed motor power (kW)	2500
Mill shell speed (rpm)	35.9

Table 3. Design parameters of the Horomill®.

http://dx.doi.org/10.5772/64427

2.6.4.2. Mass balance calculations

Some errors are inevitable in any sampling operation. These errors result from dynamic nature of the system, physical conditions at particular point, random errors, measurement errors and human errors. Mass balancing involves statistical adjustment of the raw data to obtain the best fit estimates of flow rates. In this context, by using the particle-size distributions and the control room data, an extensive mass-balancing study was performed around Horomill®#3 circuit. Tonnage flow rates (t/h) and particle sizes of the streams are calculated by JKSimMet mass balance software. The success of the mass balance was checked by plotting the experimental and calculated (mass-balanced) particle-size distributions as shown in **Figure 17**. These results plotted in a 45° line indicate the quality of both sampling operation and laboratory studies.

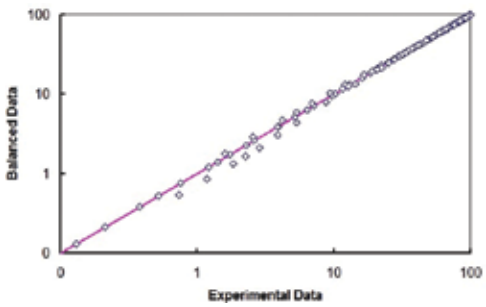

Figure 17. Comparison of mass-balanced and experimental particle-size data of each sample across the grinding circuit.

According to the result of mass balance calculations, if there had been a statistically significant difference between experimental and calculated values (scattering data), the data would have been rejected and not be used for performance evaluation studies. In this research, data obtained as a result of sampling and experimental studies were found to be in a satisfactorily good fit. Mass balance model of the circuit with the calculated tonnage flow rates (t/h) in every stream and fineness as 45 μm% residue is shown in **Figure 18**.

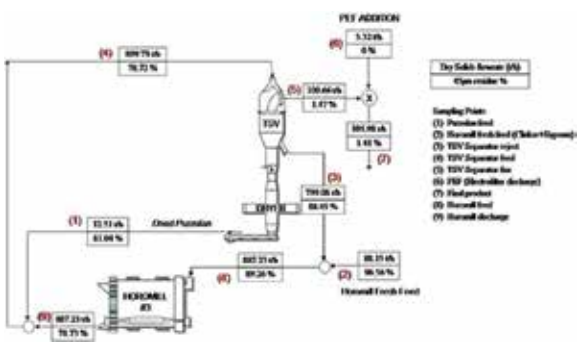

Figure 18. Calculated flow rates (t/h) and fineness after mass balancing around the circuit.

F_{80} and P_{80} particle-size values from the mass-balanced size distributions can be used to calculate the ratio of size reduction which can be given by Eq. (1):

$$S.R = \frac{F_{80}}{P_{80}} \tag{1}$$

where F_{80} is the 80 % passing size of the Horomill® feed determined as 1.06 mm and P_{80} is the 80 % passing size of the Horomill® discharge determined as 0.56 mm. It means that the ratio of size reduction is 1.88.

Using the F_{80} (13.21 mm) and P_{80} (0.024 mm) size values from the mass-balanced size distributions of the fresh feed and the TSV® fine, the ratio of the overall size reduction was calculated as 550.42 by Eq. (1):

$$S.R = \frac{F_{80}}{P_{80}} = \frac{13.21\ \text{mm}}{0.024\ \text{mm}} = 550.42$$

Circulating factor (CF) can be defined by Eq. (2)

$$\text{C.F} = \frac{\text{Mill feed}\ (\text{t/h})}{\text{Total fresh feed}\ (\text{t/h})} \tag{2}$$

$$\text{C.F} = \frac{887.23}{100.66} = 8.81$$

and recycling factor (RF) can be defined by Eq. (3)

$$\text{R.F} = \frac{\text{TSV reject}\ (\text{t/h})}{\text{TSV fine}\ (\text{t/h})} \tag{3}$$

$$\text{R.F} = \frac{799.08}{100.66} = 7.94$$

Circulating and recycling load percentages are determined as 881 and 794 %, respectively.

http://dx.doi.org/10.5772/64427

2.6.4.3. Specific energy consumption (Ecs) calculation

Horomill® motor power (2,126 kW) is the average operating mill motor power reading from the control room during the sampling survey and used in the calculation. Total fresh feed tonnage is the dry tonnage amount used in the mass balance calculations represented by the TSV fine stream tonnage flow rate which is 100.66 t/h. Thus, the specific energy consumption (Ecs) can be calculated by Eq. (4):

$$E_{CS} = \frac{\text{Mill power}\ (\text{kW})}{\text{Total fresh feed}\ (\text{t/h})} \tag{4}$$

$$E_{CS} = \frac{2126}{100.66} = 21.12\ \ kWh/t$$

When the final cement tonnage is considered which is 105.53 t/h, specific energy consumption (Ecs) is calculated by Eq. (5):

$$E_{cs} = \frac{\text{Mill power}\ (\text{kW})}{\text{Final cement}\ (\text{t/h})} \tag{5}$$

$$E_{CS} = \frac{2126}{105.53} = 20.15\ \ kWh/t$$

2.6.4.4. Tromp curve of the TSV® separator

The performance of any classifier, in terms of size separation, is represented by an efficiency (TROMP) curve. An example for a classifier is shown in **Figure 19**. It describes the proportion of a given size of solids which reports to the coarse product. Mass-balanced particle-size distributions and tonnage flow rates around the separator were used to evaluate the performance of the separator. Percentage of any fraction in the feed pass to the coarse product (%) is defined as partition coefficient and expressed by Eq. (6):

$$P = \frac{Uu_i}{Ff_i} \tag{6}$$

where U is the separator coarse tonnage (t/h), F the separator feed tonnage (t/h), u_i is the % of size fraction (i) in separator coarse and f_i is the % of size fraction (i) in separator feed.

Actual TROMP curve established for TSV® is presented in **Figure 19**.

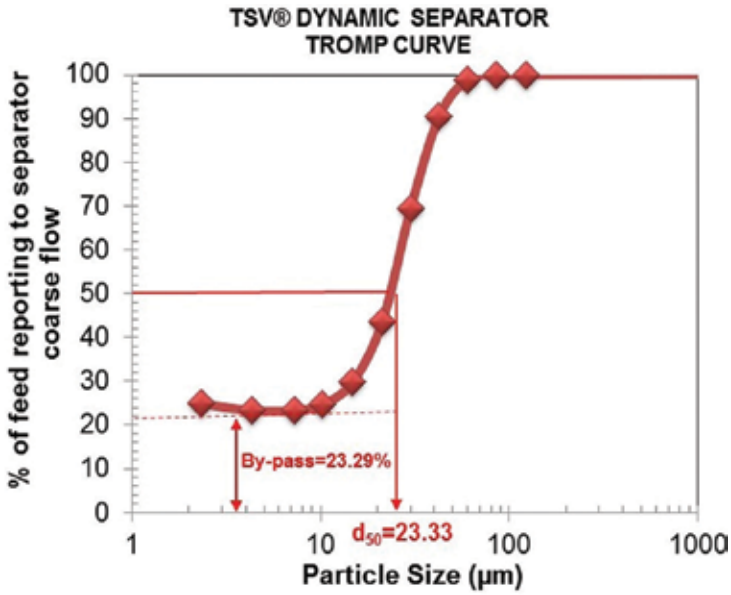

Figure 19. Actual TSV® TROMP curve.

The d_{50} size corresponds to 50 % of the feed passing to the coarse stream. It is therefore the size which has equal probability of passing to either coarse or fine streams. When this size is decreased, the fineness of the product increases. The operational parameters that affect the cut size are rotor speed and separator air velocity. Cut size for the TSV® was determined as 23.33 μm. The percentage of the lowest point on the tromp curve is referred as the bypass. It is the part of the feed which directly passes to the coarse stream (separator reject) without being classified. Bypass value is a function of the separator ventilation and separator feed tonnage. The bypass value of TSV® was 23.29 % which indicated a consistent performance for this separator. Fish-hook effect (β) is the portion of fines returning back into separator reject stream. When there is incomplete feed dispersion at the separator entry, or even within the classification zone, aggregates of fine particles may be classified as coarse particles and thus report to the coarse stream. Fish-hook amount of TSV® was 1.58 % which also indicated how effectively it is operating:

$$\text{Fish} - \text{hook} = 24.87 - 23.29 = 1.58\%$$

The sharpness of separation was defined as d_{25}/d_{75}

where d_{75} is the particle size whose 75 % is reported to the separator reject and d_{25} is the particle size whose 25 % is reported to the separator reject.

For the TSV®, parameter values determined from the TROMP curve are d_{75} as 32.36 μm and d_{25} as 10.50 μm.

The range of this parameter *k* (acuity) depends on the type of separator. This parameter can be calculated by Equation 7 as 0.32:

$$\kappa = \left[\frac{d_{25}}{d_{75}} \right] \tag{7}$$

$$\kappa = 0.32$$

Usually, for TSV®-type separator, it is between 0.55 and 0.7. When the normal range for sharpness (*k*) parameter is considered, it is found to be not in the normal range [16]. When the normal range for sharpness (*k*) parameter is considered, it was found to be not in the normal range. The imperfection of separation is defined by Equation 8, and I was calculated as 0.47:

$$I = \left[\frac{d_{75} - d_{25}}{2d_{50}} \right] \tag{8}$$

$$I = 0.47$$

The value of I indicated that separation performance is sufficiently good.

Operational parameters	**Horomill® circuit**	**Polysius® two-compartment ball mill circuit**
Production type	CPP-30R pozzolanic	CPP-30R pozzolanic
Pre-crushing stage	–	HPGR
Fresh feed (t/h)	87.95	134.88
Fresh feed (clinker + gypsum) t/h	83.18	83.48
Pozzolan %	11.80	16.52
Electrofilter dust %	5.02	–
Separator type	TSV™	SEPOL®
Recirculated load %	881	257
Specific energy consumption (kWh/t)	21.12	38.25
Specific energy consumption HPGR	–	3.1
Critical speed %	161.92	77.69
Fresh feed fineness (f80) mm	13.21	5.62
Separator fine (p80) mm	0.024	0.033
Final product + 45 μm%	1.44	10.66
Reduction ratio = f80/p80 f80 fresh feed/p80 separator fine	550.42	169.28

Table 4. Operational characteristics of Horomill® and Polysius® HPGR/Polysius® two-compartment ball mill and classification closed-circuit operations at the same cement production type.

2.6.5. Operational results from an industrial scale Horomill® grinding and HPGR/two-compartment ball mill and classification closed circuit

Typical operating conditions for the Horomill® and two-compartment ball mill grinding with HPGR pre-crushing and classification circuits are compared in **Table 4** for the same production type. As can be seen from **Table 4**, Horomill® production configuration has resulted in energy savings of 50 % as compared to HPGR/two-compartment ball milling configuration [16].

2.6.6. Comparison of different grinding technologies

Typical specific energy consumption comparison between Horomill® product and HPGR hybrid system for pozzolanic cement with a 4,200 Blaine is as follows [13]:

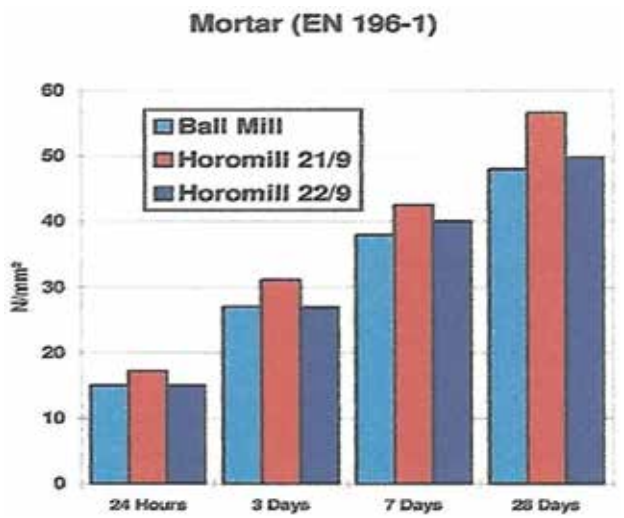

Figure 20. Compressive strength on mortar [15].

- Pozzolanic cement 4,200 Blaine:
  Horomill®, 23.1 kWh/t
  Hybrid system, 32 kWh/t
- Portland cement 3,100 Blaine:
  Horomill®, 28.3 kWh/t
  Hybrid system, 39 kWh/t

It was also reported that concrete workability from a portland cement with a 3,200 Blaine which is a Horomill® product is equal or better than an equivalent ball mill product. Mortar and concrete strengths are always higher as shown in **Figures 20** and **21**. The closed-circuit recirculation factor is noted as about six in Horomill® grinding [17]. A comparison between the grinding systems and conventional ball mills applied in cement grinding circuits is given

http://dx.doi.org/10.5772/64427

in **Table 5**. Grinding efficiencies of different systems in grinding of cement to a fineness according to a Blaine of 3,000 cm^2/g were compared in **Table 6**.

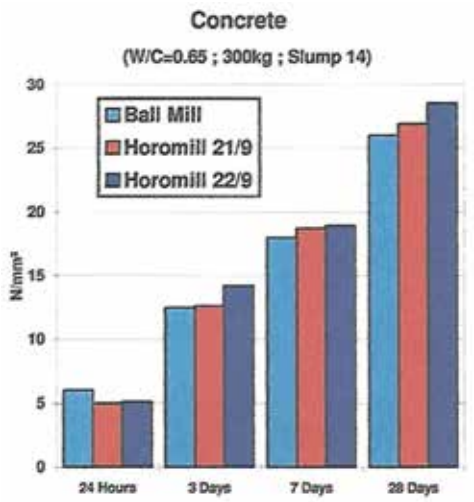

Figure 21. Compressive strength on concrete [15].

Mill type	Application	Capacity increase %	Energy savings %
Vertical roller mill	Pre-grinding	40–55	15
Vertical roller mill	Finish grinding	–	15–25
HPGR	Pre-grinding	30–40	10–15
HPGR	Finish grinding	–	35–50
Barmac VSI	Pre-grinding	30–100	20
CKP pre-grinder	Pre-grinding	60–120	25–30
Cemex®	Finish grinding	–	40
Horomill®	Finish grinding	–	30–50

Table 5. Comparison between the grinding systems and conventional ball mills applied in cement grinding circuits.

Mill type	Efficiency
Ball mill	1.00
Horizontal roller mill (Horomill®)	1.50
Roller mill	1.65
High-pressure grinding rolls (HPGR)	2.15

Table 6. Comparison of typical mill-grinding efficiencies.

The efficiency of a two-compartment ball mill is defined to be 1.0. This efficiency reflects the power consumption of the mill only and does not include any auxiliary equipment like conveyors and dust collectors nor the separator.

3. Conclusions

Comparisons between different energy-efficient grinding technologies and applications were presented for production of cement with energy savings. Industrial-scale data related to Horomill® and Polysius® HPGR/two-compartment ball mill circuit provided insights into the operational and size-reduction characteristics of Horomill® and HPGR/two-compartment ball mill-grinding process with indications that Horomill® application could produce the same type of pozzolanic portland cement at lower grinding energy requirement. The specific energy consumption figures indicated approximately 50 % grinding energy savings in Horomill® process.

Author details

Ömürden Genç

Address all correspondence to: ogenc@mu.edu.tr

Muğla Sıtkı Koçman University, Department of Mining Engineering, Muğla, Turkey

References

[1] Fujimoto S. Reducing specific power usage in cement plants, *World Cement*, 1993; 7: 25-35.

[2] Jankovic A, Valery W, Davis E. Cement grinding optimization. *Minerals Engineering*. 2004; 17: 1075-1081.

[3] Lynch AJ, *Comminution Handbook*, The Australasian Institute of Mining and Metallurgy, Spectrum 21; Australia: 2015.

[4] Barmac Thousand Series Duopactor™ Rock-on-Rock VSI Crushers, Svedala Crushing and Screening Brochure, Svedala New Zealand Ltd, New Zealand: 1995.

[5] Ghosh SN, *Cement and Concrete Science and Technology*, Volume I, Part I, ABI Books Private Ltd, First Edition, New Delhi: 1991.

[6] Aydoğan NA, *An Investigation of the Performance of High Pressure Grinding Rolls in Cement Industry*. PhD Thesis. Mining Engineering Department. University of Hacettepe; Ankara, Turkey: 2006.

[7] http://www.gebr-pfeiffer.com/en/equipment/equipment/mps-roller-mill, 2016

[8] Duda WH, *Cement-Data-Book*, Vol. 1, International Process Engineering in the Cement Industry. French & European Pubns. 3rd edition; 1985.

[9] Nobis R. Experience with grinding slag and clinker in a Loesche mill. *ZKG International*. 2001; 54 (4): 196-204.

[10] Tiggesbaumker P. Trends and developments in dry raw material and clinker grinding. *Ciments, Betons, Platres, Chaux*. 1982; No. 744-5/83: 272-284.

[11] Dupuis J, Rhin C. Increased grinding capacity at R.A.K. *World Cement.* 2003: 79-83.

[12] Cemax® ring roller mill brochure: F.L.Smidth & CO. Denmark:1-8.

[13] Brunelli G. A proven partnership. *International Cement Review*. Buzzi Unicem Group. Italy: 2001.

[14] Buzzi S, The Horomill a new mill for fine comminution. *ZKG International*. 1997; Nr.3: 127-138.

[15] Cordonnier A. A new grinding process Horomill®. 8th European Symposium on Comminution. Stockholm, Sweden: 1994.

[16] Genç Ö, Benzer AH. Horizontal Roller Mill (Horomill®) application versus Ball Milling in Finish Grinding of Cement. 6th International Comminution Symposium (Comminution 08), 2008.

[17] Buzzi S. Horomill to offer grinding advances. *International Cement Review*. 1993: 42-43.

Chapter 7

Concretes with Photocatalytic Activity

Magdalena Janus and Kamila Zając

Additional information is available at the end of the chapter

http://dx.doi.org/10.5772/64779

Abstract

This chapter is a short review about the modified concretes with photocatalytic activity. In the beginning, the photocatalysis process is explained; the authors are focused on the mechanism of organic contamination and nitrogen oxide decomposition. Next the three main methods for concretes modification are presented: the first group is when the concrete is covered by thin layer of TiO_2 materials, e.g., paints or TiO_2 suspensions. The second group is the concretes with thick layer of photoactive concrete on the top. The third group constitutes concretes modified in mass with TiO_2. The two main methods for photocatalytic activity of the modified concrete determination were shown: an air purification by a nitrogen oxide decomposition and the self-cleaning properties by dyes decomposition. Also in this chapter the mechanical properties of the modified concrete are presented. In the end, the examples of the buildings made of photocatalytic concretes are shown.

Keywords: modified concretes, photocatalysis, air purification, mechanical properties

1. Introduction

In this chapter the information about photoactive concretes are shown. For many years the researchers were interested in preparation of modified building materials with the special properties. It was found that using titanium dioxide as additive to such materials gives them self-cleaning, antibacterial and antifungal properties, moreover it was found that in some cases the mechanical properties are also improved. This chapter contain five parts. First, the photocatalysis process is described. The mechanism of hydroxyl radical production during titanium dioxide irradiation is presented. In the literature, mainly the used method could be divided into three groups: the first group is when the concrete is covered by thin layer of TiO_2 materials, e.g., paints or TiO_2 suspensions. The second group is the concretes with thick layer

of photoactive concrete on the top. The third group is the concretes with different weight percent of TiO_2 in the mass (substituted cement), then the results of photoactive tests of such materials are presented, mainly focused on the air cleaning from nitrogen oxides. Afterwards, the mechanical properties of photoactive concretes are presented. In this chapter, TiO_2 effect on hydration process of cement, TiO_2 effect on the compressive strength, TiO_2 effect on carbonation of concretes, the fire resistance of photocatalytic concrete and the influence of TiO_2 on abrasion resistance and shrinkage are presented. In the end of the chapter, the examples of building and objects built with using photoactive concretes are presented.

2. Description of photocatalysis process

The beginning of photocatalysis is considered a year of Fujishima and Honda article publication in 1972 [1]. The article presents the results of electrochemical photolysis of water at a semiconductor electrode. Although various definitions and interpretations of the term "photocatalysis" have been proposed, "photocatalysis" or "photocatalytic reaction" is defined by Ohtani [2] as a chemical reaction induced by photoabsorption of a solid material, or "photocatalyst", which remains chemically unchanged during and after the reaction. The principle of photocatalysis is often explained with an illustration like **Figure 1**. An electron (e^-) from the valence band (VB) is excited by photoirradiation to a vacant conduction band (CB). After excitation, a positive hole (h^+) appears in the VB, these electrons and positive holes take part in the reduction and oxidation reactions of compounds adsorbed on the surface of a photocatalyst. The common photocatalyst is TiO_2. Then the possible ways for concretes modification are presented.

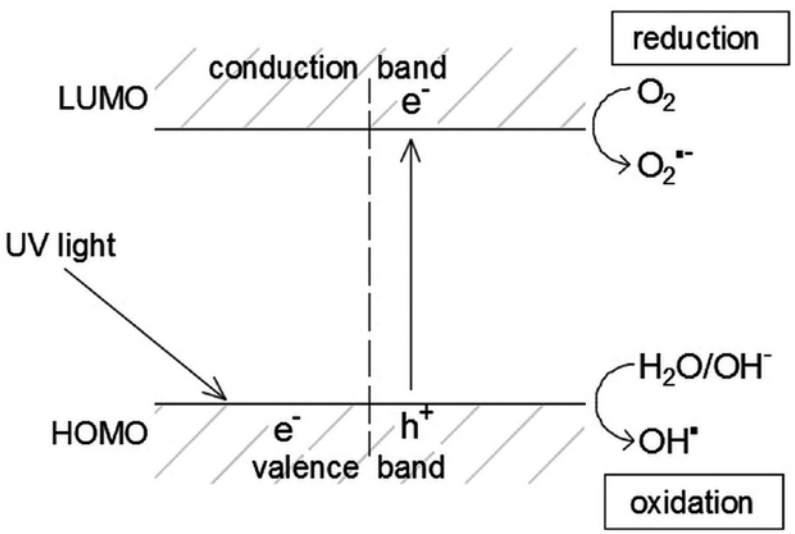

Figure 1. A schematic representation of the electronic structure of semiconducting materials.

http://dx.doi.org/10.5772/64779

The mechanism of the photocatalysis is summarized in Eqs. (1)–(12). First the production of electrons (e^-) and holes (h^+) in conduction band and valence band occurs (Eq. (1)). The photogenerated holes that escape direct recombination (Eqs. (3) and (4)) reach the surface of TiO_2 and react with surface adsorbed hydroxyl groups or water to form trapped holes (Eq. (2)). The trapped hole ($\equiv TiO^{\bullet}$) is usually described as a surface-bound or adsorbed $OH^{\bullet}$ radical $OH^{\bullet}_{ads}$. According to (Eq. (7)), $OH^{\bullet}$ generates at the surface of semiconductor and leaves the surface to bulk solution to form free $OH^{\bullet}$ $\left(OH^{\bullet}_{free}\right)$. If electron donors ($Red_{org}$) are present at the TiO_2 surface, electron transfer may occur according to Eqs. ((5), (6) and (8)). In aerated systems, oxidative species, such as $O_2^{\bullet -}$ and H_2O_2 generate from the reduction site [3]:

charge-carrier generation:

$$TiO_2 + hv \rightarrow h^+ + e^- \tag{1}$$

hole trapping:

$$h^+ + \equiv Ti^{IV}OH \rightarrow \left\{\equiv Ti^{IV}OH^{\bullet}\right\}^+ \rightarrow \equiv Ti^{IV}O^{\bullet} + H^+ \tag{2}$$

charge-carrier recombination:

$$h^+ + e^- \rightarrow heat \tag{3}$$

$$e^- + \equiv Ti^{IV}O^{\bullet} + H^+ \rightarrow \equiv Ti^{IV}OH \tag{4}$$

charge transfer at the oxidation site:

$$h^+ + Red_{org} \rightarrow Ox_{org} \tag{5}$$

$$\equiv Ti^{IV}O^{\bullet} + Red_{org} \rightarrow Ox'_{org} \tag{6}$$

$$h^+ + H_2O \rightarrow H_2O^{\bullet +} \rightarrow H^+ + OH^{\bullet} \tag{7}$$

$$OH^{\bullet} + Red_{org} \rightarrow Ox''_{org} \tag{8}$$

charge transfer at the reduction site:

$$e^- + O_{2(ads)} \rightarrow O_2^{\bullet -} \tag{9}$$

$$O_2^{\bullet -} + e^- \left(+2H^+\right) \rightarrow H_2O_2 \tag{10}$$

$$O_2^{\bullet -} + H_2O_2 \rightarrow OH^{\bullet} + OH^- + O_2 \tag{11}$$

$$H_2O_2 + h\nu \rightarrow 2OH^{\bullet} \tag{12}$$

It is necessary to say that the photocatalysis process depends on: type and concentration of photocatalysts, type of eliminated contaminations, energy and intensity of used light. To determine the best possible conditions to perform photocatalytic process, all of these aspects are essential to consider. In the case of modified concrete, to have photocatalytic activity, most of tests are focused on air purification especially nitrogen oxide reduction and self-cleaning properties are tested during dyes decomposition.

For laboratory test of modified concrete activity, the nitrogen oxides are used. Below equations showed the mechanism of photocatalytic NOx oxidation on active concrete under UV illumination [4]. First the charge-carrier generation occurred (Eq. (1)).

The adsorption of the reactants onto the photocatalyst surface takes place:

$$TiO_2 + H_2O \leftrightarrow TiO_2 - H_2O \tag{13}$$

$$TiO_2 + O_2 \leftrightarrow TiO_2 - O_2 \tag{14}$$

$$TiO_2 + NO \leftrightarrow TiO_2 - NO \tag{15}$$

$$TiO_2 + NO_2 \leftrightarrow TiO_2 - NO_2 \tag{16}$$

$OH^{\bullet}$ radicals produced according Eqs. (7) and (12) take part in the nitrogen oxide oxidation, as follows:

$$NO + OH^{\bullet} \rightarrow HNO_2 \tag{17}$$

$$HNO_2 + OH^{\bullet} \rightarrow NO_2 + H_2O \tag{18}$$

http://dx.doi.org/10.5772/64779

$$NO_2 + OH^{\bullet} \rightarrow NO_3^- + H^- \quad (19)$$

3. The methods of modified concrete preparation

The methods of concrete preparation can be divided into three main groups (**Figure 2**). The first group is when the concrete is covered by thin layer of TiO_2 materials, e.g., paints or TiO_2 suspensions (**Figure 2a**). The second group is the concretes with thick layer of photoactive concrete on the top (**Figure 2b**). The third group is the concretes with different weight percent of TiO_2 in the mass (substituted cement) (**Figure 2c**).

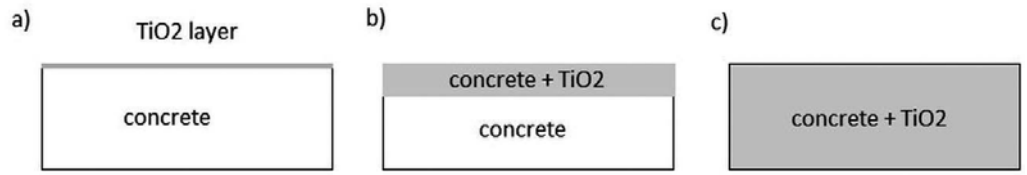

Figure 2. Scheme of possible ways for concrete modification by photocatalysts.

3.1. The first group: the concrete is covered by thin layer of TiO_2

Chen and Chu [4] covered the surface of the concrete by a different types of the slurries. The authors tested eight application methods, five of them showed over 95% static NO reduction and over 89% static automobile exhaust (toluene, trimethylbenzene and nitrogen oxide) reduction. The slurries were brushed onto the surface of a previous concrete.

CWB—commercial water-based TiO_2.

CWLS—thin slurry with low cement concentration and TiO_2 uniformly mixed together.

DIPM—a transparent liquid driveway protector (siliconate, water-based concrete sealer) and TiO_2.

TIW—water and TiO_2 uniformly mixed.

PUR—PURETI commercial water based TiO_2 applied to the surface with a special electrostatic sprayer.

Not only water is used for the slurry preparation, organic solvents are also used. Smits et al. [5] used ethanol to prepare dispersions. Photocatalyst was dispersed in ethanol (50 mg/ml) by sonication. The one layer of coating was performed by applying ethanol slurry on top of the mortar sample with the pipette. The coatings contain an equal amount of TiO_2 (24 ± 2 mg) on samples' surface, equivalent to 267 μg/cm^2. Building materials coated with TiO_2 show self-cleaning properties as all coated samples are able to remove soot.

3.2. The second group: the concretes with thick layer of photoactive concrete on the top

These concretes consist two parts, lower layer is unmodified concrete, the top part of concrete consist cement with TiO_2. The amount of TiO_2 used in the top layer is different for example Folli et al. [6] used about 40 kg/m^3 of concrete. Under ideal weather and irradiation conditions, i.e. summer months, the monthly average NO concentration in proximity of the photocatalytic area was around 22% lower than the references are [6]. Fiore et al. [7] tested the concrete covered with photocatalytic cement mortar, with thickness of 3 and 5 mm. The results of the experimental tests have shown that the concrete carbonation depth can be significantly reduced by adopting photocatalytic surface layers. The results have also indicated that the application of titanium dioxide, modifies cementinous materials on the external surface of reinforced concrete elements, improves the corrosion performance of reinforcing bars in presence of carbonation of concrete.

3.3. The third group: the concretes with different weight percent of TiO_2 in the mass (TiO_2 substituted cement)

In these examples, the titanium dioxide modified concrete in mass substitute cement. Usually the commercial titanium dioxide is used, for example: P25 (Evonic) or PC-105 (Millennium). The amounts of used photocatalysts: 0.5, 1, 2.5, 5 and 10 wt.% [8–10].

4. The results of photoactive tests

The activity of photoactive concretes is usually tested during an air purification especially NO_X removal. The self-cleaning properties are tested during dye removal from modified concretes surface. A lot of air purification tests are conducted according to method ISO 22197-1. The ISO standard employs an inert flat-bed photoreactor system designed to hold 5 × 10 cm^2 sample under illumination with UV-A light (irradiance = 1mW/cm^2). Humidified (RH = 50% at 25°C) air and dry NO at concentration 1.0 ppm with flow 3.0 dm^3/min via mass flow rate controllers (**Figure 3**). The outlet gas stream from the reactor is sampled through a valve attached to a suitable NOx detection system usually based on chemiluminescence [11].

Among the research concerning the transformation of the photocatalytic concrete materials to a larger scale the majority of the experiments refer to NOx reduction, because the compounds are currently one of the main causes of a poor quality in large cities [7–9]. Blocks of the photocatalytic concrete are analysed towards the different features: the thickness of the photocatalytic layer, types of TiO_2, content of incorporated photocatalyst. It was also observed that in a real condition the blocks with more porous surfaces showed better results for the rate of NOx degradation [12]. However, it is worth pointing out that apart from NOx the volatile organic compounds (VOCs) are the target pollutants to remove using new concrete elements. Shen et al. [13] have made the attempts towards VOCs degradation during application of photocatalytic pavement.. Even though VOC displayed a significant variability in the removal efficiency, the reduction achieved level of nearly 90%. Other efforts were taken in a case of a durability of titanium dioxide photocatalyst coating for the concrete pavement. Hassan et al.

http://dx.doi.org/10.5772/64779

[14] determined abrasion and wear resistance properties of TiO_2 coating and its effect on the coating environmental performance. The application of a special tester, which employs a scaled dynamic wheel passing back and forth over the sample, indicated on the acceptable durability and a wear resistance of the prepared photocatalytic concrete.

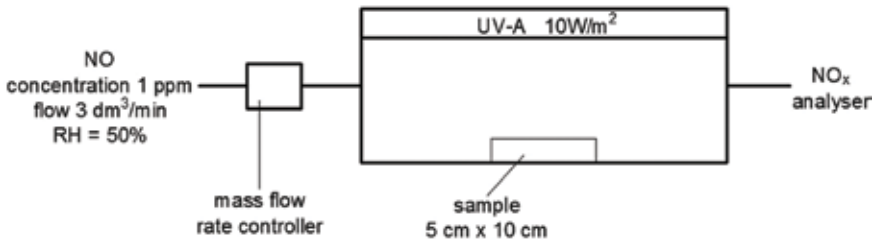

Figure 3. Photoreactor according to ISO 22197-1.

Figure 4. Separate parking lanes at the Leien of Antwerp with photocatalytic pavement blocks [15].

The scientific group Boonen et al. [15] performed the research in the laboratory and the pilot scale. As a result, the samples were active and the efficiency towards the reduction of NOx increased with a longer contact time, a lower relative humidity and a higher intensity of light. Then they convert the results obtained in the laboratory scale to a real application. 10,000 m^2 of a photocatalytic pavement blocks were constructed on the parking lanes of a main road ace in Antwerp (**Figure 4**). The pavement demonstrated a good efficiency and durability towards NOx abatement. Repeated measurements of the concrete pavement blocks confirm the efficiency after more than 5 years of using. It was observed the reduction in the efficiency due to the deposition of the nitrate on the surface. However, the original efficiency could be regained by washing the surface.

Most of the scientific works are focused on the commercial TiO_2 as additives to the concretes. Some of the researchers tried to use a modified titanium dioxide as the additive. They found that carbon and nitrogen co-modified titanium added to the cement in the amount of 5%wt increased the photocatalytic activity of the concrete more than addition of the commercial P25.

The surface of a modified building material after covering by dyes and after 25 and 100 h of a visible light irradiation in **Figure 5** is presented. The higher activity of TiO_2-N,C is explained by the presence of the carbon and the nitrogen. It is a generally claimed that the carbon doping improves the adsorption of the organic pollutants molecules on the catalyst surface. Moreover, the carbon doping can enhance the TiO_2 conductivity, as it can facilitate the charge transfer from the bulk to the surface region of TiO_2 structure, where the desired oxidation reactions take place [17].

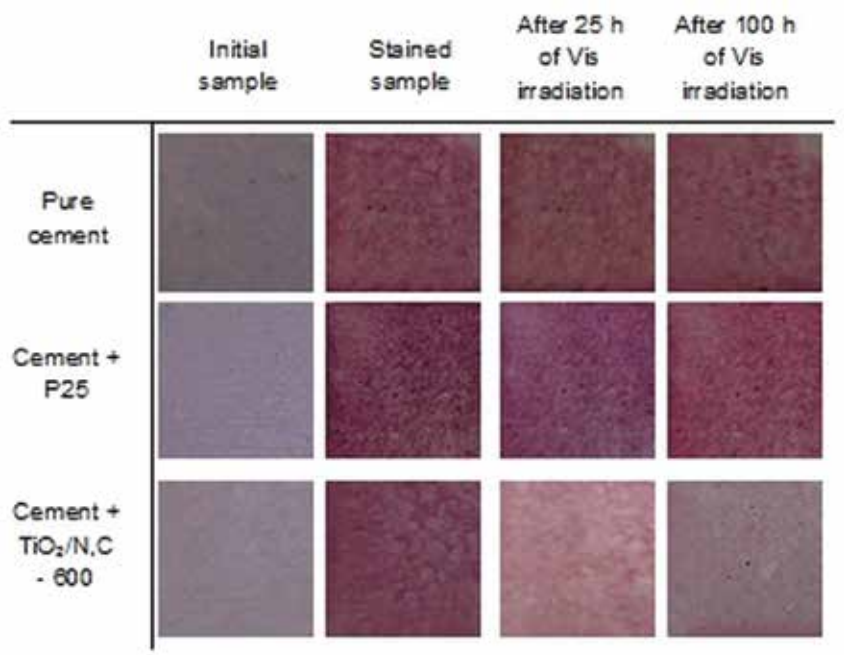

Figure 5. The photographs of cement plates stained with RR 198 (azo dye) and treated of Vis irradiation. The comparison of pure cement with cement containing TiO_2/N,C—600 (5 wt.%) and commercial P25, towards photocatalytic response.

5. The results of mechanical properties of modified concretes

Photocatalytic concretes as a new functional materials are also studied in detail towards their mechanical properties. For a real wide application, the evaluation of a specific mechanical performance is required. It is worth stressed that the addition of TiO_2 into concrete material can influence on some properties as a heat of hydration, a workability, a setting time, a chemical shrinkage, a mechanical strength, an abrasion resistance, a fire resistance, a freeze resistance, a water absorption, etc. [18].

http://dx.doi.org/10.5772/64779

5.1. TiO_2 effect on hydration process of cement

Our concerns about a nature of TiO_2 effect on the concrete should be started from the hydration process of the cement. It was proved that nano-TiO_2 acts not only as a photocatalyst but it is also a catalyst in the cement hydration reaction. Chen et al. [19] performed the detailed analyses of the hydration process in a case of the cement pastes and the mortars blended with TiO_2. The TiO_2 particles acted as a potential nucleation sites for the accumulation of the hydration products. The addition of nano-TiO_2 powders significantly accelerated the hydration rate and promoted the hydration degree of the cementitious materials at the early ages. Simultaneously, TiO_2 was inert and stable during the cement hydration process. Meanwhile, the observed [20] acceleration of the hydration rate and changes of microstructrure (after loading of TiO_2 into cement the total porosity of the cement pastes decreased and the pore size distribution was altered) affected the physical and the mechanical properties of the cement-based materials.

5.2. TiO_2 effect on the compressive strength

After loading of TiO_2 into cement, it was observed that the compressive strength of the mortar was enhanced (at early ages). The initial and final setting time was shortened and more water was required to maintain a standard consistence due to the addition of the smaller nano-TiO_2 particles. The relationship between hydration process and photocatalytic cementitious material properties was also by other scientists investigated [20–22]. However, other authors [23] the changes in mechanical properties in modified cementitious materials assigned to other phenomena. Using XRD technique they analysed the orientation index of CH crystal in different cement mortars with nano-TiO_2. Test results indicated that when cement was substituted by nano-TiO_2 the strength of cement mortar at early ages increased a lot and the fluidity and strength at evening ages decreased. They claimed that the main reason for the improvement of strength is the decrease and modification of orientation index for the nucleation function, not the increasing amount of hydration products. Experimental date showed the entirely different tendency between the intensity of (0 0 1) crystal plane and that of (1 0 1) crystal plane for various samples without or with various photocatalysts. Namely, it was showed that the orientation index has an obviously effect on the strength of cement mortar.

The effect of loaded TiO_2 into cementitious materials might be considered from the point of view of mictrostructural changes as well. Lucas et al. [9] added a photocatalyst to mortars prepared with aerial lime, cement and gypsum binders to determine the way the microstuctural changes affect the properties of the modified materials. In case of cement based mortar the porosity distribution was different between the mortar without and with TiO_2. In the initial material the porosity distribution was divided in two intervals: a set of pores of larger size which ranged between 10 and 60 μm and another group between 0.02 and 1 μm. Up to 1 wt. % titania added to the cement matrix the compressive strength increased. Simultaneously, for these samples the larger pores completely disappeared remaining solely pores between 0.02 and 1 μm and the total porosity was reduced. The cement based mortar showed a mechanical strength reduction with increasing in additive content but the reduction was relatively low. It was explained by emerging a set of nanopores combined with the disappearance of the macropores. It clarified why the mechanical strength did not decrease so significantly. For the

maximum TiO_2 content (5 wt.%), the nanoporosity increased notably and even with the presence of residual micropores (1.5–2.7 μm), the mechanical strength remained stable. In general, it was concluded that the presence of low size pores, particularly in the range between 1 and 0.1 μm helps to minimize the detrimental effect of the loading of nanoadditives. Beside changes occurring during setting and hardening the microstructure of concrete and mortars evolves in time during the service life of structures [24]. Diamanti et al. [10] focused on mechanical and durability aspects of TiO_2-containing photocatalytic concrete by examining mutual influences between TiO_2 and concrete components, and their evolution with the material aging. Materials were produced by adding the commercial form of TiO_2 (P25) to concrete. In the beginning it was observed that despite the presence of nanoparticles which could play a positive filler effect, a slight decrease in a mechanical strength was observed in TiO_2-containing specimens. SEM analysis showed a slight increase in the concrete porosity and to a non-even distribution of TiO_2 particles that in some cases were present as clusters.

According to Zhao et al. [25] the compressive strength was reduced with increase of titania content in cementitious composites. A 12% compressive strength reduction was observed when 10 wt.% TiO_2 was added to the cement matrix. It was attributed to the flocculation of nano-TiO_2 particles which introduced a weak zone as flaws. In most papers is related that both, the strength and water permeability of the photocatalytic concrete are improved by adding TiO_2 nanoparticles in the cement paste up to 2.0 wt.% [26], 3.0 wt.% [27] or 4.0 wt.% [28]. Ma et al. [29] studied the effects of nano-TiO_2 (NT) on the toughness of hardened mortars. The flexural and tensile strength of cement-based materials with different TiO_2 dosage were tested. Results showed that the tensile and flexural strength increased with increasing NT content up to 3 wt.%. The appropriate amount of nanoparticles in mortars significantly improved the crystal orientation of CH between hardened cement pastes and aggregates and grain size of CH is also decreased, both of which can control the crystallization process of hydration products in an appropriate state. In addition, more compact C-S-H gels are formed under the nanometer hydration induction effect, which can significantly improve the mechanical properties of cement mortars. Using too high nanoparticles dosage, drying shrinkage distortions of mortars are enlarged, leading to more microcracks in the interface of hardened pastes and aggregates. Simultaneously, excess nano-TiO_2 is difficult to spread evenly and some internal defects would likely form in mortars.

During examination of new photocatalytic cementitious materials, the mechanical properties have been often estimated by compressive strength values. In order to present the tendency in effects, briefly, the table with results of several works was attached (**Table 1**). To obtain comparative results in each case the effect of analysis of reference material and material with the exemplary TiO_2 dosage was shown. Mostly, TiO_2 photocatalyst added in relatively low amount increased the compressive strength of cementitious materials. The mechanical properties measured in a form of the compressive strength were enhanced even 82 and 58% after 7 and 28 days of aging, respectively [27]. However, generally, the increase did not exceed the 10–12% determined at 7 days of curing or 18–23% in a case of 28 days.

Author	Exemplary TiO_2 dose (wt.%)	Age (days)	Compressive strength (MPa)	
			Reference sample	Photocatalytic sample
Nazari et al. [27]	4	7	20.6	37.6
		28	31.6	50.1
Nazari et al. [28]	3	7	16.0	27.4
		28	43.7	59.6
Noorvand et al. [46]	1.5	7	51.5	57.0
		28	64.0	76.2
Salemi et al. [26]	2	7	27.1	30.3
		28	42.1	51.7
Li et al. [47]	1	28	59.1	69.7
Behfarnia et al. [48]	1	28	35.7	28.3
Shekari et al. [35]	1.5	28	92.3	113.3

Table 1. Compressive strength of different photoactive cementitious materials.

5.3. TiO_2 effect on carbonation of concretes

The addition of TiO_2 led to a decrease in the resistance to carbonation in time. Increasing in carbonation coefficient was connected with the parallel, and analogous, decreasing in the compressive strength of tested materials. Carbonation has the primary negative consequence of inducing corrosion of an embedded steel reinforcement. It also leads to the changes in the microstructure of cement paste and in the composition in a pore solution [31]. It was showed [10] that on one side the presence of TiO_2 influenced the carbonation rate, while, on the other side, the carbonation induced modifications that have influenced the photoactivity of the materials. Self-cleaning efficiency decreased with the material aging, however, certain photoactivity was maintained, and the decreasing can be limited by increasing the initial amount of TiO_2. The similar self-cleaning reduction was observed in a several works [20, 30] and was probably due to the shielding of TiO_2 nanoparticles by the carbonate precipitates and the obstruction of the surface pores. These work indicated that testing the properties of a freshly produced photocatalytic concrete materials is not indicative of their real behaviour. The experiments carried out after a few weeks, or the months, when the carbonation alters the surface, would give the proper information about the structures built with such materials. Some contradictory date, compared to the above described results, regarding the photocatalytic cement mortars, was obtained by Rao et al. [36]. The researchers used the self-compacting mortars with the addition of nano titanium in an amorphous state and 30% replacement of the cement with the fly ashes. First of all, the family mortars with nano-TiO_2 did not show any carbonation effect (or a relatively low carbonation depths) up to 91 days of the exposure in the accelerated carbonation chamber. Generally, in their results, the compressive strength increased with an age and decreased with the nanomaterials addition ratio.

5.4. The fire resistance of photocatalytic concrete

The next clue issue is a fire resistance of the photocatalytic concrete. The normal concrete is a flameproof and reveals good resistance to the fire, though it is not considered as a refractory material. Biloxi et al. [32] examined the property of a white high performance concrete containing titanium dioxide. The concrete specimens were thermally treated at temperatures of 250, 500 and 750°C in an electrical radiant oven. The test results revealed number of significant variations in the mechanical strengths for the specimens exposed up to 250°C. However, the significant damage was observed for higher treatment temperatures, 500 and 750°C. The most important is that the similar observations were found for photocatalytic as well as for the ordinary concrete made with a similar aggregate. The effects of a damage were in the form of the microcracking. In the specimens treated up to 500°C, SEM images showed cracking of the concrete distributed s randomly along the edges. In the specimens treated up to 750°C, the microcracks were more widespread and of larger dimensions. The only effect of high temperature on photocatalytic concrete, in a contrast to the original concrete, involved loss of photocatalytic capability at 750°C due to the transformation of titanium dioxide from anatase to rutile. Salemi et al. [26] focused on the frost resistance of the concrete containing various nanoparticles. In order to determine the property, the change in compressive strength, the change in the length, the loss of a mass and increasing in a water absorption in the specimens were measured during the cycle of a freezing and the thawing. The strength loss of the concrete containing nanoparticles appeared to be much lower than that of the plain concrete. The concrete containing 2 wt.% of nano-TiO_2 showed only 11.5% the strength loss after 300 cycles of freezing and thawing, while the strength loss of the plain concrete after 300 cycles was 100%. It is worth pointing out that the contribution of nano-TiO_2 in the improvement of the mechanical properties and durability of the concrete was higher than the other particles (e.g. Al_2O_3, ZnO_2, Fe_2O_3).

5.5. Influence of TiO_2 on abrasion resistance and shrinkage

The influence of TiO_2 presence in a concrete on an abrasion resistance was studied by Li et al. [33]. The measurements were carried out after 28 days of curing in a standard moist room at the temperature 20°C. The test results indicated that the abrasion resistance of concretes containing nanoparticles was a significantly improved. The abrasion resistance of the concrete containing nano-TiO_2 in the amount of 1% by weight of a binder increased by 180% for the surface index. However, the effectiveness of TiO_2 in the enhancing abrasion resistance increased with the decrease of photocatalyst content (5 wt.% < 3 wt.% < 1 wt.%). The important observation is that the abrasion resistance of the concrete containing nanoparticles increased with the increasing the compressive strength and the relationship appeared to be a linear.

Regarding to the further mechanical properties of the concrete modified with titanium dioxide, it should be mentioned the influence of TiO_2 presence on a shrinkage, a workability and the setting time of the cementitious materials. Below was presented a general tendency of the impact. The inclusion of TiO_2 in the cementitious matrix increases the chemical shrinkage. The higher TiO_2 content resulted in a greater chemical shrinkage. It resulted from the directly relation and a proportionality to the degree of a hydration. The workability decreases with

http://dx.doi.org/10.5772/64779

increasing TiO_2 content. It is probably related to the higher surface area of TiO_2 particles that needs more water to wetting the cement particles. Similarly, as the content of photocatalyst increases as the initial and the final setting time decreases. This is explained by a rapid consumption of a free water speeded up to the bridging process of gaps and as a result, the viscosity increases and the solidification occurs earlier. There is also the possibility that due to the large surface area of photocatalyst a greater availability of nucleation sites is provided and leads to faster hydration rate and shorter setting time [18].

6. The examples of building and objects built with using photoactive concretes

In many studies, it was demonstrated that incorporation of titanium dioxide into the concrete materials is very effective solution towards degradation of a various hazardous and the toxic compounds. Therefore, its subsequent application in a real elements appeared to be a promising technology for the reduction in the environmental pollution. Among photocatalytic concrete products, it is worth to mention the pavement blocks, the titles, and the walls of the buildings. The essential benefits of photocatalytic concrete elements are that it decomposes chemicals that contribute to soiling and air pollution, keep the concrete cleaner, and a reflect much of the sun's heat, because their white colour [34]. The construction materials might be the easily available medium to distribute photocatalysts over the widest surface area possible. It involves the high efficiency of the materials and simultaneously the increase in the materials costs is limited. Considering the self-cleaning attitude of the concrete materials it should be mentioned the simultaneous occurrence of two effects: photocatalytic degradation of deposits accumulating on their surface and photo-induced superhydrophilicity. As a consequence, the washing away of a reaction product is relatively easy [16]. The scheme of photocatalytic concrete action (example of NOx degradation) was illustrated in **Figure 6** [15].

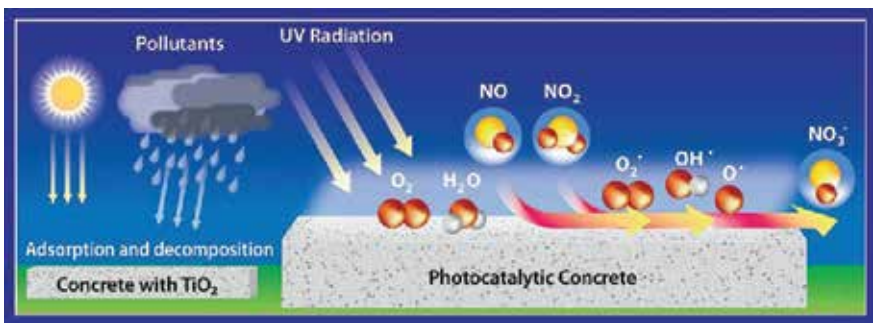

Figure 6. Scheme of photocatalytic air purifying pavement [15].

The first country where TiO_2-based cement has been marketed was Japan since the late 1990s [35, 37]. Nowadays, the white cement containing TiO_2 is also used for the construction of buildings in Europe [16]. The patent of the application of TiO_2 in pavement blocks is held by

Murata et al. (Mitsubishi Materials Corporation), as well as Cassar and Pepe (Italcementi S.p.A.) [38, 39]. Before we present the specific examples of buildings built from photocatalytic concrete, which exist in the world, we try to perform the studies focusing on the transformation from laboratory to real scale in a reference to the described materials.

The implementation of products, obtained in the laboratory, into a real scale demand taking into account a lot of parameters. On the final reduction rate of the pollutants influence the geometrical situation, the speed of the traffic, the speed and the direction of the wind, the temperature, humidity, etc. Namely, it is important that the exhaust gaseous pollutants stay in the contact with the photoactive surface during a certain period. Moreover, the real conditions require additional aspects of the new products connected with their multiple usages. In the case of a concrete pavement blocks, e.g., TiO_2 is placed in the whole thickness of wearing layer of the pavers. It means that even some abrasion takes place by the traffic, new TiO_2 will be present at the surface to maintain the photocatalytic activity. Another possibility is using a double layered concrete with addition of TiO_2: in the mass and/or as dispersion on the surface [15]. The implementation efforts of the scientific group realizations [32] were taken in Belgium. Photocatalytic cementitious materials have been applied on the side walls and the roof of the Leopold II tunnel in Brussels. The states of the object before and after photocatalytic renovation were presented in **Figure 6**. About 100 m in length of the photocatalytic materials was applied. Inside the tunnel was observed the effect on the air pollution (NOx, VOC's, CO_2, O_3, etc.). A dedicated UV lightning system was installed inside the tunnel. which could be modulated (on/off) to directly see the action of the photocatalytic walls (see **Figure 7**).

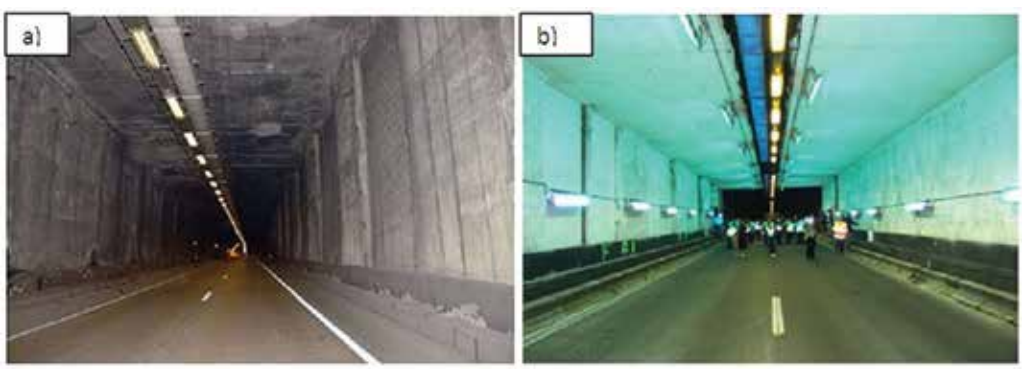

Figure 7. Inside view of test site within Leopold II tunnel in Brussels **(a)** before renovation, **(b)** after renovation with using photocatalytic walls [15].

Folli et al. [6] reported the results of a field test study concerning the use of photocatalytic paving elements in Denmark to decrease NOx pollution. The large scale studies were preceded by the experiments in the lab. The test area was in a Copenhagen central street located close to the Central Railway Station. The test area involved 200 m long × 2 (both side of the road) sidewalk pavers. Hundred meter were built from ordinary concrete blocks and 100 m from concrete blocks containing titanium dioxide as a photocatalyst. Over the entire year, the daily

http://dx.doi.org/10.5772/64779

average NO concentration was maintained to very low values (below 40 ppb) in the area paved with the concrete elements containing TiO_2. The important aspect is that seasonal variation was observed. NO conversion decreased with increasing relative humidity as a result of competition between water and NO for catalytic sites. Meanwhile, NO conversion increased with increasing temperature due to a higher diffusivity of the gaseous pollutants towards the photocatalytic surface.

The experiments concerning a full-scale demonstration of air purifying pavement were also by Ballari and Brouwers [40] presented. In Hengelo, The Netherlands, the full width of the street was provided with concrete pavement containing TiO_2 over a length of 150 m. The NOx concentration in the modified street and in control street together with weather parameters was measured. The results were directly connected with the weather conditions. Generally, the NOx concentration was 19% lower in comparison to the reference system. However, considering only afternoons or under high radiation and low relative humidity the value was 28% or 45% lower than in case of reference, respectively. The proposed solutions are promising techniques to reduce a number of air contaminants, especially at sites with a high level of pollution, such as: highly trafficked canyon streets or road tunnels.

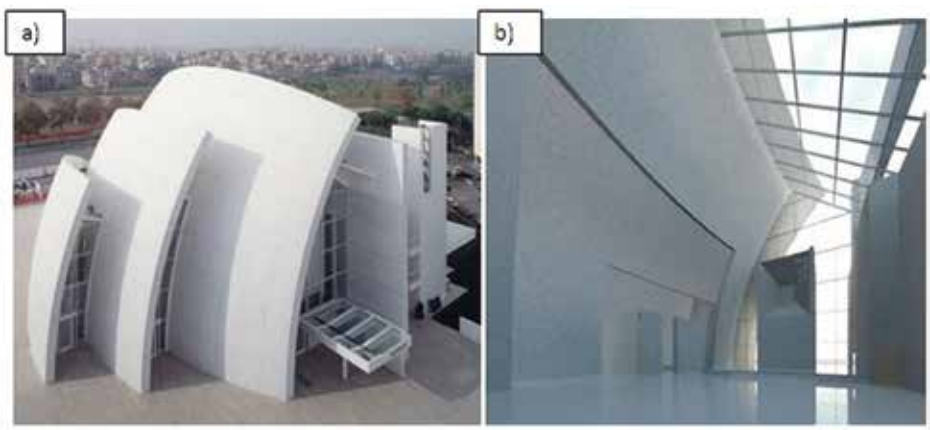

Figure 8. Dives in Misericordia Church in Rome **(a)**, zoom insight **(b)** [41].

Self-cleaning elements are mostly used in white concrete buildings. The first real project of building with the self-cleaning activity through TiO_2 in cementitious materials was started in 1996 during realization of church Dives in Misericordia in Rome, Italy. The project was completed in 2003 by Italcementi S.p.A.—an Italian cement company (architect Richard Meier). The photos of the project were shown in **Figure 8**. It was found that over a six-year monitoring period, only a slight difference was observed between the white exterior and interior walls. The next clue example of objects built from photocatalytic cementitious material is Cité de la Musique et des Beaux- Arts in Chambéry, presented in **Figure 9**, which was completed in 2000. Monitoring for approximately five years indicated that in the Chambéry City Hall the primary colour remained almost constant in different facade position (on West, North, East and South)

[42, 43]. It is impressive that according to Fujishima and Zhang [44] by 2003, self-cleaning TiO_2-based tiles had been used in over 5000 buildings in Japan. Among them the most famous is the Maru Building, located in Tokyo's main business district.

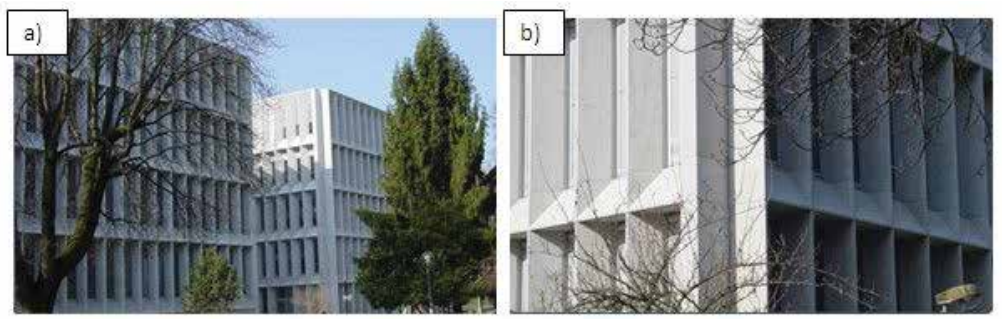

Figure 9. Cité de la Musique et des Beaux- Arts in Chambéry [45].

7. Conclusions

The presented studies show that prepared concretes have photocatalytic activity and may purified an air from for example nitrogen oxides or the volatile organic compounds. Application of titanium dioxide into cement increased the mechanical properties of obtained concretes. Despite these advantage, some disadvantages unfortunately still exist.

1. Sometimes the by-products produce during photocatalytic decomposition of contamination are more toxic than substrates, it is possible to eliminate this by strong adsorption of by-products on the surface of photocatalysts until its overall mineralization.

2. The commercial photoactive cements are mainly activated under UV light irradiation; the researchers tried to find the photocatalyst active under visible light irradiation.

3. Increasing the weight addition of photocatalyst into cement, increasing its photocatalytic activity but mainly when the addition is higher than 5 wt.% the mechanical properties of modified cement decreased.

4. A price of the commercial photoactive cements (such asTioCEM®, Górażdże, Poland, TX Active®, Italcement Group, Italy) are still from eight to ten times more expensive than pure cement.

Beside these disadvantages, the advantages of new concretes as: air purification, better mechanical properties and self-cleaning properties, makes photoactive concretes the future building materials.

Author details

Magdalena Janus* and Kamila Zając

*Address all correspondence to: mjanus@zut.edu.pl

Faculty of Civil Engineering and Architecture, West Pomeranian University of Technology, Szczecin, Poland

References

[1] Fujishima A, Honda K. Electrochemical photolysis of water at a semiconductor electrode. Nature. 1972;238:37–38. doi:10.1038/238037a0

[2] Ohtani B. Photocatalysis by inorganic solid materials: revisiting its definition, concepts, and experimental procedures. Advanced in Inorganic Chemistry. 2011;63:395–430. doi: 10.1016/B978-0-12-385904-4.00001-9

[3] Chen Y, Yang S, Wang K, Lou L. Role of primary active species and TiO_2 surface characteristic in UV-illuminated photodegradation of Acid Orange 7. Journal of Photochemistry and Photobiology. 2005;172:47–54. doi:10.1016/j.jphotochem.2004.11.006

[4] Chen M, Chu JW. NOx photocatalytic degradation on active concrete road surface—from experiment to real-scale application. Journal of Cleaner Production. 2011;19:1266–1272. doi:10.1016/j.jclepro.2011.03.001

[5] Smits M, Chan CK, Tytgat T, Craeye B, Costarramone N, Lacombe S, Lenaerts S, Photocatalytic degradation of soot deposition: self-cleaning effect on titanium dioxide coated cementitious materials. Chemical Engineering Journal. 2013;222:411–418. doi: 10.1016/j.cej.2013.02.089

[6] Folli A, Strøm M, Madsen TP, Henriksen T, Lang J, Emenius J, Klevebrant T, Nilsson Å. Field study of air purifying paving elements containing TiO_2. Atmospheric Environment. 2015;107:44–51. doi:10.1016/j.atomsenv.2015.02.025

[7] Fiore A, Marano GC, Monaco P, Morbi A. Preliminary experimental study on the effects of surface-applied photocatalytic products on the durability of reinforced concreto. Construction and Building Materials. 2013;48:137–143. doi:10.1016/j.conbuildmat.2013.06.058

[8] Aissa AH, Puzenat E, Plassais A, Herrmann JM, Haehnel C, Guillard C. Characterization and photocatalytic performance in air of cementitious materials containing TiO_2. Case study of formaldehyde removal. Applied Catalysis B: Environment. 2011;107:1–8. doi:10.1016/j.apcatb.2011.06.012

[9] Lucas SS, Ferreira VM, Barroso de Aguiar JL. Incorporation of titanium dioxide nanoparticles in mortars—influence of microsturcture in the hardened state properties and photocatalytic activity. Cement Concrete Research. 2013;43:112–120. doi:10.1016/j.cemconres.2012.09.007

[10] Diamanti MV, Lollini F, Pedeferri MP, Bertolini L. Mutual interactions between carbonation and titanium dioxide photoactivity in concrete. Building and Environment. 2013;62:174–181. doi:10.1016/j.buildenv.2013.01.023

[11] Mills A, Elouali S. The nitric oxide ISO photocatalytic reactor system: measurement of NOx removal activity and capacity. Journal of Photochemistry and Photobiology A: Chemistry. 2015;305:29–36. doi:10.016/j.photochem.2015.03.002

[12] Staub de Melo JV, Trichês G, Gleize PJP, Villena J. Development and evaluation of the efficiency of photocatalytic pavement blocks in the laboratory and after one year in the field. Construction and Building Materials. 2012;37:310–319. doi:10.1016/j.conbuildmat.2012.07.073

[13] Shen S, Burton M, Jobson B, Haselbach L. Pervious concrete with titanium dioxide as a photocatalyst compound for greener urban road environment. Construction and Building Materials. 2012;35:874–883. doi:10.1016/j.conbuildmat.2012.04.097

[14] Hassan MM, Dylla H, Mohammad LN, Rupnow T. Evaluation of the durability of titanium dioxide photocatalyst coating for concrete pavement. Construction and Building Materials. 2010;24:1456–1461. doi:10.1016/j.conbuildmat.2010.01.009

[15] Boonen E, Beeldens A. Photocatalytic Road: from lab tests to real scale applications. European Transport Research Review. 2013;5:79–89. doi:10.1007/s12544-012-0085-6

[16] Spasiano D, Marotta R, Malato S, Fernandez-Ibañez P, Di Somma I. Solar photocatalysis: materials, reactors, some commercial, and pre-industrialized applications. A comprehensive approach. Applied Catalysis B: Environmental. 2015;170–171:90–123. doi:10.1016/j.apcatb.2014.12.050

[17] Janus M, Zatorska J, Czyżewski A, Bubacz K, Kusiak-Nejman E, Morawski A. Self-cleaning properties of cement plates loaded with N,C-modified TiO_2 photocatalysts. Applied Surface Science. 2015;330:200–206. doi:10.1016/j.apsusc.2014.12.113

[18] Rashad AM. A synopsis about the effect of nano—titanium dioxide on some properties of cementitious materials—a short guide for civil engineer. Reviews on Advanced Materials Science. 2015;40:72–88.

[19] Chen J, Kou SC, Poon CS. Hydration and properties of nano-TiO_2 blended cement composites. Cement and Concrete Composites. 2012;34:642–649. doi:10.1016/j.cemconcomp.2012. 02.009

[20] Lackhoff M, Prieto X, Nestle N, Dehn F, Niessner R. Photocatalytic activity of semiconductor-modified cement—influence of semiconductor type and cement ageing.

Applied Catalysis B: Environmental. 2003;10:205–216. doi:10.1016/S0926-3373(02)00303-X

[21] Senff L, Tobaldi DM, Lemes-Rachadel P, Labrincha JA, Hotza D. The influence of TiO_2 and ZnO powder mixtures on photocatalytic activity and rheological behavior of cement pastes. Construction and Building Materials. 2014;64:191–200. doi:10.1016/j.conbuildmat.2014. 04.121

[22] Sugrañez R, Álvarez JI, Cruz M, Mármol I, Morales J, Vila J, Sánchez L. Enhanced photocatalytic degradation of NOx gases by regulating the microstructure of mortar cement modified with titanium dioxide. Building and Environment. 2013;69:55–63. doi: 10.1016/j.buildenv.2013.07.014

[23] Meng T, Yu Y, Qian X, Zhan S, Qian K. Effect of nano—TiO_2 on the mechanical properties of cement mortar. Construction and Building Materials. 2012;29:241–245. doi:10.1016/j. conbuidmat.2011.10.047

[24] Bertolini L. Steel corrosion and service life of reinforced concrete structures. Structure and Infrastructure Engineering. 2008;4:123–137. doi:10.1080/15732470601155490

[25] Zhao A, Yang J, Yang EH. Self-cleaning engineered cementitious composites. Cement and Concrete Composites. 2015;64:74–83. doi:10.1016/j.cemconcomp.2015.09.007

[26] Salemi N, Behfarnia K, Zaree SA. Effect of nanoparticles on frost durability of concrete. Asian Journal of Civil Engineering. 2014;15:411–420.

[27] Nazari A, Riahi S. TiO_2 nanoparticles effects on physical, thermal and mechanical properties of self-compacting concrete with ground granulated blast furnace slag as binder. Energy and Buildings. 2011;43:995–1002. doi:10.1016/j.enbuild.2010.12.025

[28] Nazari A, Riahi S. The effect of TiO_2 nanoparticles on water permeability and thermal and mechanical properties of high strength self-compacting concrete. Materials Science and Engineering A: Structure. 2010;528:756–763. doi:10.1016/j.msea.2010.09.074

[29] Ma B, Li H, Mei J, Li X, Chen F. Effects of nano-TiO_2 on the toughness and durability of cement-based material. Advances in Materials Science and Engineering. 2015;2015:10 p. doi:10.1155/2015/583106

[30] Chen J, Poon CS. Photocatalytic construction and building materials: from fundamentals to applications. Building and Environment. 2009;44:1899–1906. doi:10.1016/j.builenv. 2009.01.002

[31] Bertolini L, Elsener B, Pedeferri P, Polder RB. Corrosion of steel in concrete: prevention, diagnosis, repair. Weinheim:Wiley-VCH;2004

[32] Biloxi L, Di Luzio G, Labuz JF. Mechanical properties of photocatalytic white concrete subjected to high temperatures. Cement and Concrete Composites. 2013;39:73–81. doi: 10.1016/j.cemconcomp.2013.03.016

[33] Li H, Zhang MH, Ou JP. Abrasion resistance of concrete containing nano-particles for pavement. Wear. 2006;260:1262–1266. doi:10.1016/j.wear.2005.08.006

[34] Puzenat E. Photocatalytic self-cleaning materials: principles and impact on atmosphere. The European Physical Journal Conferences. 2009;1:69–74. doi:10.1140/epiconf/e2009-00911-2

[35] Fujishima A, Zhang X, Tryk DA. TiO_2 photocatalysis and related surface phenomena. Surface Science Reports. 2008;63:515–582. doi:10.1016/j.surfrep.2008.10.001

[36] Rao S, Silva P, de Brito J. Experimental study of the mechanical properties and durability of self-compacting mortars with nano materials (SiO_2 and TiO_2). Construction and Building Materials. 2015;96:508–517. doi:10.1016/j.conbuildmat.2015.08.049

[37] Guo S, Wu ZB, Zhao WR. TiO_2—based building materials: above and beyond traditional applications. Chinese Science Bulletin. 2009;54:1137–1142. doi:10.1007/s11434-009-0063-0

[38] Murata Y, Tawara H, Obata H, Murata K. NO-cleaning paving block. EP-patent 0786283A1, Mitsubishi Materials Corporation, Japan, 1997.

[39] Cassar L, Pepe C. Paving tile comprising an hydraulic binder and photocatalyst particles. EP-patent 1600430A1, Italcementi S.p.A., Italy, 1997

[40] Ballari MM, Brouwers HJH. Full scale demonstration of air-purifying pavement. Journal of Hazardous Materials. 2013;254–255:406–414. doi:10.1016/j.hazmat.2013.02.012

[41] Lea-Catherine Szacka. Panorama Living Italian Style [Internet]. 2011. Available from: http://www.panoramitalia.com/en/lifestyle/design-architecture/modern-italian-architecture/561/ [Accessed: 20.04.2016]

[42] Cassar L, Pepe C, Tognon G, Guerrini GL, Amadelli R. White cement for architectural concrete, possessing photocatalytic properties. In: Proceeding 11th International Congress on the Chemistry of Cement, The Cement and Concrete Institute of South Africa, Durban, 2003;4:2012–2021

[43] Guerrini GL, Plassais A, Pepe C, Cassar L. Use of photocatalytic cementitious materials for self-cleaning applications. In: RILEM International Symposium on Photocatalysis Environment and Construction Materials, Florence, Italy, 2007;55:219–226

[44] Fujishima A, Zhang X. Titanium dioxide photocatalysis: present situation and future approaches. Comptes Rendus Chimie. 2006;9:750–760. doi:10.1016/j.crci.2005.02.055

[45] IDBAT Prefabrication. Available from: http://www.idbat.com/#Realisations/Education-et-Formation [Accessed: 250.04.2016]

[46] Noorvand H, Ali AAA, Demiboga R, Farzadnia N, Noorvand H, Incorporation of nano TiO_2 in black rice husk ash mortars. Constr Build Mater. 2013;47:1350–1361. DOI: 10.1016/j.conbuildmat.2013.06.066

http://dx.doi.org/10.5772/64779

[47] Behfarnia K, Keivan A, Keivan A. The effects of TiO_2 and ZnO nanoparticles on physical and mechanical properties of normal concrete. Asian J Civil Eng. 2013;14:517–531.

[48] Shekari AH, Razzaghi MS. Influence of nano particles on durability and mechanical properties of high performance concrete. Procedia Engineering. 2011;14:3036–3041. DOI:10.1016/j.proeng.2011.07.382

Chapter 8

High-Performance Alkali-Activated Cement Concretes for Marine Engineering Applications

Pavel V. Krivenko, Hai Lin Cao, Lu Qian Weng and Oleg N. Petropavlovskii

Additional information is available at the end of the chapter

http://dx.doi.org/10.5772/64525

Abstract

The contribution covers results of studies on the alkali-activated cement concretes intended for marine engineering applications. Such properties as strength, wear, corrosion, freeze-thaw, weather resistance and many others have been studied, and the results are reported and discussed in detail. The obtained results suggested to draw a conclusion on high potential of the alkali-activated cement concretes for marine engineering applications, since in their performance properties these concretes are highly advantageous over other concretes used as marine concretes and big savings can be expected in the future due to the longer span of service life. The results are supported by long-term observations in real conditions. The above advantages are attributed to more perfect micro- and macrostructure of the alkali-activated cement stone. The authors have summarized their own experience and results collected by PhD and DSc students under their supervision dedicated to assessment of durability of these concretes, in particular, for marine engineering applications. In order to bring these advanced materials into practice of construction worldwide, two *rilem* (International Union of Laboratories and Experts in Construction Materials, Systems and Structures) committees have been founded: "Alkali-activated Materials" (2010–2013) and "Durability Testing of Alkali Activated Materials" (2013–ongoing).

Keywords: alkaline activation, cement, concrete, marine engineering

1. Introduction

Marine concretes are used for making concrete structures that are permanently or from time to time immersed in sea water. In accordance with service conditions in sea water, these marine

concretes are classified into those that work under water, above water and concretes for zones of alternate level of sea water.

The requirements for marine concrete structures vary depending upon location (zone) of service of the concrete in structures (**Table 1**) [1, 2].

Requirements for concretes	**Massive structures**						**Non-massive structures**		
	Outer zone			**Inner zone**					
	Zones relatively water level								
	Under water	**Alternating level of sea water**	**Above water**	**Under water**	**Alternating level of sea water**	**Above water**	**Under water**	**Alternating level of sea water**	**Above water**
Water resistance	+	+	+	+	+	−	+	+	+
Water impermeability	+	+	+	+	+	−	+	+	+
Freeze-thaw resistance	−	+	+	−	−	−	−	+	+
Low heat of hydration	+	+	+	+	+	+	−	−	−
Weather resistance	−	+	+	−	+	+	−	+	+
Corrosion resistance	+	+	+	+	+	+	+	+	+
Abrasion resistance	+	+	−	+	+	−	+	+	−

Table 1. Requirements for marine concretes vs. service conditions.

Especially, strict requirements are applied to marine concretes working in the zone of alternating sea level and the "above water" zone of the outer sides of the marine concrete structures.

Compressive and flexural strength at the age of 28 or 60 or 180 days are main characteristics of concretes intended for contemporary marine structures. Usually, concretes with compressive strength of 40–50 MPa are used as marine concretes.

Among the most important characteristics of marine concretes which determine durability are: freeze-thaw resistance, water permeability, resistance to corrosive exposure of sea water (marine environment), weather resistance, protective properties of concrete with regard to corrosion of reinforcement, abrasion resistance, etc.

As a rule, these requirements are met through a proper concrete mix design and by taking measures on protection of concrete and reinforcement in order to guarantee service life reaching 50 years.

http://dx.doi.org/10.5772/64525

On the other hand, one of the main criteria of global sustainable development concept is an issue of durability (lifespan of concrete over 100 years).

Existing widely used cements due to a four-phase principle of compositional build-up and hydration product phase composition are not able to guarantee such durability of concretes.

That is why the only way to proceed is to use alternative cements. The alkali-activated cements represent one of such alternatives (**Table 2**) [3, 4].

Cement type	Early strength	Durability	Chemical resistance
Portland cement	++	++	+
Blended cement	+	+++	++
High alumina cement	+++	+	+++
High sulphate cement	+	++	+++
Sulphoaluminate cement	+++	++	+++
Alkali activated cement	+++	+++	+++

Note: (+) low, (++) medium, (+++) high.

Table 2. Comparative properties of various cements.

High efficiency of the alkali-activated cement concretes is proved by a vast experience collected from over 50-year use in structures for marine engineering, hydro-engineering, road and agricultural construction as well as residential, industrial, public buildings all over the world [5].

2. General information on alkali-activated cements

As long ago as in 1957, Viktor Glukhovsky, a scientist from Kiev (USSR, Ukraine), has discovered that compounds of alkali metals (Li, Na, K, Rb, Cs), the elements of the first group of the Periodic Table, could exhibit hydraulic binding properties similar to those of alkali earth metals (Mg, Ca, Sr, Ba), the elements of the second group [3].

As a result, an idea of creation of cementitious materials has been transformed as the following:

"Old scheme" (portland cement, high-alumina cement)

$$\left.\begin{matrix} CaO - SiO_2 \\ CaO - Al_2O_3 \end{matrix}\right\} + H_2O \rightarrow \begin{matrix} CaO - SiO_2 - H_2O \\ CaO - Al_2O_3 - H_2O \end{matrix} \quad (1)$$

"New scheme" (alkali-activated cement) (AAC)

$$\left.\begin{matrix} Al_2O_3 - SiO_2 \\ CaO - Al_2O_3 - SiO_2 \end{matrix}\right\} + R_2O + H_2O \rightarrow \begin{matrix} R_2O - Al_2O_3 - SiO_2 - H_2O \\ CaO - R_2O - Al_2O_3 - SiO_2 - H_2O \end{matrix} \quad (2)$$

where R—Na, K, Li, Rb, Cs.

The idea of using these systems as cementitious materials was based, first of all, on geological data about sodium-potassium-calcium aluminosilicate compounds, which have the higher stability and resistance to atmospheric reagents and are widely present in the Earth's Crust. Second, this idea was based on the results of experimental studies, which proved that alkali hydroxides and salts of alkali metals came into interaction with clay minerals, aluminosilicate glasses and crystalline substances of natural and artificial origin with the formation of water-resistant alkaline and alkaline-alkali earth aluminosilicate hydration products analogous to natural minerals of the zeolite and mica types [6, 7].

A classification proposed by Pavel Krivenko in [8] is based on characteristic features of hydration products of the alkali-activated cements, the "edge" variants of which may be represented by the compounds of two types: alkaline aluminosilicate hydrates of the system R_2O-Al_2O_3-SiO_2-H_2O and alkali earth silicate hydrates of the system CaO-SiO_2-H_2O.

A variety of mixed alkaline-alkali earth aluminosilicate hydrates may fall within these "edge" variants. A cement stone hydration product phase composition is determined by constituent raw materials (**Table 3**).

Cement type	Initial solid phase	Alkali content (R_2O), %	Hydration product
portland cement	portland cement clinker	< 0.6	0% 100%
alkali activated portland cement	portland cement clinker+ R_2O	1…5	
blended alkali activated portland cement	portland cement clinker+ additive (metallurgical slag, ash, basalt) + R_2O	2…5	
alkali activated slag cement	metallurgical slag + R_2O	4…8	
alkali activated ash cement	ash–product of coal combustion	5…10	
geocement	clay + R_2O	10…20	100% 0%

Table 3. Mineralogical composition of cement hydration products vs. type of initial aluminosilicate component.

Strength classes of the alkali-activated cements (compressive strength at age of 28 days) are designated in the national standard of Ukraine DSTU B V.2.7-181:2009 "Cements, alkaline" [9]. High properties of the alkali-activated cement stone are attributed to its structure, which is

http://dx.doi.org/10.5772/64525

different from that of portland cement, considerably lower solubility of hydration products and absence in them of $Ca(OH)_2$ and calcium sulphoaluminate hydrates [10, 11].

3. Alkali-activated cement concretes

3.1. Strength properties

According to the national standard of Ukraine [12], heavyweight and super heavyweight alkali-activated cement concretes are designated in classes in compressive strength at standard age (28 days).

In compressive strength, the alkali-activated cement concretes are designated, similar to EN-206, as below:

C8/10; C12/15; C16/20; C20/25; C25/30; C30/37; C35/45; C40/50; C45/55; C50/60; C55/67; C60/75; C70/85; C80/95; C90/105; C100/115; C110/125.

In flexural strength, the alkali-activated cement concretes are designated as below:

in axial tension: $C_t0.8$; $C_t1.2$; $C_t1.6$; $C_t2.0$; $C_t2.4$; $C_t2.8$; $C_t3.2$; $C_t3.6$; $C_t4.0$.

in tensile bending strength: $C_{tв}0.8$; $C_{tв}1.2$; $C_{tв}1.6$; $C_{tв}2.0$; $C_{tв}2.4$; $C_{tв}2.8$; $C_{tв}3.2$; $C_{tв}3.6$; $C_{tв}4.0$; $C_{tв}4.4$; $C_{tв}4.8$; $C_{tв}5.2$; $C_{tв}5.6$; $C_{tв}6.0$; $C_{tв}6.4$; $C_{tв}6.8$; $C_{tв}7.2$; $C_{tв}7.6$; $C_{tв}8.0$; $C_{tв}8.4$; $C_{tв}8.8$.

where C_t is the characteristic strength in axial tension (MPa) and $C_{tв}$ is the characteristic tensile bending strength (MPa).

As a rule, tensile strength of coarse aggregates in the alkali-activated cement concrete constitutes 10–20% of compressive strength, depending upon type and density of alkaline activator and alkali-activated cement composition.

Strength of the alkali-activated cement concretes is kept under control, chiefly, by a proper choice of alkaline activator and its content. The greatest effect on strength characteristics is made by soluble sodium silicates. The alkali-activated cement concretes made using sodium silicates have high compressive strength reaching 120–140 MPa. They have close values of compressive strength measured on cubes not depending upon a modulus of basicity and slag content. This is especially clearly expressed in the steam-cured alkali-activated cement concretes. A conclusion was drawn that the lowering of the slag content in the concrete mix from 500 to 300 kg per 1 m^3, the alkaline activator represented by sodium silicates, would affect early strength gain and has no any effect on values of final compressive strength. Strength of the alkali-activated cement concretes made using sodium carbonate as alkaline activator varies between 45 and 80 MPa. Type of slag also affects strength gain, and this is especially clearly expressed in the alkali-activated cement concretes that hardened in normal conditions, which continue to attain strength at the later ages. With decrease in blast-furnace slag basicity and slag content, the strength of these concretes will decrease by 10–15 MPa. The highest compressive strength (116–123 MPa) is characteristic of the steam-cured alkali-activated cement concretes made using neutral blast-furnace slags and low-modulus sodium silicates (silicate

modulus Ms = 1–2). Strength of the steam-cured alkali-activated cement concretes increases with decrease in silicate modulus of sodium silicate and is higher than that of the concretes that hardened for 28 days in normal conditions. The concretes hardening in normal conditions, similar to steam-cured concretes, exhibit the highest compressive strength in case of using neutral slags and low-modulus sodium silicates. The alkali-activated acid slag cement concretes have rather slow early strength gain. However, after two years the strength has increased by 2–2.6 times. High-modulus sodium silicates are not recommended for the alkali-activated cement concretes in which acid slags are used and for hardening in water. The above combination of cement components can be used under condition that basicity of the binding system will be increased by introduction of high-basic additives [13, 14].

As follows from Ref. [15], not depending upon slag characteristics and nature of alkaline activator, the alkali-activated cement concretes continue to gain strength steadily in normal conditions, in the air and in water even after they have already gained a 28-day strength.

3.2. Water permeability

Water permeability is the most widely used key characteristic of permeability of concrete and is expressed as the highest pressure of water at which water still does not penetrate into the test specimen and this characteristic is called a "filtration coefficient". This coefficient is expressed as a quantity of liquid penetrating through a unit of cross section per unit of time at head gradient of 1.

The alkali-activated cement concretes, to which more strict requirements (low water permeability and high corrosion resistance) are applied, are classified with regard to water permeability as the following: W2; W4; W6; W8; W10; W12; W14; W16; W18; W20; W25; W30 (W—water permeability, pressure in atm) [12].

Specific features of pore structure of the alkali-activated cement concretes, their high water retaining capacity and lack of segregation in the alkali-activated cement concrete mixtures result in possibility to design concretes with the lower water permeability [16].

Density of the alkali-activated cement concretes increases, and water permeability decreases with time and depends upon chemical-mineralogical composition, slag fineness, and cement content (**Tables 4** and **5**).

Characteristics of water permeability	**Slag fineness (m^2/kg) (measured by Blaine)**				
	230	**300**	**420**	**510**	**600**
Pressure at which filtration occurs (MPa)	2.5	3.7	4.1	4.3	3.6
Filtration coefficient ($K_f \cdot 10^{-13}$) (cm/s)	4.7	3.1	0.6	0.1	0.9

Table 4. Water permeability of alkali-activated slag cement stone vs. slag fineness.

http://dx.doi.org/10.5772/64525

Concrete mix design (%)		w/c	Water adsorption (%)	Compressive strength (MPa)	Pressure at which filtration is observed (MPa)	Filtration coefficient (cm/s)
Slag	Sand					
15	85	0.60	8.3	30.1	0.4	1.3×10^{-6}
20	80	0.40	7.2	39.7	0.8	5.3×10^{-7}
25	75	0.36	4.1	45.5	1.8	0.8×10^{-10}
30	70	0.33	3.7	56.7	3.4	0.4×10^{-11}

Table 5. Water permeability of fine aggregate alkali-activated slag cement concretes vs. slag content.

Strength gain and decrease in water permeability of the alkali-activated cement concrete depend upon the cement content: with the cement content reaching 20%, a decrease in water permeability while hardening of the concrete specimens in high humidity conditions has been reported: by 20 times after 1 year and as much as by 200 times after 5 years. The concretes with the cement content between 25 and 40% at this age were dense enough not to allow water to penetrate into them even at pressures of 4–5 MPa [15].

Water permeability of the alkali-activated cement concretes decreases in case of using aggregates with properly selected particle size distribution providing minimum void content. So, the lowest value ($K_f = 0.9 \times 10^{-12}$ cm/s) corresponds to void content of 32.3%. Water permeability of the alkali-activated cement concretes can be improved by addition of clays, which, participating in the structure formation processes, increase density of the concrete. A determining role is played by mineralogical composition of clays. The fine aggregate alkali-activated cement concrete with the highest density was produced using sands containing 10% of coal and mining wastes. Glauconite clay, in its action on water permeability, is similar to kaolinite clay, and its maximum allowed quantity is 5%. The use of bentonite clay is found to be of no favour due to its coagulation during mixing with alkaline activator solutions.

Filtration coefficient of the alkali-activated cement concretes made using aggregates containing up to 15% of clay, at the initial test ages, due to its slow interaction with alkaline activators, remained rather high ($K_f = 3 \times 10^{-9}$ cm/s). However, after 1 year it has decreased by 5–7 times, after 5 years by 20 times. The decrease in water permeability can be provided by application of special techniques of mixing, in particular, under vibration which was found to decrease filtration coefficient by 25–30 times compared to mixing in traditional mixers.

The most favourable conditions which allow for to reach similar low water permeability, as those of the concretes hardened in normal conditions, are: steam curing in closed moulds at $T = 373$ K with a temperature rise for 3–4 h and isothermal heating for 4 h. The longer isothermal curing has no sense since a density of the concrete does not change.

According to long-term test results, strength, density, and water permeability of the alkali-activated cement concretes tended to improve with time (**Figure 1**) not depending upon applied curing conditions, but with the higher rate when the concrete specimens were allowed to cure in water and in high humidity conditions.

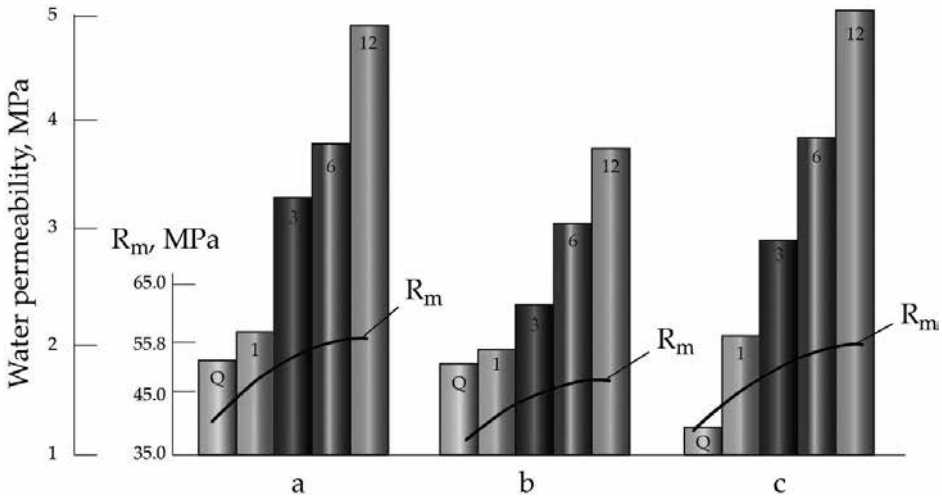

Figure 1. Compressive strength gain (MPa) and water permeability (MPa) of alkali-activated cement concretes vs. cure conditions: **a**—high humidity; **b**—dry; **c**—in water and cure regimes: Q—after steam curing; 1, 3, 6, 12—at age of 1, 3, 6, and 12 months, respectively.

Due to specific features of a capillary pore structure, water permeability of the alkali-activated cement concretes remained almost unchanged and still rather low after attacks of cyclic unfavourable conditions: heating-cooling, wetting-drying, freezing-thawing (**Table 6**). Water permeability as a function of concrete structure is the most important physical characteristic defining degree of deterioration under exposure of various aggressive environments, since corrosion processes start at the interfacial surface of external environment and concrete and proceed inward the concrete-reaching pores and capillaries.

Water permeability of the alkali-activated cement concrete can be improved by optimization of its composition with application of conventional techniques.

Composition no	Heating-cooling Cycles			Wetting-drying			Freezing-thawing		
	50	100	200	50	100	200	50	100	200
	Permeability expressed as pressure (MPa)								
1	1	8	7	13	15	14	15	17	16
2	5	5	4	9	10	11	11	12	13

Notes
1. Concrete mix design (composition no. 1), 1 m^3: ground granulated blast-furnace slag—500 kg, ultrafine (desert) sand—300 kg, coarse aggregate (5/20)—1175 kg, and sodium metasilicate (density = 1220 kg/m^3)—200 l.
2. Concrete mix design (composition no. 2), 1 m^3: portland cement—500 kg, river sand—300 kg, coarse aggregate (5/20)—1175 kg, and water—200 l.

Table 6. Changes in water penetration of alkali-activated slag cement concrete after cyclic exposures.

http://dx.doi.org/10.5772/64525

3.3. Corrosion resistance in mineral environments

Durability of the alkali-activated cement concrete in mineral salt solutions is affected by ion composition, concentration and exposure conditions and is predetermined by specific features of micro- and macrostructure affected by slag composition, type and quantity of alkaline activator, as well as by cure conditions. The alkali-activated cement concretes exhibit high resistance in solutions of magnesium chlorides and nitrates considerably exceeding those of sulphate-resisting portland cements [17].

Resistance of the alkali-activated cement concretes in sulphate solutions is determined by cations of sulphate salts as well as by alkali-activated cement composition. In sodium sulphate solutions, the alkali-activated cement concretes, not depending upon alkali-activated cement composition, are not subjected to deterioration. This is attributed to lack of conditions for the formation of insoluble corrosion products.

Sulphates of polyvalent metals (magnesium, manganese, aluminium, nickel, copper, zinc, etc.), as well as those of ammonia that form insoluble (silicate hydrates, hydroxides) or volatile (ammonia) compounds, are more aggressive environments. These compounds react actively with the alkali-activated cement stone solid phase with the formation of gypsum dehydrate. A degree of aggressiveness of these sulphate compounds is determined by properties of cations, permeability of corrosion products and pH-values of the formed hydroxides.

Depending upon properties of cation, resistance of the alkali-activated slag cements in sulphate solutions decreases in the following sequence: $Na^{+} > Zn^{2+} > Cu^{2+} > Ni^{2+} > A1^{3+} > NH_4^{+} > Mg^{2+} > Mn^{2+}$ [18].

Nos	Alkaline activator	Coefficient of corrosion resistance after immersion, duration in months							
		3% concentration				6% concentration			
		1	3	6	12	1	3	6	12
1	Sodium hydroxide	1.02	1.00	0.63	0	1.15	–	–	–
2	Sodium carbonate	1.10	0.74	0.65	0	1.18	0.42	0.29	0
3	Sodium metasilicate	1.01	1.04	1.24	0	1.49	0.43	0.27	0
4	Sodium disilicate	1.37	1.28	3.60	1.35	1.51	1.40	2.87	1.07
5	Sodium silicate (Ms = 3.0)	2.97	4.49	9.90	3.09	3.62	9.05	13.96	2.50

Table 7. Corrosion resistance of alkali-activated slag cement concretes made with various alkaline activators in $MgSO_4$ solutions.

Corrosion of the alkali-activated cement stone in $MgSO_4$-solutions takes place similar to corrosion of portland cement stone: occurrence of cracks, mainly perpendicular to a longitudinal axis of a specimen, curvature of the specimen, increase in linear dimensions and volume, deterioration.

At equal densities of alkaline activators, the corrosion resistance of the alkali-activated cements in $MgSO_4$ solutions tends to improve depending upon a type of alkaline activator in the following sequence: $NaOH < Na_2CO_3 \approx Na_2SiO_3 < Na_2Si_2O_5 < Na_2O \cdot 2.65SiO_2$ (**Table 7**).

An alkaline activator solution content to slag content ratio affects corrosion resistance in $MgSO_4$ solutions. The higher is this ratio, the lower is the corrosion resistance due to the higher porosity and higher is the permeability of the resulted stone.

Heat-treated alkali-activated cement concretes made with sodium silicate (Ms = 1–3) have the lower resistance compared to that of similar concretes that hardened in normal conditions. The use in this case of non-silicate compounds of alkali metals has positive effect on corrosion resistance of the alkali-activated cements in $MgSO_4$ solutions.

In general, the comparative test results of the alkali-activated, portland and sulphate-resisting portland cements showed that in the conditions of full immersion, the alkali-activated cement concretes had higher resistance in the solutions of sodium sulphates ($K_{r24} \geq 1$), magnesium chloride, and nitrate and had similar corrosion resistance in marine environment to that of sulphate-resisting cement ($K_{r24} \geq 0.55$. Whear: K_r—ratio of strength of a specimen exposed to aggressive environment to that of a specimen stored in water; $_{24}$—a number of months).

Analysis of specific deterioration of the alkali-activated cement stone and known types of corrosion suggested that alkali-activated cement hydration products were represented by four groups of substances varying in resistance in aggressive environments:

– the most easily dissolved—"free" (unbound) alkaline activator;

– less dissoluble compared to alkalis, but relatively easily dissoluble substances of the sodium silicate or calcium-sodium silicates types that are present in a gel-like state;

– relatively resistant to dissolution calcium silicate hydrates and calcite;

– the most poorly dissoluble crystalline calcium silicate hydrates and sodium aluminosilicate hydrates.

Prevalence of one of these or those groups in the cement hydration products determines variations in corrosion resistance.

3.4. Corrosion resistance in organic environments

Corrosion resistance of the alkali-activated slag cement concretes in organic environments is dependent upon an alkali-activated cement composition, character of pore structure of the resulted concrete as well as reactivity of aggressive environments.

Corrosion resistance expressed by K_r was measured on the specimens made from alkali-activated and portland cement concretes 24 months after immersion in hydrocarbon media (kerosene, diesel, mineral oil, petroleum) and water as reference medium (K_{r24}) (**Table 8**). A conclusion was drawn that corrosion resistance of the alkali-activated cement concretes was higher than that of portland cement concretes. This is explained by formation of the concrete

http://dx.doi.org/10.5772/64525

structure with the lower capillary porosity and continuation of hydration processes in the alkali-activated cement in organic environments [19].

Aggressive environment			Variations of Kr_{24} after storage in the conditions of full immersion of concrete specimens made from	
Name	**pH**	**Acidity measured by titration (mol/l)**	**Alkali-activated cement**	**Portland cement**
Gasoline	–	0.0005	0.98…0.99	0.98…0.99
Benzene (benzole)	–	0.0007	0.96…1.00	0.70…0.90
Kerosene	–	0.0008	0.92…0.99	0.60…0.78
Mineral oil	–	0.0011	0.64…0.96	0.50…0.70
Diesel	–	0.0009	0.72…0.94	0.50…0.67
Sulphur-bearing crude	–	0.0013	0.5…0.97	0.56…0.40
Animal fat	–	0.0500	0.56…0.97	Destroyed
Solution of sugar 30% concentration	–	0.0100	0.68…1.18	0.30…0.64
Pickle (saline) solution of meat processing factory	–	–	0.68…1.18	0.30…0.64
Acetic acid of 10% concentration	2.80	–	0.25…0.45	0.15…0.24
Milk acid of 10% concentration	3.45	–	0.3…0.79	0.20…0.35

Table 8. Resistance of fine aggregate alkali-activated cement and portland cement concretes in various organic environments after 24 months.

Depending upon the alkaline activator used, resistance of the alkali-activated cement concretes in aggressive petroleum environments increases in the following sequence: NaOH > soda-alkali melt (by-product of chemical industry) > Na_2CO_3 > Na_2SiO_3 > $Na_2O_2SiO_2$.

High-molecular organic environments are less aggressive for the alkali-activated cement concretes. After 24 months of storage of the specimens in pickle (saline) solution, animal fat and 30% concentration solution of sugar, the resistance was more than by three times higher compared to that of portland cement concrete.

Resistance of the alkali-activated cement concrete in low-molecular compounds (glycerine, acetic and milk acids) is comparable to that of portland cement concrete and somewhat exceeds it. This may be attributed to the lower solubility of hydration products of the alkali-activated cements and lack of $Ca(OH)_2$, high-basic calcium silicate and aluminate hydrates in the hydration products.

Thus, on the contrary to conventional cements, the alkali-activated cements exhibit the higher physico-mechanical properties such as strength, water permeability, corrosion resistance. The alkali-activated cements possess a complex of the above properties and can be classified as cements with polyfunctional properties.

3.5. Biodegradability and bio-fouling

Capability with regard to biodegradability and bio-fouling was tested according to the following: the specimens were stored in solution of sulphuric acid (pH = 3–4) [20].

After exposure to aggressive environment, the concrete specimens were tested to determine compressive and flexural strength characteristics.

When a ratio of strength after testing to that before testing is higher than 0.8, the cements are classified as corrosive resistant cements. Test results are given in **Table 9**.

Concrete class	Compressive/flexural strength (MPa) after					
	3 months		6 months		9 months	
	Normal curing	In sulphuric acid	Normal curing	In acid solution	Normal curing	In sulphuric acid
C45/50	53.4/11.4	50.5/10.7	54.7/9.6	60.6/11.1	60.7/10.6	55.6/10.5
C100/115	122.6/12.1	105.4/11.0	113.1/10.3	93.2/12.1	115.8/12.0	105.8/12.0

Table 9. Strength variations after exposure of aggressive environment.

From given results, both concretes under study showed stability of strength properties even after storage in aggressive environment for 9 months. So, it is clear that the alkali-activated slag concretes are resistant to biodegradability and bio-fouling.

3.6. Chloride diffusion

Replacement of portland cement with blast-furnace slag suppresses chloride diffusion in the hardened cement pastes, mortars and concretes [20]. Other study [5] has indicated that the addition of alkalis to blended portland slag cement not only increased cement strength but also decreased chloride diffusion in the cement paste significantly (**Figure 2**). The other clear trend is that diffusion rate of chloride decreases with increase in slag substitution.

The developed diffusion cell test is often used to measure the apparent diffusivity of Cl^- through hardened cement pastes and concrete. Chloride diffusion test on both the F-cement (a variety of alkali-activated cement) and portland cement pastes indicated that the diffusion rate of Cl^- through F-cement pastes is about 30–40 times slower than that through portland cement pastes for a given water-to-cement or water-to-slag ratio (**Table 10**). It was also noticed that cracks of 10–50 microns wide, induced by drying below 50% relative humidity, did not show any influence on the Cl^- diffusion rate of the specimens. However, the specimens with cracks wider than 50 microns running through the specimens had much higher Cl^- diffusion rate [20].

http://dx.doi.org/10.5772/64525

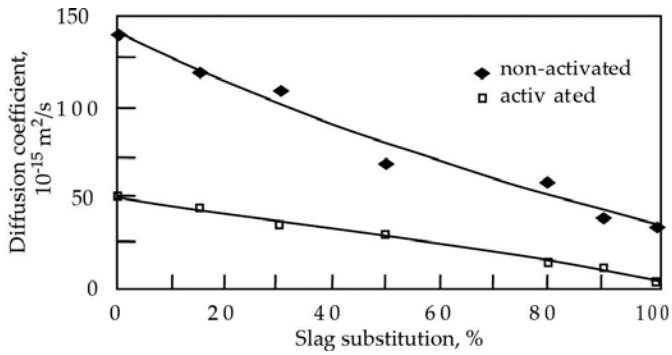

Figure 2. Effect of alkaline activation on chloride diffusion in portland slag cement.

Nos	Cement paste	Water to cement (slag) ratio	Diffusion coefficient (cm^2/s)
1	Portland cement	0.23	321×10^{-12}
2	Alkali-activated slag cement	0.23	75×10^{-12}
3	Portland cement	0.35	6390×10^{-12}
4	Alkali-activated slag cement	0.35	240×10^{-12}

Table 10. Chloride permeability test results of various cements [20].

Age	Voltage—30 V; time—24 h						
	No	I0/mA	T0/	If/mA	Tf/	L/cm	Dfucc/$\times 10^{-12}$
3 days	CH1	21.9	23.8	17.8	22.5	1.33	2.91
	CH2	29.1	23.7	28.0	21.4	1.53	3.37
	CH3	29.5	23.5	19.2	22.2	1.55	3.42
	Mean						3.23
7 days	CH1	22.8	25.9	16.4	23.7	1.27	2.78
	CH2	18.6	25.8	15.8	23.6	1.22	2.67
	CH3	23.6	25.5	21.7	23.8	1.37	3.01
	Mean						2.82
28 days	CH1	16.8	24.2	20.3	22.8	0.81	1.71
	CH2	19.4	24.1	16.4	22.8	0.79	1.66
	CH3	21.7	23.9	20.8	22.7	1.04	2.53
	Mean						1.71

Notes: I0, T0, initial current (T); If, Tf—final current (T); L—diffuse depth; Dfucc—diffusion coefficient.

Table 11. Chlorine ions diffusion parameters [20].

Analysis of the obtained results showed that all concretes had good resistance to chloride ions penetration. According to ASTM standard, such properties are characteristic of exclusively for polymer concretes. Thus, it is possible to predict high durability of all tested concretes.

Dependences between chloride diffusion and age of concrete are shown in **Table 11**.

3.7. Freeze-thaw resistance

A key factor affecting durability of a cement stone is its pore structure which determines, in particular, its freeze-thaw resistance. For example, frost destruction of water-saturated portland cement stone takes place, chiefly, during spasmodic freezing of microcapillary water during a period starting from ice formation and until T = 253 K.

Frost destruction of the water-saturated alkali-activated cement stone occurs when the remaining portions of microcapillary moisture get frozen at temperatures below T = 223 K.

At temperatures of 243 K, the alkali-activated cement stone is subjected to residual deformations; after cooling to T = 233 K, the residual deformations were 0.01 mm/m, after cooling to T = 213 K—0.15 mm/m (**Figure 3**) or of about 10% of residual deformations after freezing to 173 K and thawing [21].

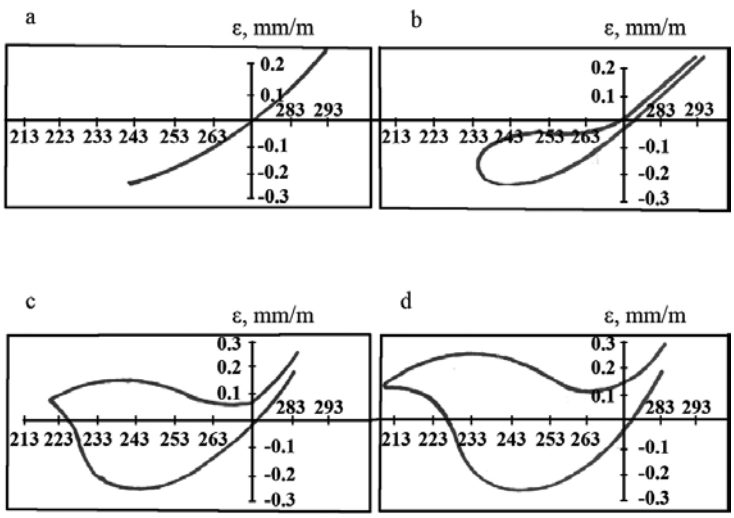

Figure 3. Deformations of alkali-activated slag cement concrete (water-to-slag ratio = 0.3) under attacks of freezing-thawing: **a**—T = 243 K; **b**—T = 234 K; **c**—T = 219 K; **d**—T = 212 K.

Differences in mechanism of temperature-induced deformations of the water-saturated portland cement and alkali-activated cement stones are attributed to the presence in the capillaries of the latter of true solutions of strong electrolytes, the lowering of the freezing temperature and promoting step-by-step removal of water due to freezing. Mechanism of water removal from a pore space of the alkali-activated cement stone is different from that in portland cement stone, thus determining a difference in the rate of their deformations in the

http://dx.doi.org/10.5772/64525

process of cooling and heating. Pore liquid in portland cement stone capillaries gets frozen spasmodically with elimination of meniscus and in the capillaries of the alkali-activated cement stone step-by-step, with maintaining the meniscus in a frozen state, resulted in the lowering of temperature of precipitation (settling-out) of eutectic mixtures.

A freezing temperature of pore liquid is largely determined by a type of alkaline activator. For example, in case of potash a freezing temperature of the eutectic mixture is 237 K, in case of soda only 270.9 K. The other reason causing different behaviour of the frozen water-saturated specimens from portland cement and alkali-activated slag cement concretes is attributed to specific features of their pore structure; in particular, the alkali-activated cement stone is characteristic of the increased microcapillary porosity.

A temperature of ice formation in the alkali-activated cement concretes is shifted to the region of the lower temperatures, since contents of fine pores (3–8 nm) in the alkali-activated cement stone are somewhat higher than those in portland cement concrete.

The alkali-activated cement concretes made with soluble sodium silicates have the highest freeze-thaw resistance, high density and strength. Their freeze-thaw resistance, depending upon production technology and other factors affecting strength characteristics, is 300–1300 cycles [22].

3.8. Weather resistance

Alternate (cyclic) wetting-drying, carbon dioxide and temperature variations are among factors associated with weather exposure.

Long-term cyclic wetting-drying will increase irreversible shrinkage deformations and deterioration of the concrete structure and may cause in the future loss of its load carrying ability.

Alternate wetting-drying of the alkali-activated cement concretes has no effect on its compressive strength: after 50 cycles of wetting-drying, a compressive strength of the alkali-activated cement concrete made with sodium carbonate of technical grade (commercial product) in solution has lowered by 4%, with sodium metasilicate—by 1.5% [13].

Strength properties of the alkali-activated cement concrete exposed to alternating atmospheric conditions can be improved through regulation of rate of crystallization of a gel phase, adjustment of the hydration product phase composition and directed synthesis of the materials with a required pore structure The influence of these factors on durability of the artificial stone is evident and may be taken in account in choosing the appropriate process parameters for manufacture of the alkali-activated cement concrete with desired physico-mechanical characteristics.

Weather resistance was tested according to the prescribed testing procedure [23]. The specimens were immersed in water for 4 h and then dried at temperatures of 378–383 K for 15 h.

Three characteristics were studied: compressive and flexural strength and mass changes after testing. Test results are given in **Tables 12** and **13**.

Sample No	Drying-wetting				Normal curing			
	C70/85		C100/115		C70/85		C100/115	
	Flex.	Comp.	Flex.	Comp.	Flex.	Comp.	Flex.	Comp.
After 75 cycles (MPa)								
Sample no 1	8.2	76.9	11.0	116.3	9.9	50.9	10.8	103.0
Sample no 2	7.1	75.6	9.9	113.8	9.8	46.4	11.7	110.1
Sample no 3	6.4	74.5	10.0	116.3	9.0	48.1	11.2	105.3
Mean strength	7.2	75.7	10.3	115.5	9.6	48.5	11.2	106.1
After 100 cycles (MPa)								
Sample no 1	8.7	88.1	11.4	115.1	9.5	51.3	11.6	113.1
Sample no 2	8.5	87.1	12.1	117.8	9.1	52.3	11.8	108.5
Sample no 3	7.6	88.2	12.1	115.6	9.7	58.0	11.8	110.2
Mean strength	8.3	87.8	11.9	116.1	9.4	53.9	11.7	110.6
After 150 cycles (MPa)								
Sample no 1	7.4	83.3	11.1	119.1	8.2	48.9	11.9	112.9
Sample no 2	7.8	79.3	10.4	120.9	10.1	44.2	11.9	113.6
Sample no 3	8.5	83.3	11.5	117.3	8.5	46.7	11.6	110.7
Mean strength	7.9	82.0	11.0	119.1	8.9	46.6	11.8	112.4
After 200 cycles (MPa)								
Sample no 1	9.2	86.7	11.0	110.1				
Sample no 2	8.2	92.2	11.5	125.1				
Sample no 3	8.1	85.1	9.0	112.4				
Mean strength	8.5	88.0	11.3	113.9				

Table 12. Residual strength characteristics of alkali-activated slag cements concretes vs. curing conditions.

Test results showed that both concretes passed 200 cycles without any sign of deterioration.

3.9. Wear resistance

Wearing can be classified into three categories: abrasion, erosion and cavitation [20].

Specific features of wear in abrasion of the alkali-activated cement stone are attributed to its mineralogical and phase compositions, size of crystals and specific surface of a solid phase. Due to intensive processes of structure formation, a time-based approach to assessment of this characteristic was applied.

Tests were carried out according to a standard procedure on cube specimens (70 × 70 × 70 mm). A standard river sand was used as an abrasive material. Wear in abrasion was expressed as changes of mass and linear dimensions of the specimens subjected to wear. The results of wear in abrasion of the alkali-activated slag cement concrete are reported in (**Table 14**) [24].

http://dx.doi.org/10.5772/64525

	C70/85		C100/115	
	Before	**After**	**Before**	**After**
After 75 cycles (g)				
Sample no 1	559.0	558.0	562.0	560.0
Sample no 2	561.0	560.0	562.0	556.0
Sample no 3	563.0	563.0	570.0	564.0
Mean mass	561.0	560.3	564.7	560.0
Mass change (%)	0.125		0.832	
After 100 cycles (g)				
Sample no 1	553.0	555.0	562.0	559.0
Sample no 2	564.0	567.0	578.0	571.0
Sample no 3	558.0	561.0	573.0	573.0
Mean mass	558.3	561.0	571.0	567.7
Mass change (%)	−0.484		0.578	
After 150 cycles (g)				
Sample no 1	554.0	555.0	578.0	572.0
Sample no 2	553.0	554.0	563.0	555.0
Sample no 3	555.0	558.0	571.0	561.0
Mean mass	554.0	555.7	570.7	562.7
Mass change (%)	−0.307		1.402	
After 200 cycles (g)				
Sample no 1	567.0	562.0	573.0	568.0
Sample no 2	564.0	559.0	566.0	561.0
Sample no 3	562.0	556.0	562.0	560.0
Mean mass	564.3	559.0	567.0	563.0
Mass change (%)	0.939		0.705	

Table 13. Mass changes of alkali-activated slag cement concretes.

Wear resistance of the alkali-activated slag cement concrete decreases with its compressive strength increase. This dependence can be approximated to a linear one and described by the following expression [25]:

$$W = C - K \cdot R_m \tag{3}$$

where W is the wear of concrete in abrasion, g/cm^2; C, K is the dimensionless coefficients; R_m is the compressive strength of concrete measured on cubes (MPa).

Sodium carbonate				Sodium silicate			
Normal conditions		Steam curing		Normal conditions		Steam curing	
Compressive strength (MPa)	Wear in abrasion (g/cm²)	Compressive strength (MPa)	Wear in abrasion (g/cm²)	Compressive strength (MPa)	Wear in abrasion (g/cm²)	Compressive strength (MPa)	Wear in abrasion (g/cm²)
35.0	0.470	33.0	0.550	37.5	0.462	40.0	0.497
37.0	0.437	34.0	0.547	44.5	0.441	42.0	0.484
47.5	0.450	41.0	0.540	59.5	0.465	61.5	0.455
52.5	0.394	48.5	0.490	65.0	0.420	64.0	0.418
54.5	0.420	51.0	0.470	66.5	0.377	67.5	0.423
62.0	0.358	59.0	0.453	80.0	0.379	83.5	0.362
67.5	0.330	60.5	0.430	88.5	0.368	89.5	0.375

Table 14. Wear in abrasion of alkali-activated slag cement concretes vs. compressive and curing conditions.

Wear in abrasion of the alkali-activated cement concrete tends to reduce with time, especially until the age of 180 days, that is, during a period of intensive structure formation. Analyzing the results of measurements of wear of the alkali-activated cement concrete specimens for a period of 24 months suggested to reveal a correlation between age of the alkali-activated cement concrete and express it mathematically [24]:

$$W = \frac{W^{28}}{0.61\mathrm{g}T} \tag{4}$$

where W is the wear of concrete in abrasion, g/cm^2; W^{28} is the same, at age of 28 days; and T is the age of concrete, days.

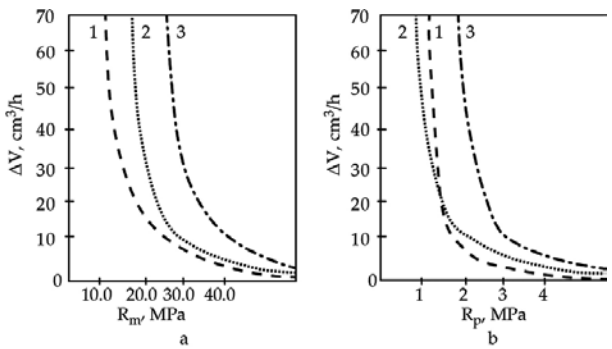

Figure 4. Correlation between the rate of cavitation-induced degradation of various concretes vs. compressive **(a)** and tensile strength **(b)**: 1—fine aggregate alkali-activated cement concrete; 2—fine aggregate portland cement concrete; 3—coarse aggregate portland cement concrete.

http://dx.doi.org/10.5772/64525

The alkali-activated cement concretes exhibit not only high wear resistance in normal service conditions, but are resistant to cavitation damage (**Figure 4**). Cavitation resistance of the alkali-activated cement concrete, expressed as specific mass change of the concrete per unit of time (measured rate of deterioration, cm^3/h), correlates well with strength characteristics and is described by a hyperbolic-type equation.

Cavitation-induced wear (cavitation damage) on concrete surface is most common in case of spillway in dams. This leads to cracks on the concrete surface which further increases the risk of damage to concrete due to sulphate attack, freeze-thaw, alkali-silica reaction and other means. Cavitation damage occurs on concrete surface when discontinuity or irregularities is encountered in the path of high velocity water flow.

According to Ref. [16], cavitation resistance of the alkali-activated cement concrete structures working in the zones of wave-cut/break is higher than that of portland cement concretes. In high humidity service conditions, the alkalis that are present in the alkali-activated cement stone allow for self-healing of the zones of stress concentrations and strengthening of the alkali-activated cement concrete due to "renewal" (re-start) of the processes of hydration and hardening resulting in densification of the concrete structure and filling of its defects (pores, etc.) with hydration products (**Table 15**).

Curing/exposure conditions	Alkali activated slag cement concrete			Portland cement concrete		
	Strength (MPa)		Wear (cm^3/h)	Strength (MPa)		Wear (cm^3/h)
	Compressive	Tensile bending		Compressive	Tensile bending	
28 days in normal conditions	50.00	4.00	8.27	40.50	4.40	6.36
(after steam curing)	39.00	4.00	9.11	30.00	2.80	12.25
180 days in sweet water	53.50	6.14	6.21	43.00	5.20	6.21
	41.50	5.40	7.38	32.40	3.30	10.36
180 days in sea water	55.60	8.24	5.42	41.50	4.13	6.43
	45.00	7.23	5.96	28.60	3.18	11.34

Note: Fine aggregate alkali-activated slag cement concrete (soluble sodium carbonate as alkaline activator).

Table 15. Wear caused by cavitation (cavitation resistance) of alkali-activated cement and portland cement concretes vs. curing/exposure conditions.

Thus, durability of the alkali-activated cement concretes, assessed in terms of endurance and wear resistance, is comparable and even exceeds that of portland cement concretes, especially in unfavourable (extremely severe) service conditions.

3.10. Corrosion due to alkali-aggregate reaction (AAR-induced corrosion)

One of the reasons associated with concrete durability is an alkali-aggregate reaction (AAR), which is a reaction between alkali of cement and alkali-susceptible aggregate. Rate of this

reaction is determined by a type and quantity of alkalis, and type and content of reactive silica. In case of the alkali-activated cements, which contain alkalis in much higher contents compared to that of portland cements, this problem is important. For this, a number of research projects have been performed [26–28], which showed a possibility to keep the AAR under control with a so called "positive" effect. The results of study showed that it could be possible due to introduction into the cement or concrete composition of aluminate-containing additives, in the presence of which a destructive ("negative") process of corrosion converts into a constructive ("positive") one. This is attributed to binding of the corrosion products with the formation of the alkali-activated aluminosilicate hydrates according to the following scheme:

$$Na_2O \bullet SiO_2 \bullet nH_2O + Al_2O_3 \bullet SiO_2 \rightarrow Na_2O \bullet Al_2O_3 \circ 2SiO_2 \bullet nH_2O$$

The resulted compound forms a dense and strong cage (shell) around the aggregate thus preventing corrosion processes.

This conclusion coincides well with the results of the following experiment: the metakaolin additive in a quantity of 15% was introduced into the cement composition to minimize influence of the destructive processes in the interfacial transition zone.

The influence of additive type on expansion deformations is shown in **Figure 5**. As follows from **Figure 5a**, non-admissible high expansion deformations were observed in the concretes made from portland cement with the increased content of Na_2O (1.3%) and from the alkali-activated portland cement with the Na_2O content of 2.5% in which andesite rock was used as coarse aggregate.

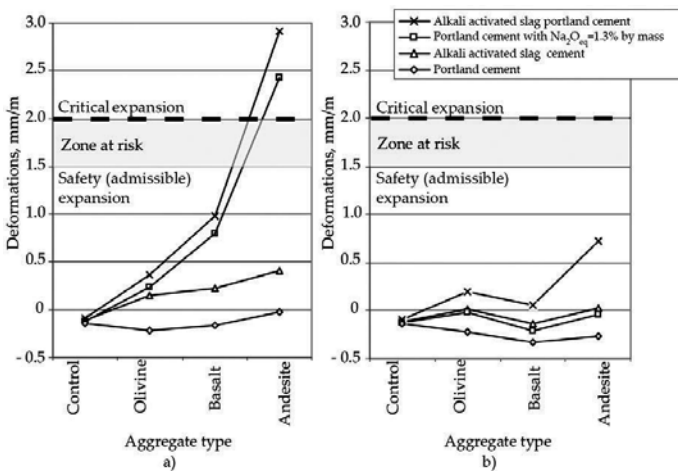

Figure 5. Influence of aggregate type (olivine, basalt, andesite) and metakaolin additive on deformations of the concrete specimens: **(a)** without additive; **(b)** with the metakaolin additive (15%); curing conditions—28 days of continuous steam curing at T = 343 K and relative humidity = 100%.

http://dx.doi.org/10.5772/64525

Corrosion products in the interfacial transition zone and microcracks occurring in the aggregates of the concretes made using portland cement with the increased contents of Na_2O and the alkali-activated slag portland cement are clearly seen in the electron microscope images. On the contrary, the use of the alkali-activated cements is not at any risk, and the interfacial transition zone "cement stone—alkali-susceptible aggregate" remained clear.

The introduction of the additive will allow to shift all concrete compositions not only from the zone of not allowable critical expansion and deterioration, but also from the zone of risk, not depending upon a cement type and aggregate type. The interfacial transition zone in this case is clear and without sign of corrosion. This may be attributed to the fact that conditions required for synthesis of alkaline zeolite-like aluminosilicate hydrates of the general formula $Na_2O \cdot Al_2O_3 \cdot mSiO_2 \cdot nH_2O$ are created in the interfacial transition zone in the presence of reactive Al_2O_3 in a strongly alkaline medium, that is, the alkali starts to bind very quickly.

The alkali-activated cement stone has low deformation expansions even without the metakaolin additive. This may be attributed to high contents of reactive Al_2O_3 in the glass phase of the slag.

4. Practical experience

Theoretical data in combination with those obtained experimentally that have been collected by a scientific school headed by Professor Viktor Glukhovsky (currently is headed by Professor Pavel Krivenko) allowed as early as in 1958 to launch first pilot scale production of the alkali-activated cement concrete products and to continue in 1962 with industrial-scale production of a number of concrete small-size building elements and structures.

The majority of alkali-activated slag cement concrete structures manufactured in 1960s was intended for hydro-engineering, in particular, marine engineering application that work in extreme service conditions (corrosive exposure of running waters, alternate freezing-thawing in winter, wetting and drying in summer, etc).

Regular continuous observations over the alkali-activated cement concrete small-size building elements and structures showed their higher performance properties compared to those of portland cement concretes as reference (**Tables 16–18**).

From these tables, performance properties of these concretes tended to increase during the whole period under review. This may be attributed to permanent deepening of the hydration processes, resulted in the formation of low basic calcium silicate hydrates and zeolite-like water-resistant final products of the alkaline as well as mixed (alkaline- alkali earth) composition. Low water permeability and high resistance of the alkali-activated cement concretes in aggressive environments can be explained by nature of their hydration products [17, 29].

The results of chemical analysis showed that quantities of free (unbound) alkalis in the alkali-activated cement concretes varied from 0.3 to 0.5%. A pH-index inside the alkali-activated slag cement concretes was 12.7–12.9. This is an evidence of presence in these concretes of an alkaline

medium which is required for the further flow of processes of hardening in the alkali-activated cements as well as for passivation of reinforcement steel. The alkalis are released in very small quantities. This is attributed to the increased density of the alkali-activated slag cement concrete, closed porosity and nature of hydration products.

Structure (small-size building element)	Mnfg year	Aggregate	Alkaline activator	Initial strength (MPa)	Test results (1973)	
					Freeze/thaw resistance (cycles)	Strength (MPa)
Cast-in-situ facing concrete covering of main irrigation channel (under water level)	1962	Heavy sandy loam	Na_2CO_3	15	900	42.60
The same, above water	1962	The same	Na_2CO_3	15	900	40.00
Pre-stressed precast concrete elements of irrigation system	1964	Sea sand (fineness modulus = 0.9…1.1)	Na_2CO_3	25	700	59.50
Precast concrete piles	1964	The same	Na_2CO_3	30	600	71.80
Cast-in-situ road pavement	1965	The same	Na_2CO_3	10	250	47.60
Cast-in-situ breakwater massive elements	1965	The same	Na_2CO_3	30	570	62.00
Prefabricated pavement slabs	1965	The same	Na_2CO_3	25	437	67.00
Centrifuged pipes (d = 100 mm)	1966	River sand (fineness modulus = 1.65)	Na_2CO_3	30	–	83.00
Large-size wall blocks	1967	Waste of shell rock	Na_2CO_3	10	300	31.30

Table 16. Performance properties of alkali-activated cement concretes after long-term service in various exposure conditions.

Type of concrete	Design compressive strength (MPa)	Compressive strength (MPa) after exposure in sea water during			
		1 year	3 years	5 years	7 years
Slabs of embankment					
Alkali activated slag cement (alkaline activator—sodium carbonate)	40.0	40.0	47.8	53.8	57.0
Portland cement	39.0	39.0	38.5	Destroyed	
Slabs immersed in sea water (under layer of biomass)					
Alkali activated slag cement (alkaline activator—sodium carbonate)	40.0	40.0	59.6	60.1	61.4
Portland cement	39.0	39.0	47.6	51.6	50.0

Table 17. Performance properties of alkali-activated cement slag concretes after service in sea water (Black Sea, Odessa, Ukraine).

Large-scale production of the alkali-activated cement concretes in the USSR showed their high efficiency. Cost savings (30–40%) were achieved due to the use of by-products and waste materials, as well as longer span of service life, especially in extreme conditions. These alkali-activated materials are in line with principles of global sustainable development: near-zero carbon dioxide emissions, low-energy consumption (no high temperature processes), preservation of natural resources, etc.

Structure (small-size building element)	Age of concrete (years)	Water permeability (MPa)	
		Initial (1 month after placing)	After service
Cast-in-situ concrete facing of main irrigation channel (under water level)	12	0.6	1.8
Chutes, pre-stressed, precast Pre-stressed precast concrete elements of irrigation system	9	1.0	2.0
Massive (large-size) water breaks, precast blocks Cast-in-situ breakwater massive elements	8	0.8	2.0
Slabs in service under layer of biomass	8	0.8	2.0
The same, isolated from biomass	8	0.8	2.0

Table 18. Water permeability of alkali-activated slag cement concretes after long-term service.

5. Conclusions

Numerous studies held on alkali-activated cement concretes supported by test results showed that they could work successfully with high efficiency in various structures withstanding extreme service conditions (alternate freezing-thawing, aggressive environments, dynamic and static loads, etc.). In their performance properties (freeze-thaw resistance, water permeability, corrosion resistance, etc.), the alkali-activated cement concretes are superior to portland cement ones and can be recommended for marine engineering applications, especially for so called "responsible use" structures that are in service in extreme weather conditions and under exposure of alternating loads and aggressive environments.

Author details

Pavel V. Krivenko[1*], Hai Lin Cao[2], Lu Qian Weng[2] and Oleg N. Petropavlovskii[1]

*Address all correspondence to: pavlo.kryvenko@gmail.com

1 V.D. Glukhovsky Scientific Research Institute for Binders and Materials, Kiev National University of Construction and Architecture, Kiev, Ukraine

2 Advanced Materials Research Institute, Shenzhen Academy of Aerospace Technology, Shenzhen, P.R. China

References

[1] Verbetsky GP. Strength and Durability of Concrete in Water. Moscow: Stroyizdat; 1976. 127 p.

[2] Dvorkin LY, Dvorkin OL, Dorofeev VS, Mishutin AV. Concretes for Hydroengineering Application and Roads. Odessa: LLC Zovnishreklamservis; 2012. 216 p.

[3] Glukhovsky VD. Soil Silicates. Kiev: Gosstroyizdat; 1959. 154 p.

[4] Krivenko PV. Alkaline cements. In: Proceedings of the First International Conference on Alkaline Cements and Concretes. Kiev: VIPOL Stock Company; 1994. p. 11–129.

[5] Krivenko P. Alkaline cements, concretes and structures: 50 years of theory and practice. In: Proceedings of the International Conference on Alkali-Activated Materials, Research, Production and Utilization. Prague: Agentura Action M; 2007. p. 313–332.

[6] Glukhovsky VD. Soil Silicate Building products and Constructions. Kiev: Budivelnyk; 1967. 155 p.

[7] Glukhovsky VD. Selected Works. Kiev: Budivelnik; 1992. 208 p.

[8] Krivenko P. Alkaline cements: terminology, classification, aspects of durability. In: Proceedings of the 10th Int. Congress on the Chemistry of Cements (10th ICCC). Goeteborg: Amarkai AB and Congrex; 1997. p. 4 iv 046

[9] National Standard of Ukraine DSTU B V.2.7-181:2009 "Cements, Alkaline". Kiev: Ministry of Regional Development and Building; 2009.

[10] Krivenko PV. Synthesis of cementitious materials in a system R_2O-Al_2O_3-SiO_2-H_2O with required properties [DSc thesis]. Kiev: Kiev Polytechnical Institute; 1986.

[11] Krivenko PV, Runova RF, Sanitskiy MA, Rudenko II. Alkaline Cements. Kiev: Osnova LLC; 2015. 448 p.

[12] National Standard of Ukraine DSTU BV.2.7-25:2011 "Heavyweight Concretes, Alkaline". Kiev: Ministry of Regional Development and Building; 2009.

[13] Glukhovsky VD, editor. Alkaline and Alkaline-Alkali Earth Hydraulic Binders and Concretes. Kiev: Vyscha Shkola Publish; 1979. 232 p.

[14] Glukhovsky VD, editor. Fine Aggregate Slag Alkali Activated Cement Concretes. Kiev: Vyscha Shkola Publish; 1981. 224 p.

[15] Krivenko PV, Pushkarjeva EK. Durability of Slag Alkaline Cement Concrete. Kiev: Budivelnyk; 1993. 223 p.

[16] Goncharov V. Study of resistance of fine aggregate alkaline cement concretes in anti-sliding structures and coastal defense structures [PhD thesis]. Kiev: Kiev Civil Engineering Institute; 1973.

http://dx.doi.org/10.5772/64525

[17] Krivenko PV. Special Slag Alkaline Cements. Kiev: Budivelnyk; 1992. 192 p.

[18] Mironenko A. Resistance of slag alkaline cement concretes in solutions of mineral salts [PhD Thesis]. Kiev: Kiev Civil Engineering Institute; 1985.

[19] Goncharov N. Corrosion resistance of slag alkaline binders and concretes in organic aggressive environments [PhD Thesis]. Kiev: Kiev Civil Engineering Institute; 1984.

[20] Shi C, Krivenko P, Roy D. Alkali-Activated Cements and Concretes. London and New York: CRC Press; 2006. 376 p.

[21] Muhammedgaleeva S. Study of properties and manufacturing technology of alkali activated slag cements in the conditions of the Far North [PhD Thesis]. Kiev: Kiev Civil Engineering Institute; 1976.

[22] Krivenko P, Cao H, Petropavlovskiy O, Weng L, Pushkar V. Effect of technology of manufacturing the alkali activated cement concretes porous structure and frost resistance. In: Proceedings of the Int. Conference on Non-traditional Cement and Concrete V. Brno: NOVPRESS s.r.o.; 2014. p. 119–122.

[23] Krivenko P, Cao HL, Weng LQ. Manufacture of alkali activated slag cement concretes for marine structures in the PR of China. Journal "Budivnytstvo Ukrainy". 2013; 4: 29–32.

[24] Solodky SY. A slag alkaline cement concrete for construction of rigid road pavements [PhD Thesis]. Kiev: Kiev Civil Engineering Institute; 1991.

[25] Fujii T, Zako M. Fracture Mechanics of Composite Materials. Moscow: Mir; 1982. 232 p.

[26] Krivenko PV, et al. A role of metakaolin additive on structure formation in the contact zone "cement-alkali-susceptible aggregate". In: Proceedings Int. Symp. on Non-traditional Cement and Concrete II. Brno: Brno University of Technology; 2005. p. 83–95.

[27] Krivenko PV, Gelevera AG, Kavalerova ES. Comparative study of alkali–aggregate reaction in the OPC and alkaline OPC concrete. In: Proceedings 16. Int. Baustofftagung 2, Weimar; 2006. p. 0389–0398.

[28] Krivenko P, et al. Mechanism of preventing the alkali–aggregate reaction in alkali activated cement concretes. Cement and Concrete Composites. 2014;45:157–165.

[29] Butt YM, Rashkovich LN. Hardening of Binders at Elevated Temperatures. Moscow: Stroyizdat Publish; 1965. 240 p.

Chapter 9

Application of Polypropylene Fibrillated Fibres for Reinforcement of Concrete and Cement Mortars

Jan Broda

Additional information is available at the end of the chapter

http://dx.doi.org/10.5772/64386

Abstract

Polypropylene fibres have been applied for reinforcement of cement mortars and concrete for many years. The fibres restrict crack propagation and positively affect several concrete parameters. To improve the adhesion of polypropylene to cement matrix, geometrically deformed or modified fibres are commonly used. Good results are obtained by application of fibrillated fibres with the net-like structure obtained from the polypropylene types. The fibrillated polypropylene fibres were produced. The fibres were chopped to specified lengths and used for the reinforcement of concrete and cement mortars. The parameters of fresh concrete and mechanical parameters of reinforced concrete and mortar were determined. It was stated that the fibres do not affect the compressive strength of the reinforced concrete and mortar. The beneficial effect of fibres on the compressive strength of concrete is revealed after freezing and thawing cycles. The fibres influence the bending strength of the mortars. For mortars reinforced with fibrillated fibres a significant increase in the bending strength is observed. The increase in the bending strength results from enhanced interfacial adhesion and mechanical anchoring, which results from opening of the network structure and splitting of fibrillated fibres.

Keywords: polypropylene fibrillated fibres, concrete, mortar, adhesion, compressive and bending strength

1. Introduction

The application of fibres in improving the mechanical properties of construction materials has been known for a long time. In the ancient times the primitive mud huts were built of clay doped with straw. In the next centuries bricks baked from clay with straw and later lime and cement

mortars with horse bristle were used. In the nineteenth century the concrete with addition of asbestos fibres became very popular. In the beginning of the twentieth century the first attempts of reinforcing the concrete with steel fibres were undertaken. Few decades later natural and chemical fibres for reinforcement of concrete came into use. The literature on the subject describes the successful attempts of applying various natural, as well as glass, carbon, polyaramide and other typical synthetic fibres [1–7].

From the group of synthetic fibres the polypropylene fibres are the most frequently applied [8, 9]. The great interest in polypropylene fibres results from their relatively low price, abundant availability and several valuable properties [10, 11]. The fibres are safe and easy to use and compatible with all concrete chemical admixtures. The fibres are chemically inert and possess high chemical and biological resistance, including very good resistance in concrete's alkaline environment [12]. Thanks to high resistance the fibres are rust free and do not corrode during the utilisation of concrete. The fibres are hydrophobic, show practically no wet absorption and do not absorb water during the mixing of cement paste. Due to low density of fibres, much lower than the density of steel, the reinforcement is light and does not load the constructions additionally.

Short polypropylene fibres distributed uniformly in the whole capacity of concrete sew lips of cracks and restrict their propagation [13–15]. The reduction of cracking is of great importance especially in the first hours after pouring, when the concrete possesses low tenacity and low Young's modulus, and the stresses arising as a result of shrinkage exceed its strength [16].

Fibres effectively restrict the propagation of contraction cracks through dispersing the internal stresses. In the moment when the crack is formed some fibres break, some, after the breaking of bonds connecting them with the concrete, are partially pulled out and some bridge the widening cracking [17]. All these processes lead to dissipating stresses occurring at the ends of the crack. Although the ability of single fibres to dissipate the stresses is not high, with greater amount of fibres the accumulation of the effect is observed and effective restriction of spreading the cracks occurs.

Apart from reducing crack propagation, the addition of fibres positively affects other concrete parameters. Concrete reinforced with polypropylene fibres possesses high strength and high resistance to cracking at bending, high resistance to dynamic loads, improved fatigue resistance and lower grindability comparing to the classical concrete [18–22]. Fibres improve the fire resistance of the concrete and its thermal resistance to sudden temperature changes. In higher temperatures fibres are melted and partially absorbed by the cement matrix. The fibres generate a permeable network that allows the outward gas migration, decreasing the pore pressure in the material and, consequently, eliminating the possibility of explosive spalling occurrence [23, 24]. Adding fibres improves also the freeze resistance of concrete. In this way fibres prolong significantly the concrete durability [25, 26].

In recent years fibre-reinforced concrete is getting widely used for the construction of roads and highways, airport pavements, watersides and many other engineering objects [27–29].

The performance of the fibre-reinforced concrete depends on interaction between the cement matrix and the fibres, which depends on the adhesion and the friction forces [30–33]. By weak

http://dx.doi.org/10.5772/64386

stresses the adhesion forces ensure the cohesion of interfacial area. In this circumstance, the internal stresses are transferred by both composite ingredients, and the displacements of the fibres and the matrix at the phase border are compatible. At larger stresses, in a view of significant difference of fibres' and matrix' elastic moduli, breaking of adhesive bonds between the fibres and the matrix occurs. After the break of such bond the process of pulling the fibres out begins, during which the friction forces play the main role [34–36].

Polypropylene fibres, due to their chemical structure and low surface energy, show extremely low wettability and poor adhesion to cementitious matrix. The literature describes various methods for modification of fibres, aimed at increasing the wettability and improving their adhesion capacity. One method consists in introducing polar groups on the surface of the fibres through reactions occurring during the plasma treatment or other reactions initiated by UV or γ radiation [37–42]. The second method of improving the adhesive properties consists in the increase of roughness of fibres' surface by chemical and physical treatment [43]. This method includes chemical etching, flame treatment, corona discharge or microwave radiation [44]. The significant improvement of adhesive capacity is obtained by the deformation of the fibres by crimping or twisting [45, 46]. Other interesting option is application of fibrillated fibres with the net-like structure obtained from the polypropylene types [47–49].

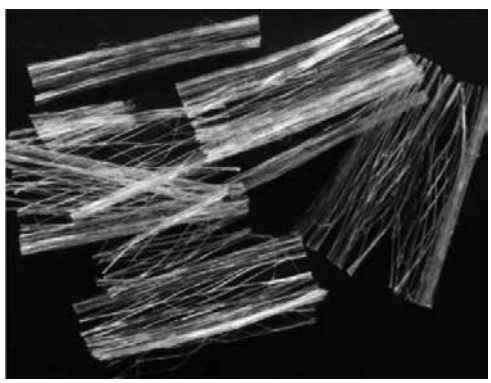

Figure 1. The network structure of polypropylene fibrillated fibres.

The fibrillated polypropylene fibres are produced since the early 1960s [50]. Because of relatively simple and inexpensive procedure as well as good mechanical properties, the production of such fibres became quickly a reasonable alternative for classical melt spinning. In next years, the technology was often used in the industrial practice and the fibres found a broad application on a large-scale production of sack cloth, ropes and carpet backing fabrics as well as agro-, geo- and different technical textiles.

The production of the fibrillated fibres is a multistage process. The process starts from the extrusion of the polypropylene melt through a flat die. The film is solidified by water quenching and then uniaxially drawn and thermally stabilised. Efficient quenching in liquid media allows higher stretching in subsequent proceedings steps. After stabilisation the film is cut into narrow tapes of width in the range of 1–20 mm and then split into fibrous material by needle

roller fibrillation unit. Finally, the fibres are taken-up on the winding device. By cutting and splitting of fibres regular network-like structure is achieved (**Figure 1**). The particular operations and processing conditions have a considerable influence on the structure and final properties of the fibres [51]. By the change of the formation parameters fibres with various mechanical and thermal parameters can be obtained [52].

For the reinforcement of concrete the fibrillated fibres chopped to the specific length between few mm and tens mm are used. The thickness of commercially available fibres corresponding to the thickness of the film ranges from 15 to 100 μm. For fibres the width of the individual fibrils equals 100–600 μm. The fibres have the specific surface area in the range of 80–600 mm^2/mm^3. The Young's modulus of fibres is in the range of 3–5 GPa, what is many times lower than the modulus of cementitious materials (15–40 GPa). The tensile strength of used fibres is about 140–690 MPa [8].

2. Experimental study

2.1. Samples

Two series of polypropylene fibrillated fibres were obtained. Fibres were produced in industrial conditions in Bezalin SA (Bielsko-Biala, Poland). For the production DPM and Starlinger StarEx 1500 production lines were used. The fibres were formed from the commercial polypropylene resin Moplen HP 456 J (Orlen Polyolefins, Poland) characterised by melt flow index 3.4 g/10 min with addition (2%) of polyethylene Bralen FB 2-30 (Slovnaft Petrochemicals, Slovakia).

Polypropylene films were extruded through a flat die into water and then were cut into narrow strips. After drawing and heat stabilisation, the strips were locally cut with a needle roller and split with the final stretching unit. The fibres with the linear density of 1000 tex were produced.

For the first series produced on DPM line two draw ratios: 8.66 and 9.83 and three velocities of the needle roller: 150, 180 and 200 [m/min] were applied. For the second series produced on Starlinger StarEx 1500 line, two draw ratios: 10 and 12 and four velocities of the needle roller: 155, 175, 195 and 215 m/min were used.

Selected fibres from the first series characterised by the best mechanical parameters: the highest tenacity and the highest Young's modulus were cut into segments with the length of 19 mm and were used for the preparation of samples of reinforced of concrete. The standard cubic samples with dimensions 150 mm × 150 mm × 150 mm were prepared. The fibres were mixed with the concrete in proportion 0.9 kg of fibres per cubic metre of concrete. After formation the samples were cured for 28 days.

The fibrillated fibres selected from the second series were chopped to specified lengths of 5, 10 and 15 mm and were mixed with the cement mortar. The cement mortars were prepared using Portland cement CEM I 42,5 R, sand and tap water in accordance to EN 197-1:2002 and EN 197-2:2002 standards. The mixtures with different content of fibres: 0.25, 0.5, 0.75 and 1%

http://dx.doi.org/10.5772/64386

by weight were obtained. The components were mixed with the laboratory mixer Multiserw. Wet mortars were poured into the rectangular prism moulds with dimensions 40 mm × 40 × 160 mm and allowed to harden in the open space. Then the samples were cured in water for 28 days.

2.2. Methods

The morphology of fibres and their mechanical properties were investigated. The morphology of fibres was studied using a scanning electron microscope JEOL JSM 5500 LV. Observations were carried out for the fibres sputtered with gold in JEOL 1200 ionic sputter.

The mechanical parameters of the fibrillated fibres: tenacity, elongation at break and Young's modulus were determined according to PN-EN ISO 5079 standard. The measurements were performed using a tensile machine INSTRON 1026.

Workability of the fresh concrete, density and air content were investigated according to the Polish standards PN-EN 12350-2:2001, PN-EN 12350-6:2001 and 12350-7:2001, respectively. According to the Polish norm PN-EN 12390-3-2002, the compressive strength of concrete before and after 150 freeze-thaw cycles was measured. According to the Polish norm PN-88/B the investigations of water absorbability were performed.

Basic mechanical parameters of mortars: the compressive and bending strength were determined according to the norm EN 196-1:2006. The measurements were carried out by the TECNOTEST KE 200/A tensile machine. For comparison the plain mortar specimen without fibres was tested.

After mechanical tests the morphology of the interfacial area of broken samples was analysed. The studies were performed with scanning electron microscope JEOL JSM 5500 LV.

3. Results

3.1. The morphology, supermolecular structure and properties of fibrillated fibres

Figure 2 presents SEM microphotographs of the surface of the fibres. **Figure 2a** presents longitudinal cuttings on the polypropylene strips produced by the needle roller mounted before the final drawing unit. At higher magnifications on the surface of the strips the fibrillar structure is clearly visible (**Figure 2b**). Fibrils are closed packed and well oriented along the strips. The diameter of the fibrils equals ca. 0.1 μm.

After cutting the strips with the needle roller and drawing, the splitting of the fibrils is observed. Due to weak intermolecular forces in polypropylene the cuttings propagate easily. As a result, strips partially disintegrate into fibres connected together in a network-like structure formed from flat fibres with the rectangular cross section and the diameter approximately of 500 μm. Between the adjacent fibres many links are still observed (**Figure 2c**). By intense drawing the number of links between the fibres decreases (**Figure 2d**).

For the fibres drawn at ratio 9.83 the tenacity is slightly higher. For both series of fibres, drawn at 8.66 and 9.83, the largest tenacity exhibit the fibres produced at the smallest needle roller velocity 150 m/min. With the increase in roller velocity the tenacity of fibres slightly decreases. In comparison to the fibres drawn at 8.66, elongation at break for the fibres drawn at 9.83 is higher. For both series of fibres elongation at break does not change with the change in the needle roller velocity. Fibres drawn at lower ratio 8.66 possess lower value of the Young's modulus, which is independent of the needle roller velocity. For the fibres drawn at ratio 9.83 the value of Young's modulus is higher. The fibres produced at low needle roller velocity possess the highest value. With the increase in the roller velocity the Young's modulus decreases.

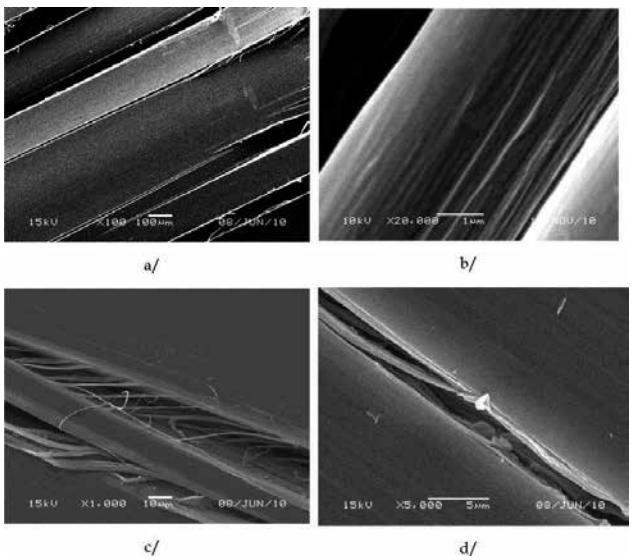

Figure 2. Surface morphology of fibrillated fibres: **(a)** longitudinal cuttings of polypropylene strips, **(b)** fibrillar structure of the strips, **(c)** links between adjacent fibres, and **(d)** splitting of fibres.

Table 1. presents mechanical parameters determined for the first series of investigated fibres.

Draw ratio	Needle roller velocity [m/min]	Tenacity [cN/tex]	Elongation at break [%]	Young's modulus [cN/tex]
8.66	150	37.5	32	1.92
	180	36.9	28	1.95
	200	34.7	30	1.89
9.83	150	38.0	21	3.2
	180	37.0	23	2.9
	200	37.0	23	2.7

Table 1. Mechanical parameters of fibrillated fibres produced on DPM line.

http://dx.doi.org/10.5772/64386

Table 2. presents mechanical parameters determined for the second series of fibres produced on Starlinger StarEx 1500 line.

Draw ratio	Needle roller velocity [m/min]	Tenacity [cN/tex]	Elongation at break [%]	Young's modulus [cN/tex]
10	155	42.3	24.7	2.61
	175	41.7	24.9	2.55
	195	41.4	25.0	2.70
	215	39.0	25.3	2.40
12	155	49.0	22.8	3.55
	175	47.7	23.1	3.20
	195	42.5	21.6	3.40
	215	41.0	21.5	2.95

Table 2. Mechanical parameters of fibrillated fibres produced on Starlinger StarEx 1500 line.

For this series larger tenacity exhibits fibres drawn at ratio 12. The largest tenacity possesses fibres fibrillated at 155 m/min. With the increase in the needle roller velocity the tenacity of fibres decreases. The elongation at break for fibres drawn at the higher ratio 12 is minimally lower in comparison to fibres drawn at the ratio 10. The elongation at break does not significantly change with the change in the needle roller velocity. The Young's modulus of fibres drawn at the ratio 12 is higher than the modulus of fibres drawn at the ratio 10. By the increase in the needle roller velocity the Young's modulus decreases.

3.2. Reinforcement of concrete

Table 3 presents parameters determined for the fresh concrete.

Sample	Workability [cm]	Density [kg/m^3]	Air content [%]
Without fibres	13	2329	1.9
With fibres	10	2315	2.3

Table 3. Parameters of fresh concrete for samples prepared with and without fibres.

The workability of the fresh concrete with fibres is lower in comparison to the sample without fibres. Addition of fibres results in a decrease in the concrete density and an increase in the air content.

Table 4 presents parameters determined for the unreinforced concrete and concrete reinforced with fibres.

Sample	Compressive strength [MPa]		Strength decrement [%]	Water absorbability
	Before freezing	After 150 freeze-thaw cycles		
Without fibres	45.4	33.3	26.7	6.5
With fibres	43.7	35.7	18.3	4.7

Table 4. Parameters of concrete for samples unreinforced and reinforced with fibrillated fibres.

For the concrete reinforced with fibres the compressive strength is minimally lower.

The influence of fibres on concrete compressive strength was repeatedly investigated. It was revealed that the compressive properties of fibre-reinforced concrete are relatively less affected by the presence of fibres as compared to the properties under tension and bending [53]. Studies of Naaman et al. [54] showed that with the addition of fibres there is an almost negligible increase in strength for mortar mixes. Richardson [55] stated that the compressive strength of concrete containing polypropylene fibres is significantly reduced. Mindess [56] reported that the compressive strength of concrete reinforced with fibrillated fibres is increased by 25%. Parveen and Sharma [57] observed the increase in the compressive strength of concrete at low fibres dosage up to 0.2% and the reduction in compressive strength above 0.2%. Alhozaimy et al. [18] suggested that polypropylene fibres have no statistically significant effect on compressive strength of concrete. Similarly, Aulia [58] revealed that the use of a certain amount of fibres in the concrete does not influence detrimentally its main mechanical parameters.

After freeze-thaw treatment the compressive strength of the concrete decreases significantly. For the reinforced concrete the decrement of the compressive strength is much lower. After 150 cycles the compressive strength of reinforced concrete becomes higher in comparison to the unreinforced concrete. Simultaneously, after freezing and thawing cycles the water absorbability of the reinforced concrete becomes considerably lower. On the surface of the unreinforced concrete many cracks are observed. In contrast, on the surface of the fibre-reinforced concrete microcrackings are not visible.

The obtained results clearly show that addition of fibres delays the concrete deterioration caused by repetitive freeze/thaw cycles.

It is known that freezing is harmful to porous and brittle materials as concrete. The influence of freezing on the concrete was repeatedly investigated and some freezing and thawing theories of concrete were proposed [59]. In investigations the positive effect of polypropylene fibres on the concrete compressive strength after freeze/thaw action was documented [55, 60, 61].

The resistance of fibre-reinforced concrete to freeze/thaw cycles is explained by the formation of air void system. The fresh concrete, which contains fibres, reveals lower density and higher air content. When the paste dries out, due to retained water, or low bleed characteristics, in

http://dx.doi.org/10.5772/64386

the concrete small water voids are created. Formation of fibres' water voids provides an air entrained system, which ensures subsequent freeze/thaw protection. Additionally in comparison to the surrounding concrete the fibres exhibit lower modulus of elasticity and lower density. When subject to freeze/thaw action the polypropylene yields under hydrostatic pressure before the concrete, thus providing further pressure relief. Richardson stated that fibres assist in blocking capillaries [60]. In this way fibres reduce water ingress, which contributes to lower water absorption of fibre-reinforced concretes.

3.3. Reinforcement of cement mortar

Table 5 shows the determined values of compressive and bending strength of cement mortars with fibres by different fibres' length and different fibres' dosage. For all fibres, regardless of the length of the fibres and their content, the compressive strength does not significantly change. The determined values are close to the compressive strength of the plain mortar [62].

Similarly as for reinforced concrete the influence of fibres on the compressive strength of mortars is less visible.

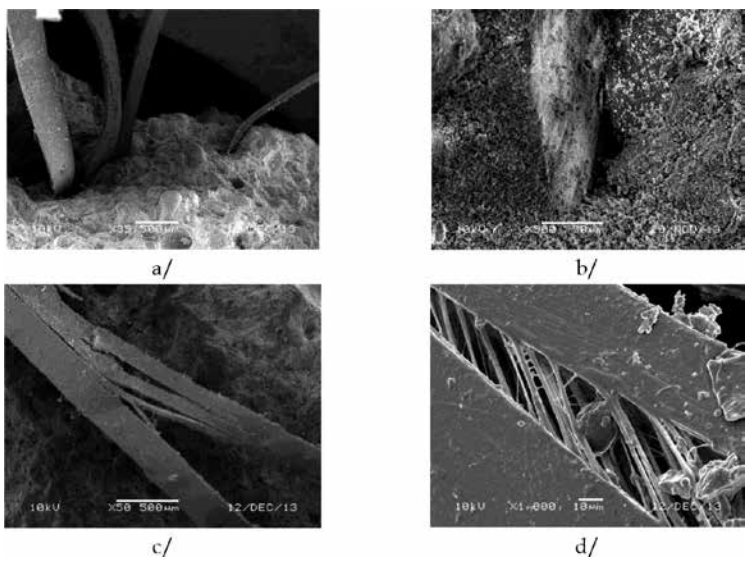

Figure 3. The SEM microphotographs of the fracture of mortars reinforced with fibrillated fibres. **(a)** Fibres anchored in the matrix, **(b)** the hole in the cement matrix after pulling out the fibres, **(c)** splitting of fibres, and **(d)** fibrillation of fibres.

The effect of fibres is more pronounced in the case of the bending strength. For mortars reinforced with the short and medium length fibres the bending strength is higher than the strength of the plain mortar. For these fibres with the increase in the fibre content till 0.75% the bending strength increases and then at the highest content decreases. For the longest fibres the bending strength is comparable with the strength of the plain mortar. At the lowest dosage

the bending strength is the highest. At medium dosages the bending strength is lower and then at the highest dosage is higher again.

In **Figure 3**, SEM microphotographs of fractures of samples after the mechanical tests are presented. In the pictures, the fibres' ends with different lengths, which protrude in different directions from the cement matrix, are visible (**Figure 3a**). Particular fibres are well separated and evenly distributed throughout the volume of the sample. The protruding ends are well anchored and cannot be manually pulled out from the mortar. In the second microphotograph the hole in the matrix, which remains after pulling out of fibres, is visible (**Figure 3b**).

One can observe that in the concrete the network structure of the fibrillated fibres is partially opened. Simultaneously further splitting into smaller particular fibrils is observed (**Figure 3c**). As a result of these processes the specific surface area of fibres increases, what significantly enhances their adhesion ability.

Length [mm]	Content [%]	Compressive strength [MPa]	Bending strength [MPa]
No fibres	–	16.3	5.5
5.0	0.25	16.5	5.8
	0.50	16.3	6.0
	0.75	16.4	5.6
	1.00	16.0	5.4
10.0	0.25	16.2	5.2
	0.50	16.3	6.0
	0.75	16.1	6.2
	1.00	16.3	5.8
15.0	0.25	16.2	5.9
	0.50	16.1	5.5
	0.75	16.1	5.3
	1.00	16.2	5.6

Table 5. The compressive and bending strength of reinforced mortars by different fibres' content and lengths.

Moreover, it is seen that the mortar ingredients can penetrate in the mesh between the individual fibrils and create additional mechanical bonds between fibres and matrix (**Figure 3d**).

In previous investigations it was revealed that the opening of the network structure and splitting contribute to the fibres matrix interaction and support mechanical anchoring of fibres in the matrix [63]. Bentur et al. stated that by the use of fibrillated fibres two effects contribute to the fibre-matrix interaction: interfacial adhesion and mechanical anchoring. The first is

http://dx.doi.org/10.5772/64386

apparently due to the intimate contact at the interface and the dense matrix developed in the transition zone. The second is associated with a combination of filamentising, where the fibres separate into multifilament strands, branching of fibrils and forming tiny fibrillations on the fibres' surface [64].

On the basis of obtained results one can conclude that during bending the pulling out of fibres' ends occurs. At the beginning of bending the interfacial zone is deformed. Due to the high difference in Young's modulus, deformations of the fibres and the surrounding cement matrix are not compatible. As a result, the adhesive connections linking fibres with cement mortar are disrupted. By further bending one end of a fibre stays firmly anchored in the mortar, while the other is pulled out from the cement matrix (**Figure 4**).

The highest bending strength was registered for fibre length of 10 mm and the fibre content of 0.75%. By this length, during mixing of the mortar, the fibres remain straight and do not bend or tangle. Fibres of this length have relatively large contact surface to form a sufficient number of adhesive connections with the mortar components and to provide high friction forces during pulling fibres' ends out of the matrix. For shorter fibres the contact area is smaller, what consequently leads to the lower number of adhesive connections and lower friction. Fibres longer than 10 mm exhibit greater contact surface, but have a tendency to bend and tangle. Such tendencies reduce efficiency of reinforcement and leads to the decrease in the bending strength of the mortar. The fibre content of 0.75% ensures the sufficient number of connections sewing lips of the crack.

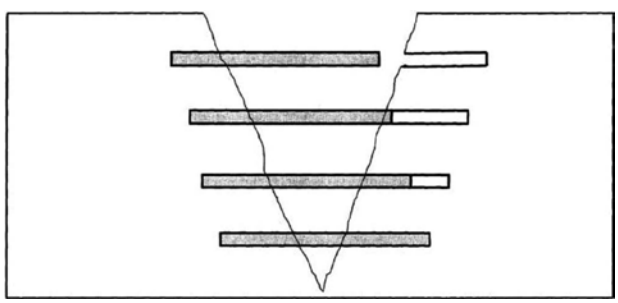

Figure 4. The mechanism of fibres/matrix interaction during bending.

4. Conclusions

The mechanical parameters of fibrillated polypropylene fibres are strongly influenced by the formation parameters. High draw ratio and low needle roller velocity promote formation of fibres with high tenacity and high Young's modulus. By optimizing the formation parameters, the appropriate fibres for the reinforcement of concrete can be produced.

Fibres added to the concrete improve the parameters of a fresh concrete. Fibres have a relatively little effect on the compressive strength of concrete before freezing. The beneficial effect of

fibres is revealed after freezing and thawing cycles. After multiple freeze/thaw cycles the compressive strength of reinforced concrete exceeds the strength of plain concrete. Simultaneously, the reinforced concrete exhibits lower water absorbability.

The fibrillated fibres do not affect the compressive strength of the reinforced cement mortars. Independently on the fibres' length and their dosage the compressive strength of the reinforced mortar does not change and is equal to the strength of the plain mortar. The fibres cause the change of the mortar bending strength. The increase in the bending strength results from enhanced interfacial adhesion and mechanical anchoring, which results from opening of the network structure and splitting of fibrillated fibres.

Author details

Jan Broda

Address all correspondence to: jbroda@ath.bielsko.pl

University of Bielsko-Biala, Bielsko-Biala, Poland

References

[1] Naaman AE. Engineered steel fibers with optimal properties for reinforcement of cement composites. Journal of Advanced Concrete Technology 2003;1:241–252.

[2] Swamy RN. Fibre reinforcement of cement and concrete. Materials and Structures 1975;8:235–254.

[3] Zheng Z, Feldman D. Synthetic fibre—reinforced concrete. Progress in Polymer Science 1995;20:185–210.

[4] Petri M. Wlasciwosci zapraw modyfikowanych ultrakrotkimi włoknami PAN, Cement, Wapno, Beton. 1999;4/66:45–48.

[5] He J, Huang XQ, Tian CY. Experimental study on the anti-cracking property of basalt fiber for cement-based materials. Advanced Materials Research. 2011;328–330:1351–1354.

[6] Pakravan HR, Jamshidi M, Latifi M, Pacheco-Torgal F. Cementitious composites reinforced with polypropylene, nylon and polyacrylonitrile fibres. Materials Science Forum. 2013;730–732:271–276.

[7] Mukhopadhyay S, Khatana S. A review on the use of fibers in reinforced cementitious concrete. Journal of Industrial Textiles. 2014;45:1–26.

http://dx.doi.org/10.5772/64386

[8] Bentur A, Mindess S. Fibre Reinforced Cementitious Composites. New York: Taylor & Francis; 2007. ISBN: I0:0-415-25048.

[9] Gu J, Shen Q, He X, Yan B. Combined impacts of polypropylene fibres on workability, strength and permeability of SCC. Magazine of Concrete Research 2014;66:127–140.

[10] Song PS, Hwang S, Sheu B. Strength properties of nylon and polypropylene fiber reinforced concretes. Cement and Concrete Research 2005;35:1546–1550.

[11] Zhang S, Zhao B. Effect of polypropylene fibres on the toughness of concrete materials. Advanced Materials Research 2012;535–537:1965–1968.

[12] Segre N, Tonella E, Joekes I. Evaluation of the stability of polypropylene fibres in environments aggressive to cement-based materials. Cement and Concrete Research 1998;28:75–81.

[13] Banthia N, Gupta R. Influence of polypropylene fiber geometry on plastic shrinkage cracking in concrete. Cement and Concrete Research 2006;36:1263–1267.

[14] Aly T, Sanjayan JG, Collins F. Effect of polypropylene fibers on shrinkage and cracking of concretes. Materials and Structures 2008;41:1741–1753.

[15] Bagherzadeh R, Sadeghi AH, Latifi M. Utilizing polypropylene fibers to improve physical and mechanical properties of concrete. Textile Research Journal. 2011;82 (1): 88–96.

[16] Barluenga G. Fibre-matrix interaction at early ages of concrete with short fibres. Cement and Concrete Research 2010;40:802–809.

[17] Zollo RF. Fiber-reinforced concrete: an overview after 30 years of development. Cement and Concrete Composites 1997;19:107–122.

[18] Alhozaimy AM, Soroushian P, Mirza F. Mechanical properties of polypropylene fiber reinforced concrete and the effects of pozzolanic materials. Cement and Concrete Research 1996;18:85–92.

[19] Sun Z, Xu Q. Microscopic, physical and mechanical analysis of polypropylene fiber reinforced concrete. Materials Science and Engineering 2009;527:198–204.

[20] Khaliq W, Kodur V. Thermal and mechanical properties of fibre reinforced high performance self-consolidating concrete at elevated temperatures. Cement and Concrete Research 2011;41:1112–1122.

[21] Kakooei S, Akil HM, Jamshidi M, Rouhi J. The effects of polypropylene fibres on the properties of reinforced concrete structures. Construction and Building Materials 2012;27:73–77.

[22] Cifuentes H, Garcia F, Maeso O, Medina F. Influence of the properties of polypropylene fibres on the fracture behaviour of low-, normal- and high-strength FRC. Construction and Building Materials 2013;45:130–137.

[23] De Castro AL, Tibba PRT, Pandolfelli VC. Polypropylene fibers and their influence on the behaviour of concretes exposed to high temperatures. Review. Cerâmica 2011;57:22–31.

[24] Liu X, Ye G, Schutter GD, Yuan Y, Taerwe L. On the mechanism of polypropylene fibres in preventing fire spalling in self-compacting and high-performance cement paste. Cement and Concrete Research 2008;38:487–499.

[25] Richardson AE, Coventry K, Bacon J. Freeze/thaw durability of concrete with recycled demolition aggregate compared to virgin aggregate concrete. Journal of Cleaner Production 2011;19:272–277.

[26] Richardson AE, Coventry KA, Wilkinson S. Freeze/thaw durability of concrete with synthetic fibre additions. Cold Regions Science and Technology. 2012;83–84:49–56.

[27] Cen GP, Ma GP, Wang ST, Zhang L. Durability of synthetic fiber reinforced concrete for airport pavement. Journal of Traffic and Transportation Engineering. 2008;8:43–45+51.

[28] Zhang H, Wang XS, Hao PW. Study on the performance of polypropylene fiber concrete. Applied Mechanics and Materials. 2012;174–177:91–96.

[29] Kumar R, Goel P, Mathur R. Suitability of synthetic fiber for the construction of concrete pavements. Journal of Scientific and Industrial Research 2014;73:448–452.

[30] Tu L, Kruger D, Wagener JB, Carstens PAB. Wettability of surface oxyfluorinated polypropylene fibres and its effect on interfacial bonding with cementitious matrix. Journal of Adhesion 1997;62:187–211.

[31] Li VC, Stang H. Interface property characterization and strengthening mechanisms in fibre reinforced cement based composites. Advanced Cement Based Materials 1997;6:1–20.

[32] Yue CY, Cheung WL. Interfacial properties of fibre-reinforced composites. Journal of Material Science. 1992;27:3843–3855.

[33] Singh S, Shukla A, Brown R. Pullout behavior of polypropylene fibers from cementitious matrix. Cement and Concrete Research 2004;34:1919–1925.

[34] DiFrancia C, Ward TC, Claus RO. The single-fibre pull-out test. 1. Review and interpretation. Composites: Part A. 1996;27A:597–612.

[35] DiMaggio R, Franchini M, Guerrini G, Poli G, Migliaresi C. Fibre-matrix adhesion in fibre reinforced CAC-MDF composites. Cement and Concrete Composites 1997;19:139–147.

[36] Peled A, Zaguri E, Marom G. Bonding characteristic of multifilament polymer yarns and cement matrices. Composites: Part A 2008;39:930–939.

[37] Inagaki N, Tasaka S, Imai M. Hydrophilic surface modification of polypropylene films by CCl_4 plasma. Journal of Applied Polymer Science 1993;48:1963–1972.

[38] Carstens PAB, Marais SA, Thompson CJ. Improved and novel surface fluorinated products. Journal of Fluorine Chemistry 2000;104:97–107.

[39] Bhat NV, Upadhyay DJ. Plasma induced surface modification and adhesion enhancement of polypropylene surface. Journal of Applied Polymer Science 2001;86:925–936.

[40] Carrino L, Moroni G, Polini W. Cold plasma treatment of polypropylene surface: a study on wettability and adhesion. Journal of Materials Processing Technology 2002;121:373–382.

[41] Felekoglu B, Tosun K, Baradan B. A comparative study on the bending performance of plasma treated polypropylene fibre reinforced cementitious composites. Journal of Materials Processing Technology 2009;209:5133–5144.

[42] López-Buendía AM, Romero-Sanchez MD, Climent V, Guillem C. Surface treated polypropylene (PP) fibres for reinforced concrete. Cement and Concrete Research 2013;54:29–35.

[43] Peled A, Guttman H, Bentur A. Treatments of polypropylene fibres to optimize their reinforcing efficiency in cement composites. Cement and Concrete Composites 1992;14:277–285.

[44] Mirabedini SM, Rahimi H, Hamedifar S, Mohseni M. Microwave irradiation of polypropylene surface: a study on wettability and adhesion. International Journal of Adhesion and Adhesives. 2004;24:163–170.

[45] Merhej T, Cheng LL, Feng DC. Polypropylene fiber reinforced concrete for rigid airfield pavement. Advanced Materials Research. 2011;228–229:627–633.

[46] Sounthararajan VM, Thirumrugan S, Sivakumar A. Reinforcing efficiency of crimped profile of polypropylene fibres on the cementitious matrix. Research Journal of Applied Sciences, Engineering and Technology 2013;6:2662–2667.

[47] Goel P, Kumar R, Mathur R. An experimental study on concrete reinforced with fibrillated fiber. Journal of Scientific and Industrial Research 2012;71:722–726.

[48] Goel P, Kumar R, Mathur R. Performance of concrete containing polypropylene multifilament fibre vis-a vis fibrillated fibres. Indian Concrete Journal 2014;88:16–24.

[49] He X, Cao Y. Mechanical properties o self-compacting concrete reinforced with fibrillated polypropylene fiber and their relationship. Journal of Basic Science and Engineering. 2014;22:501–511.

[50] Krassig HA. Fiber Technology: From Film to Fiber. Marcel Decker Inc., 1984. ISBN: 0-8247-7097-8.

[51] Baczek M, Slusarczyk C, Broda J. Crystalline and lamellar structure of polypropylene fibrillated fibres. Solid State Phenomena. 2013;203–204:439–442.

[52] Broda J, Przybylo S, Lewandowski S. Selection of optimal formation parameters of polypropylene fibrillated fibres designed for concrete reinforcement. Fibres & Textiles in Eastern Europe 2012;20:69–74.

[53] Mazaheripour H, Ghanbarpour S, Mirmoradi SH, Hosseinpour I. The effect of polypropylene fibres on the properties of fresh and hardened lightweight self-compacting concrete. Construction and Building Materials 2011;25:351–358.

[54] Naaman AE, Moavenzadeh F, MaGarry FJ. Probabilistic analysis of fiber reinforced concrete. Journal of Engineering Mechanics 1974;100:397–413.

[55] Richardson AE. Compressive strength of concrete with polypropylene fibre additions. Structural Survey 2006;24:138–153.

[56] Mindess S. Properties of concrete reinforced with fibrillated fibres under impact loading. Cement and Concrete Research 1988;18:109–115.

[57] Parveen, Sharma A. Structural behaviour of fibrous concrete using polypropylene fibres. International Journal of Modern Engineering Research. 2013;3:1279–1282.

[58] Aulia TB. Effects of polypropylene fibres on the properties of high-strength concretes. Lacer. 2002;7:43–59.

[59] Pentalla V. Surface and internal deterioration of concrete due to saline and non-saline freeze–thaw loads. Cement and Concrete Research 2006;36:921–928.

[60] Richardson AE. Freeze/thaw durability in concrete with fibre additions. Structural Survey 2003;21:225–233.

[61] Cavdar A. Investigation of freeze–thaw effects on mechanical properties of fiber reinforced cement mortars. Composites: Part B 2014;58:463–472.

[62] Broda J, Brachaczek W. Influence of the polypropylene fibres geometry on mechanical properties of cement mortars. Fibres & Textiles in Eastern Europe 2015;23:123–129.

[63] Nanni N, Meamarian N. Distribution and opening of fibrillated polypropylene fibres in concrete. Cement and Concrete Research 1991:13:107–114.

[64] Bentur A, Mindess S, Vondran G. Bonding in polypropylene fibre reinforced concretes. International Journal of Cement Composites and Lightweight Concrete 1989;11:153–158.

Edited by Salih Yilmaz and Hayri Baytan Ozmen

Concrete is widely used because of its versatility, affordability, and availability of raw materials, strength, and durability. Urban development that took place through the world in the last few decades yielded significant developments for concrete technology. The term high-performance concrete (HPC) is relatively new, and it refers to many properties such as strength, durability, sound and heat insulation, waterproofing, and side advantages such as air purification, self-cleaning, etc. Researchers and engineers are constantly working for improving concrete properties. This book provides the state of the art on recent progress in the high-performance concrete applications written by researchers and experts of the field. The book should be useful to graduate students, researchers, and practicing engineers in related fields.

ISBN 978-953-51-5786-1

Photo by stillfx / Can Stock

IntechOpen